Atomic clock comparisons with a 3×10^{-16} uncertainty via geostationary satellites

Von der Fakultät für Mathematik und Physik
der Gottfried Wilhelm Leibniz Universität Hannover

zur Erlangung des akademischen Grades
Doktorin der Naturwissenschaften
Dr. rer. nat.

genehmigte Dissertation von

Dipl.-Phys. Franziska Riedel

2021

Referent: PD Dr. Ekkehard Peik
Korreferentin: Prof. Dr. Tanja Mehlstäubler
Korreferent: Prof. Dr. Philip Tuckey
Tag der Promotion: 30.07.2020

Abstract

Optical clocks are superior to all other clocks, reaching 10^{-18} in their uncertainty. This makes them not only attractive for the field of fundamental research, like testing General Relativity or examining the variance of fundamental constants, but marks them also as potential candidates for the new definition of the second. An essential step towards that direction is the possibility to carry out comparisons of optical clocks at remote sites to have consistency checks of clocks constructed mostly independently by different groups.

Satellite-based techniques offer the possibility of simultaneous comparisons over a large variety of baselines. Their instability, however, has been demonstrated to be in the low 10^{-15} range at 1 d averaging time for most measurements. In case of two-way satellite time and frequency transfer (TWSTFT), the instability is limited by the modulation bandwidth of the signal. For this work, the full bandwidth of 20 Mchip/s of the commonly used TWSTFT equipment, a SATRE modem, is employed, providing a potential improvement of a factor of 20 with respect to the currently performed TWSTFT measurements for the time scale comparisons contributing to TAI.

This technique is used in this work to compare five optical clocks and six microwave fountain clocks located at four different European metrology institutes simultaneously over a period of 26 d. In order to prepare this measurement, extensive studies on the SATRE modem are carried out and presented, and other aspects that need to be taken into account for TWSTFT measurements with low instabilities are discussed, such as atmospheric delays, geometric and relativistic effects and laboratory and roof station setups.

The link instability of TWSTFT during the measurement campaign is presented, and compared to the instability of GPS Precise Point Positioning, that is implemented as an additional, independent comparisons technique for the campaign.

Relative frequency differences of the optical and the fountain clocks are calculated. For that, a processing was introduced that combines phase and frequency data of different noise types and gaps. A respective estimator for the statistical uncertainty, based on the correlation on the data, is established. The results of both satellite-based techniques show good agreement with each other, and also clocks based on the same frequency transition agree within a 1-σ-uncertainty. The overall uncertainties obtained for TWSTFT are between 2.7×10^{-16} and 3.5×10^{-16} for the optical clock comparisons. Limitations for the uncertainties of the measurements are discussed in detail, the available satellite-based techniques are evaluated with respect to their advantages and drawbacks for similar measurements in the future.

Keywords: Frequency comparison, TWSTFT, Optical clock.

Contents

1 Introduction **1**
1.1 Towards a redefinition of the second with a new generation of atomic clocks . . . 2
1.2 This work . . . 3

2 Frequency standards and their comparison **7**
2.1 Statistical analysis of frequency and time signals . . . 7
2.2 Frequency standards . . . 11
2.2.1 Primary frequency standards . . . 11
2.2.2 Other frequency standards . . . 12
2.2.3 Frequency standards and time scales . . . 12
2.3 Comparison of frequency standards . . . 13
2.3.1 Two-way satellite time and frequency transfer (TWSTFT) . . . 14
The TWSTFT setup . . . 16
Non-reciprocal delays on the signal path and other sources of disturbance . . . 19
The instability of TWSTFT . . . 21
2.3.2 Frequency transfer using Two-Way Carrier Phase . . . 22
2.3.3 Time and frequency transfer via GNSS satellites . . . 23
2.3.4 Other methods of comparison . . . 25
Transportable atomic clocks . . . 25
Optical fibers . . . 25

3 Setup and preparation of the broadband TWSTFT clock comparisons **27**
3.1 SATRE Modem measurements at high chip rates . . . 28
3.1.1 Instabilities at different chip rates . . . 29
3.1.2 Long-term instability . . . 31
3.1.3 Sources of disturbances and irregularities . . . 34
Temperature sensitivity . . . 34
Internal frequency cross-talk . . . 38
Phase jumps at relock onto the signal . . . 39
3.1.4 PRN code dependence . . . 40
3.2 Preparation of the ground stations . . . 43
3.3 Selection of satellite . . . 47
3.4 Scheduling of the TW links . . . 48

4 The satellite link test campaign **51**
4.1 Data recorded during the campaign . . . 51
4.2 Data processing . . . 55
4.3 Satellite link instability . . . 55

5 The clock comparison campaign **61**
5.1 Changes in setup and schedule . . . 61

5.2 Events during the campaign . . . 62
5.3 Satellite link analysis . . . 64
5.3.1 Comparison of broadband TWSTFT and TWCP during the campaign . . . 68
5.3.2 Broadband TWSTFT and GPS PPP during the campaign . . . 69
5.4 Corrections of TWSTFT measurements . . . 71
5.4.1 Correction of atmospheric effects on TWSTFT . . . 71
Influence of ionosphere . . . 73
Influence of troposphere . . . 81
5.4.2 Correction of the Sagnac effect . . . 81

6 Analysis of the clock comparisons 85
6.1 Clocks operated during the campaign . . . 86
6.2 Calculating the relative frequency difference between optical clocks . . . 88
6.2.1 The tool for the uncertainty estimation . . . 90
6.2.2 The calculation of the mean . . . 91
6.2.3 Estimation of the statistical uncertainty . . . 93
6.2.4 Estimation of the systematic uncertainty . . . 94
6.3 Calculating the relative frequency difference between microwave frequency standards (fountain clocks) . . . 95
6.3.1 Estimation of the uncertainty . . . 96
6.4 Discussion of results . . . 98

7 Conclusion 105

A Technical parameters and setup details for the measurement campaigns 111
A.1 Supplementary material for the SATRE modem characterization measurements . . . 111
A.2 Technical parameters and setups during the link test campaign . . . 114
A.3 Technical parameters and setups during the clock comparison campaign 114

B Derivation of a tool for determining the statistical uncertainty 117
B.1 Finding an estimator for ρ . . . 119
B.2 Accounting for gaps on the data . . . 121
B.3 Comments on biases . . . 124
B.4 Discussion of the correlations on the data used in this work . . . 125

Bibliography 127

List of Abbreviations

Institutes and laboratories

BIPM	**B**ureau **I**nternational des **P**oids et **M**esures
DLR	**D**eutsches **L**uft- und **R**aumfahrtzentrum
ESA	**E**uropean **S**pace **A**gency
INRIM	**I**stituto **N**azionale di **RI**cerca **M**etrologica
JPL	**J**et **P**ropulsion **L**aboratory
LNE-SYRTE	**L**aboratoire **N**ational de métrologie et d'**E**ssais - **SY**stème de **R**éférences **T**emps-**E**space
LUH	**L**eibniz **U**niversität **H**annover
METAS	**MET**rologie und **A**kkreditierung **S**chweiz (Acronym used for Eidgenössisches Institut für Metrologie)
MPQ	**M**ax **P**lanck Institut für **Q**uantenoptik
NICT	**N**ational Institute of **I**nformation and **C**ommunications **T**echnology
NIST	**N**ational **I**nstitute of **S**tandards and **T**echnology
NOAA	**N**ational **O**ceanic and **A**tmospheric **A**dministration
NPL	**N**ational **P**hysical **L**aboratory
NRCan	**N**ational **R**essources **Can**ada
PTB	**P**hysikalisch-**T**echnische **B**undesanstalt
ROB	**R**oyal **O**bservatory of **B**elgium
USNO	**U**nited **S**tates **N**aval **O**bservatory

Other abbreviations

AC	**A**tomic **C**lock
ACES	**A**tomic **C**lock **E**nsemble in **S**pace
ACF	**A**uto**c**orrelation **F**unction
CCS	**C**ode **C**ombination **S**ession
CIPM	**C**omité **I**nternational des **P**oids et **M**esures
CP	**C**arrier **P**hase
CSO	**C**ryogenic **S**apphire **O**scillator
cw	continuous **w**ave
DC	**D**own**c**onverter
DLL	**D**elay-**L**ocked **L**oop
EAL	**É**chelle **A**tomique **L**ibre (Free Atomic Time)
FC	**F**ountain **C**lock
FTZ	**F**irst **T**ransition through **Z**ero
GLONASS	**GLO**balnaja **NA**wigazionnaja **S**putnikowaja **S**istema
GNSS	**G**lobal **N**avigation **S**atellite **S**ystem
GPS	**G**lobal **P**ositioning **S**ystem
GS	**G**round **S**tation

GUM	**G**uide to the Expression of **U**ncertainty in **M**easurement
HM	**H**ydrogen **M**aser
IGS	**I**nternational **G**NSS **S**ervice
IPPP	**I**nteger **P**recise **P**oint **P**ositioning
ITOC	**I**nternational **T**ime Scales with **O**ptical **C**locks
ITU	**I**nternational **T**elecommunication **U**nion
LNA	**L**ow **N**oise **A**mplifier
MAD	**M**edian **A**bsolute **D**eviation
MITREX	**MI**crowave **T**ime and **R**anging **EX**periment
MJD	**M**odified **J**ulian **D**ate
NMI	**N**ational **M**etrology **I**nstitute
OC	**O**ptical **C**lock
PFS	**P**rimary **F**requency **S**tandard
PPP	**P**recise **P**oint **P**ositioning
PPS	**P**ulse **P**er **S**econd
PRN	**P**seudo-**R**andom **N**oise
RF	**R**adio **F**requency
SA	**S**pectrum **A**nalyser
SATRE	**SA**tellite **T**ime and **R**anging **E**quipment
SDR	**S**oftware-**d**efined **R**adio
SES	**S**ociété **E**uropéenne des **S**atellites
SES	**S**uper **H**igh **F**requency
SI	**S**ystème **I**nternational d'unités
SRS	**S**econdary **R**epresentation of the **S**econd
SSPA	**S**olid-**S**tate **P**ower **A**mplifier
sTEC	**s**lant **TEC**
TAI	**T**emps **A**tomique **I**nternational (International Atomic Time)
TEC	**T**otal **E**lectron **C**ontent
TIC	**T**ime **I**nterval **C**ounter
TS	**T**ime **S**cale
TTTOF	**T**ime **T**ransfer **T**hrough **O**ptical **F**ibers
TW	**T**wo-**W**ay **C**arrier **P**hase
TWCP	**T**wo-**W**ay
TWOTT	**T**wo-**W**ay **O**ptical **F**iber **T**ime **T**ransfer
TWSTFT	**T**wo-**W**ay **S**atellite **T**ime and **F**requency **T**ransfer
UC	**U**pconverter
UTC	Coordinated Universal Time/ Temps Universel Coordonné
VHF	**V**ery **H**igh **F**requency
VLBI	**V**ery **L**ong **B**aseline **I**nterferometry
VSAT	**V**ery **S**mall **A**perture **T**erminal
vTEC	**v**ertical **TEC**

Chapter 1

Introduction

Time has always played a major role in our life. Its concept has inspired countless philosophers and artists in the past and present, while daily and seasonal periodic changes put structure and organization into our lives. Today, timing is even more important since our lives had become faster and faster with respect to the flow of information and the amount of activities. The metrology of time and the way we perceive and use it is based on two fundamental aspects: the duration of a given time interval and a fixed point in time with respect to a reference, a time scale. Of course, both are not independent: While an interval can be seen as the difference of two fixed points, a time scale is created by counting intervals of a well-defined length.

For a long time, the rotation of the Earth has been the basis for any definition of a time scale or the basis time unit, the second. Until 1960, it was defined within the International System of units (SI, Système International d'unités) as the $1/86400^{\text{th}}$ part of the mean solar day. Another astronomic definition, based on the orbital revolution of the Earth around the Sun, was put into effect for a short period after. But advanced technologies had brought more precise clocks, revealing that the Earth's movement, both the rotation and the orbital revolution, is too irregular to be used for the definition of the second in the future. The new definition from 1967 on is based on a hyperfine transition within the cesium isotope ^{133}Cs: 1 s is the duration of 9,192,631,770 periods of the radiation of this transition [1, 2]. This transition is realized in Cs atomic clocks with an accuracy between 10^{-12} (in commercial clocks) and 10^{-16} (in the best laboratory setups) and can be converted into frequency and pulse signals for dissemination and the generation of a time scale. Today, the signals of more than 400 atomic clocks worldwide are compared and the data are collected to generate UTC (Universal Coordinated Time).

Applications for time and frequency measurements with high accuracy and stability range from telecommunication networks, power grids, and navigation to radio astronomy and fundamental research. A further increase of accuracy and stability and a new definition of the second with higher precision would bring benefits to all of these fields, especially navigation and research. Currently, atomic oscillators based on the Cs transition or other transition frequencies as in rubidium or hydrogen are installed on board of the satellites of all Global Navigation Satellite Systems (GNSS), as GPS (Global Positioning System), Galileo, GLONASS (GLObalnaja NAwigazionnaja Sputnikowaja Sistema) or Beidou, gaining navigation accuracies down to few meters for civil users [3–6]. In the research domain, atomic clocks can contribute to the the test of Einstein's theory of General Relativity or the question of time variation of fundamental constants [7–11]. As an example, one worldwide coordinated

research project working on these goals is the ACES project (Atomic Clock Ensemble in Space), funded by the European Space Agency (ESA), where atomic clocks will be installed on board of the International Space Station [12]. These clocks, a laser-cooled Cs clock and a hydrogen maser, will be compared as an ensemble with atomic clocks at dedicated ground stations with different techniques. High accuracies in atomic clocks do also allow for measuring the differences in the gravitational field for geodesy by determining the gravitational redshift [13–15].

1.1 Towards a redefinition of the second with a new generation of atomic clocks

Within the past fifteen years, a new generation of atomic clocks was developed, based on transitions between energy levels corresponding to radiation in the optical frequency range, hence the so-called optical clocks. Suitable transitions were identified in several elements, like strontium, ytterbium, mercury, aluminum and calcium [10, 16–20]. While the best Cs clocks today, Cs fountain clocks, can reach uncertainties down to a few parts in 10^{16} [21–27], optical clocks have been proven to exceed this lower limit by one order of magnitude or more. This marks them as promising candidates for a redefinition of the second [28–30]. For a proper redefinition, the common approach is to chose one transition, while recently also the idea of a definition based on a weighted mean of different frequencies was developed [31]. But in either way, the best transitions with respect to uncertainty, reliability and reproducibility need to be selected. For that, the few existing clocks need to undergo a careful evaluation: Clocks of the same transition are often constructed independently from each other by different institutes. For a redefinition, several comparisons with respective low uncertainties between clocks of the same and of different types need to be carried out. Although they show a low instability when measured locally against another optical clock, remote comparisons with satisfying uncertainty and instability could only be carried out rarely. The frequency evaluation of these clocks with respect to the current definition of the second is limited by the instabilities and uncertainties of the Cs clocks. In addition, although both the Cs fountains and the optical clocks are complex laboratory setups, the optical clocks require more work in most cases when in operation, leading to only short periods of measurement that might have gaps.

One of the projects representing a step towards the redefinition is the ITOC project (International Time scales with Optical Clocks), a project between several European metrology institutes [32], founded by the European Union within the European Metrology Research Programme. In order to gather as much information as possible about the optical clocks located at these institutes, local comparisons between these clocks and measurements against Cs clocks should be carried out while assessing the lowest uncertainties possible to provide the most recent and significant results for these clocks. Furthermore, transportable optical clocks should be constructed both as a proof of concept and to provide a new possibility of remote comparisons. A sophisticated calculation for analyzing all available results to check for consistency and to gain the most accurate value for a frequency transition should be developed, a frequency ratio matrix. For that, also results obtained by comparing the same pair of different optical clocks locally at different laboratories are quite important. In an additional step, the impact of optical clocks used in time scales on international

level should be evaluated. This includes the assessment of remote comparison techniques, the handling of gaps on the data but also the analysis of relativistic effects that affect either the clocks directly or the comparison techniques.

1.2 This work

To both test remote techniques and to carry out comparisons of optical clocks, one of the main goals within the ITOC project is a simultaneous remote comparison between optical clocks located at the European institutes INRIM (Istituto Nazionale di RIcerca Metrologica, Torino, Italy), LNE-SYRTE (Laboratoire National de métrologie et d'Essais - SYstème de Références Temps-Espace, Paris, France), NPL (National Physical Laboratory, Teddington, UK) and PTB (Physikalisch-Technische Bundesanstalt, Braunschweig, Germany). A simultaneous comparison enables a better cross-check of the clocks' frequencies and can be used to identify discrepancies occurring within a certain time of operation. Remote comparisons of clocks can be carried out by using transportable clocks, optical fibers or satellites. Each technique provides different advantages and drawbacks. A few transportable optical clocks have been developed [33–35], but besides their limitation in uncertainty and instability due to technical compromises and complexity in operation, comparisons between remote stationary clocks cannot be carried out simultaneously. Optical fibers provide instabilities lower than optical clocks, but are only available on a few selected baselines, so far only within one country or between neighboring countries, since a cascade of equipment like amplification and repeater is necessary [36–39]. In recent years, a few international optical clock comparison could be carried out [40–42], but the availability of links between laboratories operating optical clocks is still strictly limited.

Simultaneous remote comparisons can be best carried out by using satellites. Both navigation and geostationary satellites are used daily for comparisons of atomic clocks and time scales over all lengths of baselines from a few hundreds of kilometers up to almost ten thousand of kilometers. The signal of navigation satellites can be used to compare the reference time of several remote GNSS receivers. The accuracy of these comparisons benefits from the improvements on the signal made for a higher accuracy of navigation, but apart from these improvements parameters of the signal cannot be changed in favor of temporary time comparisons. Only with additional changes or additional steps in the post-processing of data by using additional information about the satellite and the atmosphere, and using additional aspects of the signal (measurement of pseudoranges with respect to the modulated code on the carrier and the phase of the carrier), an improvement in instability and accuracy could be achieved within the last fifteen years. A technique using both code and carrier measurements and benefiting in post-processing from data about satellite orbits and clocks and other aspects relevant for the signal path is the Precise Point Positioning (PPP) technique [43, 44]. With this, instabilities of 1×10^{-15} or lower can be achieved at 1 d averaging time [45]. In the past few years, an improvement was implemented, the so-called Integer PPP (IPPP) [46], which shows improvements for long averaging times and thus reaches instabilities below 1×10^{-15} at 1 d averaging time or even below 1×10^{-16} at 10 d, but is not openly available yet.

Another technique, called Two-Way Satellite Time and Frequency Transfer (TWSTFT), uses geostationary satellites. As indicated by the name, it is a two-way technique, i.e. based on a simultaneous bidirectional exchange of a modulated signal by the stations via the satellite. The main device of each ground station is a modem, where several parameters can be changed that have an impact on the overall instability of the signal, like signal power and modulation bandwidth. The choice of these parameters is limited by the agreement with the satellite operator, that allows only for a limited power, which is usually in a given range for all measurements, and sets the available bandwidth on the satellite transponder.

Up to now, most of all TWSTFT operations were carried out with a modulation bandwidth of 1 Mchip/s or 2.5 Mchip/s, which yield instabilities in the low 10^{-15} range at 1 d averaging time. By leasing a corresponding large bandwidth on the satellite transponder, 34 MHz, a significantly higher modulation rate of the modem can be used, 20 Mchip/s. This corresponds to the maximum modulation rate of the SATRE (SAtellite Time and Ranging Equipment) modem, which is installed in most laboratories using TWSTFT. A high bandwidth TWSTFT experiment like this was never carried out before. Measurements with bandwidths up to 5 Mchip/s predict an instability in the low range of 10^{-16} at 1 d averaging time for a bandwidth of 20 Mchip/s, thus a reduction of about a factor 10 compared to the TWSTFT operations carried out today [47].

This potential improvement was used for this work. The comparison of optical clocks located at the four different European institutes and thus developed and constructed by different research groups was carried out by using 20 Mchip/s TWSTFT. For that, the respective bandwidth was made available on a satellite transponder for approximately one month in order to further decrease the instability with longer measurement time and therefore to gain a final comparison uncertainty in the low 10^{-16}. Although this is still larger than the uncertainties of local optical clock comparisons, the simultaneity of the measurement can reveal certain aspects of the single clocks and therefore serve as consistency check. Furthermore, the campaign represents a proof-of-concept for this broadband technique and its potential benefit with respect to the instability, since broadband TWSTFT with 100 Mchip/s is part of measurements in the framework of ACES, and might be considered for other future measurement campaigns.
In parallel to TWSTFT, GPS PPP was implemented as an additional independent comparison technique for the clock comparison. Furthermore, the fountain clocks operated at the four institutes were included in the comparison campaign, since only a limited number of direct fountain comparisons for research purposes were carried out before [48–51].

This thesis starts with a short introduction into statistical tools commonly used to characterize measurements in the field of time and frequency in Chapter 2. This chapter also comprises an overview over atomic clocks used during the experiments and the most important comparison techniques, describing TWSTFT in detail. Since a modulation rate of 20 Mchip/s was never used before for a time transfer experiment via satellite, extensive preparations were required, which are covered in the next two chapters. Elaborate studies were carried out with the SATRE modem, which are presented in the first part of Chapter 3. Other preconsiderations concerning hardware and planning are described in the rest of the chapter. Furthermore, it was decided to carry out a 1-week link test campaign several months before the

actual clock comparison. The results of this campaign, including potential improvements for the main clock comparison campaign, are presented in Chapter 4. Chapter 5 discusses this main campaign with respect to the TWSTFT links, the instability achieved, as well as the corrections applied on the data, whereas the calculation of the frequency difference of the optical clocks is provided in Chapter 6. This includes a discussion about the challenges of finding an appropriate method for the calculation and uncertainty estimation in presence of gaps and disturbances on the data. The final results of this work are presented and discussed. Chapter 7 summarizes all important observations and results and provides an outlook for future experiments.

Appendix A provides supplementary information about technical parameters and setups for the modem characterization measurements and during the link test and the main clock comparison campaign, whereas Appendix B supports the discussion in Chapter 6 with a derivation of a formula.

The main results of this work and some of the discussions in Chapters 5 and 6 are published in [52].

Chapter 2

Frequency standards and their comparison

This chapter provides an overview over the frequency standards of interest for this work and summarizes the commonly considered comparison techniques for these standards. To do so, a short introduction to the tools of statistical analysis in the field of time and frequency is given at the very beginning of this chapter. These are needed to characterize the frequency standards and to select the appropriate comparison technique for the different standards.

2.1 Statistical analysis of frequency and time signals

When time and frequency measurements are analyzed over time, information about their stability, i.e. their variation with time, and the underlying noise processes can be obtained. This can be done to support classical estimates of a single mean of the measurement and to gain a better understanding of the uncertainty. Although the analysis of stability is a statistical approach, systematic effects like temperature variation have an impact on the stability, too, and an analysis can help to separate and possibly quantify different contributions to the overall uncertainty. The overall uncertainty in general is the quadratic sum of the so-called statistical uncertainty, also type-A uncertainty u_{A}, and the systematic uncertainty, type-B uncertainty u_{B}, according to the *Guide to the expression of Uncertainty in Measurement* (GUM) [53].

One tool available for this purpose is the 2-sample variance, or Allan Variance σ_y^2 [54], which is calculated for different averaging times τ: the differences of two averages, both over two distinct consecutive timing intervals τ, are calculated to gain a characteristic instability measure for this averaging time τ. For N measurements of a relative frequency y on a time grid of τ_0, it can be calculated as follows:

$$\sigma_y^2 = \frac{1}{2(M-1)} \sum_{i=1}^{M-1} (\bar{y}_{i+1}(\tau) - \bar{y}_i(\tau))^2, \tag{2.1}$$

where $\bar{y}_i(\tau)$ is the i-th average of all y_i within τ and M the amount of averages, with

$$M = \frac{N}{\tau/\tau_0} \tag{2.2}$$

Phase measurements x can be converted into frequency measurements by calculating the difference between phase values on a certain time interval and dividing it by the interval between the values. Hence, for a calculation of the Allan Variance, triplets of phase values are necessary, and Eq. 2.1 changes accordingly:

$$\sigma_y^2(x) = \frac{1}{(2\tilde{M}-2)\tau^2} \sum_{i=1}^{\tilde{M}-2} (x_{i+2}(\tau) - x_{i+1}(\tau) + x_i(\tau))^2, \tag{2.3}$$

with $\tilde{M}$ being the amount of phase values measured between time intervals of τ, hence $\tilde{M} = M + 1$.

The Allan Variance was introduced to bypass the problem that the classical variance diverges for most clock types due to the presence of flicker noise. The square root of the Allan Variance is the Allan Deviation, which is the commonly used representation of the Allan Variance. Different designated noise types on the data result in different time-domain exponential dependencies for the Allan Deviation, according to Riley [55]:

- white and flicker phase noise: τ^{-1}
- white frequency noise (random walk phase noise): $\tau^{-1/2}$
- flicker frequency noise: τ^0
- random walk frequency noise: $\tau^{1/2}$

In theory, the list can be extended to further noise types like flicker walk frequency noise (τ^1) and random run frequency noise ($\tau^{3/2}$), but in reality these noise types are almost never encountered and are thus mostly irrelevant for the analysis of time and frequency signals. In case of a frequency drift, the Allan Deviation shows a dependence of τ^1, while a linear drift in phase, i.e. a frequency offset, does not have an impact on the Allan Deviation.

The classical Allan Variance is an unbiased estimation of the true variance of frequency samples when white frequency noise is dominant. But it has still some disadvantages: it has a relatively poor confidence for large τ and it does not differentiate between white and flicker phase noise. Several different and for special purposes refined versions of the Allan Variance exist to overcome these problems and are recommended for different kinds of usage. The modified Allan Variance σ_{mod}^2 [56], which will be used in most parts of this work, shows a lower exponent for white phase noise (-3 for the Variance, and respectively $-3/2$ for the Deviation), since white phase noise is expected to be dominating for some of the measurements. Overlapping Allan Variances can be useful for a qualitative analysis for longer averaging times, because they create additional points for each τ by taking, similar to the moving average, overlapping data intervals. However, this might establish additional correlations for the data used. Other variances are designed to differentiate between a frequency drift and flicker walk and random run frequency noise [57]. The used variance types can be calculated from both phase and frequency data.

Another commonly used tool for the timing community is the so-called Time Allan Deviation (short: Time Deviation) which is the square-root of the Time Allan Variance σ_x^2 [58]. It can be directly calculated from the Modified Allan Variance by multiplying the factor $\tau^2/3$ and is used for analyzing stability in time and phase noise on data explicitly. The Time Allan Variance is an unbiased estimator of the

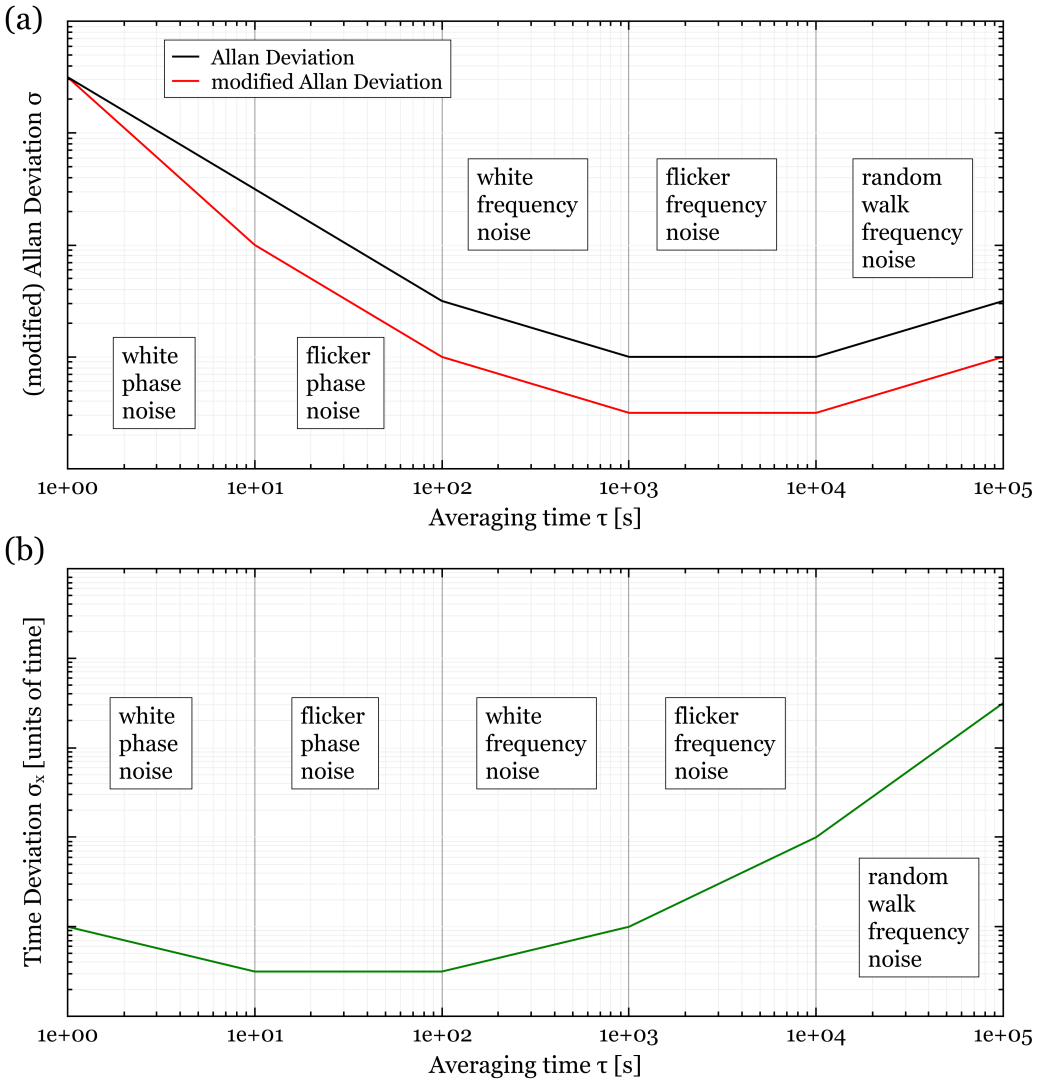

FIGURE 2.1: The different types of Allan Deviations depicted for different noise types. (a) shows both the classical Allan Deviation and the modified Allan Deviation. They have the same value for a starting point of averaging, but due to the difference for white phase noise the modified Allan Deviation can reach lower instabilities in presence of white phase noise. However, note that only the Allan Deviation is unbiased with respect to the true deviation of frequency samples affected by white frequency noise. These deviations are dimensionless. (b) shows the Time Deviation for the same noise types. It is unbiased with respect to the true deviation of phase samples dominated by white phase noise. The Time Deviation has units of time. Both have a logarithmic scale.

true variance of phase data affected by white phase noise. Fig. 2.1 (a) depicts both the Allan Deviation and the modified Allan Deviation for different noise types. In Fig. 2.1 (b) the corresponding Time Deviation can be seen. For all kinds of deviation the depiction is logarithmic, making the exponent for the relation between σ and τ the slope of the graphs.

The Allan Deviations do not only reveal different noise types, but also other structures like oscillations do appear. Fig. 2.2 shows the Allan Deviation plot of a sine function with a period of one day. In such a way instabilities due to variations with a diurnal pattern can be simulated to analyse such features in Allan Deviation plots of real measurement data.

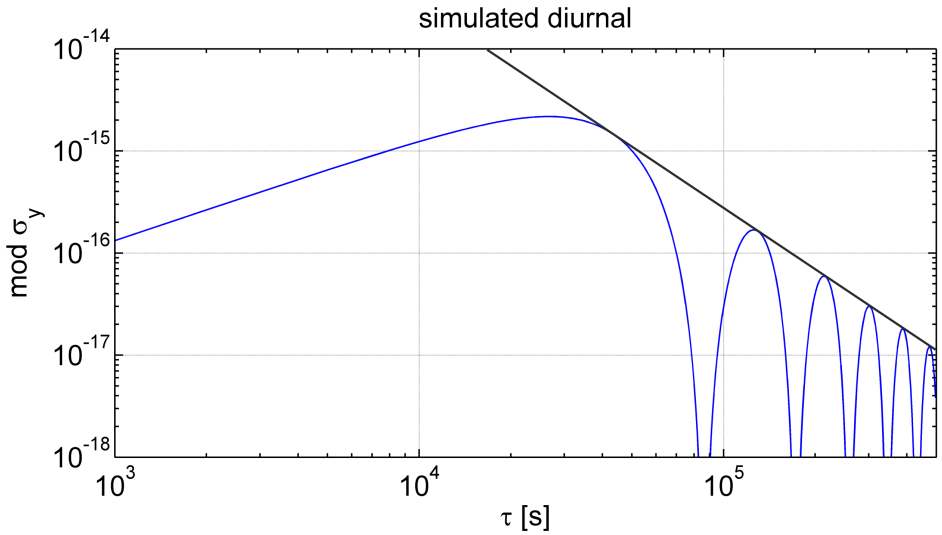

FIGURE 2.2: Modified Allan Deviation of a simulated diurnal oscillation. This results in minima at the oscillation period and maxima in between. Image taken by courtesy of E. Benkler.

The calculation of the Allan Deviation assumes the data to be continuous on a time grid with $\Delta t = \tau_0$. Gaps on data were treated either by interpolation or gap removal, i.e. considering all present data as continuous ("stitching the data together"). In general, applying these methods blindly, the calculation becomes erroneous [59, 60]. Mathematical techniques were proposed that would allow for gaps on the input data for the calculation of the Allan Deviation [61]. However, these treatments were so far only taking the classical Allan Deviation into account and are applicable for phase data only.

The value of the Allan Deviation at a certain averaging time τ serves as a qualitative estimate for a respective uncertainty u_A when the value of the relative frequency y is determined as an average with a certain weighting function. However, in order to convert the Allan Deviation quantitatively to the statistical uncertainty, a certain prefactor is needed, depending on the dominating noise type [62]. So this approach can be used to calculate the uncertainty at a certain τ which will always be smaller than the overall measurement interval, and only when a known noise type is dominating.

2.2 Frequency standards

Every clock consists of an observable recurring event of certain stability in its periodicity and a mechanism for counting these events. Atomic clocks are based on atomic transitions and use thus single atoms or an ensemble of atoms as reference for the frequency. Due to their low uncertainty and instability (several orders of magnitude with respect to mechanical clocks), they are considered as standards for the frequency. Atomic clocks are in most cases passive standards, i.e. they have an external frequency source that can be locked on the atomic transition. In some cases, build-in electronics divide the signal into a frequency of a common quantity, like 5, 10 or 100 MHz, or 1 Hz as pulse (called 1PPS (Pulse Per Second) signal), which are given as output. In other cases, the frequency of the reference is directly measured against an external oscillator or another atomic standard.

2.2.1 Primary frequency standards

Since 1967, the second within the International System of units and hence, the unit of frequency, is defined by the hyperfine transition in the cesium isotope ^{133}Cs [1, 2]. A frequency standard is called Primary Frequency Standard (PFS) under two conditions. First, it uses directly this ^{133}Cs transition as internal frequency reference to be locked on. Second, it has a fully evaluated uncertainty budget based on all known effects and their measurements or theoretical estimations. Furthermore, this uncertainty budget is always valid when the clock is operated as PFS. The first Cs clocks were beam clocks, named after an atomic beam directed through a microwave oscillator to put the atoms into an excited state. These clocks, developed between the 1950s and the 1980s, could reach relative uncertainties in the range of 10^{-10} to 10^{-14} [63, 64]. Commercially available Cs clocks are beam clocks, too. Today their uncertainty is approximately at a 10^{-13} level, but since they do not provide the complete individual uncertainty budget, but are rather directly or indirectly calibrated against a Cs clock used as reference standard, they are not referred to as PFS.

Within the last 30 years, a new type of primary frequency standard was developed, the Cs fountain [65, 66]. A different mechanism for locking the external oscillator on the Cs frequency is used: the interaction time between the external frequency source and the Cs atoms is increased via laser cooling of atoms. With this technology, this clock is enabled to reach lower systematic relative uncertainties in the range of 10^{-15} or 10^{-16} [22–25, 67–70]. The fountains usually show white frequency noise for all observed averaging times, reaching 1×10^{-15} or lower at 1 d averaging time. The instability of the external frequency source at 1 s is in general in the 10^{-13} range or below. However, frequency measurements with fountain clocks are due to their operation mode evaluated on longer time intervals, such as 100 s. Only few laboratories worldwide operate Cs fountain clocks, and improvements for the operation and a careful re-evaluation of the uncertainty budget are undertaken on a regular base. Some laboratories, including PTB and LNE-SYRTE, manage to operate their fountains with a very high "uptime", i.e. a high percentage of operation time within a given interval, which is necessary to generate a time scale.

2.2.2 Other frequency standards

Another category of frequency standards are the so-called Secondary Representations of the Second (SRS). These are clocks based on atomic transitions selected and listed by the Bureau International des Poids et Mesures (BIPM) [71]. These transitions are given as absolute frequency values, since they were measured against PFS with a corresponding uncertainty. Transitions within this list have been realized in frequency standards independently, they have been evaluated against PFS several times, with the corresponding measurements showing sufficiently low uncertainties.

Having various similar properties and a suitable hyperfine transition in the microwave range close to Cs, the rubidium isotope ^{87}Rb provides a transition for a SRS. Alongside with commercial Rb clocks several fountains with a Rb reference were built [72]. LNE-SYRTE has developed a dual-fountain with both Cs and Rb that can be operated simultaneously [73]. Since effects causing systematic frequency shifts are similar as for Cs, similar uncertainties can be reached. However, a lower collisional shift allows to operate with higher atom density which consequently leads to a better stability.

The largest group of the SRS, however, are transitions in the optical frequency range of the electromagnetic spectrum, and thus the respective frequency standards are called optical clocks. There are two major categories, optical clocks based on trapped ions and clocks based on a neutral atom ensemble, also referred to as "lattice clocks". During the past ten years, both systems made rapid progress, and many institutes report on the construction and research on these clocks. Ion clocks are based on ytterbium ($^{171}Yb^{+}$, electric quadrupole (E2) and electric octupole (E3) transition [74–76]), strontium ($^{88}Sr^{+}$ [77, 78]), calcium ($^{40}Ca^{+}$ [79–81]), aluminum ($^{27}Al^{+}$ [19, 82, 83]), and mercury ($^{199}Hg^{+}$ [84–86]). The evaluation of systematic uncertainties show uncertainties in the 10^{-17} range or even below, while the instability is in the range of 10^{-17} at around 1000 s. For lattice clocks, neutral atoms of the isotopes ^{171}Yb [87–90], ^{87}Sr [91–95], ^{88}Sr [96, 97], and ^{199}Hg [98] are used. The presently achieved uncertainties and instabilities are similar to those mentioned above for ion clocks. However, due to the higher number of atoms, lattice clocks have the potential to reach lower instabilities and thus lower statistical uncertainties in measurements. The operation of optical clocks is more complex than for other atomic clocks and thus more prone to interruptions.

Another important frequency standard is a Hydrogen Maser (HM) [99]. They are commercially available. Due to their low short-term instability and their continuous operation they are used as oscillators in time scales (see below), but also as stable reference for geodetic stations operating VLBI (Very Long Baseline Interferometry) or on board of satellites. Hydrogen masers show different noise over different regimes of averaging times, starting with white and flicker phase noise at 10^{-13} at 1 s to 100 or 1000 s, before showing white frequency noise. Between 10, 000 s and 1 d, a frequency drift increases the instability again.

2.2.3 Frequency standards and time scales

Time scales are used for synchronization on local, regional or global levels, with UTC being the international reference time scale. UTC is computed monthly by BIPM in

three steps. First, a weighted average of the data from commercial standards (HM, Cs, Rb) is computed as Free Atomic Time (Echelle Atomique Libre, EAL), with the goal to reach the best stability for an averaging time of about 30 d. In a second step, the PFS and SRS data provided by the National Metrology Institutes (NMIs) are used to steer EAL frequency so that the resulting time scale unit interval is close to the SI second. This time scale is called International Atomic Time (Temps Atomique International, TAI), it is thus completely independent of any astronomical process. Only in a final step, an integer number of seconds is added to TAI in order to keep UTC close within 1 s to the universal time UT1 which is based on the Earth's rotation.

Both UTC and TAI are time scales without any physical output, however, most local time scales by metrology institutes and several other research laboratories and companies are local physical realizations of UTC (UTC(k)) that are designed to have a rather high stability and a rather low offset to UTC, depending on the purpose of the time scale. Frequency standards for this realization are chosen according to the needs of the time scale. The time scales of some NMIs are based on an ensemble of different frequency standards with different weighting or steering algorithms. The combination of using hydrogen masers with their low short-term instability that are steered by primary frequency standards realizing the SI second such as fountains was first implemented by PTB, and has been proven to be very effective generating a time scale of high stability and accuracy with respect to UTC, i.e. a UTC(k) staying close to UTC within a few nanoseconds [100, 101].

Together with data of local comparisons, a key feature for TAI/UTC and for the access to the information of UTC – UTC(k) are comparison data between remote institutes.

2.3 Comparison of frequency standards

Frequency standards are compared for two main reasons: first, to gain the differences between standards in order to generate a time scale, as mentioned above, and second, to evaluate the frequency standards themselves for research in the development of clocks and in the field of fundamental physics. This includes the proof of consistency for comparison of frequency standards of different types, but also of the same type, yet differently constructed.

The most straight-forward approach of comparing frequency standards is a local comparison, i.e. a comparison of two clocks in the same laboratory, building, or separated by only a few hundred meters. The short distances can be overcome without any significant signal losses by using either coaxial cables for signals up to 100 MHz or optical fibers with active stabilization. When comparing a microwave frequency standard with an optical one, a frequency comb is necessary to convert the frequency range [102]. Since Cs standards provide the second according to the SI definition, comparison between these and frequency standards based on other transition (microwave or optical) are considered as absolute frequency measurements. Absolute frequency measurements of optical frequency standards are mostly limited by the uncertainties and instabilities of the Cs standards, most often fountains, and respective uncertainties in the range of low 10^{-15} down to 10^{-16} can be reached [11, 17, 20, 74, 75, 89, 103, 104]. Local comparisons of optical frequency standards can yield uncertainties in the range of low 10^{-17} [10, 105], where the estimated systematic uncertainty can have a major contribution [19, 94, 106, 107].

However, only remote comparison techniques both enable the synchronization of different local time scales in a national or international frame and grant access to the full picture of frequency standards on a global scale. For many techniques, the term "transfer" is used for the general description. This does not necessarily imply the time and frequency related information moving only from one site to another, but is in most cases an actual comparison between different time or frequency sources. This work focuses mainly on satellite-based techniques, in particular by the use of geostationary satellites, which will be covered in detail in the following sections. Other methods, which are not used in this work, are only briefly introduced in separate paragraphs at the end of this chapter.

2.3.1 Two-way satellite time and frequency transfer (TWSTFT)

Two-way Satellite Time and Frequency Transfer (TWSTFT) is a technique to compare atomic clocks located at different NMIs, and is thus used for UTC generation. It is a two-way technique, i.e. the participating stations send signals simultaneously to the satellite, where the signals are received, converted to downlink frequencies by a transponder, and transmitted back to the ground. This is illustrated in Fig. 2.3.

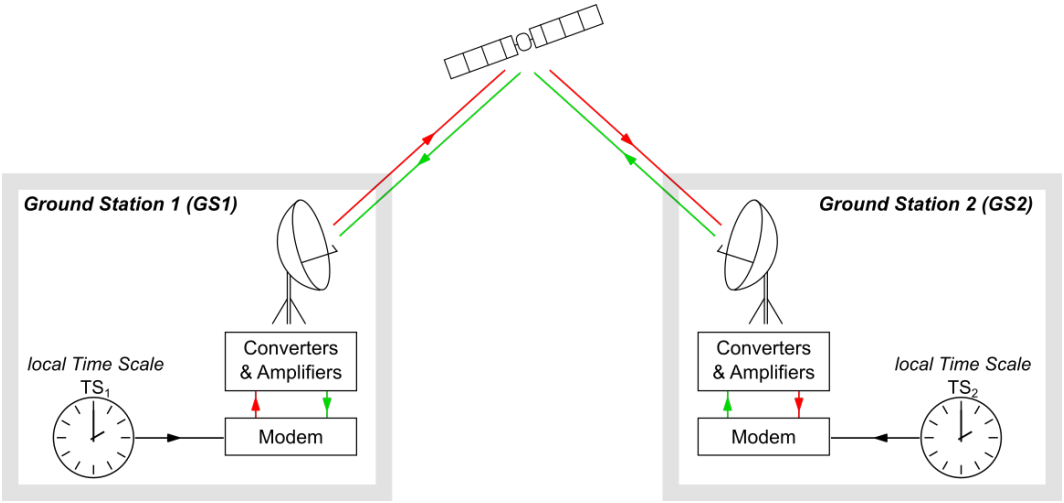

FIGURE 2.3: Illustration of the two-way (TW) principle. Signals are sent from Ground Stations (GS) 1 (in red) and 2 (in green) to the satellite simultaneously. The equipment at each station consists of a modem, several converters and amplifiers and an antenna, with the modem being referenced to the local time scales TS_1 and TS_2. This allows to perform the necessary measurements to compare both time scales.

The signals transmitted by the stations 1 and 2 are synchronized with the respective local time scales, TS_1 and TS_2. To measure the difference between both time scales, ΔTS, both stations send their signal at a coordinated point in time t_{start} considered as common, but which are in fact delayed by ΔTS with respect to each other (see Fig. 2.4):

$$\Delta TS = t_{start,1} - t_{start,2} \tag{2.4}$$

The signal from each Ground Station (GS) is traversing the transmitting equipment (TX part, corresponding to transition time τ_{TX}), sent to the satellite (uplink, τ_U),

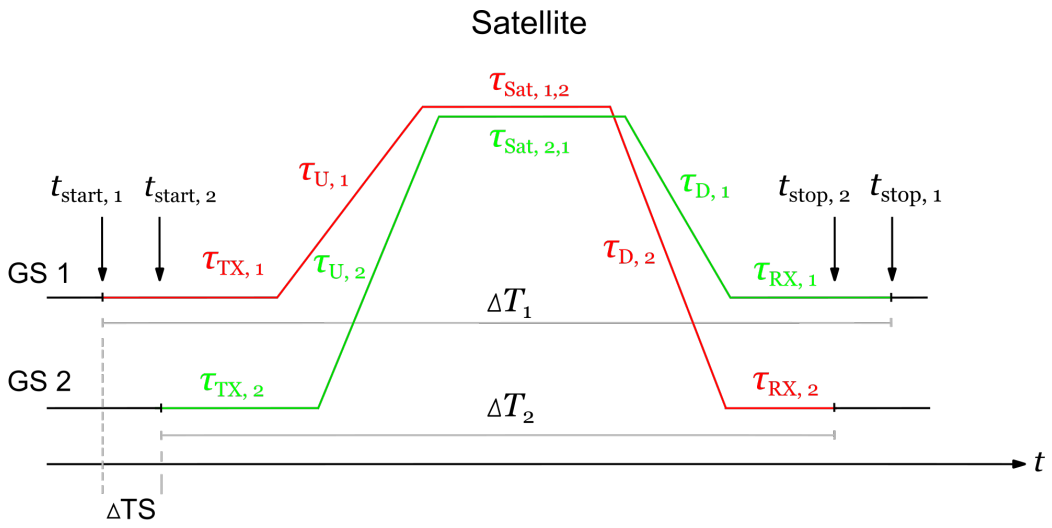

FIGURE 2.4: Derivation of the two-way equation. The single delays of the signal paths for the signals from Ground Station 1 (GS1, in red) and GS2 (in green) are depicted over time. The vertical distance to the time axis marks the location of the respective signal delay. GS1 sends its signal at the starting point $t_{start,1}$, and GS2 at the point $t_{start,2}$, which is delayed by the difference between the two time scales ΔTS. Both signals are transmitted to the satellite, then the signal from GS1 is received by GS2 at $t_{stop,2}$, and, with a delay, the signal from GS2 at GS1 at time $t_{stop,1}$. The difference between t_{start} and t_{stop} is measured as time difference ΔT at the respective ground station, as the sum of the respective delays.

passing through the satellite transponder (τ_{sat}), sent back to the Earth (downlink, τ_D), and received by the other station, with an additional delay in the receiving equipment (RX part, τ_{RX}). Thus, the propagation time for the signal sent by GS1 is $\tau_{GS1} = \tau_{TX,1} + \tau_{U,1} + \tau_{sat,1,2} + \tau_{D,2} + \tau_{RX,2}$, depicted in red in Fig. 2.4, and vice versa the delays can be written down for the signal sent by GS2 τ_{GS2}, depicted in green in Fig. 2.4. Each station measures the time difference ΔT between the start of the transmission of its own signal t_{start} and the time of arrival t_{stop} of the incoming signal of the other station. These measured time differences can be written down as:

$$\begin{aligned} \Delta T_1 &= \Delta\text{TS} + \tau_{TX,2} + \tau_{U,2} + \tau_{sat,2,1} + \tau_{D,1} + \tau_{RX,1} \\ \Delta T_2 &= -\Delta\text{TS} + \tau_{TX,1} + \tau_{U,1} + \tau_{sat,1,2} + \tau_{D,2} + \tau_{RX,2} \end{aligned} \tag{2.5}$$

Thus, to gain the difference ΔTS, both measurement results are needed:

$$\begin{aligned} \Delta T_1 - \Delta T_2 = \quad & 2 \cdot \Delta\text{TS} \\ & + \underbrace{\tau_{sat,2,1} - \tau_{sat,1,2} + \tau_{U,2} - \tau_{D,2} + \tau_{D,1} - \tau_{U,1}}_{= 0 \text{ for reciprocal path}} \\ & + \underbrace{\tau_{TX,2} - \tau_{TX,1} + \tau_{RX,1} - \tau_{RX,2}}_{= \text{const.}} \end{aligned} \tag{2.6}$$

In the ideal case, the signal paths between both antennas are symmetrical for both signals (second line in Eq. 2.6). In reality, this is not necessarily given, and various aspects as sources for non-reciprocity, given below, might need to be considered as corrections C on the result. The local equipment at each station does not allow for a complete symmetry for the signal paths for both outgoing and incoming signal, but since this difference is not expected to change over time, it can be compensated by calibration.

This finally leads to the two-way (TW) equation:

$$\Delta \mathrm{TS} = \frac{1}{2}(\Delta T_1 - \Delta T_2) + C + const. \tag{2.7}$$

In order to measure the time difference, a Time Interval Counter (TIC) is used. This suggests that the signals have the structure of 1PPS, however, as for other telecommunication purposes, it is more adequate to use a continuous wave (cw) signal.

The spread spectrum technique is used, as the signal is less sensitive to disturbances of small bandwidth. First experiments using a bidirectional exchange of a modulated signal via satellite were carried out between 1978 and 1981 [108, 109], and from these the so-called MITREX (MIcrowave Time and Ranging EXperiment) was developed [110, 111]. A binary Pseudo-Random Noise (PRN) code sequence is modulated onto a carrier frequency in the range of VHF (Very High Frequency), usually 70 MHz. This is done via phase modulation (phase shift keying). Beside the use of the spread spectrum technique, these code sequences can be used to send more than one signal within the same frequency band by sharing the sequence with the other stations. As a prerequisite, the codes have to be orthogonal.
Since no information is transmitted within this binary sequence, one single unit is not called "bit", but "chip", and the amount of chips per second in the modulated signal is called chip rate. However, the whole sequence is referred to as 1 bit (see Fig. 2.5, [111]). The length of the sequence and thus the bit rate depends on the stages n of the shift register in the modulation unit. A code can have an amount of chips p of $p = 2^n - 1$. For a modulation unit with $n = 14$ stages, which was used in the first MITREX campaigns, the maximum possible code length was $p = 16,383$ chips. For system design reasons, the code sequence was truncated to a number of some decade, in the example above to $p = 10,000$ chips.
In the case of a signal modulated with 2 Mchip/s, 1 chip has a length of $t = 0.5\,\mu s$. Thus, with $p = 10,000$ chips, the signal has a bit rate of 200 bit/s. The code sequence is repeated 199 times within one second, the 200^{th} repetition marks the beginning of a new second and serves as a pulse in a 1PPS signal.

To transmit the signal to the satellite, it is converted into the SHF (Super High Frequency) range that is usually used for all kinds of radio communication traveling through the atmosphere. Frequencies used for TWSTFT typically lie in the C (4...8 GHz), X (8...12 GHz), and K_u (12...18 GHz) bands.

The TWSTFT setup

The heart of the ground station is the modulation and demodulation unit, a modem. Today, almost all NMIs use a SATRE modem (SAtellite Time and Ranging Equipment), which is based on the MITREX modem which was developed for TWSTFT in the 1980s. The SATRE modems are commercially available equipment developed by

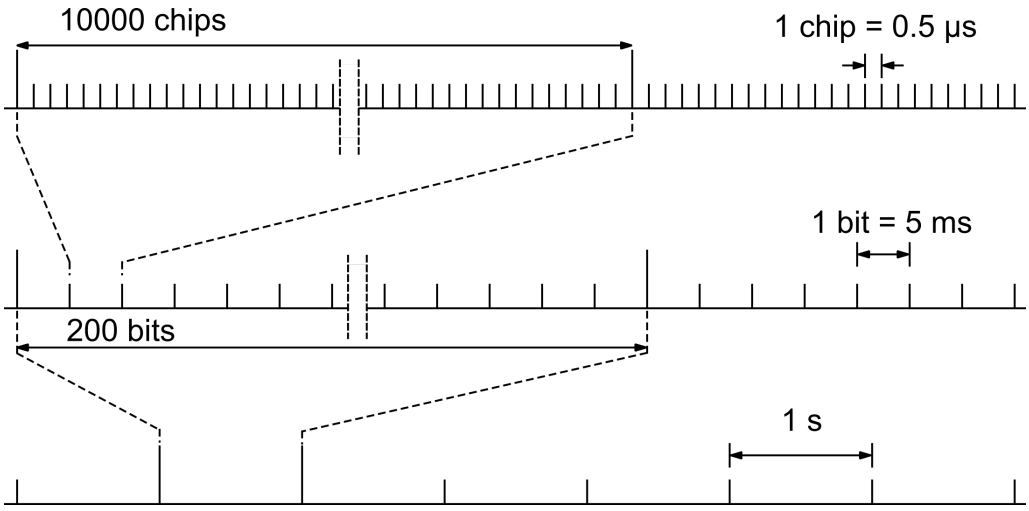

FIGURE 2.5: Structure of the code modulated onto the signal, after [111]. The chip rate depicted here is 2 Mchip/s, with a number of chips in the sequence of $p = 10,000$ chips.

TimeTech GmbH in Stuttgart, Germany. Only in Japan another modem was developed which is compatible with SATRE [112].

The SATRE modem uses three input signals from the local time scale, one 10 MHz or 5 MHz signal and two 1PPS-signals. From the first one, the 70 MHz carrier is generated. One 1PPS-signal is directly used for the generation of an internal PPS to mark the zero-crossings of the carrier for the phase measurement of ΔT, the other one as reference for the synchronization with the local time scale. The MITREX modems had 8 PRN codes of high orthogonality available. With SATRE, the user now has the choice between 32 different PRN codes, 8 of them being the original codes from the MITREX modems. Another important parameter is the modulation bandwidth. In order to enable the signal transfer, the corresponding bandwidth must be available and unused on the satellite transponder. For the TWSTFT measurements carried out on a daily base, chip rates of 1 and 2.5 Mchip/s are used [113].

For the measurement of ΔT, an internal 1PPS-signal is also generated from the incoming signal. To do so, a Delay-Locked Loop (DLL) is used after demodulation. Since the sequence of the incoming signal is known, it can be generated locally with an estimated delay $\Delta\hat{T}$ and overlapped with the incoming signal to find a maximum correlation between both, thus when $\Delta T = \Delta\hat{T}$. Here, this is done twice, with a so-called early-late correlator: the incoming signal is split and correlated with one local sequence delayed by $\Delta\hat{T} - T_c/2$ and one local sequence delayed by $\Delta\hat{T} + T_c/2$, where T_c is the length of 1 chip. The resulting correlation functions are subtracted from each other, resulting in a correlator output signal of zero in case of $\Delta T = \Delta\hat{T}$. Thus, the residual, non-zero signal can easily be used for steering $\Delta\hat{T}$. A very simplified diagram and the outcoming correlation can be seen in Fig. 2.6.

As mentioned above, different PRN sequences enable the use of several signals within the same frequency band. In order to further avoid cross-correlation with other signals, a small frequency offset of several kilohertz is introduced during the modulation, individually in size for each signal, so that the spectrum of the modulated signal is shifted insignificantly from the center of 70 MHz.

Apart from the modem, a basic TWSTFT station consists of a Very Small Aperture

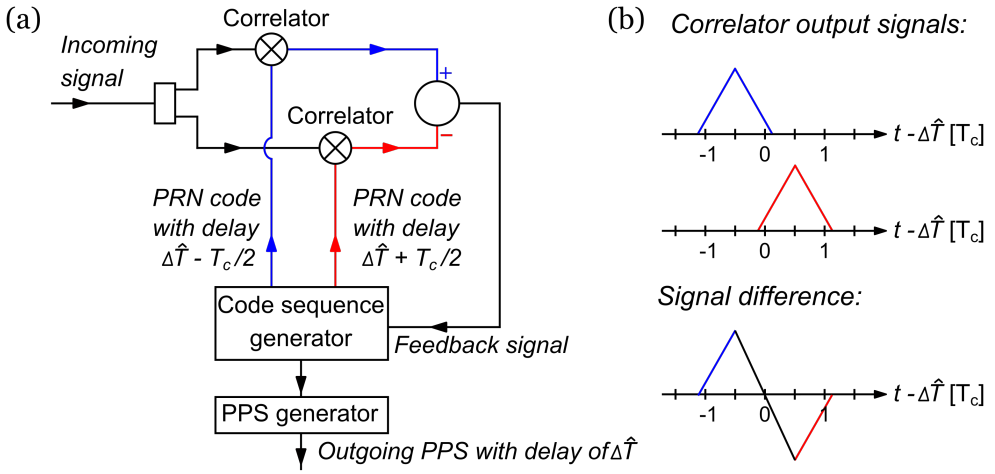

FIGURE 2.6: Simplified depiction of a delay-locked loop with an early-late correlator. (a) shows the signal paths, (b) the output signals at certain steps. The incoming signal is split and mixed in a correlator with the same PRN sequence, the upper path with the sequence delayed by $\Delta\hat{T} - T_c/2$ (in blue), the lower with the sequence delayed by $\Delta\hat{T} + T_c/2$ (in red). Here, T_c is the chip length and $\Delta\hat{T}$ is an estimated delay that is steered by the feedback signal to the actual delay of the incoming signal. The output of both correlators are autocorrelation functions (ACFs), shown in (b), each delayed in time by half a chip length. The difference of the signals, i.e. of the ACFs, is formed. The residual signal at $t - \Delta\hat{T} = 0$ is given as feedback signal to the PRN code sequence generator to steer $\Delta\hat{T}$ in a way the residual signal is zero, which is the case if $\Delta\hat{T}$ corresponds to the actual delay of the incoming signal. From that, a 1PPS-signal is generated.

Terminal (VSAT) antenna, located either on an elevated or an open-field position, an upconverter (UC) and a Solid-State Power Amplifier (SSPA) on the TX site of the signal path between the modem and the antenna, and a low noise amplifier (LNA) and a downconverter (DC) on the RX site.

The antenna is a parabolic antenna with diameters usually between 1.8 and 2.4 m. A precise orientation of the antenna towards the satellite is necessary. This is realized by maximizing the reception power of the beacon signal transmitted by the satellite. Additionally, it is common for TWSTFT in the K_u frequency band to use linearly polarized signals, which requires a careful adjustment of the polarization filter at the feed system. The signal sent to the satellite is polarized in the respective orthogonal direction to the one received from the satellite, so the latter can easily be coupled out of the transmitting signal path. The LNA is directly attached at the antenna, so that the received signal is amplified before fed into a cable connected to the DC. The LNA is thus always part of the outdoor equipment and the delay between the reception in the antenna and the amplification is as short as possible.

For the converters and the SSPA there are several possible setups, which reflects a compromise between two major constraints: The first one is the fact that the upconverted signal in the K_u band experiences high power losses even on a short distance of cable compared to the signal in the VHF range, making long distances between the ensemble of converters and SSPA on one hand and the antenna on the other unfavorable. The second one are the environmental influences that affect the equipment when located outdoors close to the antenna.

FIGURE 2.7: The roof station at INRIM (Istituto Nazionale di RIcerca Metrologica, Torino, Italy), with a transceiver attached to the antenna which comprises an amplifier for the outgoing signal and up- and downconverter. By courtesy of INRIM.

One possibility is the use of a transceiver which combines SSPA, UC, and DC. It is usually directly attached to the antenna, thus a dedicated outdoor device, minimizing the signal path between the upconversion and the amplification and the transmitting unit of the antenna. Such a roof station setup can be seen in Fig. 2.7. When using single devices instead, the equipment can be installed in a sheltered environment on the roof or in a room close to the roof, still providing signal paths within cables up to only few meters. A study on the differences between these possible setups was carried out [114].

The satellite is a geostationary satellite, owned by companies offering broadcasting and other telecommunication services. These satellites are located above the equator. The stations participating need to be located within the broadcasting footprint of the satellite used. For TWSTFT measurements, a certain frequency bandwidth on a transponder is leased. The footprint of Telstar 11N, which is currently used for operational TWSTFT measurements within Europe and between Europe and the USA, is shown in Fig. 2.8. Since the sending directions of Europe and America differ significantly, the TWSTFT measurements for comparing time scales within Europe and the ones comparing time scales intercontinentally require two different transponders.

Non-reciprocal delays on the signal path and other sources of disturbance

One source of non-reciprocities in the signal paths between the up- and downlink paths of the stations is the propagation through the atmosphere, caused by the difference in up- and downlink frequency. The impact on the measurement depends on the overall path length through the atmosphere and thus on the elevation angle

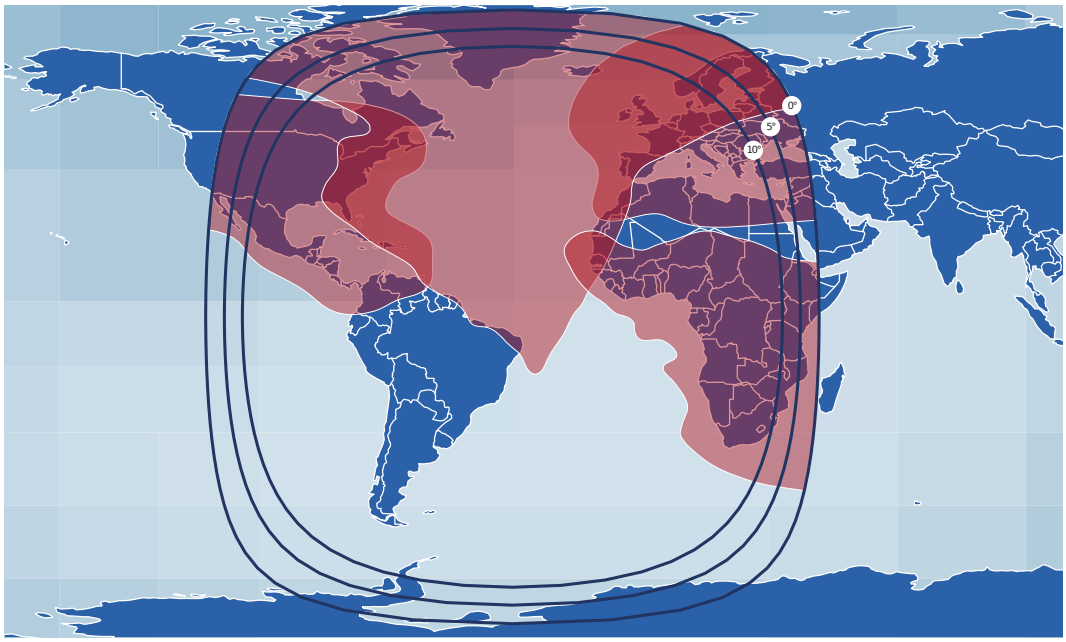

FIGURE 2.8: Footprint of Telstar 11N. The different regions, mostly located on the northern hemisphere, are covered by using different antennas on the satellite. Image taken from www.telesat.com [115].

of the satellite. Influences of the troposphere and influences of the ionosphere are considered separately because of their different impact on signals traveling with different frequencies through them.
The propagation through the ionosphere shows a strong dependence on the frequency due to its ionized particle composition. The recommendation of the International Telecommunication Union (ITU) for operational TWSTFT measurements provides a formula with the delay difference for up- and downlink showing a linear dependence on the Total Electron Content (TEC) [116]. Estimating the order of magnitude of the ionospheric delay difference for these operational TWSTFT measurements by using maximum TEC values and frequencies typically used for up- and downlink resulted in values of a few hundreds of picoseconds, a value lower by a factor of 3 or more than typical calibration uncertainties for TWSTFT links [117, 118]. Hence, corrections are not calculated for most operational TWSTFT links, especially within Europe.
The dispersion in the troposphere depends on pressure, humidity and temperature. A study investigating this relation and other effects has been carried out for a TWSTFT link between the National Institute of Information and Communications Technology (NICT, Japan) and PTB in order to estimate the order of magnitude of atmospheric delay differences [118]. As a conclusion, the tropospheric influence was found to be small enough to be neglected for operational TWSTFT measurements, even on long-baseline links with small elevation angles of the satellite.

Non-reciprocity also originates from one geometric and one relativistic effect. The Sagnac effect, which is the relativistic effect, is caused by the rotation of the reference system of ground stations and satellite. The influence of the Sagnac effect can be calculated as constant offset by using the ground stations' coordinates and the position parameters of the satellite. However, a residual satellite motion within this reference system, originating mostly from the gravitation of Earth, Sun and Moon, leads to a periodic change of the Sagnac offset. Depending on the location of the satellite

and the ground stations, the Sagnac offset can accumulate to several hundreds of nanoseconds, with a diurnal variation of a few hundreds of picoseconds [118, 119]. This residual motion also causes the geometric effect, called path delay difference. If the signals from the stations arrive at different times at the satellite, the distance between the satellite and the ground station is not the same for the uplink signal as for the downlink signal, since the satellite moved in the meantime. The peak-to-peak variation can cover up to a few tens of picoseconds, depending on how much time passes between the arrival of signals at the satellite [117].

Additional errors can occur due to disturbances changing delays in the ground stations that are considered to be constant, e.g. temperature. This concerns conditions in the laboratories as well as the sensitivity of the roof station equipment to environmental effects [117]. Usually, these impacts are estimated for temperature by using typical values of temperature coefficients of the equipment used and typical values of temperature changes (laboratories are temperature-controlled areas with only a 1...3 K in peak-to-peak difference), and then considered as contributions to the systematic uncertainty (u_B) for the calibration. Temperature-induced contributions to u_B are usually between a few tens up to a few hundreds of picoseconds.

Also, the introduction or removal of additional delays in the setup, e.g. cables, splitters or connectors with known delays, or their exchange, can cause changes in the overall measurement that are larger than the actual delay value. First, the additional measurement of any delay can be only carried out with a finite uncertainty, and thus, it introduces a new source of error. The uncertainty of an absolute, i.e. non-differential, delay measurement of a standard TIC is considered to be 0.5 ns, which corresponds to the uncertainty the manufacturer claims for one of the commonly used TICs within the field, a Stanford SR620 [120]. Second, reflections of the signal can occur at points of impedance mismatch within the path. These can be connections between cables or impurities within the cables. The signal then interferes with its reflection, which can lead to a different delay measurement at the correlator within the modem [121, 122]. This is called multipath effect. By changing the physical signal path, the multipath effect changes. Also, a temperature-induced change of the delay in the same cable can lead to different multipath-induced erroneous results. This is currently not considered in the operational TWSTFT, although this can lead to measurement changes up to several nanoseconds in a worst-case scenario, depending on the chip rate, the overall delay length of the cables and the correlator used [122].

The instability of TWSTFT

The measurement noise in TWSTFT depends on both the operational parameters and the hardware. The noise process visible with the modified Allan Deviation shows white phase noise for averaging times up to a few minutes, and flicker phase noise as dominant noise type for longer averaging times. The short-term instability is inversely proportional to the chip rate, and furthermore depends on the carrier-to-noise density ratio (C/N_0) in the RX module. At $C/N_0 = 55$ dBHz, which is typically observed during the TWSTFT measurements for UTC(k) comparisons, the expected 1PPS jitter of the received signal is about 500 ps at 2.5 Mchip/s, or about 1.3 ns at 1.0 Mchip/s [47]. Simultaneous transmissions by other stations with different PRN codes appear as increased noise for the measurement, which reduces C/N_0 and thus

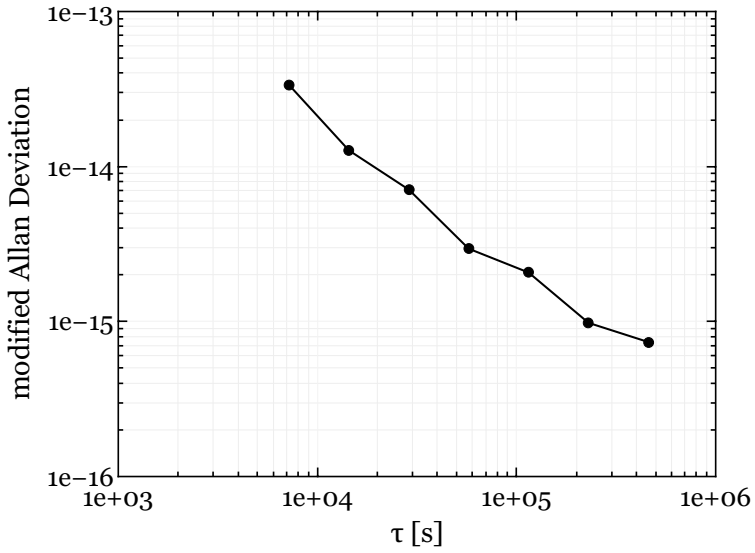

FIGURE 2.9: The modified Allan Deviation of a HM comparison between PTB and METAS (Eidgenössisches Institut für Metrologie, Bern, Switzerland), carried out with TWSTFT at a chip rate of 2.5 Mchip/s. Since TWSTFT measurements via the satellite transponder used for inner-European TWSTFT measurements are carried out on a schedule in sessions every 2 h, this τ resembles τ_0 for most TWSTFT measurement depictions in terms of the Allan Deviation or other related deviations. The data, as published in [47], was provided by D. Piester.

increases the instability. Transmitting the signal with increased power could compensate for this, increasing C/N_0 for that specific link, but this would consequently also increase the noise on other links, and operating power levels require careful control and optimization. The instability at 1 s and the noise characteristics at longer averaging times lead to frequency transfer instabilities of around 1×10^{-15} for an averaging time of 1 d when operated at 1 Mchip/s. However, the effects discussed above can impact the long-term instability. Most prominent are diurnal oscillations, due to temperature, but also of unknown origin [113, 123–125]. The modified Allan Deviation of a TWSTFT measurement carried out at a chip rate of 2.5 Mchip/s can be seen in Fig. 2.9. There, the hydrogen masers between PTB and METAS (Eidgenössisches Institut für Metrologie, Bern, Switzerland) were compared. An instability of about 2×10^{-15} could be reached for 1 d averaging time, and for larger averaging times, an instability below 1×10^{-15} can be reached. The figure is recreated after a figure in [47], with the data being provided by D. Piester.

2.3.2 Frequency transfer using Two-Way Carrier Phase

The Two-Way Carrier Phase (TWCP) technique is based on the operational TWSTFT and was developed for frequency transfer with the aim of reducing the instability compared to the use of coded signals [126]. The main idea is to profit from the steeper slopes of the carrier waveform with respect to modulation envelopes. This comes at the expense of an ambiguity at the level of the carrier wavelength, which must be resolved by additional means. To use the phase information to determine the frequency offset $\mathrm{d}f$ between the reference clocks of two ground stations, three

additional unknown quantities must be determined: the first-order Doppler coefficients for both links from the stations to the satellite, and the frequency of the local oscillator of the satellite transponder [127]. The four required quantities can be obtained by four measurements (measuring the two-way signal of the remote station and the ranging signal of the local station on both sites), resulting in an equation set with four equations, which can only be solved in a numerical way or by simplifying it with some assumptions [128].

As this technique was originally developed as an extension to the TWSTFT already in use, the measurements can be carried out with the same equipment (including the SATRE modem) without requiring additional hardware. This way, first test experiments over zero and short baselines were performed (PTB vs. DLR (Deutsches Zentrum für Luft- und Raumfahrt, Oberpfaffenhofen, Germany); USNO (United States Naval Observatory, Washington DC, USA) vs. NIST (National Institute of Standards and Technology, Boulder, USA)) [126, 129]. They show a low short-term instability (2×10^{-12} at $\tau = 1\,\mathrm{s}$), but display a mixture of flicker phase, white frequency and flicker frequency noise for longer averaging times. Ground station equipment, reference clocks and measurement time limited the stability of the tests. Other tests between collocated stations or over a long baseline (PTB – USNO) show slight improvements with respect to both the short-term instability (at a few seconds) and the noise behavior over longer averaging times, but show oscillations at 1000 s or more of unknown origin [127]. Another TWCP measurement carried out with the SATRE modems was performed in 2011 by LNE-SYRTE between two collocated stations [130]. Here, a lower instability was achieved, although it was still higher than that of a simultaneous measurement carried out with GPS, and the oscillations were still observed. Even very short interruptions of the measurement, such as single missing data values, destroy the phase coherence. So the length of a continuous measurement interval remains a limiting factor for the stability.
NICT developed a setup independent from the SATRE technique and performed two campaigns within Japan, a common clock setup and an experiment over a short baseline of 150 km. Another campaign over a very long baseline to PTB for an optical clock frequency comparison was carried out by NICT [128, 131]. This short baseline experiment was clearly limited by the hydrogen maser used, but the double difference of GPS and TWCP showed that an instability lower than 1×10^{-15} was surely reached. For the measurement with PTB, the influence of the atmosphere could be investigated and an ionospheric correction was calculated. The instability here reached 5×10^{-16} at $\tau = 1\,\mathrm{d}$ in the GPS – TWCP double difference.

The advantages of this technique are the lower short-term instability in comparison to code-based TWSTFT and that it requires only a small frequency band on the satellite transponder. However, due to unexplored effects and the need for a practically uninterrupted measurement, it has only been used on an experimental basis so far.

2.3.3 Time and frequency transfer via GNSS satellites

In contrast to TWSTFT, time and frequency transfer using GNSS satellites is a one-way transfer technique. Both remote stations, comprising of an antenna, an antenna cable and a GNSS receiver referenced to the local time scale, receive the signal of a satellite and can perform a time-of-flight measurement for the signal traveling between the satellite and the station, which is called pseudo-range. The idea is that due to the known coordinates of the station and of the satellite, the difference between

the local time and the satellite time is left over as measured result at each station, and when making a comparison, the two measurements of the stations are subtracted so the satellite time cancels out. Having the satellite time cancel out this way is only possible when the satellite is seen by both stations at the same time, which is called common view technique. Using additional information about the clocks of the single satellites compared to the system time of the GNSS in question allows the use of all satellites in view and to carry out comparisons even if no satellite is seen by both stations at the same time [132]. This is called all-in-view.

It is most common to use GPS satellites, and GPS was also used in parallel to the TWSTFT measurements in this work, so the descriptions and specifications will be given for GPS only.

For what concerns this work, GPS satellites emit modulated signals on two carrier frequencies: L1 (1.57542 GHz) and L2 (1.2276 GHz). L1 is modulated with the C/A-code (Coarse/Acquisition), a civilian code (L1C) and the P-code (Precision), whereas L2 is only modulated with the P-code, and in newer generations of satellites with a civilian code L2C. Since it is a one-way technique, environmental disturbances on the signal path like the dispersion within the ionosphere do not cancel out. However, by linearly combining both P-code measurements of the different frequencies, the dispersion of the ionosphere can be averaged out down to a few tens of picoseconds. This is the so-called ionosphere-free solution, or P3 solution, which has been used after the P-code modulation became accessible for common use [133].

Another approach is to take the measurement of the Carrier Phase (CP) into account, which, similar to TWCP, improves the short-term stability significantly [43, 44, 134], but it cannot be used independently for time transfer due to the phase ambiguity [135]. Thus, it needs a calibration, either by using an additional method of time transfer in parallel like TWSTFT or by using the code measurement.

One technique that combines both CP and code measurements is the PPP technique [43, 44, 136, 137]. It is an all-in-view technique, and it allows to calculate the time difference between the local receiver time of one single station and the system time of the International GNSS Service (IGS), the IGS time. In addition, it calculates the antenna position of the station with high accuracy. However, precise information of both satellite clocks and orbits are necessary, which are available as IGS products for post-processing. The CP measurement enables a low short-term instability compared to GPS time transfer based on code measurements (up to two orders of magnitude at averaging times of $\tau = 1000\,\mathrm{s}$). However, the code measurements impact the long-term instability of PPP. PPP data are calculated in batches, and for each batch the code is used to estimate the phase ambiguity. Due to the instability of the code, boundary discontinuities occur between consecutive batches. They are of the order of a few tens or hundreds of picoseconds up to several nanoseconds for daily batches, which is the standard processing length of a batch [138]. Analyses show that the code noise is non-white and thus does not average out for longer batches, but instead can increase over time [139]. They are partly caused by systematics of station hardware, similar to the ones discussed for TWSTFT, like temperature sensitivity, multipath effect in cables, splitters and filters. For GPS, multipath at antenna level, i.e. the reception of signals reflected by the environment before reaching the antenna, plays a larger role due to the omnidirectional antennas used, but is not systematically investigated yet. Although this is a limiting factor for PPP time transfer, the technique can reach instabilities in the low range of 10^{-15} [44, 140] or even below [45].

In the past few years an enhancement of GPS PPP was developed, IPPP [46, 141, 142]. This technique resolves the phase ambiguity with integers of the wavelength of the signal, which allows for batch processing without boundary phase jumps. Furthermore, since errors concerning the ambiguity resolution in PPP occur typically between the passings of the single satellites, i.e. at a few hours averaging time, IPPP provides a better stability from this averaging time on than classical PPP. Common clock experiments and comparison with other techniques have revealed that IPPP can reach instabilities below 1×10^{-16} for about 10 d averaging times [143].

2.3.4 Other methods of comparison

Transportable atomic clocks

The transport of frequency standards was never carried out for regular comparisons contributing to TAI/UTC, however, it can be used to compare time scales or single clocks in laboratories with a better short term stability than what the state-of-the-art techniques for remote comparisons could provide, or to overcome parts of the distances where no sufficient techniques are available.
For time comparisons, the clock needs to be in operation during the transport. Commercial Cs clocks were used in the past for time transfer as a complement technique to GPS time transfer to calibrate TWSTFT links [144], or can be used to synchronize remote stations [145]. Depending on the accuracy requirement, the effects of General Relativity should be considered by following the trajectory of the traveling standard between the visited sites.
For frequency comparisons, the clock only needs to be operated at the different sites. Within Europe, the transportable fountain clock of LNE-SYRTE was used to perform absolute frequency measurements of various optical or microwave frequency standards, e.g. a hydrogen frequency transition at MPQ (Max Planck Institut für Quantenoptik, Garching, Germany), and a calcium ion transition at the University of Innsbruck in Austria [80, 146]. Several transportable optical frequency standards were developed in the past years or are currently under construction [33–35, 147–149]. Recently, a transportable optical clock by PTB was used to measure the gravity potential difference between two different sites [150]. However, this technique is always extensive in work for organization, and the operation of a transportable clock is hindered by technical compromises. In addition, the comparisons of the fixed, remote time scales or clocks never take place simultaneously.

Optical fibers

Frequency transfer via optical fibers can achieve short-term instabilities of 1×10^{-14} and lower and long-term instabilities below 1×10^{-20}. It is thus suited for comparing highly accurate and stable frequency standards as optical clocks [39, 151, 152]. However, the main limitation is the availability of the fiber itself and the need for additional infrastructure. Up to now, fiber link distances of up to 1800 km have been used [152].

The frequency instability scales with the 3/2 power of the fiber length [153] and is limited by various effects, like power loss, phase noise or signal distortion. For counteracting the attenuation, different amplification techniques have been developed and improved [37, 39], and the noise can be compensated by active and passive fiber

stabilization. Here, the bandwidth of the active noise cancellation is limited by the propagation time in the fiber loop. The transient loss (so-called cycle slips) is the main limitation for continuous measurement time and therefore reduces the stability at the respective averaging times. Several days of cycle-slip-free operation have been demonstrated [39].

Three approaches depending on the application are used for frequency transfer via optical fibers: using only the optical carrier as the transfer signal, modulating a radio frequency (rf) signal onto an optical carrier, and transmitting the full span from microwave signals to optical signals by using a frequency comb [154]. The transfer of an optical carrier (cw) is most suitable for the purpose of frequency comparison, as there is no noise contribution from modulation and demodulation, and polarization-mode-dispersion as well as chromatic dispersion can be neglected. Instabilities of lower than 1×10^{-20} can be achieved at averaging times of several days over long distances ($\sim 1400\,\mathrm{km}$), making this technique the only one capable of comparing remote optical frequency standards at the level of their estimated uncertainty [39, 152]. Currently, more and more fiber links are being established within several European, American and Asian countries, but also across borders [40, 41, 155–157].

Fiber links can also be used for time transfer, but the requirements and thus the elements of the infrastructure used are partly different. For a comparison of two frequency standards or time scales, two-way time transfer is used, so both sites send a modulated rf signal simultaneously through one fiber, and the time of arrival is measured at both sites with respect to the starting time when the signal was sent. This is sometimes called TTTOF (Time Transfer Through Optical Fibers), or TWOTT (Two-Way Optical Fiber Time Transfer) [158–160]. In an additional step, active stabilization can be implemented. This technique is often used to realize a time scale at a remote position, i.e. to synchronize time scales. The data of the comparison between two UTC(k) realizations in Poland is collected by the BIPM [160]. Many laboratories analyzed the possible stabilities and accuracies both within the laboratory and over baselines up to several hundreds of kilometers. Depending on the lengths and the equipment used, values of a few hundreds of picoseconds down to sub-ps were reported for the time instability at 1 s [159, 161–166].

Chapter 3

Setup and preparation of the broadband TWSTFT clock comparisons

The main goal of this work is to carry out remote frequency comparisons of optical frequency standards located at INRIM, LNE-SYRTE, NPL and PTB via TWSTFT. This kind of comparison requires, in addition to the satellite link equipment and the optical frequency standards, a connection between both elements: A continuously running oscillator, serving on one hand as reference for the TWSTFT ground stations and, on the other hand, the optical clocks can be measured locally against this oscillator. In the ideal case, i.e. all measurements are carried out without interruptions, the fluctuations of the oscillator cancel out. Since the operation of optical clocks is less stable than, for example, the operation of cesium fountains, interruptions occur more frequently. In that case, the oscillator can be used as a so-called flywheel, bridging possible gaps in data [167]. Therefore, low instabilities, especially for shorter averaging times, are desirable.
In this experiment, hydrogen masers take this role. They run without interruption, and their frequency instability is in the low range of 10^{-13} at 1 s averaging time. White and flicker phase noise are the dominating noise process for averaging times up to 100 or 1000 s, and at 1 d instabilities around 1×10^{-15} or below can be achieved. The optical frequency regime of an optical frequency standard needs to be transferred into the microwave frequency regime of the hydrogen maser, which is done with an optical frequency comb.
In addition, direct comparisons of the fountains located at the four institutes were implemented into the planning of the campaign. In contrast to the optical clocks, the fountains are working at frequencies in the microwave range and can be measured against a hydrogen maser without a frequency comb. Furthermore, a comparison with GPS PPP in parallel to TWSTFT was planned, so dedicated GNSS receivers at each laboratory should be used and have the same HM as the TWSTFT equipment as reference.
From that, the basic setup is deduced. It is depicted in Fig. 3.1.

While tests with chip rates up to 5 Mchip/s were already carried out before [47], a TWSTFT measurement with a chip rate of 20 Mchip/s was never realized before. This means that several components of the setup had never been operating under these conditions, and the expected instability for both short and long averaging times had never been in a range where the influence of effects canceling the reciprocity and technical aspects like temperature sensitivity become crucial. On the

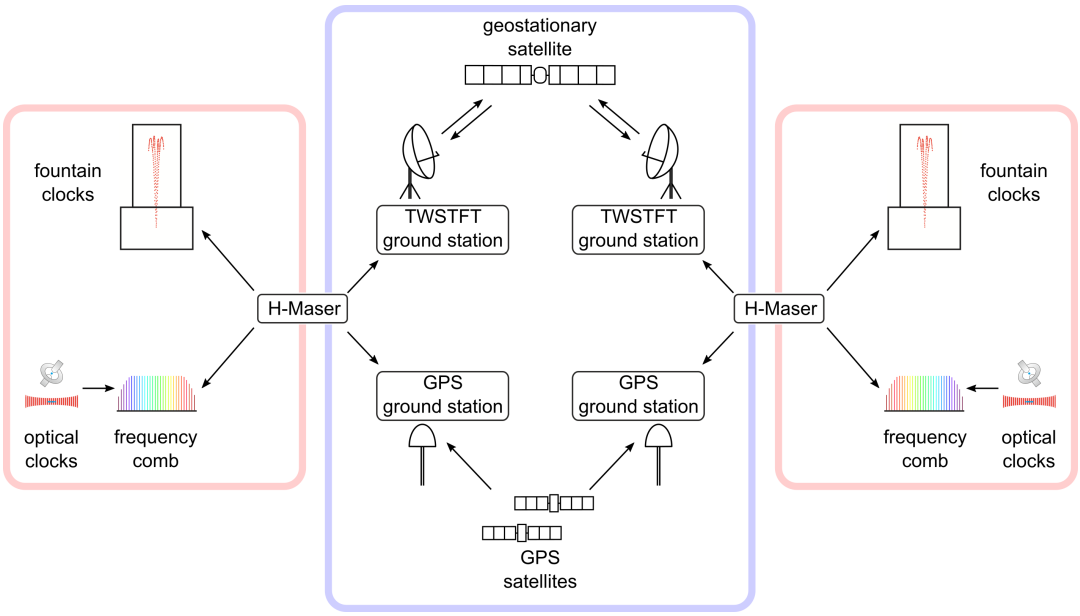

FIGURE 3.1: Setup principle for the comparison of optical and fountain clocks via satellite.

other hand, the high chip rate requires the availability of a high bandwidth on the satellite transponder, and thus the time of operation is limited to a fixed interval of a few weeks because of the costs of such a high bandwidth.
Considering this, a careful investigation of the SATRE modem as the key component of each station needs to be carried out beforehand, including the optimization of settings like PRN sequences and frequency offsets and an analysis of environmental sensitivity. The roof station design is re-evaluated.
In addition, the high frequency accuracy that is targeted defines requirements for the satellite chosen for this experiment.

Another challenge is the coordination between the institutes. A general unification of the laboratory setup is desirable, including common equipment software and output format. Also, with only a limited number of RX channels available, switching between the links is necessary, requiring a schedule.

3.1 SATRE Modem measurements at high chip rates

As mentioned before, the SATRE modems are commercially available products. All institutes involved in the experiment use one or two modems for the TWSTFT operations within the framework of their contributions to TAI/UTC and the UTC(k) time scale comparisons, and have at least one modem as spare equipment available. Thus, when carrying out test measurements with selected SATRE modems at one institute, this allows to a certain extend the deduction of the general behavior of the SATRE modems used at all institutes for the optical clock comparison. The modem investigations were carried out at PTB with three different available SATRE modems with serial numbers 76, 410 and 427 (hereafter short "S76", "S410" and "S427"), and two, three and one RX channels, respectively.

3.1.1 Instabilities at different chip rates

In a first step, the relation between the timing jitter of the measurement (short-term instability) and the carrier-to-noise-density ratio (C/N_0) was analysed in order to confirm the expected improvement with respect to the noise with increasing chip rate. It follows the equation [168]:

$$\sigma = \sqrt{\frac{B_{\mathrm{DLL}}}{2C/N_0}} R_{\mathrm{chip}}^{-1} + \sigma_0 \tag{3.1}$$

Here, σ is the timing jitter of the measurement in one modem, B_{DLL} the bandwidth of the delay-locked loop, which is the same for all SATRE modems, R_{chip} the chip rate and σ_0 the internal noise floor of the modem [111]. So σ was determined at different carrier-to-noise-density ratios and at different chip rates.

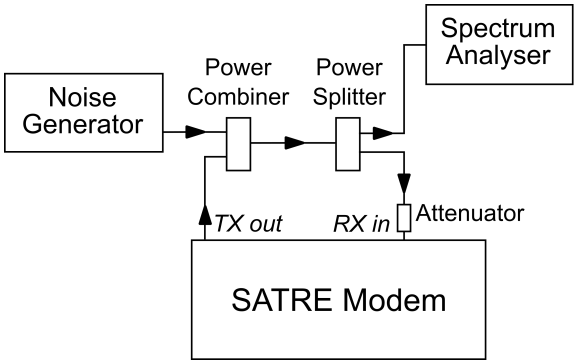

FIGURE 3.2: Setup for the determination of timing jitter vs. signal-to-noise ratio

The setup is shown in Fig. 3.2. The core is a simple "loop-back" experiment, i.e. the transmitted signal (TX output) of a modem is directly fed back into the RX channel via a short cable. The data output of a modem in general that corresponds to ΔT in Chapter 2.3.1 (ΔT_1 or ΔT_2), is a phase time series $x(t)$ and will be called "raw range" hereafter. Since only one modem is involved in a loop-back experiment, this is taken as measurand. In this setup, white phase noise is simulated by using a noise generator and mixing its output via a power combiner with the output of the modem, and thus creating white phase noise on the signal. This type of noise is always present during real measurements: Since the signal needs to be amplified various times to compensate the power loss occurring mainly on the path between station and satellite, the background noise is increased. The noise generator provides an adjustment of the injected noise power. A power splitter enables the direct monitoring of the input signal with a spectrum analyser (SA). With this constellation, the carrier-to-noise-density-ratio measurement can be carried out internally in the modem and independently by the SA.
In the loop, the carrier power is attenuated such that it is always ≈ -55 dBm as measured by the modem. The carrier-to-noise-density ratio (C/N_0) is thus adjusted by manually varying the added noise power. For each C/N_0, the modulation of the signal is switched off at first in order to observe the power of the unmodulated carrier with respect to the noise background on the SA. Then, the modulation was switched on again and a modem schedule is started which automatically cycles through the

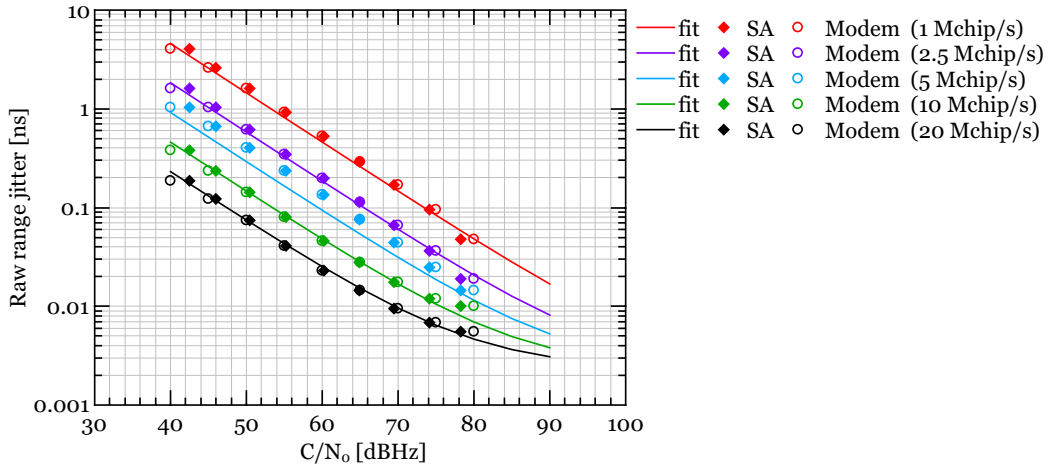

FIGURE 3.3: Dependence of raw range jitter of signal-to-noise-density ratio for different chip rates. The diamonds and the circles show the measurement results, with the filled diamonds marking the results based on the C/N_0 from the SA, and the open circles based on C/N_0 of the modem display. The lines show the fit based on Eq. 3.1, carried out with the C/N_0 of the SA. Since one fit was carried out for all chip rates, the agreement between fit and data better for some chip rates than for others.

TABLE 3.1: Fit parameter for the results of RX 1, RX 2, and the mean values of both channels.

Channel	B_{DLL} in Hz	σ_0 in ps
RX 1	0.409	2.63
RX 2	0.430	2.08
Mean of RX 1 and RX 2	0.419	2.36

different chip rates and measures the timing data. The timing jitter is then determined from respectively 600 raw range data values measured by the modem. For a better reproducibility, the measurement was repeated several times and a mean value for this jitter was formed. Also, the measurement was carried out with both RX channels.

In Fig. 3.3 the results are shown. The diamonds and the circles show the measurement results, with the filled diamonds marking the results based on the C/N_0 from the SA, and the open circles based on C/N_0 of the modem display. These results are a mean value of both channels. In addition, a fit according to Eq. 3.1 was performed over the data, based on the results with the C/N_0 measured with the SA. It is shown as line. The fit was carried out as one single fit for all chip rates simultaneously, i.e. σ in Eq. 3.1 is fitted as a function $\sigma(C/N_0, R_{\mathrm{chip}})$ with the fit parameters B_{DLL} and σ_0. These are listed in Table 3.1, both for the channel mean results and the single channels.

As a conclusion, it is found that the overall behavior can be described with Eq. 3.1: The short-term instability scales linearly inversely with the chip rate used. The signal-to-noise density ratio usually observed during the operational TWSTFT measurements is 55 dBHz. Assuming a similar value for the planned experiment with 20 Mchip/s, a 1 s timing jitter of approx. 40 ps can be expected, which corresponds

to a relative short-term instability of about 7×10^{-11} (Allan Deviation at 1 s averaging time). The assumption of pure flicker phase noise as dominating process for all averaging times results in a relative frequency instability of 7×10^{-16} for 100,000 s averaging time. Taking into account white phase noise for averaging times up to 100 s and choosing a corresponding averaging process, even lower instabilities ($< 5 \times 10^{-16}$) can be expected for an averaging time of $\tau = 1$ d. This is consistent with a previous measurement carried out with 2.5 Mchip/s, where fountain clocks were compared over long baselines (both within Europe and between Europe and the US) with both TWSTFT and GPS [49]. There, the timing jitter at $\tau = 1$ s is between 0.2 and 0.4 ns, and a relative frequency instability between 1×10^{-15} and 1.5×10^{-15} could be observed for 1 d averaging time.

The channels were also investigated separately in order to cross-check how much the channels of one modem deviate from each other. Both channel results differ insignificantly by approx. 7 % on average, with RX2 having a little higher jitter for almost all measurements. Only for high chip rates and high carrier-to-noise-density ratios, RX2 shows a lower jitter. The difference between both channels was observed to be the highest for a chip rate of 2.5 Mchip/s with approx. 15 %. However, this can still be considered as insignificant and the overall behavior and order of magnitude is the same for both channels.

3.1.2 Long-term instability

For analyzing the long-term stability at 20 Mchip/s, several measurements were carried out. At first, a simple loop-back experiment was performed for all three modems (see Fig. 3.4 (a)), running for approx. 12 d. The modems were operated with similar settings: a chip rate of 20 Mchip/s, a frequency offset to 70 MHz of 17 Hz and a TX output power adapted to an RX input power of approx. -55 dBm. Without any additional noise, this results in a high C/N_0, larger than 69 dBHz, and a respective short-term instability. Some of the phase measurements (raw range) and the modified Allan Deviations are shown in Fig. 3.5.

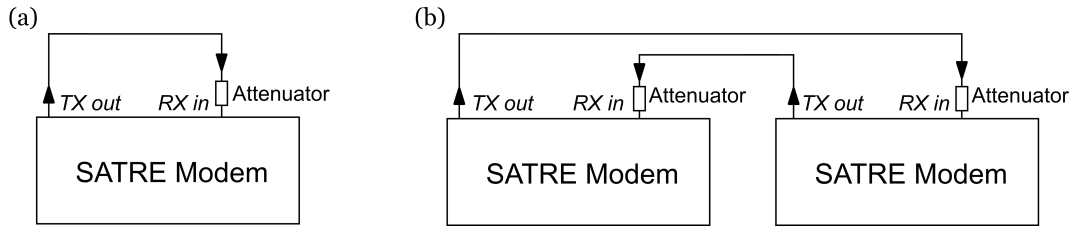

FIGURE 3.4: Setups for instability measurements. (a) shows the loop-back setup, with the TX signal output directly fed back to the RX input of the same modem. (b) shows the two-way setup via separate cables. For analyzing the instability, accuracy for time transfer is not needed, and thus it is not necessary to use one single cable or cables of the same length.

At this point, a general remark about data representation over time in this work shall be given. Since the use of the Gregorian calender date with days, months and years is mostly inconvenient for the mathematical purpose of having a continuous time axis, it is common in the time and frequency metrology field to use the Modified Julian Date (MJD). It represents a continuous scalar on an interval of 1 d. The fourteen days of measurement in Fig. 3.5, starting at MJD 56769, correspond to the period between

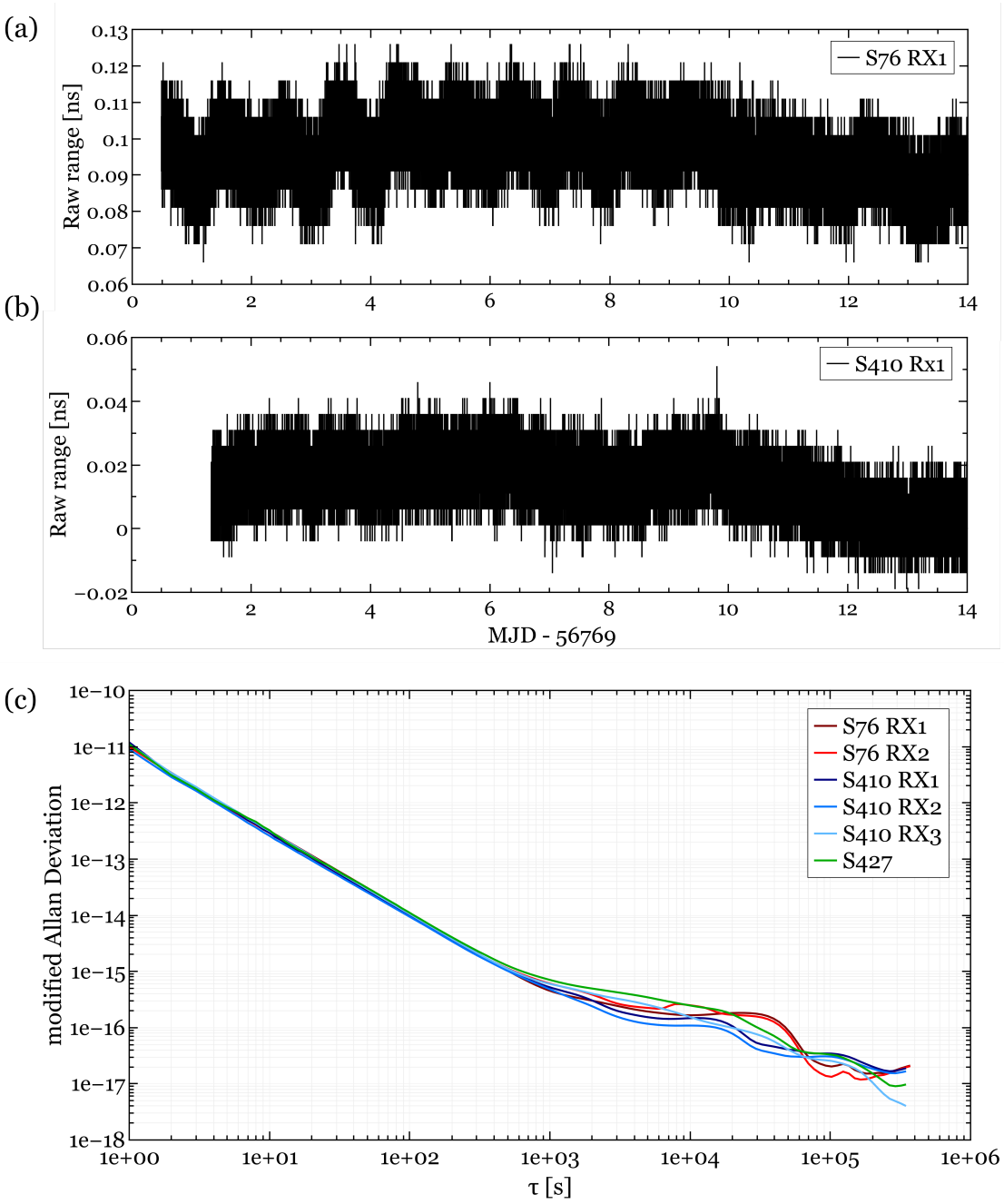

FIGURE 3.5: Results of loop-back measurements of three modems with an overall number of six RX channels. All measurements were running approx. 12 d. The settings were the same for each channel apart from the TX output power, which was adapted in a way the receiving power of the channels is around -55 dBm. Without additional noise, this corresponds to a large signal-to-noise ratio of more than 69 dBHz. In (a) and (b), the phase measurements (raw range) of two example RX channels are shown (with an arbitrary offset subtracted). The RX channel of S76 shows a diurnal-like oscillation during most of the measurement. The resolution of the measurement in the modem, 5 ps, can be seen. In (c), the modified Allan Deviations of all channels are shown. Phase noise is dominant up to averaging times of 500 s, whereas the long-term instability is dominated by fluctuations and drifts. The modified Allan Deviations show relative frequency instabilities smaller than 5×10^{-17} for averaging times of 1×10^5 s.

the 22nd of April and the 6th of May of 2014. Tools for conversion can be found on the web, for example in [169].

From the example phase measurements depicted in (a) and (b), it can be seen that both follow roughly the same trend, maybe caused by an environmental influence on the cable. In addition, both show a quantization of 5 ps, which is the measurement resolution by the SATRE modem. The RX channel of S76 features a diurnal-like oscillation during most of the measurement. This can also be seen in the modified Allan Deviations of both RX channels of S76, both are dominated by a bump at around 30,000 s averaging time. For averaging times up to 500 s, all six channels of the three modems show white phase noise. The instability at 1s corresponds to a measurement with 20Mchip/s at approx. 75 dBHz, according to the results found in Section 3.1.1, which is consistent. Not only the two channels of S76 show common behavior at averaging times larger than 500 s, but also RX1 and RX2 of S410. A bump at approx. 15,000 s indicates an oscillation with a period of several hours, which is not evident from the raw range graph. The third channel of S410, however, shows a different behavior and is more similar to S427. Both show a rather smooth averaging behavior of white frequency noise, i.e. without any dominant oscillation-like structure. A general difference in S410 between RX1 and RX2 on one hand, and RX3 on the other hand, can be explained by the setup of the modem. The first two RX channels share one input, whereas RX3 is connected to the monitoring output of the first two RX channels. However, this alone cannot explain the presence of the oscillation on the first two, and the absence on RX3. But, even with non-white phase noise at longer averaging times, the relative frequency instability reaches values smaller than 5×10^{-17} for averaging times of 1×10^5 s.

In addition to the loop-back experiment, two modems were connected with each other with separated cables, and thus separated and not necessarily reciprocal signal paths between the modems. In addition, non-correlated white noise of two different noise generators was added to the particular signal paths (see Fig. 3.6). The additional noise simulates the C/N_0 of 55 dBHz which is expected for the upcoming measurement campaign.

The results are shown in Fig. 3.7. In (a), the phase measurements of the modems (S76 and S410, RX1 respectively) can be seen. Due to the additional noise, the measurement resolution is not visible anymore in the phase measurements. Again, a weak diurnal oscillation can be observed. Interestingly, both this oscillation and the trend at the beginning of the measurement period appear inverted on both modems. The modified Allan Deviations in (b) show both the same characteristics, but also strong similarities with the instability discussed above for both channels of S76. White phase noise dominates up to 500 s, followed by a short period of flicker phase noise, and above 10,000 s, the instability of both channels are dominated by the diurnal oscillation. Due to the injected noise, the modified Allan Deviation here is increased for all averaging times by approximately one order of magnitude with respect to the case without any noise. The value at 1 s is consistent with the 1-s-jitter at 55dBHz. It is interesting to note that the same averaging behavior can be achieved with a higher C/N_0, and that even what is considered to be caused by the environmental influences like the diurnal oscillation scales qualitatively in the same way as the short-term instability. With this C/N_0, an instability of approx. 1×10^{-16} can be reached.

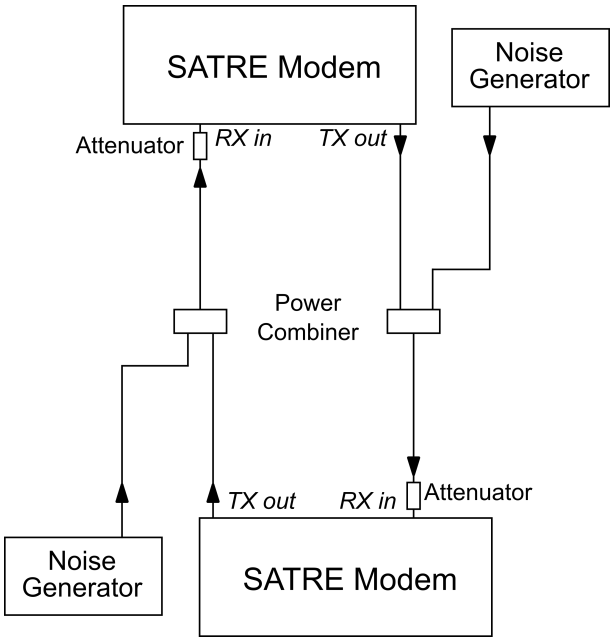

FIGURE 3.6: Setup for a measurement with two modems connected with non-correlated white noise on both signals. With this, a C/N_0 of 55 dBHz is generated. The modems S76 and S410 were used for this experiment.

3.1.3 Sources of disturbances and irregularities

As in the previous section already pointed out, some effects can be observed that lead to a deviation from the expected flicker phase noise behavior at averaging times longer than 1000 or 10,000 s, thus deteriorate the stability. Some of these effects cause oscillations of the measured phase, but not all oscillations that are observed have the same period. This section discusses some of the sources leading to such behavior.

Temperature sensitivity

At first a possible correlation between the temperature of the laboratory and the measurements of the modem was analyzed. For that, the modems were set up in loop-back measurements (see Fig. 3.4 above) at different locations, where temperature sensors were installed to monitor the temperature of the laboratory. The results can be seen in Figs. 3.8 and 3.9.

From the first figure (3.8) it can be seen that a correlation between the temperature of the laboratory and the modem raw range exists. The modem was operated without any change in settings or other interruptions. From MJD 56733 onwards, both the temperature and the raw range measurement show a diurnal oscillation. The diurnal temperature oscillation of less than 0.5 K from peak-to-peak caused an oscillation with an amplitude of about 5 ps. The two days of stable temperature before the observation of diurnal oscillation can be attributed to weekend days without any manual operations in the laboratory.

A second modem was installed in a laboratory with active climatization. The settings of the air conditioning system caused a temperature fluctuation with peak-to-peak differences of about 1.8 K and a period of approx. 1 h 45 min (see Fig. 3.9). The

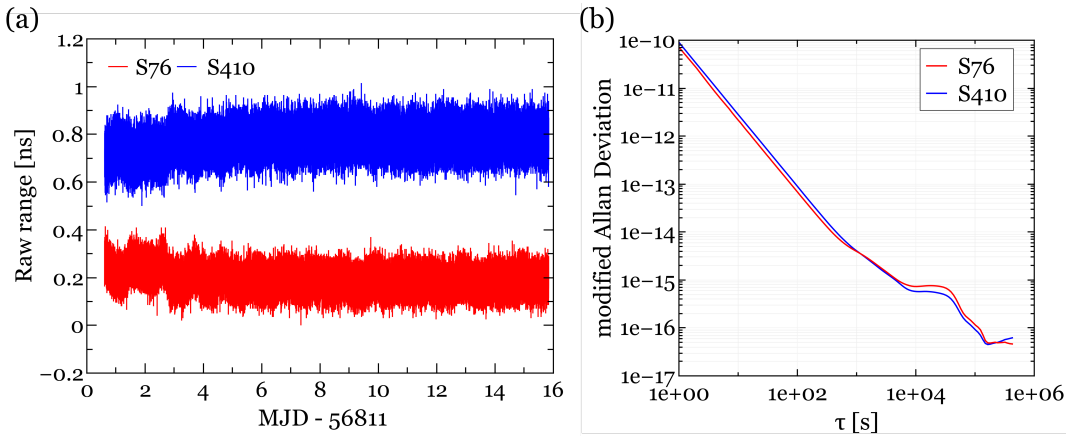

FIGURE 3.7: The result of a long-term measurement in a setup depicted in Fig. 3.6. On the left, the phase measurement can be seen, with arbitrary offsets subtracted for better visibility. On the right, the modified Allan Deviations are displayed.

raw range of the modem shows again a correlation with these fluctuations, with an amplitude of approx. 15 ps, but the opposite sign.

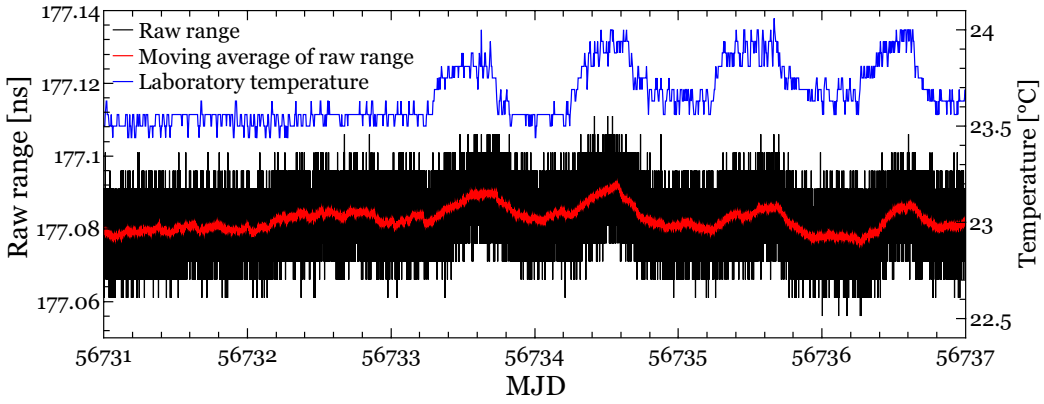

FIGURE 3.8: Result of a loop-back measurement of S76, with the modem located in one of the standard laboratories for time transfer equipment. The black curve shows the raw range, the red curve a moving average of the raw range with an averaging window of 5 min. The curve in blue depicts the temperature in the laboratory. Both the temperature and the raw range show a clear diurnal oscillation from MJD 56733 onwards, whereas both do not show any significant structure the two days before, which shows that both are correlated. The temperature rise is absent for the first two days since these days are a saturday and a sunday, and no manual operation was taking place in the laboratory.

To further analyze the sensitivity and to estimate a temperature coefficient of the equipment, another measurement was prepared: S76 and S410 were connected via two separate short cables in one laboratory where a part of the room could be isolated with a curtain-like partition wall. The temperature could be set via a program

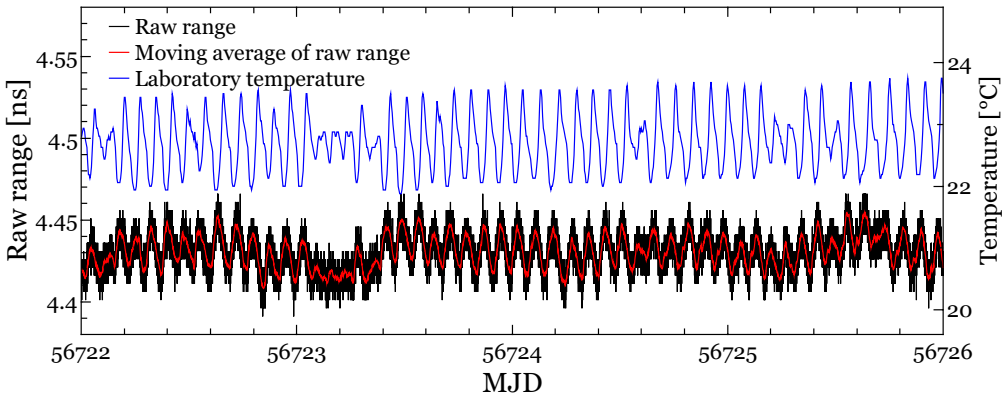

FIGURE 3.9: Result of a loop-back measurement of S427, with the modem located in a laboratory with active climatization. The black curve shows the raw range, the red curve a moving average of the raw range with an averaging window of 5 min. The curve in blue depicts the temperature in the laboratory. A correlation between raw range and temperature can be observed, with an opposite sign. The oscillation in temperature is caused by the control period of the climatization system of the laboratory. In addition to this short-term oscillation, a weak diurnal oscillation can be observed on the raw range, too.

for the two parts of the laboratory separately. In one part of the room, the temperature was kept stable, and in the other one, heating and cooling cycles with a peak-to-peak temperature difference of 4 K were executed. A temperature sensor was attached to both of the modems. The cable connections between the two modems were held short (approx. 3 m within the temperature-changing environment, and 7 m for the full cable length), so the impact of the temperature on the cables was considered to be negligible. The position of both modems was exchanged after several days, so each modem was both for some time in a temperature-stabilized environment, and for some time in an environment with temperature changes. The result can be seen in Fig. 3.10.

For the first measurement with S410 in the temperature changing environment, the temperature detected at the modem varies for approx. 4 K(see Fig. 3.10(a)). S410 and S76 show a raw range variation of 80 ps and 90 ps peak-to-peak, respectively, with S76 showing a positive correlation with temperature and S410 a negative one. The same correlation behavior can be observed in the opposite case of S76 being in the temperature changing part of the laboratory(see Fig. 3.10(b)). Here, the temperature variation at the modem is a little lower of approx. 3 K, causing a peak-to-peak raw range variation of approx. 300 ps for S76 and 200 ps for S410. So for each measurement, the raw range variations are in the same order of magnitude, with S76 showing a slightly higher variation, and both raw range variations always correlate with the same sign for the respective modem. This could mean that one modem is much more impacted by the temperature than the other one, and that both TX and RX have a separate impact that add up in the final measurement. Thus, only a residual effect is seen in the loop-back measurements discussed before, with a common mode impact of TX and RX canceling out, but becoming visible in the raw range measurement with another modem connected. It also has to be noted that in this

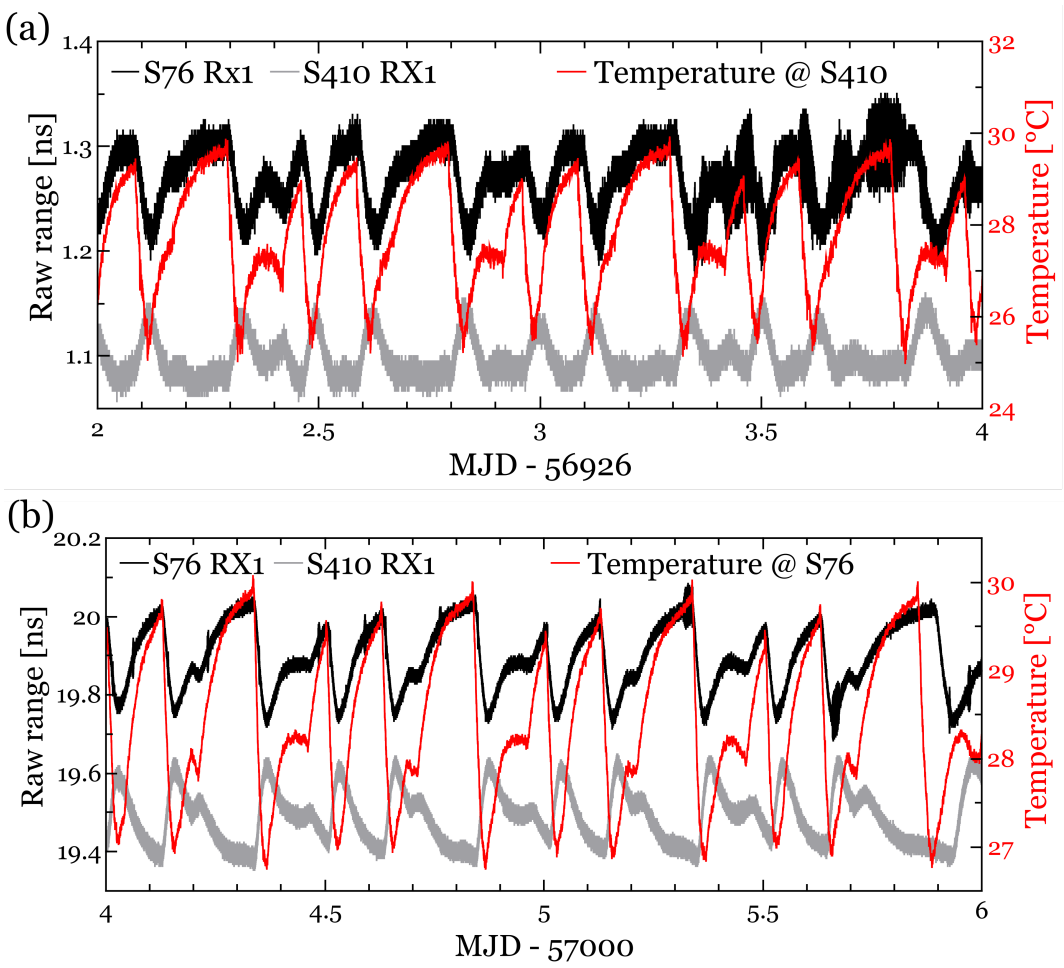

FIGURE 3.10: The raw range measurements of both modems, with the temperature measured at the modem located in the environment of changing temperature. (a) shows the measurement with S410 under influence of temperature change, and (b) the one with S76 located in the temperature changing environment. It can be seen that in both cases the raw ranges show a reciprocal behavior. Also, the impact on the raw range of both modems is in the same order of magnitude for each measurement, respectively. The measurements are shifted for better visibility.

experiment here, a residual temperature fluctuation can be observed in the stabilized environment due to the non-perfect isolation of the movable wall, following the same heating and cooling ramps, but reaching only about 0.5 to 0.7 K in peak-to-peak difference.

To make a rough estimate of the temperature coefficients, the following assumption can be made for the temperature-induced raw range measurement of modem S1 connected to modem S2:

$$\Delta T_{\mathrm{S1,\,temperature}} = \tau_{\mathrm{RX,\,S1,\,temperature}} + a \cdot \tau_{\mathrm{TX,\,S2,\,temperature}} \tag{3.2}$$

In this case, S1 is in the environment of temperature fluctuations, while S2 is in an environment of temperature fluctuations reduced by a damping factor a, which is approx. 1/6 in the experiment here. The signs are convention. Using the results above,

the following approximate temperature coefficients for the TX and RX units can be found: -69 ps/K (TX, S76), 99 ps/K (RX, S76), 6 ps/K (TX, S410), and -8 ps/K (RX, S410). The TW equation (Eq. 2.7 in Chapter 2.3.1), calculating the phase difference between the references of the modems, can be used to estimate the temperature-induced phase difference on that link for the case of one modem being exposed to a temperature change of 1 K:

$$\Delta \mathrm{TS}_{\mathrm{temperature}} = \frac{1}{2}(\tau_{\mathrm{RX,S1,temperature}} - \tau_{\mathrm{TX,S1,temperature}}) \tag{3.3}$$

For S76 being exposed to $+1$ K temperature change, the phase change on the link between the modems is 84 ps, in case of S410 being exposed to the same temperature change, the phase changes by -7 ps. These numbers are very different, and it has to be noted that these numbers are also only valid for measurements with RX1 of the respective modems. The second channels, RX2, show in general approximately the same behavior, but not necessarily having the same temperature coefficient, and it was seen in the previous section (Chapter 3.1.2) that RX3 of S410 did not show the same oscillation as RX1 and RX2. Hence, to apply a proper temperature correction to measurements, a respective full evaluation of all modems involved in the planned measurement campaign would be required. This was not considered to be feasible. Therefore, a rough estimation of 50 ps/K was taken as mean absolute coefficient for the contribution of one modem to a TW measurement.

Internal frequency cross-talk

In addition to the temperature-induced oscillations discussed above, several oscillations with a period between 1 h and 2 h could be observed at different TX frequencies used for both loop-back and TW measurements. As a consequence, some sets of measurements were performed in order to verify a systematic influence of the frequency set for the TX.

From the regular TW operations used for the comparisons of UTC(k) and the contributions to TAI/UTC, it is known that frequency offsets, i.e. the difference to the main carrier frequency of 70 MHz, should not be an integer in kHz, and especially not a multiple of 5 kHz, since this was found to deteriorate the stability of the signal, possibly due to cross-correlation effects within the modem. Correspondingly, for the measurements here mostly non-even values are taken as frequency offsets: 17 Hz, 7713 Hz and 13713 Hz, applied at the modems during different periods of time. For comparison, an offset frequency of zero was applied in one measurement. An example of the resulting raw range can be seen in Fig. 3.11.

The measurement depicted and other measurements show that a TX frequency value of 70 MHz leads indeed to oscillations with with a period of approx. 1 h 20 min and amplitudes up to 90 ps. However, certain offset frequencies, too, even though being a non-even number, can lead to oscillations with a period of approx. 2 h 15 min and amplitudes of up to 10 ps. In fact, out of the frequency values tested, only the offset frequency of 17 Hz does not show any significant oscillation. How this behavior is originating from the cross-talk in detail, however, is still unknown.

It was confirmed later by the manufacturer that there is some internal frequency cross-talk, and a minimum interaction between the signals could be achieved by taking frequencies with differences of about 17 kHz [170], which cannot be used

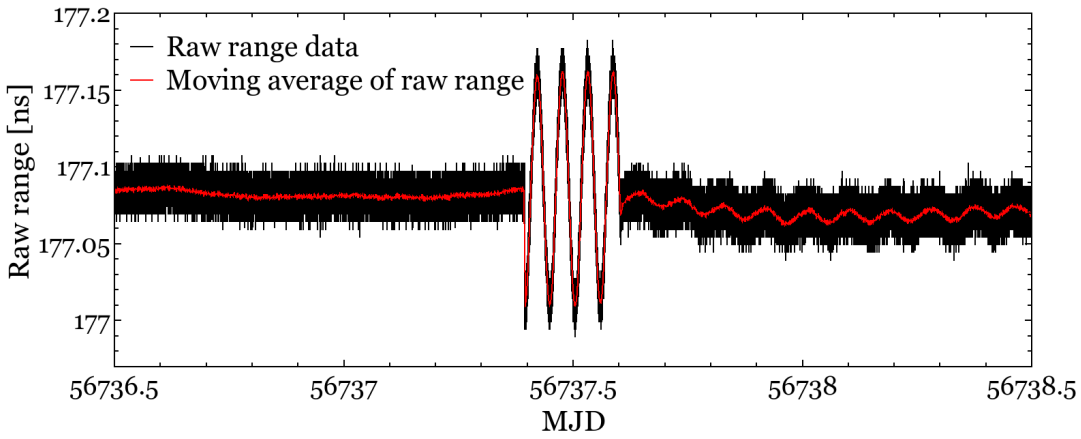

FIGURE 3.11: Loop-back measurement of S76, with different TX frequencies. In black the raw range measurement is depicted, in red the moving average over 300 points (5 min). During the first days, a frequency of 70,000,017 Hz was used, then precisely 70 MHz, and from MJD 56737.6 on, the frequency was set to 70,007,713 Hz. The modem was located in a laboratory with a diurnal change in temperature, thus, the diurnal oscillation reflects the impact of the temperature.

in the operational TWSTFT due to smaller bandwidth available. So for the clock comparisons, respective frequencies were chosen. A table with the frequency and other measurement parameters for the campaign can be found in Appendix A.

Also, when changing the frequency, a jump in phase of approx. 10 ps can occur. This observation was considered to be non-critical, since during the experiment the frequency offset should not change, and the absolute phase measurement is not of interest for frequency comparisons.

Phase jumps at relock onto the signal

Another phenomenon that was observed during all kinds of measurements with the SATRE modems is the impact of relocking onto the signal. Depending on the settings and the channels, outliers of several tens to hundreds of picoseconds were observed at the beginning of a session, i.e. during relock process. There is also a possibility that the modem locks onto a sideband, resulting in an offset and an unstable lock in general that can last for the whole measurement session until the modem gets the command of unlock and relock again. These measurements, although the phase noise is not significantly higher, show often low signal power and some fluctuations in the RX frequency.

A different issue was observed with modem S410. During several experiments it showed significant jumps of 20 ps at most relocks on all three channels. This is shown in Fig. 3.12. These jumps are between two defined states of locks, and randomly occur over the channels. The manufacturer stated that this can refer to the data polarity: the modem locks onto the signal in three steps: first, a code lock is achieved, than a carrier lock and in a last step a so-called data lock. The signal is modulated in a way that also some data is transmitted with the signal: the modem ID from the remote modem and the measured raw range from the last 10 seconds, enabling a calculation of an uncalibrated clock difference shown on the display of

the modem. This information can be found in the code modulation, by having a modulation with 0° (normal modulation) or 180° (inverted modulation) onto the signal, denominated as data polarity with "+" or "-". The internal calibration by the manufacturer adjusts the two locking states to the same delay, but there might be a residual offset. A software update was provided by the manufacturer later on, which would include the data lock sign as output. However, it turned out that the jumps do not correlate with the data lock sign.

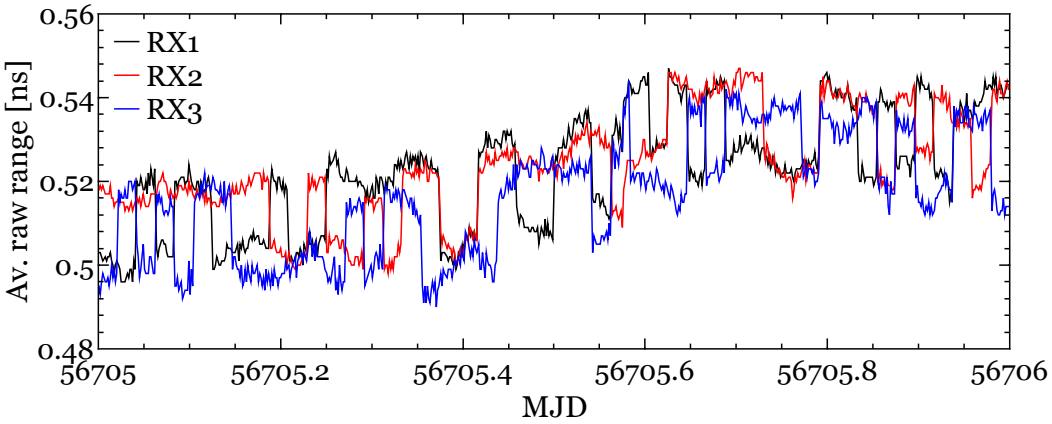

FIGURE 3.12: Raw range of S410, averaged over 2 min, for all three channels, during one day. The schedule used for this measurement forces a relock every 20 min. All three channels show random jumps of approx. 20 ps between two different locking states. The measured values have a constant offset for each channel for better visibility.

This effect was not observed for S76 nor S427. The only possible solution for using S410 during the campaign would be to keep it in continuous operation without relock, which is also in general seen preferable for the operation of any SATRE modem for such a campaign.

As discussed above for the TX frequency, phase jumps can occur when changing a setting. The same can be observed for the change of the PRN code (see Fig. 3.13). For this measurement, the modem S427 was operated in a loop-back setup (see Fig. 3.4 above), with a relock and a change of code every 20 min, resulting in phase jumps up to 20 ps. This observation is, like for the frequency, nothing to be taken into account for the planned experiment, since the settings are not expected to be changed during the campaign. However, it can also be seen in the figure that the noise for one of the codes (PRN code #2) is slightly higher than for the other two (#0 and #1). This was analyzed in a seperate experiment.

3.1.4 PRN code dependence

Ideally, the PRN sequences are all equivalent and show a high orthogonality with respect to each other. In reality however, potential cross-correlations or other disturbing effects might occur within the combination of different codes due to the way how the codes were developed and the truncation of the codes and thus due to the non-perfect orthogonality of these codes. These effects were investigated in order to find a combination of four PRN codes for the four participating institutes that gives the best result with respect to the jitter and locking behavior. Since only three modems were available to carry out tests, only combinations of three different

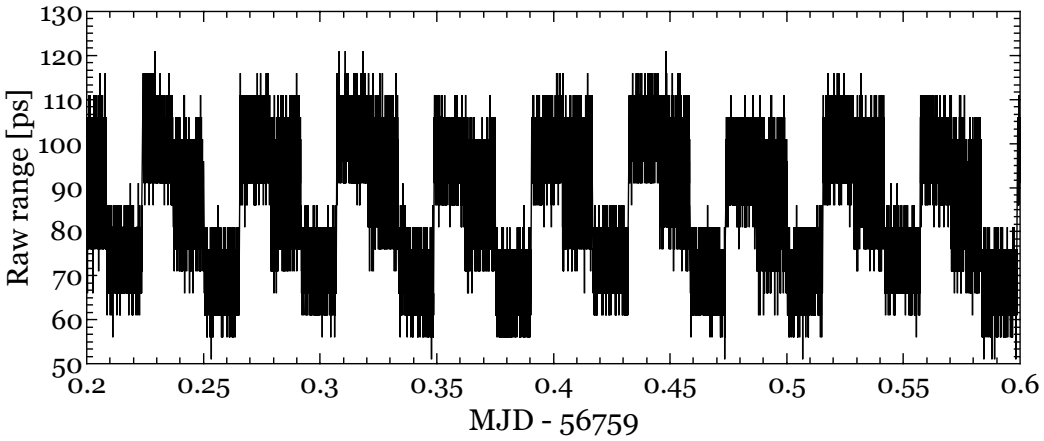

FIGURE 3.13: Raw range of S427, setup in a loop-back experiment, with a change in code every 20 min. Each code results in a different mean value for the raw range. Starting from the left, the PRN codes #2, #0 and #1 were set. It can be seen that #2 shows a slightly increased noise in comparison to the other two.

PRN codes could be investigated, and in a next step, from these combinations a set of four codes was found. To test combinations of three codes, a setup of all three modems was designed, with the transmitted signal of each modem fed into the RX input of each modem (see Fig. 3.14). In addition, white phase noise was added to simulate real measurement conditions ($C/N_0 = 55$ dBHz). A schedule, repeated each day, switched through a different 3-code-combination every 20 min. Only the codes $0 \ldots 7$ were chosen for the investigation: These first 8 codes were the first codes used for TWSTFT measurements with the MITRIX modems, and had been investigated with respect to their orthogonality to each other as a group in more detail [110], while other SATRE codes have been derived from these MITREX codes [170]. They are considered to show the least cross-correlation.

TABLE 3.2: The first code combination sessions (CCSs) carried out each day within the schedule. For each period of 20 min, three codes out of $0 \ldots 7$ were chosen, so every possible combination of these codes could be tested. A few combinations were tested more than once, but with a different modem assignment or a different transmitting/receiving direction for the modems.

Time slot	CCS ID	S76 sends / receives	S410 sends / receives	S427 sends / receives
0:00 – 0:20	1	PRN # 0 / 1	PRN # 1 / 2	PRN # 2 / 0
0:20 – 0:40	2	PRN # 3 / 2	PRN # 2 / 0	PRN # 0 / 3
0:40 – 1:00	3	PRN # 0 / 4	PRN # 4 / 2	PRN # 2 / 0
1:00 – 1:20	4	PRN # 0 / 2	PRN # 2 / 5	PRN # 5 / 0
... – ...	...	PRN # ... / ...	PRN # ... / ...	PRN # ... / ...

For simplicity, for most combinations of codes only one modem constellation was measured within the schedule, and only for few combinations the direction of emitting/receiving was changed or the codes were permuted over the modems. So with this experiment, potential differences between code combinations in general could be detected, and the potential impact of the modems could be observed, too. Also, potential differences between the different RX channels could be revealed. To avoid

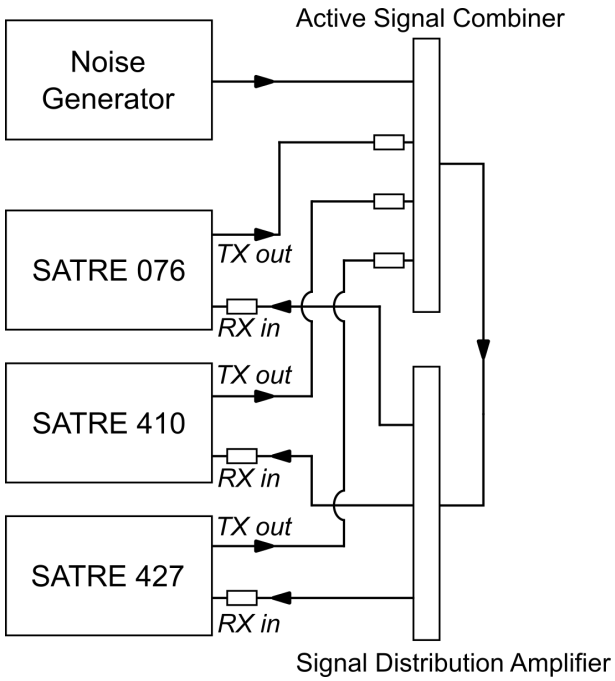

FIGURE 3.14: Setup for the measurement of different code combinations, with an active signal combiner and a signal distribution amplifier. In addition, white noise was added to the signal to simulate the real measurement conditions.

confusion with the terms "code combination" and "session" from here on, the different measurement blocks of the schedule will be called hereafter "code combination session", or short "CCS". The schedule was then running for 17 d, so each CCS was running seventeen times, each one for 20 min. Table 3.2 shows the way the CCSs are constructed and set up in a schedule. The complete list of the CCSs is given in Table A.1 in Appendix A.

The 1-s-jitter was calculated for each session, and all 17 jitter values (one from each day) for one CCS were averaged and the standard deviation was calculated.

The criteria to identify four codes out of the CCSs with three codes are the following:

- All CCSs with three of the four codes should have a reasonable low jitter for all modem channels.
- All CCSs with three of the four codes should have a low variation of this jitter, thus, not an increased rate of outliers for any measurement.
- All CCSs with three of the four codes should show a smooth and fast locking procedure (within 1 min).

Fig. 3.15 is showing the results. The numbers refer to the CCS number as shown in Table 3.2 or Table A.1 in Appendix A. It turned out that in general differences between the various CCSs are rather insignificant, compared to the differences between the modem channels. Especially the high jitter of S410's RX3 stands out. For all other channels, the jitter of a modem channel varies only within 3 ps over most CCSs. However, it was found that the origin of this observation is mostly due to the impact of the TX channel rather than due to the RX channel characteristics alone. For most CCSs, the transmitting direction is the following: S76 locks on the signal

of S410, S410 locks on the signal of S427, and S427 on the signal of S76. When this direction is reversed (as for CCSs #8, #57, #60 – #63, #67, #68 and #70 – #72), the jitter values change, especially for RX3 of S410, which has now one of the lowest jitter for these CCSs. This is also consistent with the jitter values obtained from various ranging sessions, which were included in the schedule for approx. 1 min each hour. So overall it can be said that for each modem, the jitter is the lowest when locking onto the signal of S76, and the highest when locking on the signal of S427. Code permutations within one signal direction do not give any significant changes, and the change of code combinations in general do not cause a significant change in the jitter. Furthermore, no significant changes were found in locking time.

In a previous experiment investigating the same subject but without any additional noise, significant differences between the CCSs due to different codes were observed in addition to the differences between the modem channels. From there, the PRN codes 1, 4, 5, and 6 were identified as optimum. However, it was later found that the setup showed reflections at passive elements and mixed only two out of three codes. Since the result above does not show any negative impact of these codes with each other, the codes 1, 4, 5, and 6 were kept (in Fig. 3.15, combinations of these codes correspond to the CCSs #31, #32, #34, and #53). Also, it cannot be excluded that differences between the CCSs in this flawed experiment originate indeed from cross-correlation between the codes that can only be observed at a high C/N_0 of 70 dBHz.

Beside the choice of the settings for the experiments, also the decision which modem to use had to be made. Although some of the experiments reveal a slightly worse performance for S410 than for S76 and S427 with respect to noise, these differences were considered to be negligible compared to the advantage of having 3 RX channels and thus the possibility of receiving all three of the other participating laboratories. So the modem S410 was chosen for the campaigns.

3.2 Preparation of the ground stations

From the possible setups of roof stations introduced in Chapter 2.3.1, the institutes participating in the experiment chose different approaches, corresponding to the availability of equipment and the possible use of secondary stations ready for operation. At PTB the possibility was given to set up the station from scratch.

The roof station of PTB can be seen in Fig. 3.16. PTB chose the approach of single equipment (SSPA, UC and DC as single devices) located in a roof box which not only provides a protection from humidity and direct sunlight exposure, but also a temperature-controlled environment, cooling the equipment if the temperature rises above 35 °C. The box was located as close as possible to the antenna without disturbing any operation. From there, a 3 m long flexible waveguide was used to feed the upconverted, amplified signal to the antenna. The waveguide was isolated and protected against sunlight, and the interior of the waveguide was kept dry and under constant pressure.

In contrast to the converters or transceivers used by the partners, the converters here provided frequency bands that allowed a loop measurement by directly downconvert the output signal of the upconverter again and feed it back to the modem located in the lab. With this, it was possible to directly measure the general instability of the

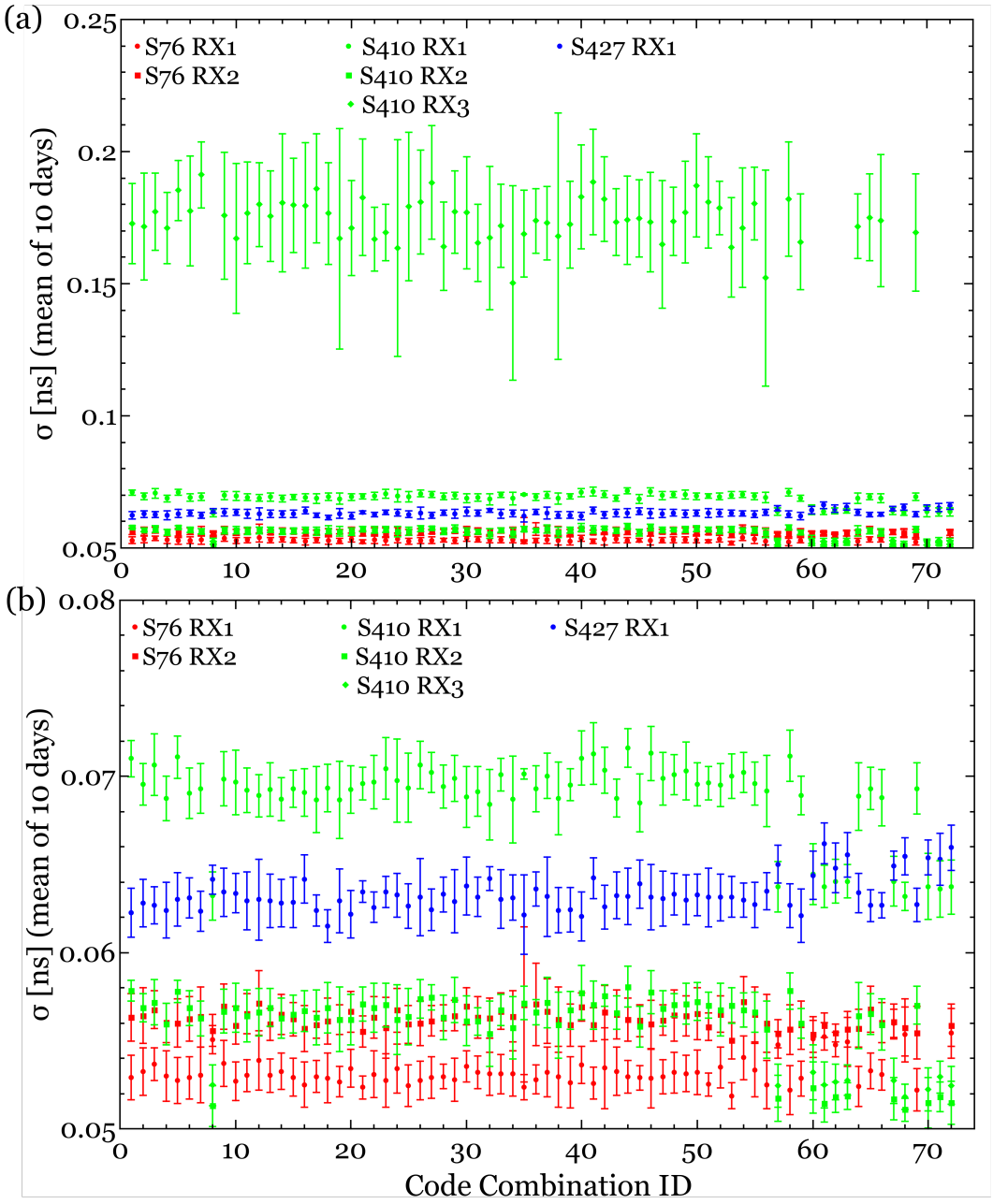

FIGURE 3.15: The mean instability at 1 s (mean jitter) for each code combination session over ten measurements. The error bar indicates the standard deviation for all ten measurements carried out for one CCS. (a) shows the results for all modem channels, in (b) the y-axis is limited to the region of 50 ps to 80 ps. The complete list of code combinations for the CCS IDs is given in table A.1 in appendix A.

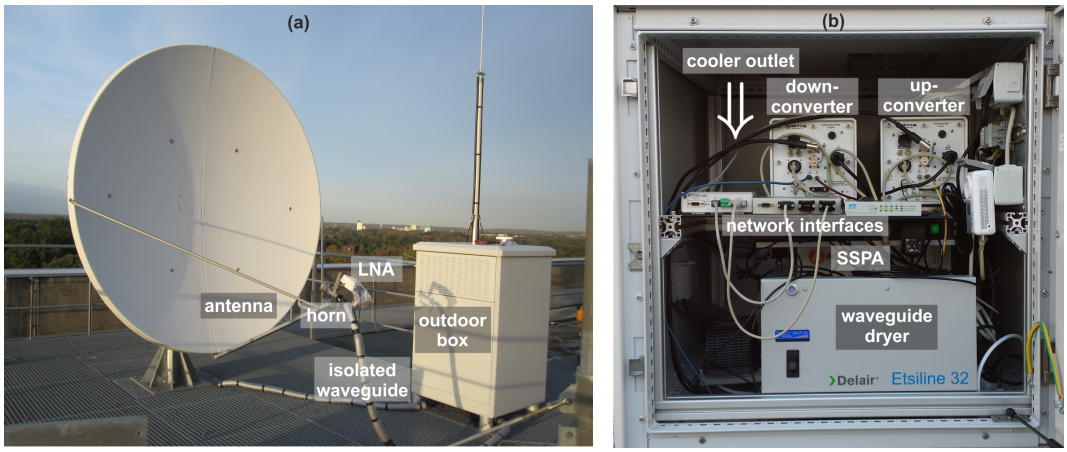

FIGURE 3.16: Pictures illustrating the setup of the roof station at PTB. (a) shows a photo of the antenna with the location of the LNA, the waveguides and the roof box. (b) shows the equipment on the inside of the box.

ensemble of modem, UC and DC before the installation in the roof box. The setup is shown in Fig. 3.17 (a). The comparison between the long-term-instability of a simple loop-back measurement in the laboratory (see Chapter 3.1.2) and a loop-back with the signal passing UC and DC can be found in Fig. 3.17 (b) in the form of modified Allan Deviations. One can see that the instability is the same for averaging times up to 400 s, and also not significantly different for longer averaging times. The loop-back including the converters show a slightly increased instability, but the diurnal oscillation induced by temperature in the laboratory is dominant. The difference between both Allan Deviations at averaging times larger than 100,000 s might be caused by either the increased uncertainty of the Allan Deviation due to the limited length of the data set or by long-term disturbances on the simple loop-back measurement.

In a second step, the converters were installed in the roof box. In this experiment, two modems were connected via two separate signal paths, with one passing through the converters on the roof (see Fig. 3.18). The result can be seen in Fig. 3.19.

In (a), the measurements of both modems and the temperature in the roof box are shown for the whole measurement period over several days. The temperature was measured by an external sensor close to the downconverter. The phase measurement by S76 which is receiving the signal traveling through both converters follows clearly the trend of the temperature with no significant delay, leading to excursions of a few hundreds of picoseconds. The measurement by S410 on the other hand is only varying within a range of several tens of picoseconds, and no significant dependence on the temperature can be observed. However, in the middle of the measuring period, some diurnal oscillation appears which, as it was found in Chapters 3.1.2 and 3.1.3, is reversed with respect to the periodic structure on the measurement of S76. It is therefore likely an effect based on the temperature in the laboratory.

In (b), a few hours are shown in detail for S76 and temperature. The saw-tooth-like structure of the temperature stabilization within the box is clearly visible in both graphs, a peak-to-peak variation of about 4 K, inducing a variation in phase with an amplitude of about 20 ps. From these measurements, a temperature coefficient for a one-way measurement through both converters can be derived, being 10 ps/K. Due

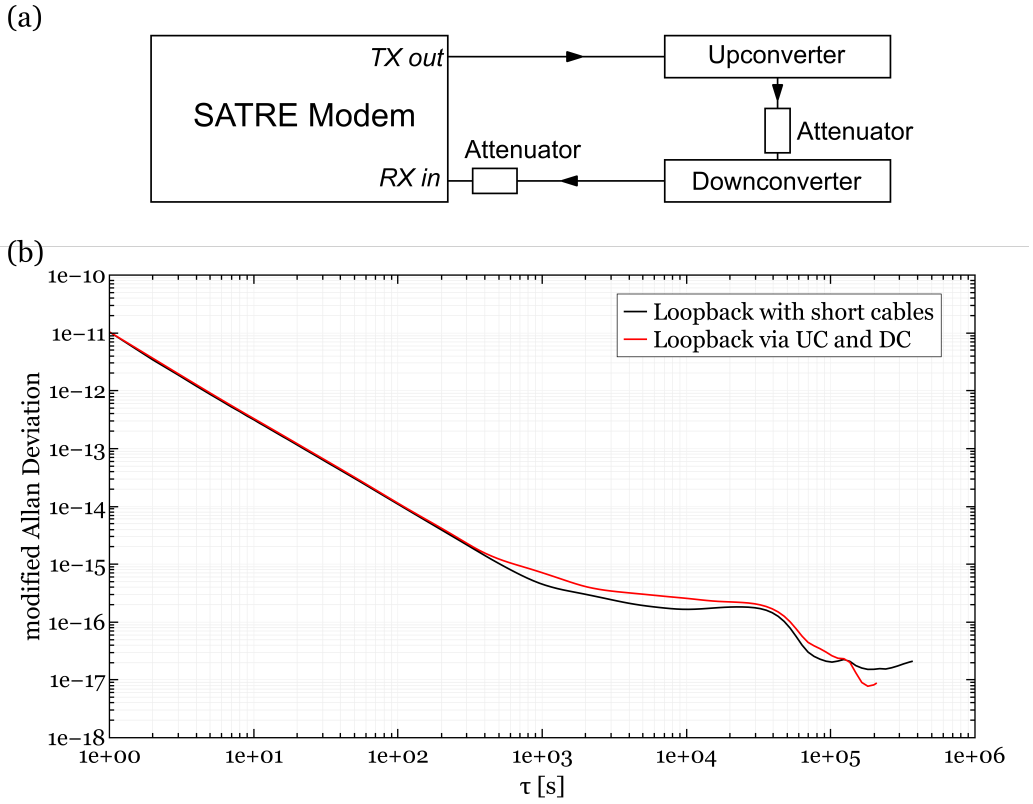

FIGURE 3.17: Loop-back experiment with the up- and downconverter included. (a) shows the setup, (b) the modified Allan Deviations of this experiment (in red) and in comparison the one of a simple loop-back carried out for the long-term instability of the modem (see Chapter 3.1.2) in black.

to the TW equation (eq. 2.7), the overall impact of the temperature at one side on the phase difference between two remote stations is divided by 2, thus the temperature coefficient becomes 5 ps/K for one of two stations.

For the connection between the roof station and the modem, reflections within the cables resulting in multipath need to be taken into account (see Chapter 2.3.1). For a non-erroneous correlation, the original signal and the reflected signal should be delayed by at least 1.5 times the chipping period [121], which is 50 ns in this case. So in order to suppress this effect as well as possible, all cables carrying the modulated signal from the modems to the roof station should be longer than 16 m.

A final aspect that is considered for the setup of the ground stations is the minimization of the impact of the path delay difference and the Sagnac effect (see Chapter 2.3.1), which are negligible in case of the regularly operated TWSTFT for UTC(k) comparisons, i.e. with instabilities of low 10^{-15} at one day measurement time. However, these effects become more important when instabilities, and thus uncertainties lower than that are expected. The variation of the Sagnac effect will be handled in post-processing, while the variation of the path delay difference can be minimized by increasing the reciprocity of the signal path. Therefore, with the position of the satellite roughly known, an artificial delay can be introduced at the stations in a way that the signals from each station arrive at the satellite at roughly the same time. These calculations were carried out by project partners at LNE-SYRTE and

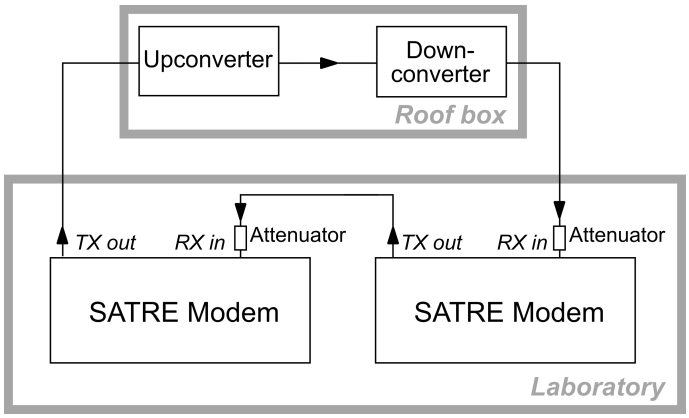

FIGURE 3.18: Setup of the two-way-like experiment between two modems (S76 and S410), with one signal path passing through the up- and downconverter located in the roof station.

NPL [171], and provided the respective delays of 0.6, 1.0 and 2.6 ms to PTB, LNE-SYRTE and INRIM, calculated with respect to the signal path from NPL to the satellite, which is the largest distance.

3.3 Selection of satellite

For operating at 20 Mchip/s, a bandwidth of 34 MHz on a satellite transponder is required.

In order to choose an appropriate satellite with such a transponder, several criteria had to be fulfilled, with having all four participating stations within the signal footprint of the satellite being the most trivial one. Furthermore, the satellite position should enable the laboratories to work with an elevation angle not too low, i.e. higher than 10 °, for an optimum higher than 20 °. Also, the criteria which are common for TWSTFT, like up- and downlink frequency range and linear orthogonal polarizations between up- and downlink were required.
As described in Chapter 2.3.1, TWSTFT measurements underlie a geometric and a relativistic effect, out of which the relativistic effect (Sagnac effect) has an impact on the choice of the satellite. The goal is to perform corrections on the final measurements to have the effects originating from the residual movement of the satellite cancel out. For the calculation of these corrections, the position and the velocity of the satellite need to be known within a certain uncertainty. Although an uncertainty lower than 1×10^{-16} at one day was not expected for the overall uncertainty, the calculation was carried out addressing an uncertainty of approx. 5×10^{-17}.

Two different approaches were used to carry out the calculations [1]. One is to perform simulations with data from the satellite used for the operational TWSTFT within Europe, Telstar 11N, operated by Telesat. With this, the order of magnitude of both effects was estimated, and following the calculations in [172], the requirements could be determined. The second one is to carry out numerical calculations following a similar approach as in [173]. Both analysis methods came to similar results: With the assumptions of a satellite residual velocity lower than $1\,\mathrm{m{\cdot}s^{-1}}$ and a residual acceleration in the rotating frame lower than $10^{-5}\,\mathrm{m{\cdot}s^{-2}}$, the satellite position should

[1] These calculations were carried out by the project partners LNE-SYRTE and NPL.

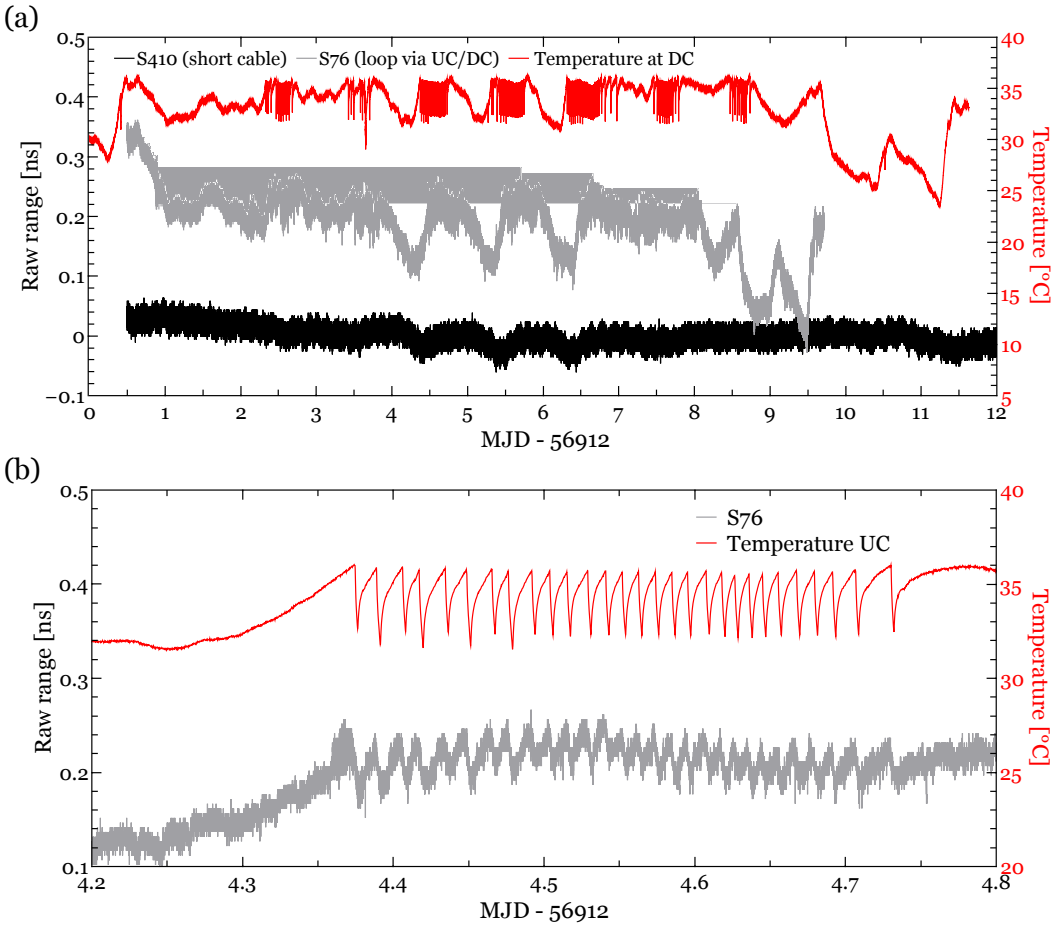

FIGURE 3.19: Measurement between two modems, with one signal path passing in a loop through up- and downconverter, located in the roof station. In (a), both measurements (raw range) are shown over the whole period, together with the temperature in the roof box, measured close to the downconverter. An arbitrary offset is subtracted of both raw range measurements for better visibility. A clear correlation between the temperature and the modem receiving the signal passing through both converters can be observed. (b) shows a few hours of one of the days. The sawtooth-like structure results from the temperature regulation within the box.

be provided with an uncertainty of 2 km or lower on an interval of around 10 minutes [174]. An explicit figure for the velocity was not considered to be necessary.

The satellite provider Société Européenne des Satellites (SES) was chosen, with the satellite ASTRA 3B fulfilling all criteria mentioned above. A footprint can be seen in Fig. 3.20. The corresponding up- and downlink frequencies of the transponders that were used for the measurements can be found in Appendix A.

3.4 Scheduling of the TW links

With S410, PTB had a 3-channel modem which could be used to receive all other three participating institutes simultaneously. So a switch for the channels between

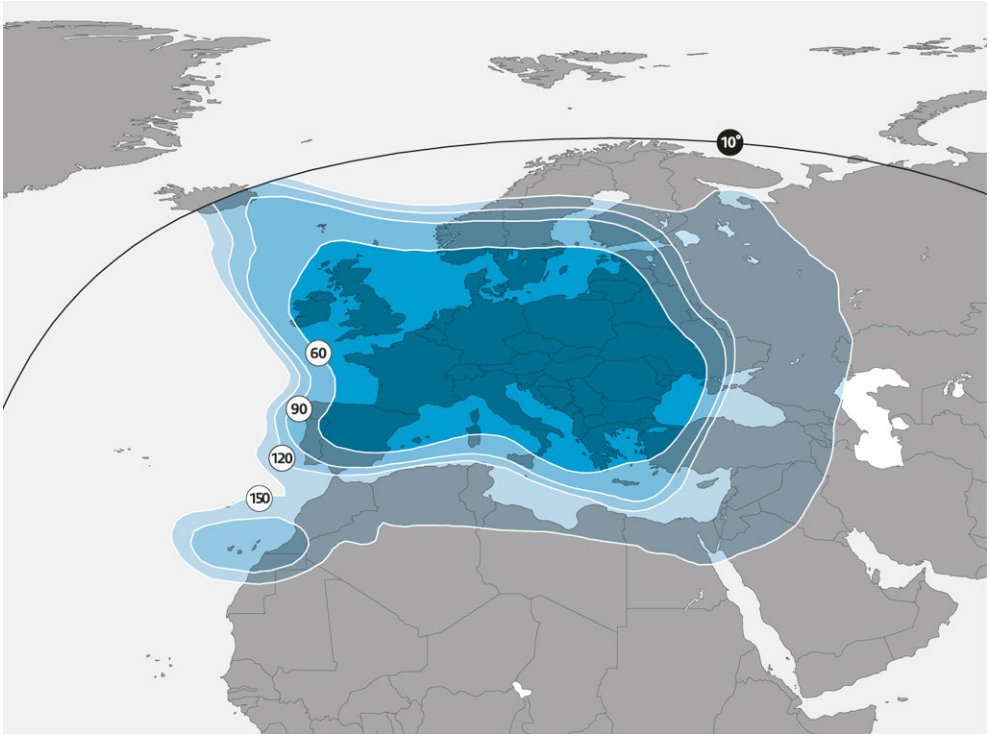

FIGURE 3.20: The footprint of the satellite Astra 3B in the K_u band (wide beam), taken from www.ses.com [175].

the stations was not necessary here. However, the other laboratories had only 2-channel-modems available. So the introduction of a schedule was necessary.

The operational TWSTFT measurements are carried out at each institute with a different software to control the modem and to generate the data files. This does not allow any flexibility in changing the links which is desired to adapt to the uptimes of the optical clocks. Also, the data recording is optimized for the generation of data files in the so-called ITU-format, which is used as universal format for TWSTFT files and contains already single values for each session, calculated by a quadratic fit over the length of the session. However, it is the aim to make use of unprocessed data in order not to loose any information, i.e. to use the raw data recorded on a 1s-time grid. For the raw data, on the other hand, no unified data format exists, which is not only problematic for the overall data analysis after the campaign, but also for the monitoring done during the campaign to identify and eliminate failures and problems as early as possible.

As a solution, two pieces of software were developed by PTB. One is a modem control software based on the software already implemented at PTB that needs a schedule configuration file as input, transfers the settings accordingly to the modem and generates data files from the raw modem output. The format of the output strings of the modem had been unified for that purpose, and files contain in addition to the raw range data information about frequency, power, signal-to-noise-ratio, internal temperature and lock status. The schedule configuration files are generated locally at PTB by a second software and distributed over various channels (cloud spaces, email) to the other institutes.

The schedule implemented switches between 3 different configurations hourly, depicted in Fig. 3.21. With this, the links between two of the three stations at INRIM,

LNE-SYRTE and NPL were only in operation for one out of 3 hours. During the time when one of the institutes was not receiving any of the other two, ranging was performed. The duration of 1 hour resembles a compromise between having continuous data for a post-processing of data to average most of white phase noise on the one hand and to avoid too large breaks in the data on the other. Also, an hourly shift could easily be realized manually by the software already implemented at the other stations in case the self-written software by PTB experiences a failure.

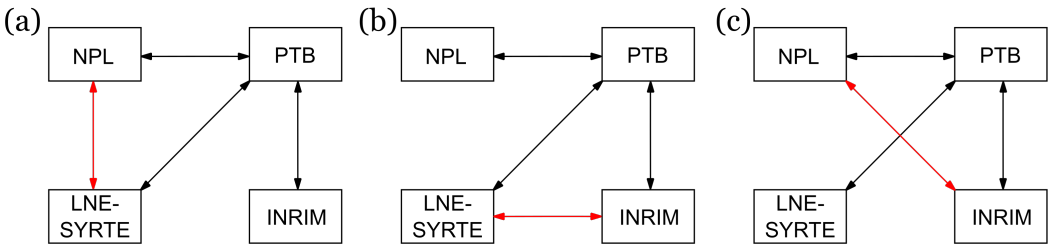

FIGURE 3.21: Link configurations for the link test campaign. A schedule switches hourly between a, b and c. The red arrows indicate the changing links.

Chapter 4

The satellite link test campaign

After an evaluation of all equipment involved, as described in the previous chapter, the last step of preparation is a test of the actual link operation with the satellite involved. For that, the time the satellite transponder was available for this project was split: out of the 28 days of the payed transponder time, seven days were scheduled several months before the actual clock comparison campaign.

This link test campaign was not only meant as a proof of concept for the goal of reaching the low 10^{-16} range in instability, but should have shown potential difficulties and flaws in the setups and coordination during the campaign. Therefore, only a trimmed-down version of the setup dedicated for the clock comparison was used, involving only the TWSTFT stations and the reference HM (see Fig. 4.1).

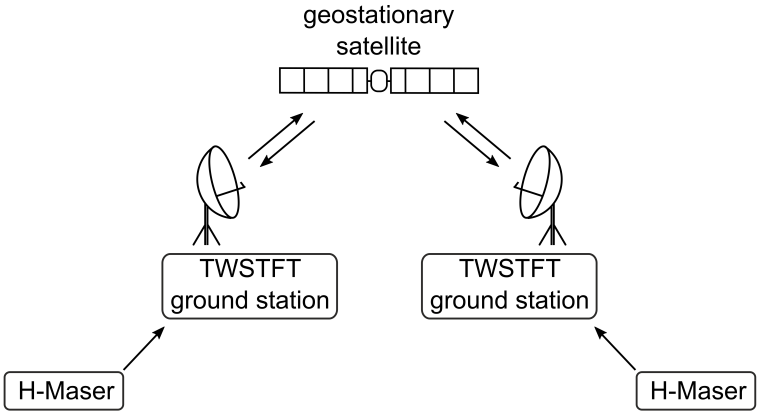

FIGURE 4.1: Setup of the link test campaign to test the operation of the TWSTFT satellite links.

The campaign could be carried out successfully, with all laboratories involved testing their equipment and signal quality. Some unforeseen incidents in hard- and software aspects showed potentials for improving the robustness of the equipment and process.

4.1 Data recorded during the campaign

For monitoring and analysis, the raw data recorded by the modems at each laboratory are collected. This includes the raw range data (ΔT in Chapter 2.3.1). An example of the raw range recorded during the campaign can be seen in Fig. 4.2. The

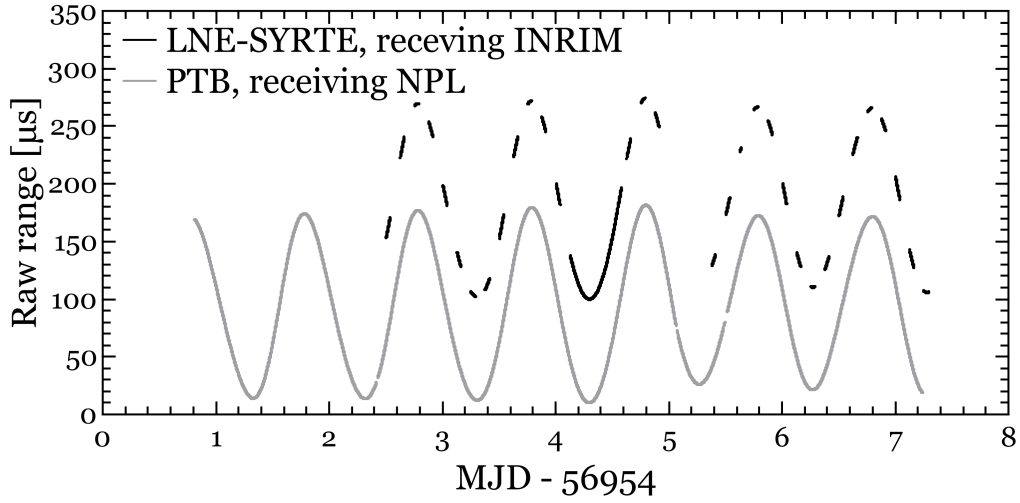

FIGURE 4.2: Raw range of two different modems during the campaign, by LNE-SYRTE receiving INRIM's signal in black, and by PTB receiving NPL's signal in gray. The measurements are shifted for better visibility: both by approx. 250 ms close to zero, which is about the time the signal takes to travel from the ground to the satellite and back, and an additional shift was applied to the curve in black to have an artificial offset of 0.1 ms between both. Note that the actual offset, approx. 0.8 ms, results from the different times-of-flight from the satellite to the respective ground station, and is twice this difference. This difference was also calculated to introduce a delay at the ground stations with respect to NPL's signal uplink path in order to suppress the path delay difference effect (see Chapter 3.2). The sinusoidal structure originates from the residual movement of the satellite.

black curve shows the raw range of a SATRE modem located at LNE-SYRTE, receiving the signal from INRIM, and the grey curve is depicting the raw range of PTBs modem, receiving the signal from NPL. Offsets are applied for better visibility. Both are in a sine-shape with an amplitude of approx. 90 µs, which reflects the extension and shortening of the signal path caused by the daily residual motion of the satellite. The raw range measured at PTB is mostly uninterrupted, since the links to PTB were operated continuously. The raw range of LNE-SYRTE shown here is already filtered for showing only the time when the channel was locked onto INRIM's signal, thus showing the 1-h-sessions every 3 h of the schedule.

Some unforeseen events disturbing the planned schedule can be exemplarily seen in the figure. An equipment failure at INRIM prevented the station from joining the campaign from the very beginning, but a quick substitution could be made, and INRIM could participate with a delay of two days. During the campaign, the upload of the configuration files failed once, resulting in an uninterrupted measurement of one single configuration for 11 hours, which can be seen as one long uninterrupted session for the link between LNE-SYRTE and INRIM. Furthermore, the modem control software at LNE-SYRTE failed once, resulting in the loss of 8 hours of data. At the end of the campaign, the hydrogen maser at PTB failed, shortening PTB's participation by a few hours.

In addition to the raw range data, each modem records the RX frequency, power, and

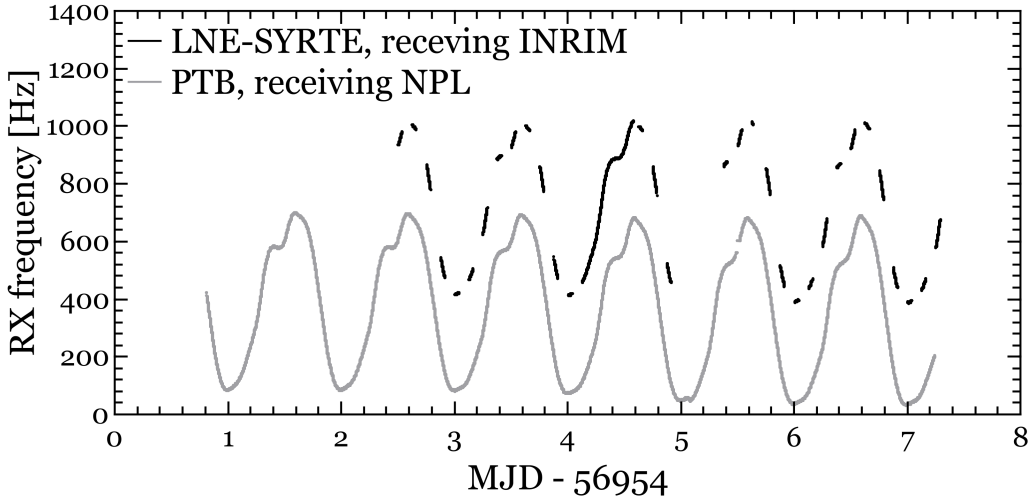

FIGURE 4.3: RX frequency of two different modems during the campaign, by LNE-SYRTE receiving INRIM's signal in black, and by PTB receiving NPL's signal in gray. Measurements are shifted for better visibility. The sinusoidal structure originates from the residual movement of the satellite.

carrier-to-noise density ratio. The RX frequencies recorded by the same channels as in the raw range depiction are shown in Fig. 4.3. Again, offsets were applied for a better visibility. The sinusoidal shape can be seen as well, it originates from the changing Doppler shift that occurs due to the residual satellite movement. There are regular patterns on the frequencies, most probably due to a shadow falling on the satellite (e.g. by one of the solar panels), which would result in a temperature change within the transponder and thus effectively a frequency change.

An example for the monitored RX power can be seen in Fig. 4.4. While the RX power from NPL recorded at PTB is mostly constant, the power recorded at LNE-SYRTE from INRIM shows a weak sinusoidal shape and a decreasing trend. This might be caused by the alignment of one (or both) of the antennas, either the one receiving at LNE-SYRTE or the one transmitting the signal of INRIM: Due to a mispointing of the antenna, the satellite is not in the center of the antenna spot and thus very small position changes of the satellite can cause noticeable changes of the signal power at the antenna. In addition, the trend might have its origin in the fact that the orientation of the antenna is not to 100 % fixed and thus slowly moving with respect to the satellite.

In addition, each modem records the internal temperature, but as an average of two sensors of unknown location within the modem. A comparison between the internal modem temperature as recorded by the modem itself and the temperature at the modem measured by an external sensor is shown in Fig. 4.5, measured at LNE-SYRTE. The temperature measured by the modem is shifted by $-12\,\mathrm{K}$. Interestingly, the both curves do not show any common features, except for the two ditches on day 5. Since an external logging has been proven to work, the focus was put on the external logging.

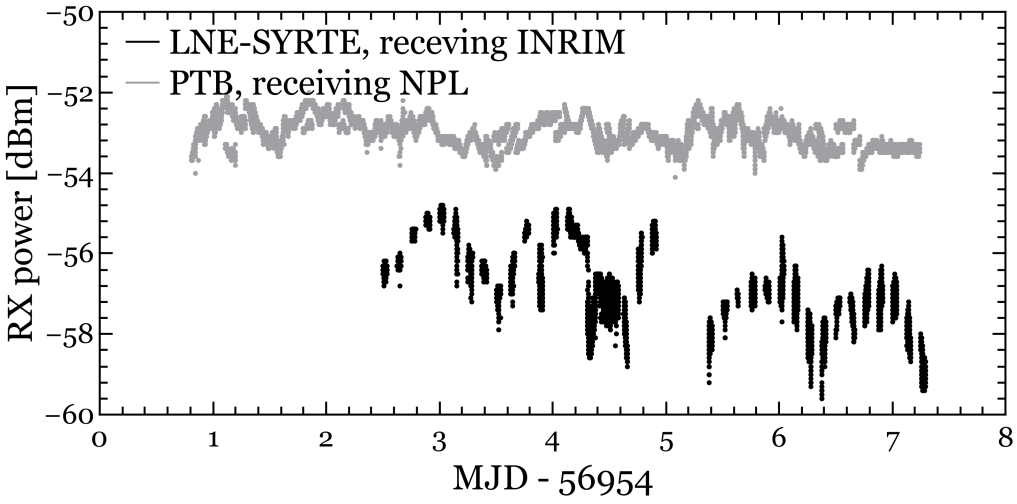

FIGURE 4.4: RX power of two different modems during the campaign, by LNE-SYRTE receiving INRIM's signal in black, and by PTB receiving NPL's signal in gray.

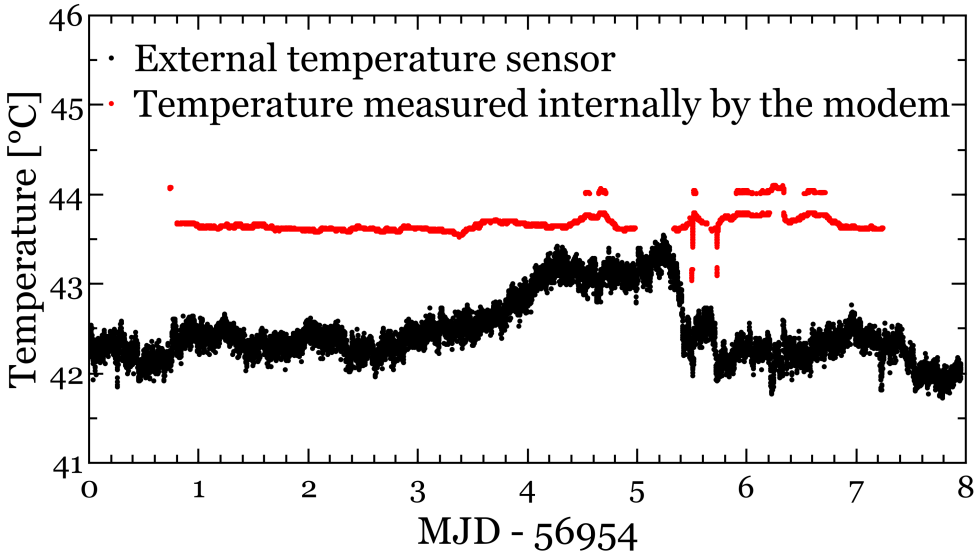

FIGURE 4.5: Modem temperature at LNE-SYRTE, recorded with an external temperature sensor (black) and internally within the modem (red). The temperature measured by the modem internally is shifted by $-12\,\mathrm{K}$. It is the average of the temperature measured by two internal sensors of unknown position.

4.2 Data processing

The raw range corresponds to ΔT in Eq. 2.5 from Chapter 2.3.1. In this case here, the signals from the two hydrogen masers used as reference for the modems represent the two time scales to be compared, so the difference ΔTS in Eq. 2.5 becomes $x(\mathrm{HM}_1 - \mathrm{HM}_2)(t)$, and the TW equation (Eq. 2.7) is rewritten:

$$\begin{aligned} x(\mathrm{HM}_1 - \mathrm{HM}_2)(t) &= \frac{1}{2}(\Delta T_1(t) - \Delta T_2(t)) + C(t) + const. \\ &= x'(\mathrm{HM}_1 - \mathrm{HM}_2)(t) + C(t) + const. \end{aligned} \tag{4.1}$$

A constant residual offset from non-reciprocities on the signal path is left, which does not need to be taken into account for a frequency comparison. Furthermore, there are some non-reciprocities fluctuating with time that can be corrected ($C(t)$). All other fluctuations are attributed to the link instability. Thus, the term $x'(\mathrm{HM}_1 - \mathrm{HM}_2)(t)$ is the calculation of the HM phase difference in a first estimate by just using the raw modem data (raw ranges), without any correction. This is done in a first step of data processing. It is calculated only for times where both $\Delta T_1(t)$ and $\Delta T_2(t)$ are available, i.e. where both have common time stamps. In a next step, outliers are removed by a two-step piecewise cubic fitting: the fit is calculated over an interval of 200 s and points deviating from the fit by a fixed threshold of 250 ps are removed. In a second step, the process is repeated, but by applying a threshold of 32.5 ps for the deviation of the data from the fitted curve. The process results in gaps on the data of 1 or 2 s in length. In addition, the corrections for the Sagnac effect are applied, interpolated on the same timestamps where $x(\mathrm{HM}_1 - \mathrm{HM}_2)(t)$ is available. As a final step, the linear drift on the phase originating from the frequency offset between the two masers is removed.

4.3 Satellite link instability

The results of this processing can be seen in Fig. 4.6. Each of the plots (a) – (d) contains all links with one laboratory in order to make common mode features for one laboratory better visible. The phase is shifted for better visibility. Some curves show diurnal-like structures, especially well visible on the link between LNE-SYRTE and PTB. Some curves also show some significant fluctuation patterns with changes of a few hundreds of picoseconds within only few hours or less, which repeat every day. Comparing (a) with the other graphs, it becomes apparent that these fluctuations are only visible on the links to INRIM. Their origin is unknown.

In a next step, the modified Allan Deviation of all links was calculated. Since the commonly available algorithms can only treat data on a continuous time grid without gaps, a new calculation method was implemented [176]: triples of phase data in intervals of τ are only taken into account for the calculation if all three values exist. This gap-tolerant modified Allan Deviation works only for phase data, and was used within this work for most calculations of modified Allan Deviations of phase data, so interpolation or discarding a lot of data could be avoided. However, so far the calculation of the uncertainty for each $\sigma(\tau)$ is not implemented yet into the calculation process and regular gaps as in the data here require a careful interpretation

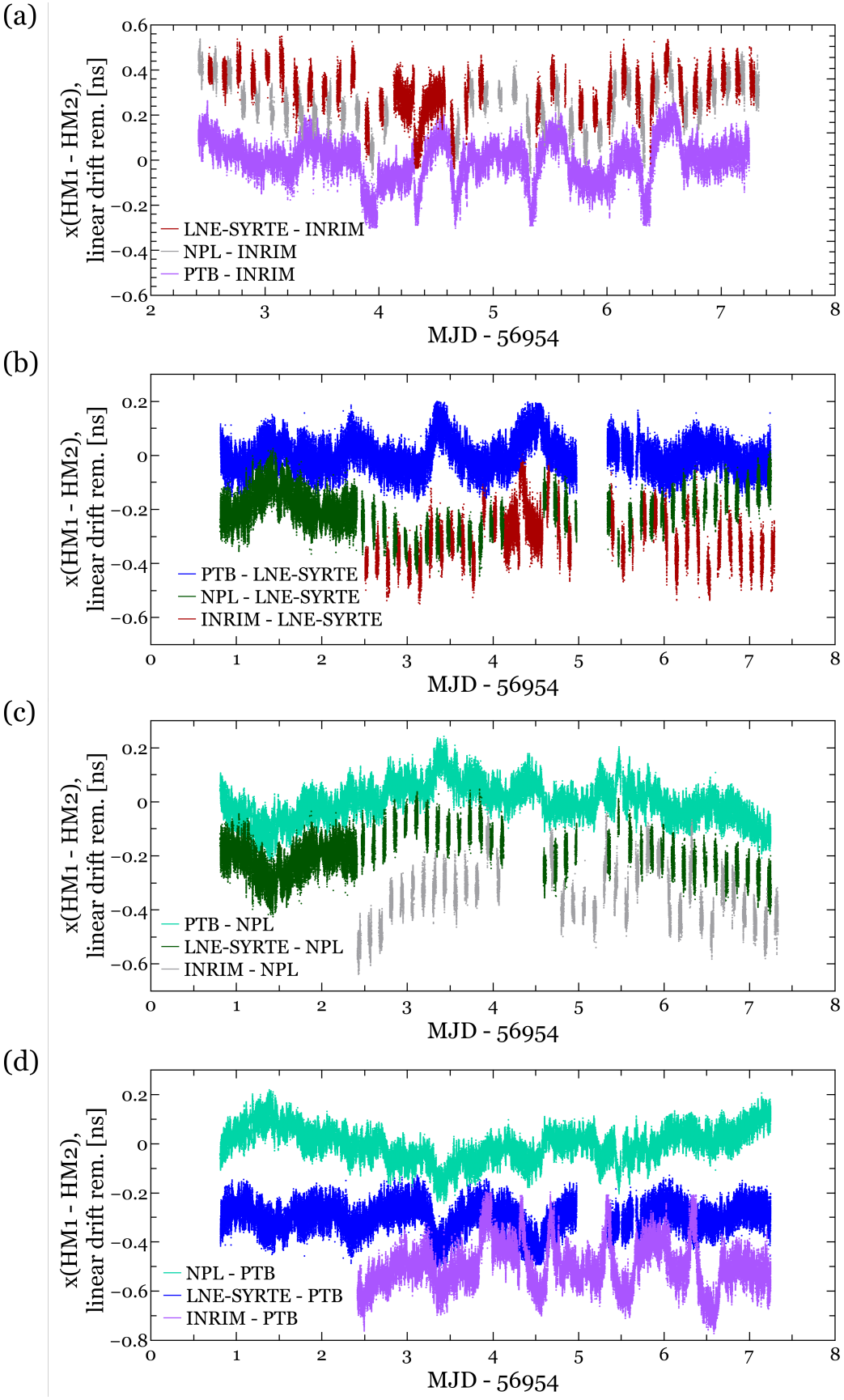

FIGURE 4.6: The phase difference between all four reference HM, as measured by the SATRE modems, with the Sagnac corrections applied, and the linear drift (frequency offset) removed. (a) shows all links with INRIM involved, (b) for LNE-SYRTE, (c) for NPL and (d) for PTB. The phase is shifted for better visibility.

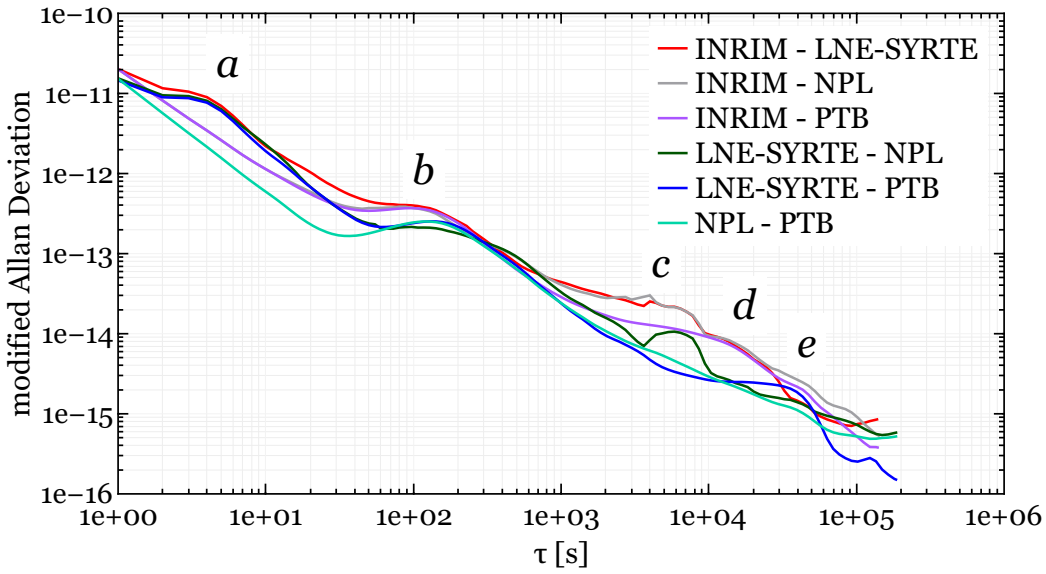

FIGURE 4.7: Modified Allan Deviation of the phase data in Fig. 4.6. It is calculated with a gap-tolerant method. Disturbances and other significant structures are marked with "a" to "e". "a" and "b" are frequency modulations on the phase data, most probably caused by reflections in ground station devices. "c" is originating from the calculation method, since it corresponds to the regular gaps on the links that were switched within the schedule. "d" are phase fluctuations on the INRIM-related links of unknown origin, and "e" diurnal oscillations which are mostly dominant on the link LNE-SYRTE – PTB.

of the calculated result. Especially the instability at averaging times in the range of the distance between regular gaps have rather high uncertainties due to the low amount of phase triples available. The resulting modified Allan Deviations can be found in Fig. 4.7.

At first, it can be noted that the instability of all links at 1 s is in the range of $1...2 \times 10^{-11}$, which corresponds to a C/N_0 of approx. 70 dBHz (see Fig. 3.3 in Chapter 3.1). The link NPL – PTB shows the lowest instability of all links up to 30 s, with almost pure white phase noise, and the instability of the links INRIM – NPL and INRIM – PTB average to the same value of τ with a combination of white and flicker phase noise. All links involving LNE-SYRTE show a characteristic bump at an averaging time of a few seconds, which is marked as "a" in the figure. Another characteristic feature is the bump $\tau \sim 100$ s, marked as "b". The fact it can be seen for all links shows that it is not only due to one station, but at least three. In fact, the maximum seems to be slightly different for the different links, with the INRIM-related links at about 100 s averaging time and the PTB-related links at about 140 s. The disturbance is lowest for the link between LNE-SYRTE and NPL, but at around the same averaging time as for LNE-SYRTE – PTB and NPL – PTB.

Both features have in common that there is not one single frequency causing the apparent quasi-periodic phase variations. For a better visualization of the effects, the phase data of two links in Fig. 4.6 (d) were enlarged, which can be seen in Fig. 4.8. In (a), the 100 s feature ("b") is well visible for both links. However, the frequency is moving, resulting in significant structures repeating every 12 h, as seen at MJD $56954 + 5.95$ and MJD $56954 + 6.45$. A moving frequency can also be seen in (b),

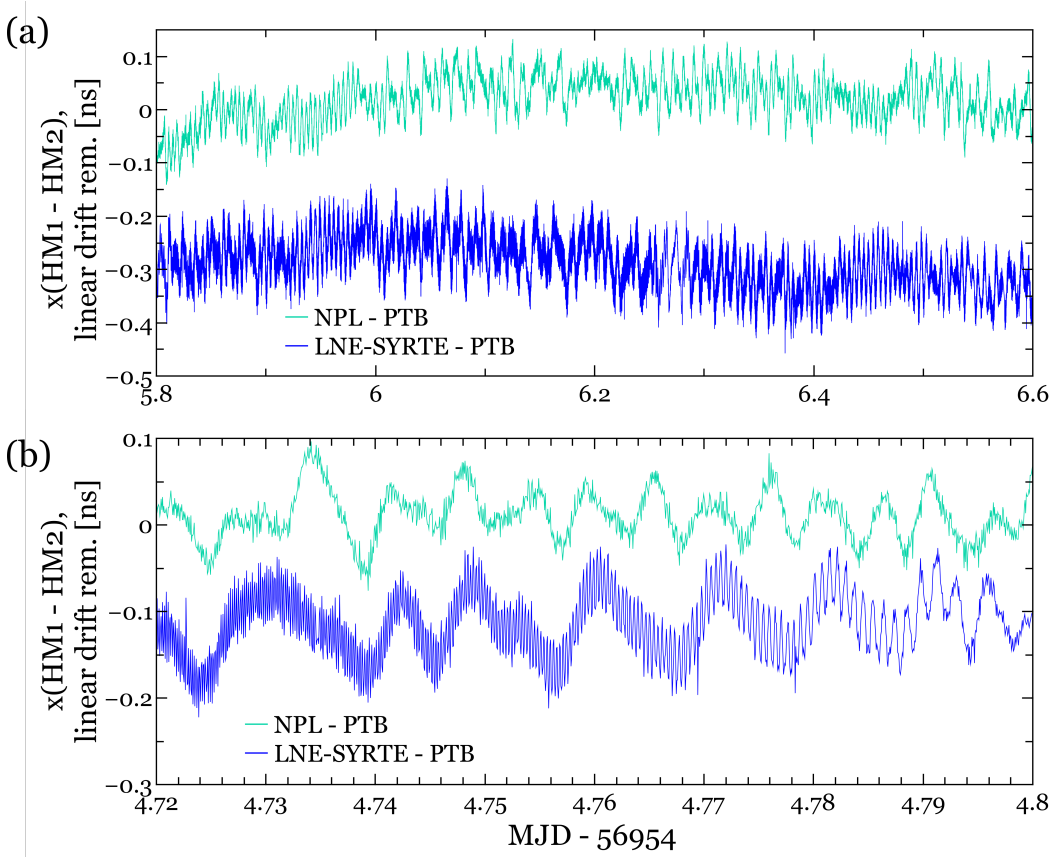

FIGURE 4.8: Enlargement of the phase data in Fig. 4.6 (d) of the links LNE-SYRTE – PTB and NPL – PTB. In (a) one can see that both underlie a frequency modulation with a period of 12 h. (b) shows an additional frequency modulation on the link LNE-SYRTE – PTB with a period between a few seconds and a few minutes, which can not be observed on the link NPL – PTB.

where a very fast oscillation is visible on the link LNE-SYRTE – PTB (causing "a"), but not on NPL – PTB. However, the period increases with increasing time in this particular displayed section, changing from a few seconds to a few minutes. This feature, too, repeats its frequency change every 12 h. It can therefore be said that both effects have something to do with the satellite motion, most probably with the frequency change of the signal due to the Doppler effect. So both are a combination of this frequency change and of a technical disturbance, like a reflection, on the signal path: the one marked as "a" only in the station at LNE-SYRTE, while "b" might occur at equipment common to each station.

The bump seen at "c" (the bump starting between 3000 and 4000 s, with a maximum at 6000 s), can be only found on the links with the sessions of 1 h, since the calculation is well possible for 3600 s, but has a very high uncertainty for averaging times up to 3 h due to the low amount of phase triples that can be used for this τ, so it is not necessarily a real increase of the frequency instability, but originates from the gap-tolerant calculation of the modified Allan Deviation. The increased uncertainty in "d" (at an averaging time between 10,000 and 20,000 s) corresponds to the fluctuations on the INRIM-related links of unknown origin, and "e" to the diurnal oscillation, which is most dominant for the link LNE-SYRTE – PTB.

It can be seen that for the PTB-related links instabilities below 6×10^{-16} at $\tau = 1$ d

are reached, which corresponds to the approximate instability of the HM. Thus, disturbances which limit the instability at shorter averaging times do not seem to have an influence on the instability at $\tau = 1\,\mathrm{d}$ and above. This is important because the cause of disturbances is unknown, so they cannot be avoided in the final setup for the clock comparison, nor corrected. The campaign therefore showed that the instability which was aimed for can be actually reached.

For the links without PTB involvement, the instability at $\tau = 1\,\mathrm{d}$ is higher, around 1×10^{-15}. Because of the lower amount of data to calculate the modified Allan Deviation for averaging times around 1 d for these links, a statement about the final instability here is not possible. For a full characteristic and for making use of the advantage of the high chip rate for the optical clock comparisons, it is thus necessary to operate all links without interruption.

Chapter 5

The clock comparison campaign

The main objective of this work is a simultaneous comparison via broadband TWSTFT (20 Mchip/s) between five optical clocks, and in addition six microwave fountain clocks located at the NMIs INRIM, LNE-SYRTE, NPL and PTB. In parallel, GPS PPP was used as an independent satellite comparison technique. For the three-week measurement campaign, various considerations needed to be taken into account, both organizational and for the computation in the post-process. In this chapter the relevant operational aspects and considerations for data processing of the links are discussed in detail, while all aspects of the final calculation of the relative frequency differences of the clocks can be found in the next chapter.

This chapter first describes changes in the setup and the schedule for this campaign in contrast to the link test. Then, an overview over all events during the campaign is given. The third section analyses the resulting instabilities of the satellite links and compares the different satellite techniques. In the last part of this chapter, the corrections necessary for the frequency comparison are discussed in detail: the atmospheric corrections and the Sagnac corrections.

5.1 Changes in setup and schedule

The link test campaign has shown that the TWSTFT links can reach an instability in the low 10^{-16} range for averaging times of 1 day or larger, which is the goal with respect to the uncertainty for this campaign. But regular gaps of one hour or more, as implemented in the schedule of the link test campaign (see previous chapter), can not be easily overcome and they have an impact on the link characteristic in general and complicate the final clock comparison calculation.

Hence, one of the major changes was to provide each institute the possibility to receive all signals simultaneously, which means to equip each TWSTFT station with at least three RX channels. This was done by shipping spare modems (S76 and S427) to other laboratories. PTB had an additional three-channel modem available during the time of the campaign (SATRE modem with serial number 280, hereafter S280), which results in the possibility to receive six signals simultaneously. The additional channels were used for ranging and redundant measurements. In LNE-SYRTE and PTB, an active splitter/combiner was used to split the signal of the RX path for distributing the signal to two modems, while at NPL and INRIM, the two modems were daisy-chained.

As discussed in the previous chapter, the sources of the frequency modulations occurring during the link test campaign (at a few seconds for the LNE-SYRTE links and around 100 s for all links) were assumed to be reflections in some parts of the stations' equipment. Some closer investigations were carried out at PTB and LNE-SYRTE, including several loop-back experiments with various parts of the signal path within the station at PTB, however, without any result. LNE-SYRTE assumed cross-correlations within the SATRE modem between signals of different PRN codes, and changed the code from 1 to 0.

In addition, within a research cooperation between LNE-SYRTE, PTB, and the National Institute of Information and Communications Technology (NICT) of Japan, another satellite-link-based technique was implemented in parallel during the campaign: TWCP frequency transfer [177]. As mentioned in Chapter 2.3.2, the technique has shown promising instabilities for short averaging times, but was in previous measurements either limited by the measurement equipment, the frequency standards used as reference, or the measurement time. Since the carrier-phase technique occupies only a few 100 kHz and thus a very small part of the overall bandwidth ($< 1\%$), the experiments could be carried out on the same transponder without an impact on each other. To realize this, additional equipment was provided by NICT: an arbitrary waveguide generator, a sampler, several amplifiers and bandpass filter, and for PTB an SSPA, an LNA, and a set of UC/DC. In case of PTB, an additional roof station was available for the TWCP measurement, so the two signal paths for broadband TWSTFT and TWCP could be kept separated. At LNE-SYRTE, only one roof station was used for both experiments, so the signal path was split.

Details on the parameters of the modems and the up- and downlink frequencies during the clock comparison campaign can be found in Appendix A.

5.2 Events during the campaign

The clock comparison campaign took place from MJD 57177 to MJD 57203 (June 4$^{\text{th}}$ to 29$^{\text{th}}$ 2015, 26 days). Originally, only a time of 3 weeks was planned, but due to some unforeseen events the satellite provider agreed to add a few days.

Since a lot of events of public interest took place during the first part of the campaign, especially the first weekend (e.g. 41$^{\text{st}}$ G7 summit and UEFA Champion's League, both in Germany), it was not possible for SES to provide the same transponder on the satellite which was used for the link test before, so a different up- and downlink frequency was assigned to the campaign. Unfortunately, it was found that the new downlink frequency of 12.605 GHz is within a frequency band used by military stations in France for terrestrial communication, so a strong signal from a station nearby prevented the modem of LNE-SYRTE to lock on any signal from the satellite with a signal-to-noise ratio higher than 45 dBHz. A spectrum as recorded by a spectrum analyser at the LNE-SYRTE station can be found in Fig. 5.1, it shows the disturbing signal at marker 2 that is dominating over a bandwidth of approx. 40 MHz. SES was informed about this issue as soon as possible, but a switch to the transponder used in the link test campaign was only possible five days after the begin of the campaign, on MJD 57182. So during the first five days, LNE-SYRTE could not participate in the broadband TWSTFT measurements, but TWCP was running during that time. Due to this incident, an additional measurement time of five days was granted by SES.

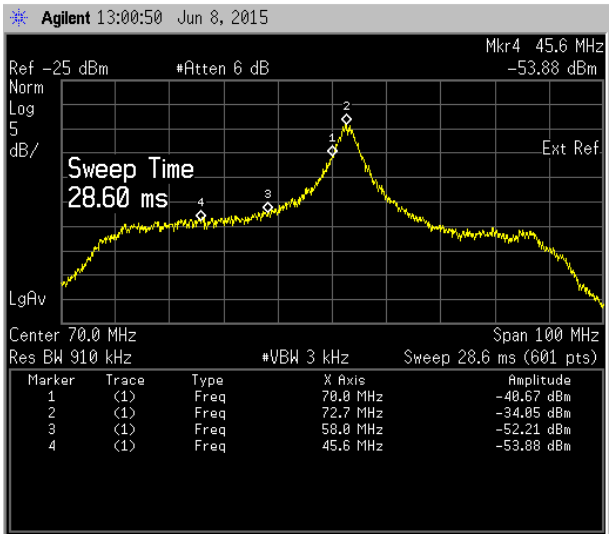

FIGURE 5.1: An image of a spectrum analyser showing the spectrum of the signal after downconverting. Marker 1 represents the center downlink frequency of the transponder. Just 2 MHz above, at marker 2, a signal of large power is received, jamming the TWSTFT signal.

Although a lot of intensive and careful preparations were carried out, several technical incidents occurred during the campaign.

With the data being monitored, it was noticed that after MJD 57186 some phase excursions of more than 1.5 ns, obviously artifacts, appeared on the two-way phase data of all links that involved PTB. They occurred around the same time of the day, between 11:00 and 15:00 UTC, lasting longer than one hour. It was found that there was a loose contact in the connection between the LNA and the cable leading to the downconverter, causing the excursion by thermal extension of the connector during sunlight exposure. The problem could only be identified and solved on MJD 57195.

The SATRE modem belonging to NPL, S74, was malfunctioning before the link test campaign, but got repaired and was implemented into the setup before the clock comparison campaign. Unfortunately, it turned out that the internal firmware was not compatible with newer generations of the modems, so the data written in the raw output strings were shifted by an unknown delay with respect to the given time stamps. A manually generated configuration file was used to solve the problem, which was installed on the modem on MJD 57190. Since S74 comprises only one channel, only one link, the link between NPL and INRIM, was affected.

On MJD 57191, the TWCP link was switched off. It was only discovered after that day, that the TWCP introduced some increased short-term instability on the RX signal of LNE-SYRTE. The reason was found to be an interference at the splitter used here to split the signal into the signal paths for the SATRE modem and the TWCP equipment.

From the beginning of the campaign, the signals of INRIM and PTB as received at the other stations (and at the channel used for ranging measurements at PTB) suffered from a frequent loss of carrier lock. The situation for PTB's signal improved once the external frequency reference for the upconverter was removed.

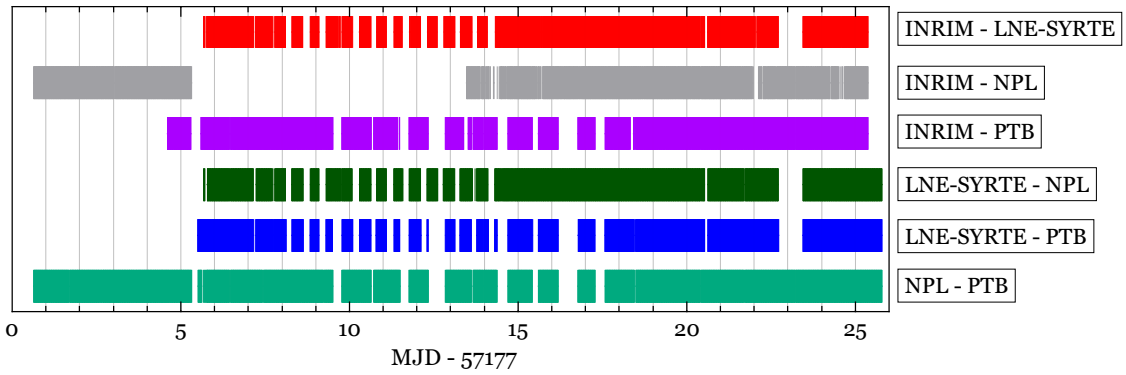

FIGURE 5.2: The measurement time of each link that can be used for the processing of data and the final calculation of clock frequency differences.

One of the modems used at LNE-SYRTE, S503, crashed several times and rebooted automatically, which lead to a loss of data for several minutes each time.

After the official end of the campaign, maintenance work was scheduled at LNE-SYRTE, but due to the additional days of measurement, this event took place when the campaign was still running. In the frame of this activity, a complete power shutdown occurred from MJD 57199 (17:30 UTC) until MJD 57200 (11:30 UTC). Also, the power was shut down by accident on MJD 57197 for about one hour in the frame of this maintenance.

Fig. 5.2 shows the measurement intervals for each link, with outliers and periods of data that cannot be used for the processing already cut out.

5.3 Satellite link analysis

For the basic link data processing, several steps of calculations were carried out. At first, as in the link test campaign, the raw range data sets $\Delta T(t)$ (see Eq. 2.5 in Chapter 2.3.1) from each modem were gathered and two of them combined to gain the first estimate (without adding any correction yet) of the phase difference between the reference hydrogen masers for each link:

$$x'(\mathrm{HM}_1 - \mathrm{HM}_2)(t) = \frac{1}{2}(\Delta T_1(t) - \Delta T_2(t)) \tag{5.1}$$

For the following calculation of outliers, a few changes had been made with respect to the link test. These adaptations were made to account for the different kinds of disturbances with respect to the link test and furthermore to more carefully identify outliers, since the processed data will be used for the calculation of the relative frequency differences between the clocks.
At INRIM, one reference 1PPS signal for the modem came from a different source than the second 1PPS and the frequency signal, so a re-synchronization between the reference signals occurred from time to time, which resulted in jumps of integer multiples of 100 ns on the raw range data, and thus in multiples of 50 ns on the corresponding link data. These jumps were detected and removed in a first step.

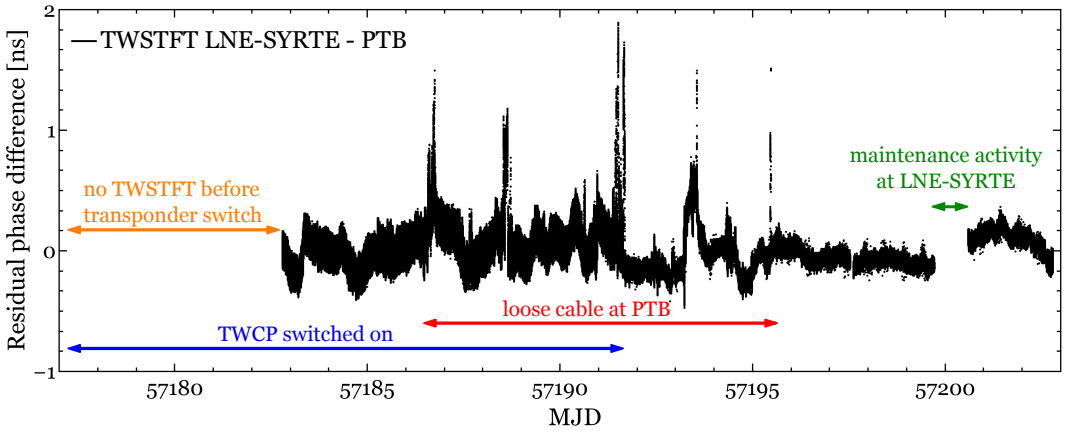

FIGURE 5.3: The TWSTFT phase data between LNE-SYRTE and PTB. The frequency offset is subtracted as a linear fit. This link was affected the most by perturbations during the campaign, the major ones can be seen clearly in the data and are marked.

In a next step, similar to the link test campaign, a piecewise cubic fitting for intervals of 200 s is calculated, and points differing by more than 250 ps are removed as outliers. However, instead of repeating this method with a lower threshold, the linear drift (frequency offset) was removed. This was done for a better visual detection of outliers and disturbances like the excursions on the PTB signal or times of the uplink tests during the satellite transponder switch in between, which were selected and cut out manually in a next step. Then, a second numerical outlier detection was carried out, using the modified z-score criterion [178]:

$$\left|\frac{0.6745 \cdot (x_i - \tilde{x})}{MAD}\right| > 3.5, \tag{5.2}$$

with $\tilde{x}$ as the median and MAD as the median absolute deviation of x.

After that, the corrections were applied, the Sagnac corrections and the atmospheric corrections (see next section, 5.4). For calculating the relative frequency difference of the atomic clocks as carried out in Chapter 6, the linear drift was added again onto the data after the last outlier removal and the application of the corrections.

Fig. 5.3 shows the TWSTFT phase data for the link LNE-SYRTE – PTB with a preliminary outlier removal, but without cutting out periods of disturbance and applying the corrections. Only the test periods at the beginning were removed, and the linear drift was subtracted for better visibility. The graph covers the whole period of the measurement campaign, and illustrates most of the events occurring during the campaign, the non-functional downlink at LNE-SYRTE at the beginning of the campaign, the noise introduction by TWCP, the loose cable contact at PTB and the maintenance activity at LNE-SYRTE at the end of the campaign.

Fig. 5.4 shows the TWSTFT phase data for the link between PTB and INRIM with the complete outlier removal, with disturbances cut out and with all corrections applied. The linear drift was removed for a better visibility. A residual quadratic drift is still visible, as well as diurnal non-sinusoidal fluctuations, which have a resemblance to the structures visible on the links to INRIM during the link test. In a next step,

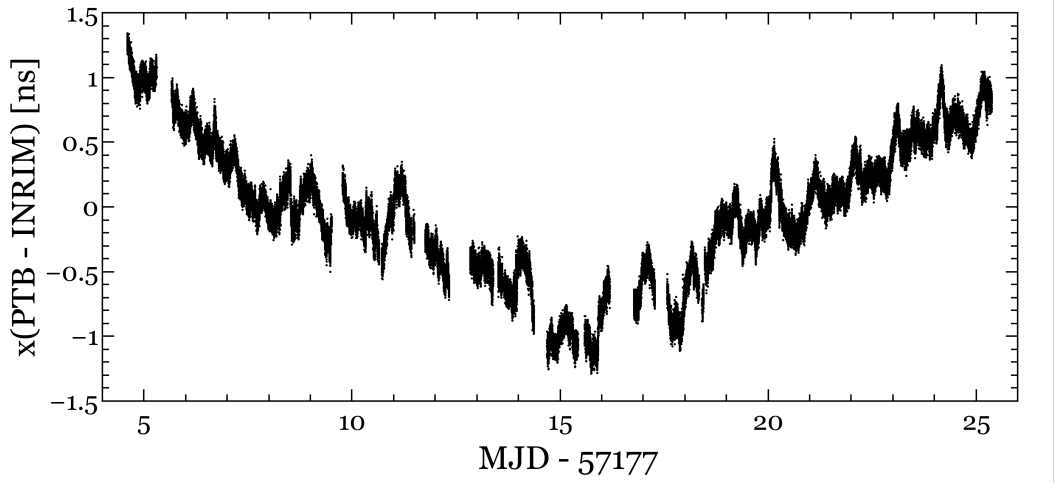

FIGURE 5.4: The TWSTFT phase data for the link between PTB and INRIM. All outliers are removed and periods of disturbance cut out, while all corrections are applied. The linear phase drift is removed, and can be added again to have this data ready for the clock comparison calculation.

the frequency offset is added again to have this data ready for the clock comparison calculation.

From the phase data, the gap-tolerant modified Allan Deviation is calculated (see Chapter 4.3). This is shown in Fig. 5.5. Compared to Fig. 4.7 in Chapter 4, most features discussed there appear again: the increased short-term instability for all links involving LNE-SYRTE (marked as "a"), the bump at about 100 – 200 s averaging time ("b"), and a bump at around the same averaging time as diurnal oscillation ("c"). For "b", the averaging time for the maximum of the bump at around 100 s seems to be the same for all links, however, the instability of the links with involvement of LNE-SYRTE is higher than during the link test, so a local maximum is barely visible for these links. Also, the instability at 1 s is higher than during the link test for most of the links, but due to slightly different slopes, they reach similar instabilities at "b". For the link between PTB and INRIM, the origin could be the carrier lock losses which were observed on the signals of PTB and INRIM. From there on, the links to INRIM are limited in their stability by the feature around "c", which seems to combine a diurnal oscillation and the phase fluctuations seen during the link test. The other links do not show a diurnal oscillation. The instability at 1 d is around 1×10^{-15} and thus higher than during the link test.

The influence of the TWCP on the TWSTFT measurement is depicted in Fig. 5.6. As shown before, it is dominant on the link between LNE-SYRTE and PTB, but the increased noise can be observed on all links to LNE-SYRTE during the time it was switched on (as shown for the link LNE-SYRTE – NPL in the figure), while it does not appear on other links during the same time. This shows that the signal itself does not have any influence on the performance of the broadband TWSTFT, but that it is originating from the setup at one station, which was later identified to be one of the splitters, as mentioned above.

Next, the results obtained with the data from the RX channels at PTB which received the same signal were compared. The modified Allan Deviation for the different channels is shown in Fig. 5.7, calculated for the whole measurement interval after the

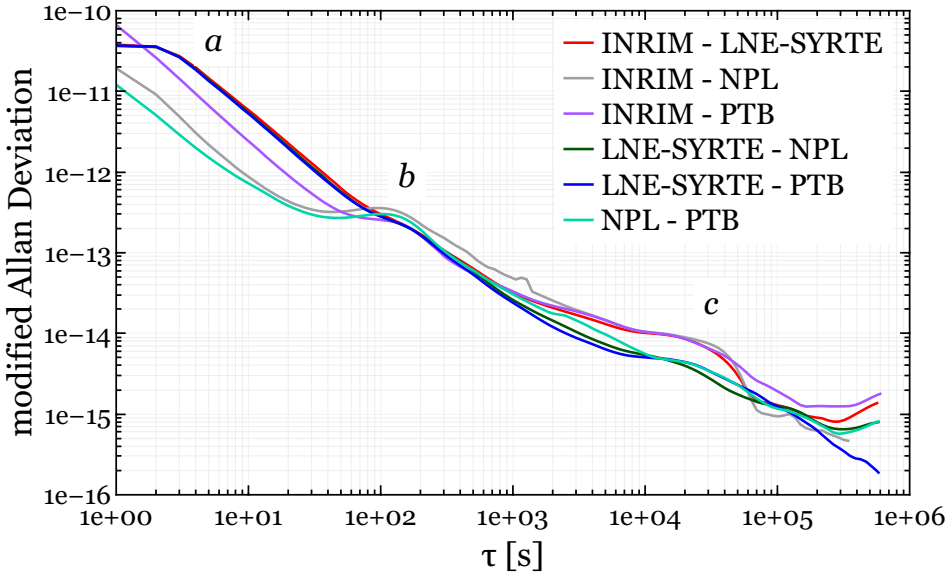

FIGURE 5.5: The modified Allan Deviation of all TWSTFT links during the campaign, for the time after the transponder change. The features marked with "a", "b" and "c" correspond to features observed during the link test campaign (the frequency modulations at a few seconds averaging time for the LNE-SYRTE links and at 100 s averaging time for all links, and the diurnal oscillation on some links).

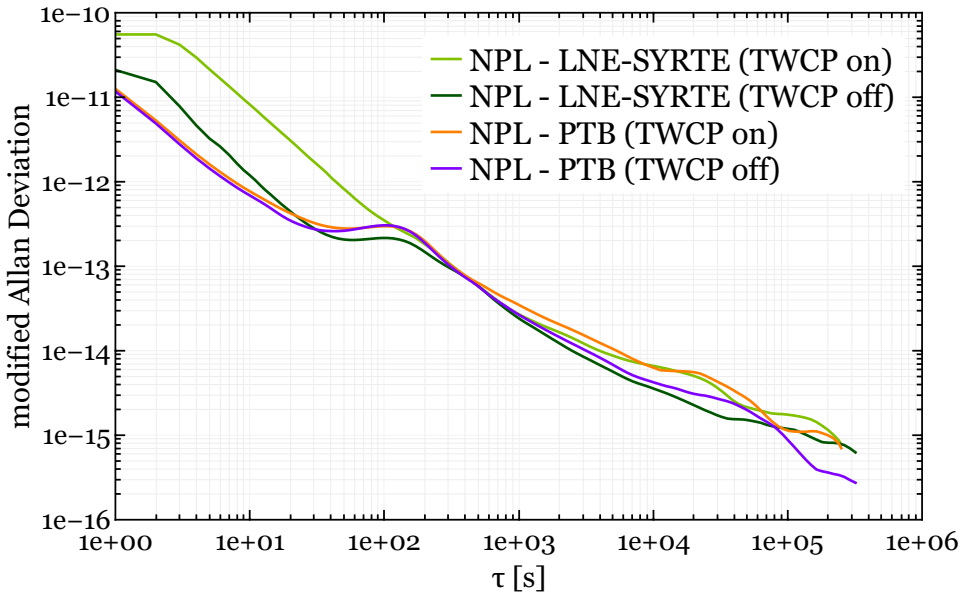

FIGURE 5.6: The modified Allan Deviations of the links LNE-SYRTE – NPL and NPL – PTB, both for the period where the TWCP was switched on and for the period after. Switching the TWCP off has an impact on the instability, which is significantly lower after the switch-off for averaging times up to 100 s. The instability of the link NPL – PTB is for both intervals approximately on the same level as the one of the link LNE-SYRTE – NPL after the switch-off, showing that NPL – PTB is not affected by the TWCP. This analysis also shows that the frequency modulation causing the bump around 100 s averaging time does not scale with the overall instability.

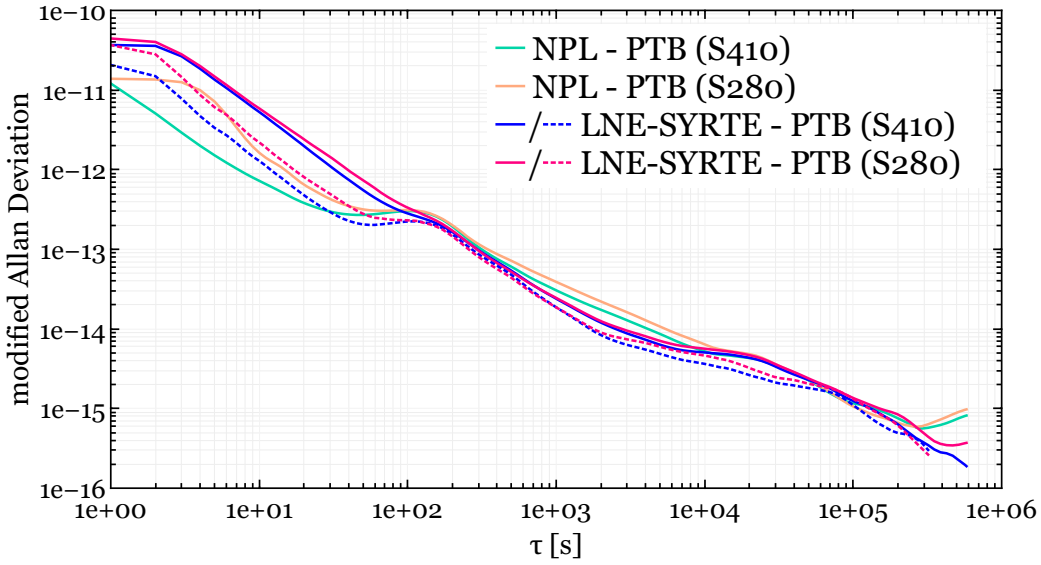

FIGURE 5.7: The modified Allan Deviations of the links LNE-SYRTE – PTB and NPL – PTB, recorded with two different modems at PTB (S410, RX1 and S280, RX1 for the reception of LNE-SYRTE, and S410, RX2 and S280, RX2 for the reception of NPL). The solid lines correspond to the whole period after the transponder switch, the dashed lines correspond to the interval after TWCP was switched off. Due to the increased instability for S280, S410 data was chosen for further calculations.

transponder switch (solid lines) and also for the period when TWCP was switched off in case for the link LNE-SYRTE – PTB. The instabilities are approximately the same for averaging times from 200 s onwards. For the link NPL – PTB there is an obvious increase of the instability for the measurement with S280 for short averaging times: a distinctive feature, similar to an oscillation with a period of just a few seconds, can be seen here. The interval after the TWCP was switched off revealed also a slightly higher instability for the link LNE-SYRTE – PTB for data of the modem S280. As discussed in Chapter 3.1, the modems have different noise properties and sensitivities to, for example, temperature. Also, the different RX channels of one single modem can behave quite differently. Here, this can be seen again. Since no tests were carried out with S280 before the campaigns, the behavior could not be observed before, but the short-term structure on the link NPL – PTB can be attributed to RX2 of S280. Due to this observation, the data recorded by S410 was used for the calculation of the relative frequency difference of the optical clocks in Chapter 6.

5.3.1 Comparison of broadband TWSTFT and TWCP during the campaign

A comparison between both techniques can be seen in Figs. 5.8 and 5.9. The TWCP data was processed by NICT and LNE-SYRTE. In the first figure, the phase data is shown with the linear drift subtracted. It can be seen that the TWCP has a much lower short-term instability than TWSTFT, which can be quantified in the modified Allan Deviations (second figure). There, the instability of TWCP at 1 s is about two orders of magnitude lower than the same for broadband TWSTFT. However, while the slope for broadband TWSTFT during the time, when TWCP was not running,

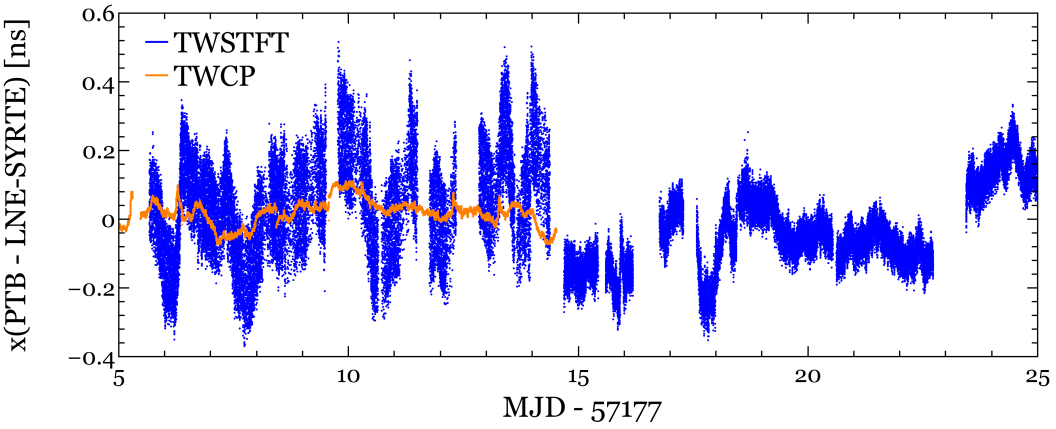

FIGURE 5.8: The phase data of both links between LNE-SYRTE and PTB, TWSTFT and TWCP, with a linear drift subtracted. The TWCP has a significantly lower short-term instability.

indicates the presence of mostly white phase noise, the TWCP measurement is dominated by flicker phase noise with parts of random walk phase noise. The disturbance at around 100 s is visible again in both techniques, but scaling with the overall instability, i.e. the local maximum of the disturbance is increased with respect to the instability at shorter averaging times by approximately the same factor for both techniques. Also, the maximum is slightly shifted to shorter averaging times for TWCP. However, there is no scaling comparing the two TWSTFT intervals, the one disturbed by the TWCP signal due to a reflection at a splitter and the one after the TWCP switch-off. This could mean that the noise arising from the splitter in the RX path when TWCP is switched on is added on top of the frequency modulation at 100 s, while the scaling between TWCP and undisturbed TWSTFT means that this effect is amplified together with other noise on the signal, which could be a hint that it is originating from something in the TX part or even within the satellite. The instability of the double difference between both, TWCP and TWSTFT, is for all observed averaging times limited by TWSTFT. However, the instability for $\tau > 100,000$ s has an increased uncertainty due to the limited measurement interval, and a limitation by the HMs cannot be excluded.

The TWCP test here shows that the instabilities of TWCP and broadband TWSTFT approach each other while decreasing, and being not significantly different for longer averaging times from $\tau = 1$ d on, but TWCP is clearly advantageous for shorter averaging times. The measurement time was limited by the disturbance introduced on the TWSTFT signal by the splitter at LNE-SYRTE, but still an uninterrupted measurement of almost 10 d could be achieved.

5.3.2 Broadband TWSTFT and GPS PPP during the campaign

GPS PPP was, in contrast to TWCP, introduced into the campaign as an additional satellite-based comparison technique for the optical clocks. Hence, it was taken care to have an undisturbed full-time operation of the receivers referenced to the HM during the campaign. However, events like the power shutdown at LNE-SYRTE that affected the TWSTFT measurements had also an impact on the GPS measurements.

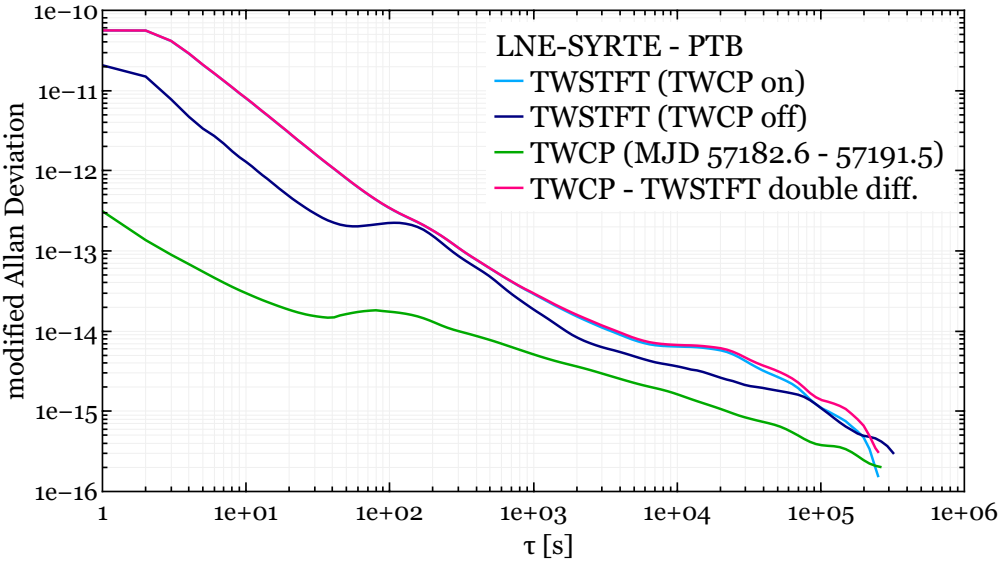

FIGURE 5.9: The modified Allan Deviations of the links LNE-SYRTE – PTB, realized with TWSTFT and TWCP, and the double difference of both. The period of TWSTFT was split in the time when the TWCP was switched on and when it was switched off. For most of the time the TWCP has a lower instability than TWSTFT, but both show a different average behaviour and thus a different noise: TWSTFT shows noise between white phase and flicker phase noise, while TWCP averages down with components of flicker phase and white frequency noise, until both reach a similar instability at $\tau = 10,000$ s. The bump at 100 s can be seen in TWCP, too.

The PPP calculations were done with the algorithm provided by National Resources Canada (NRCan) [136]. The implementation of the GPT2 model which improves the estimation of atmospheric delays was used [179]. As mentioned in Chapter 2.3.3, PPP is calculated in batches, each batch resolving the phase ambiguity separately, which leads to phase jumps at the boundaries of these batches. These jumps would hinder the calculation of the relative frequency differences of the clocks, and are thus to be avoided. However, the non-white noise of the code can add up for long batches and make these calculations erroneous. So for this calculation here, the daily batches were processed in parallel with the long-term batches over 26 d. An example can be seen in Fig. 5.10. There, the different batch-lengths are shown for the receiver of PTB, the IGS time is the reference for all PPP calculations. A quadratic fit was calculated for the long batch and subtracted from both for a better visibility. The black curve shows the daily batches, and phase jumps at midnight of up to 200 ps can be seen. The red curve displays the long batch. Both follow the main fluctuations with very small differences of tens of picoseconds, and larger differences for up to 150 ps are only visible for a few days in between. Starting at approximately the same phase value, they end at about 120 ps difference. An error of 120 ps over 26 d would end up in relative frequency error of 5×10^{-17}. The other links show differences in the same order of magnitude. Only for the receiver at INRIM, a large jump of 1 ns occurred on MJD 57198. The batch was therefore limited to MJD 57197.

For calculating the phase difference between the HMs of the laboratories, a simple subtraction of the PPP calculations for the concerning receivers was performed, so the IGS time cancels out. For the further processing, similar steps had been taken for

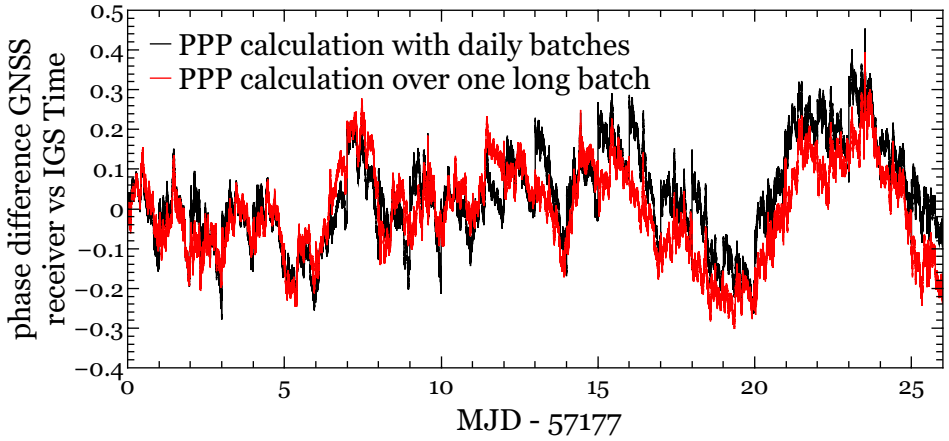

FIGURE 5.10: The PPP calculation (phase difference between IGS time and receiver reference time) for the PTB receiver used in the campaign. The black curve shows the calculation based on daily batches, the red one over one single long batch.

the outlier removal as for TWSTFT. The difference to the phase data of TWSTFT is the time grid, which is 30 s in case of PPP instead of 1 s.

The phase difference between the HMs of NPL and PTB is displayed in Fig. 5.11, with TWSTFT in blue and GPS PPP in red. The same linear drift is subtracted for both for a better comparison. The two data sets of TWSTFT before and after the transponder switch were aligned. Both TWSTFT and GPS PPP have a similar short-term noise, while TWSTFT shows more fluctuations. However, both show the same features. From the starting point on the first day of the campaign to the last day, a phase difference of about 300 ps over the measurement time of 26 d can be observed. So a difference between both techniques of about $1 \times 10^{-16} \ldots 2 \times 10^{-16}$ could be expected for this link.

Fig. 5.12 shows the modified Allan Deviations of the PPP links. The links involving LNE-SYRTE have an overall shorter measurement time than the other links, since data from the receiver dedicated to the campaign could not be used, and data from a backup receiver could be used from MJD 57182 on. The receiver at NPL shows the highest instability at 30 s, while the instability for longer averaging times is limited by the receiver of INRIM for the respective links. A weak diurnal oscillation can be seen on the links between LNE-SYRTE and PTB, and LNE-SYRTE and NPL. The link between LNE-SYRTE and PTB is the only link showing an instability lower than 1×10^{-15}, which is similar as for TWSTFT. The modified Allan Deviation of the double difference between both techniques for the link NPL – PTB is depicted in Fig. 5.13. It shows that both techniques are indeed limited by the HM at averaging times longer than 1 d.

5.4 Corrections of TWSTFT measurements

5.4.1 Correction of atmospheric effects on TWSTFT

As described in Chapter 2.3.1, atmospheric delays on the signal paths violate the reciprocity of the signal path. Hence they need to be considered for a measurement

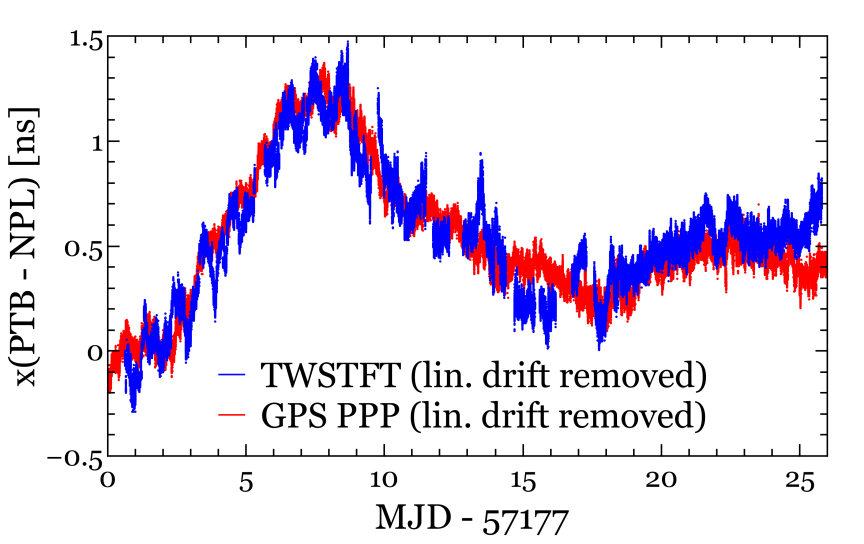

FIGURE 5.11: The phase difference between the HMs at NPL and PTB, measured with TWSTFT in blue and GPS PPP in red. The same linear drift was subtracted from both for a better visibility.

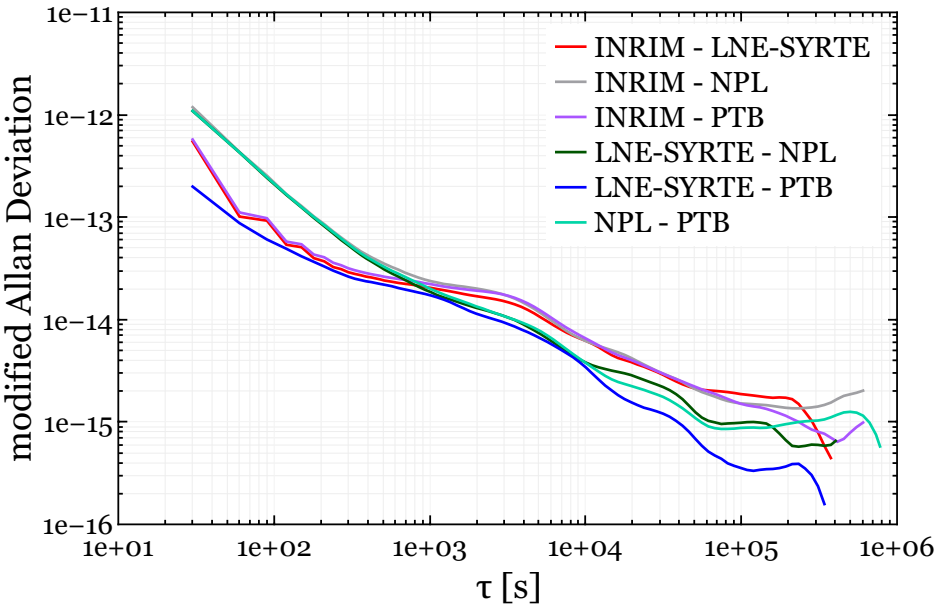

FIGURE 5.12: The modified Allan Deviations for GPS PPP links during the campaign. The short-term instability at 30 s is limited by the receivers of NPL and INRIM, while the long-term instability is highest for the INRIM-related links. Since the instability for the links at averaging times of 1 d and longer are similar, the links are limited for these averaging times by the HMs, which is shown for one example in Fig. 5.13.

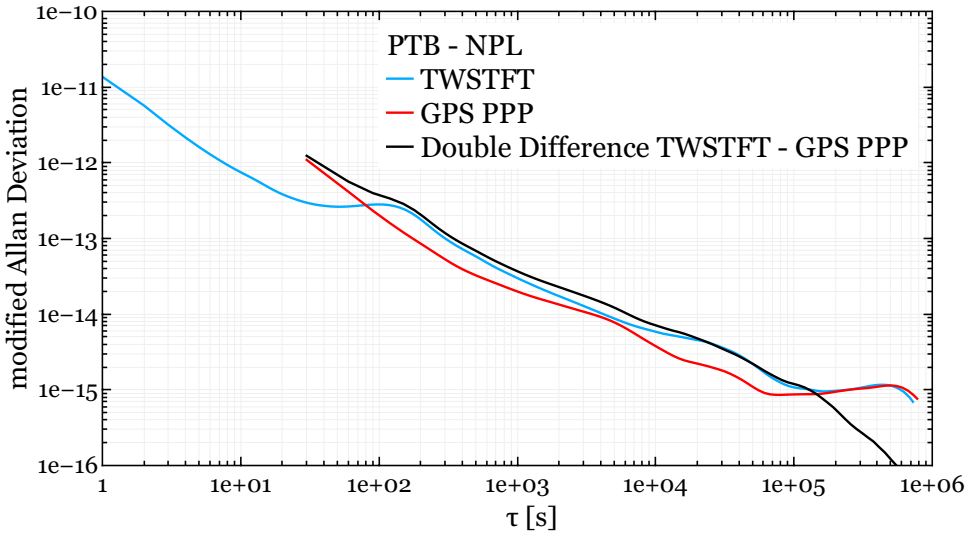

FIGURE 5.13: The modified Allan Deviations for different satellite techniques for the link NPL – PTB: TWSTFT in blue, GPS PPP in red and the double difference between both techniques in black. It can be seen that the instability for both links separately is increasing after 1 d averaging time, but decreasing further in the double difference, which proves that the instability of the links via one technique is limited here by the HMs.

aiming at high accuracy. Since both, the ionosphere and the troposphere, have a different impact on the signal, they are considered separately.

Influence of ionosphere

The delay difference between uplink (U) and downlink (D) signal paths at each station x caused by the dispersive property of the ionosphere can be calculated [116]:

$$\tau_{\mathrm{U,iono,x}} - \tau_{\mathrm{D,iono,x}} = \frac{K}{c} \cdot \mathrm{TEC}\left(\frac{1}{f_{\mathrm{U}}^2} - \frac{1}{f_{\mathrm{D}}^2}\right), \tag{5.3}$$

with c as the velocity of light, f_{U} and f_{D} as the up- and downlink frequencies, respectively, TEC as the Total Electron Content, describing the amount of electrons per m^2, and $K = 40.3\,\mathrm{m}^3/\mathrm{s}^2$ as a constant factor. With this, the two-way equation (Eq. 2.7) for the phase difference between the HMs becomes:

$$\begin{aligned} x(\mathrm{HM1} - \mathrm{HM2}) = {} & \frac{1}{2}(\Delta T_1 - \Delta T_2) \\ & + \frac{1}{2}(\tau_{\mathrm{U,iono,1}} - \tau_{\mathrm{D,iono,1}}) - \frac{1}{2}(\tau_{\mathrm{U,iono,2}} - \tau_{\mathrm{D,iono,2}}) \\ & + C_{\mathrm{misc.}}(t) + const. \end{aligned} \tag{5.4}$$

As described before, the constant parts of the link delays can be neglected, and other corrections are discussed in the next sections, so they are disregarded for now, too, and the equation becomes:

$$
\begin{aligned}
x(\mathrm{HM}_1 - \mathrm{HM}_2) = &\frac{1}{2}(\Delta T_1 - \Delta T_2) \\
&+ \frac{1}{2}[\frac{K}{c} \cdot \mathrm{TEC}_1(\frac{1}{f_\mathrm{U}^2} - \frac{1}{f_\mathrm{D}^2})] \\
&- \frac{1}{2}[\frac{K}{c} \cdot \mathrm{TEC}_2(\frac{1}{f_\mathrm{U}^2} - \frac{1}{f_\mathrm{D}^2})] \\
= &\frac{1}{2}(\Delta T_1 - \Delta T_2) \\
&+ \frac{K}{2c}(\frac{1}{f_\mathrm{U}^2} - \frac{1}{f_\mathrm{D}^2}) \cdot (\mathrm{TEC}_1 - \mathrm{TEC}_2),
\end{aligned} \tag{5.5}
$$

so the correction to calculate becomes:

$$
x_\mathrm{iono} = \frac{K}{2c}(\frac{1}{f_\mathrm{U}^2} - \frac{1}{f_\mathrm{D}^2}) \cdot (\mathrm{TEC}_1 - \mathrm{TEC}_2) \tag{5.6}
$$

The electron density strongly depends on solar radiation due to its ionizing properties, and hence changes its horizontal distribution with diurnal and annual rhythms, and also within the cycle of solar activity. A variation can be also found in the vertical direction, with the maximum moving between 250 km and 400 km in height [180]. The TEC that is used to calculate the influence of the electrons on signal path delays can be calculated as a path-dependent integral over the electron density [181]. In the specific case of an integration over the ionosphere in zenith direction, the TEC is called vertical TEC (vTEC). All other straight paths through the ionosphere give a slant TEC (sTEC). Since the geostationary satellite is in general observed at elevations lower than 90°, the sTEC needs to be used in Eq. 5.3. The relationship between the vTEC and the sTEC can be described by a mapping factor F_m [182]:

$$
\mathrm{sTEC} = F_m \cdot \mathrm{vTEC} \tag{5.7}
$$

This mapping factor can be calculated in different ways, depending on the mapping function used, but is always dependent on the elevation angle between the ground station and the satellite. The influence of the ionosphere is hence maximum for time and frequency comparisons over very long baselines in either east-west direction or between a station near the equator and one close to one of the poles. In both cases at least one station observes the satellite at a very low elevation angle, increasing the length of the signal path within the ionosphere. The effective phase difference caused by the ionosphere was already calculated for the link between PTB and NICT and found to be varying from −100 ps to 150 ps [118, 131]. For the clock comparison here, the values are expected to be smaller, since all participating stations are within a range of maximum 1000 km and observe ASTRA 3B with elevation angles between 27.1° (NPL) and 35.8° (INRIM), which is significantly larger than the elevation angles in the PTB – NICT baseline (3.7° and 16.0°, respectively). Also, like for the relativistic and geometric effects, only the changes of the delays need to be taken into account. These are also expected to be less significant than for PTB – NICT, because the time difference between the zenith position of the Sun is only about 1.5 h for the longest east-west baseline in this case (NPL – PTB).

Since the electron density has also a major influence on GNSS signals, TEC values are determined by using measurements with two different frequencies of GPS satellites, and the results are then used for modeling the atmosphere for GNSS solutions. Current values as well as TEC archives are available on various websites, e.g. on the sites by the National Oceanic and Atmospheric Administration (NOAA, USA), the Jet Propulsion Laboratory (JPL, USA) and by the Royal Observatory of Belgium (ROB) [183, 184]. For this work, TEC values from the ROB ftp server [185] were taken. There, vTEC values are provided, calculated from the sTEC measured with GNSS satellites based on the approximation of a single thin ionospheric layer in the height of 450 km. The values cover whole Europe, ranging from -15° to 25° in longitude and from 35° to 62° in latitude on a spacing of 0.5° in each direction. They are interpolated on time intervals of 15 min. The uncertainty of both the spatial and the temporal interpolation are recorded as RMS values within the files.

In order to calculate the sTEC values needed for the correction, two things have to be considered:

- choice of a proper mapping function, and
- adaptation of ground station coordinates.

In the most simplified approaches, the electron density is assumed to be distributed homogeneously along the signal path and hence the mapping factor is independent of the actual thickness of the ionosphere. Within this approximation, different geometries are possible, with the Earth and thus the ionosphere being flat as the simplest one, which is called plane mapping function (see Fig. 5.14 (a)). The mapping factor F_m is in this case just the sine of the elevation h.

Various mapping functions that take the curvature of the earth into account are described by Xu [182], with the approximation of a spherical earth in a first approach. Combined with the assumption of a homogeneously distributed electron density from above, the so-called projection mapping function can be obtained. It describes the case of a single infinitesimal thick layer in a certain height H. Here, the factor F_m becomes

$$F_m = \frac{1}{\cos \zeta_{ip}}, \tag{5.8}$$

with ζ_{ip} being the zenith angle at the ionospheric point (IP) (see Fig. 5.14 (b)). This angle can be calculated with given elevation h and height H:

$$\sin \zeta_{ip} = \frac{R}{R+H} \cdot \cos h, \tag{5.9}$$

with R = 6371 km as the mean Earth radius.
In another approach, the ionosphere is viewed as a single layer of a finite thickness $\Delta H = H_2 - H_1$. This mapping function is called geometric mapping function, and is shown in Fig. 5.14 (c). The corresponding mapping factor is calculated as follows:

$$F_m = \frac{s}{\Delta H} \tag{5.10}$$

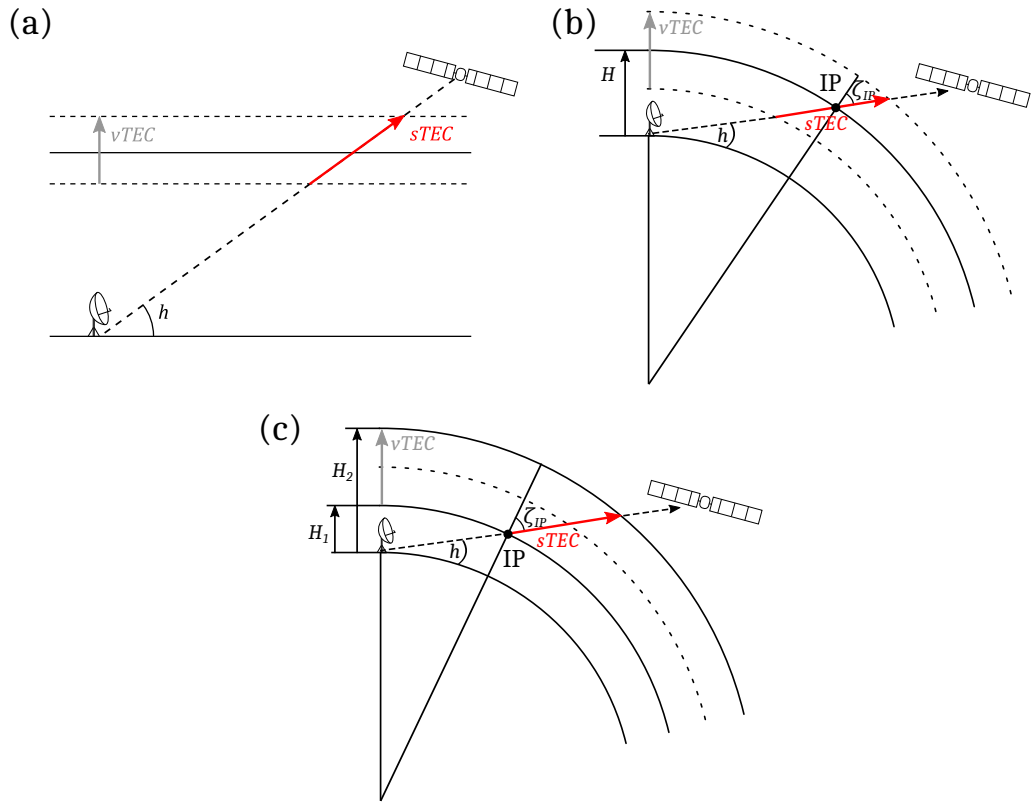

FIGURE 5.14: Depiction of different possible mapping functions: (a) plane mapping function; (b) projection mapping function, (c) geometric mapping function.

The signal propagation path within the ionosphere, s, is given by (see [182] for more details):

$$s = -(R + H_1)\cos\zeta_{ip} + \sqrt{(R + H_2)^2 - (R + H_1)^2 \cdot (\sin\zeta_{ip})^2}. \tag{5.11}$$

Table 5.1 lists F_m of all four stations for the different mapping functions discussed. Placing the height of 450 km at the center of the ionosphere and thus being in agreement with the source of the TEC data, values for H_1 and H_2 can be chosen accordingly. Here, 125 km and 775 km were chosen for H_1 and H_2, respectively, in order to match with the boundaries of the ionospheric layers with higher contribution to ionospheric delay, as given in [180].

TABLE 5.1: Mapping factors for the four stations, calculated for different mapping functions, together with the elevation angle h. For the projection mapping function, the factor is calculated for a height of the ionosphere of 450 km. For the geometric mapping function, the factor is calculated for a thickness of the ionosphere of 650 km in a height of 450 km. The satellite elevation is taken from [186].

Station	h	F_M (plane MF)	F_M (projection MF)	F_M (geometric MF)
INRIM	35.83°	1.71	1.53	2.30
LNE-SYRTE	30.40°	1.98	1.69	2.73
NPL	27.06°	2.20	1.80	3.02
PTB	29.01°	2.06	1.73	2.84

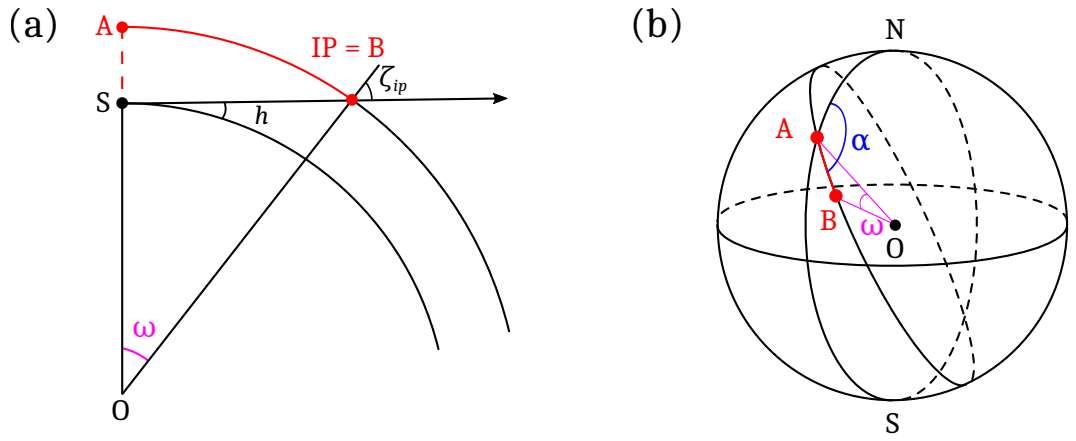

FIGURE 5.15: Steps to calculate the coordinates (latitude and longitude) of point B (IP). (a) Based on the projection mapping function, we calculate ω with given h and ζ_{ip}. Point A has the same coordinates as point S. (b) With given angle ω between A and B, the unknown coordinates of B can be calculated using the azimuth α.

Since the model used by ROB to calculate vTEC out of sTEC values is based on the projection mapping function, this mapping function was chosen for calculating the final correction that is applied to the TWSTFT measurement.

For an adequate correction, the coordinates of the station need to be adapted: not the vTEC values directly above the stations are needed, but the vTEC values in a height of 450 km in line-of-sight with the satellite, i.e. the coordinates of the ionospheric point in Fig. 5.14 (b). In order to get the latitude ϕ and longitude λ of this point, the angle ω between this point and the station (S) with known coordinates is needed (see Fig. 5.15 (a)). With ζ_{ip} calculated above in Eq. 5.9, ω becomes:

$$\omega = 90^\circ - h - \zeta_{ip} \tag{5.12}$$

Independently of ω the point S can be shifted to the position of A, with A having the same coordinates like S but being on the same sphere as B, a sphere in the distance H to the surface of the Earth. With the angle between A and B given, trigonometric relations of spherical triangles can be used:

$$\sin\phi_B = \sin\phi_A \cos\omega + \cos\phi_A \sin\omega \cos\alpha \tag{5.13}$$

and

$$\lambda_B = \lambda_A + \arccos\left(\frac{\cos\omega - \sin\phi_A \sin\phi_B}{\cos\phi_A \cos\phi_B}\right). \tag{5.14}$$

Here, α is the azimuth of point A in direction of point B. The azimuth is also the same for S and A. A similar derivation of the coordinates of point B can be found in [187]. In Table 5.2, the station coordinates and the adapted coordinates for the ionospheric correction can be found, together with the input parameters of elevation and azimuth of ASTRA 3B for each station. The coordinates and the satellite parameters are taken from [186].

TABLE 5.2: Station coordinates (latitude ϕ_S and longitude λ_S), satellite position parameters of ASTRA 3B of these stations (elevation h and azimuth α) and coordinates of the ionospheric point between the stations and the satellite (latitude ϕ_{ip} and longitude λ_{ip}).

Station S	ϕ_S	λ_S	h	α	ϕ_{ip}	λ_{ip}
INRIM	45.01°	7.64°	35.83°	158.11°	40.39°	10.06°
LNE-SYRTE	48.84°	2.33°	30.40°	152.77°	43.50°	6.07°
NPL	51.43°	-0.34°	27.06°	150.51°	45.53°	4.33°
PTB	52.30°	10.46°	29.01°	163.68°	46.30°	12.99°

With both the coordinates and the mapping factors, the ionospheric corrections can be calculated according Eq. 5.6. A plot of these delays for all links can be found in Figs. 5.16 and 5.17. As expected, the smallest baseline between two stations, which is London – Paris (355 km), is least affected by the ionosphere. The maximum effect can be observed for the link INRIM – PTB, with a maximum peak-to-peak difference of more than 40 ps. Slightly lower values, between 30 ps and 35 ps, can be found for the other two PTB links. Although having the longest baseline (930 km), the ionospheric delay for the link between INRIM and NPL reaches a peak-to-peak difference of approx. 20 ps. Another feature visible here is that the links with a higher longitude difference show a distinctive diurnal-like oscillation variation. This is also visible in the modified Allan Deviation in Fig. 5.18. In Table 5.3, the baseline distances and the difference in latitude and longitude are listed for each link, together with the instability at averaging times of 0.5 d (as reference for the diurnal oscillation) and 1 d, taken from the modified Allan Deviation plotted in Fig. 5.18. Also, the difference between the two transponders is clearly visible in Figs. 5.16 and 5.17: the first transponder, used for the time of MJD 57177 until 57182.5, has a smaller difference between up- and downlink frequency (14.105 GHz and 12.605 GHz for the first and 14.275 GHz and 11.475 GHz for the second transponder).

Comparing the ionospheric delay variation to the instability of the satellite links during the campaign, the impact of the ionosphere was found to be smaller than one order of magnitude compared with other effects. It can be thus considered to be negligible, however, it was added to the TWSTFT data for correctness.

TABLE 5.3: For each link, the relative position of the stations to each other (baseline length, difference in longitude, difference in latitude in the second, third and forth columns, respectively) are listed, since it is the most relative parameter for the impact of the ionosphere that is different for each link. The impact of the ionosphere is given as relative instability (modified Allan Deviation σ_{mod}) of the variation of the ionospheric delay for different averaging times.

Link	baseline	$\Delta\lambda$	$\Delta\phi$	σ_{mod} at $\tau = 0.5\,\mathrm{d}$	σ_{mod} at $\tau = 1\,\mathrm{d}$
LNE-SYRTE - NPL	355 km	2.67°	2.59°	3.46×10^{-17}	1.36×10^{-17}
INRIM - LNE-SYRTE	585 km	5.31°	3.83°	7.48×10^{-17}	1.96×10^{-17}
LNE-SYRTE - PTB	690 km	8.13°	3.46°	15.37×10^{-17}	3.69×10^{-17}
NPL - PTB	755 km	10.80°	0.87°	14.98×10^{-17}	3.04×10^{-17}
INRIM - PTB	825 km	2.82°	7.29°	17.75×10^{-17}	4.57×10^{-17}
INRIM - NPL	930 km	7.98°	6.42°	10.13×10^{-17}	3.03×10^{-17}

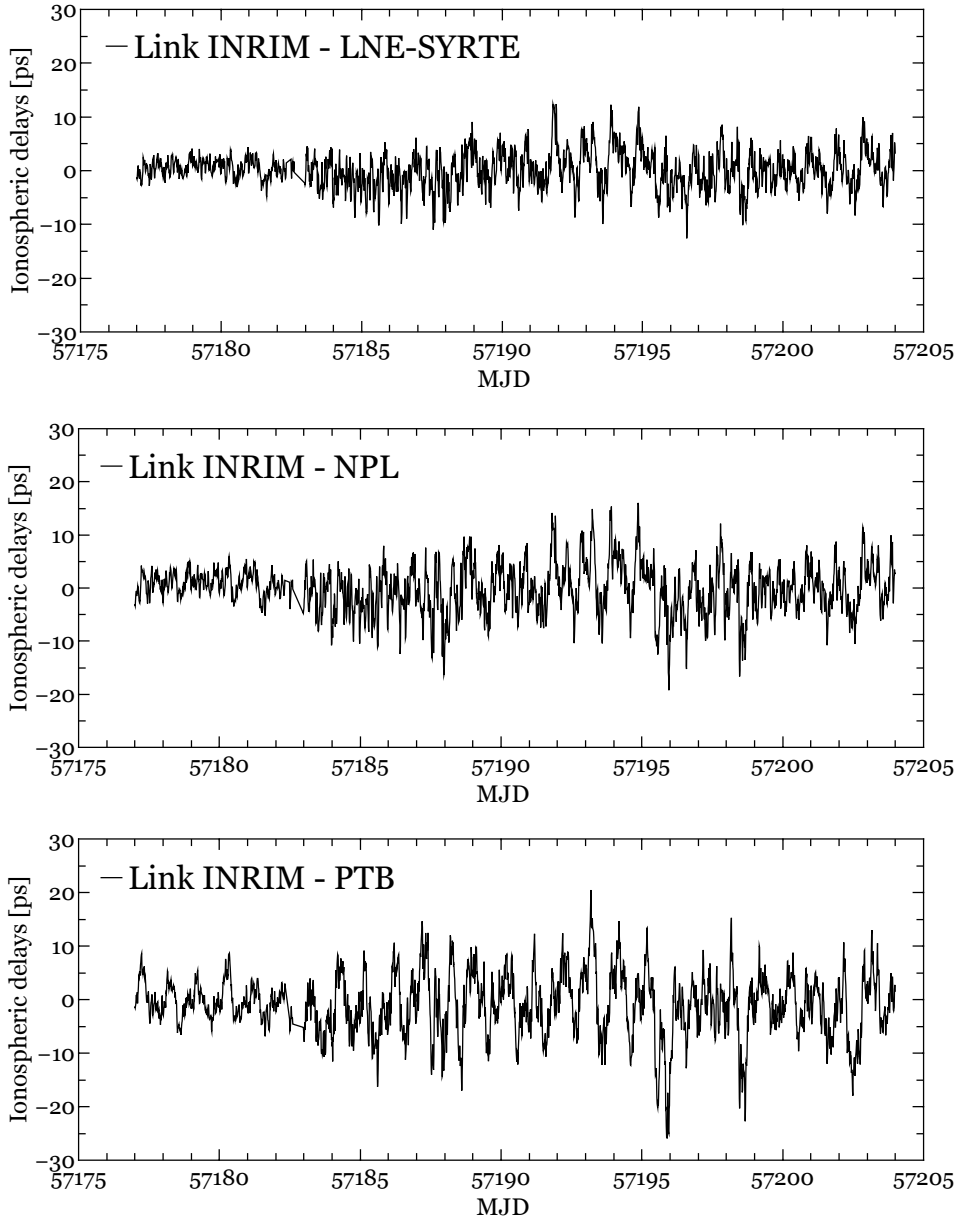

FIGURE 5.16: Ionospheric corrections for three of the links during the clock comparison campaign (first figure out of two). During the first few days, the up- and downlink frequencies were 14.105 GHz and 12.605 GHz, respectively, while after the transponder switch the frequencies 14.275 GHz and 11.475 GHz were used for up- and downlink, resulting in higher ionospheric-induced phase changes.

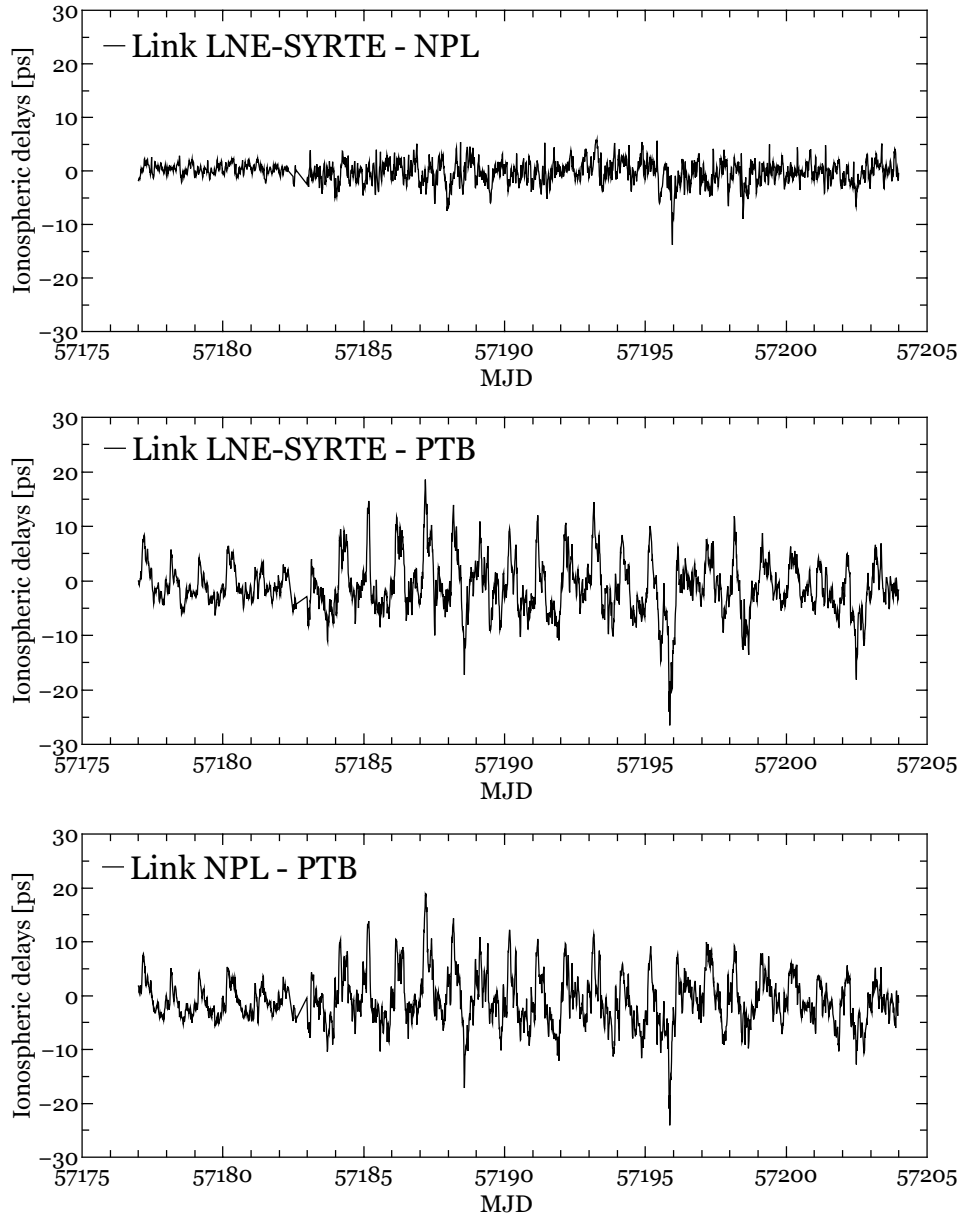

FIGURE 5.17: Ionospheric corrections for three of the links during the clock comparison campaign (second figure out of two). During the first few days, the up- and downlink frequencies were 14.105 GHz and 12.605 GHz, respectively, while after the transponder switch the frequencies 14.275 GHz and 11.475 GHz were used for up- and downlink, resulting in higher ionospheric-induced phase changes.

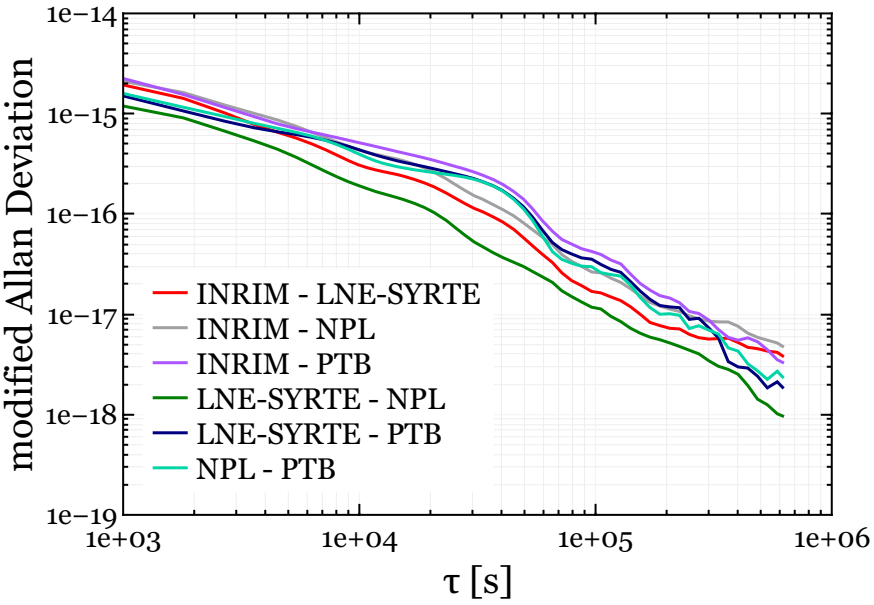

FIGURE 5.18: Modified Allan Deviation of the ionospheric corrections for all links during the clock comparison campaign.

Influence of troposphere

The dispersive property of the troposphere is considered to be so small for frequencies up to 20 GHz that the ITU recommendation for TWSTFT measurements does not provide any correction. However, predicting precise TW measurements for the future, a theoretical analysis of the influence of the troposphere for long baselines was carried out in 2007 [118].
There, calculations were carried out for the link PTB – NICT, a long baseline with low elevation angles. Like for the ionosphere, this link can be used as a worst-case-estimation: not only because of the increased signal path due to the low elevation, but also since the difference in humidity and temperature are relatively high for both stations, and the daily change of the temperature is also shifted by approximately 12 h. As a result, a maximum peak-to-peak difference of 4 ps was found over a 300 d period, and the relative frequency instability is below 1×10^{-17} for $\tau = 1$ d. Since the value found for this long-baseline link would already negligible for the measurement analyzed in this work, the non-reciprocities introduced by the troposphere were considered to be small enough to be discarded.

5.4.2 Correction of the Sagnac effect

Like the ionospheric correction, the correction of the Sagnac effect is only compensating for the variation of this effect, since a constant phase difference is irrelevant to the resulting frequency difference. As discussed in Chapter 3, station coordinates and position and velocity of the satellite are parameters needed for the calculation [1].
The stations' coordinates are already known within an accuracy of 12 m due to the

[1]The calculation of the Sagnac correction was carried out for both the link test and the clock comparison campaign by a cooperation of LNE-SYRTE and NPL, and provided to PTB

requirement for GNSS time transfer (all four NMIs have GNSS antennas close to the TWSTFT roof stations), which was found to be sufficient for the accuracy requirement for these calculations.

In Figs. 5.19 and 5.20, the time series of the final corrections are shown. Two different structures are visible, a diurnal oscillation and a periodic structure with a maximum approx. every 14 d. This is consistent with the calculations provided before the campaign based on estimations [171]. There, the Sagnac effect variation and the path delay difference variation were separately calculated based on older data provided by SES. The diurnal oscillation of the Sagnac effect can reach 36 ps in peak-to-peak difference.

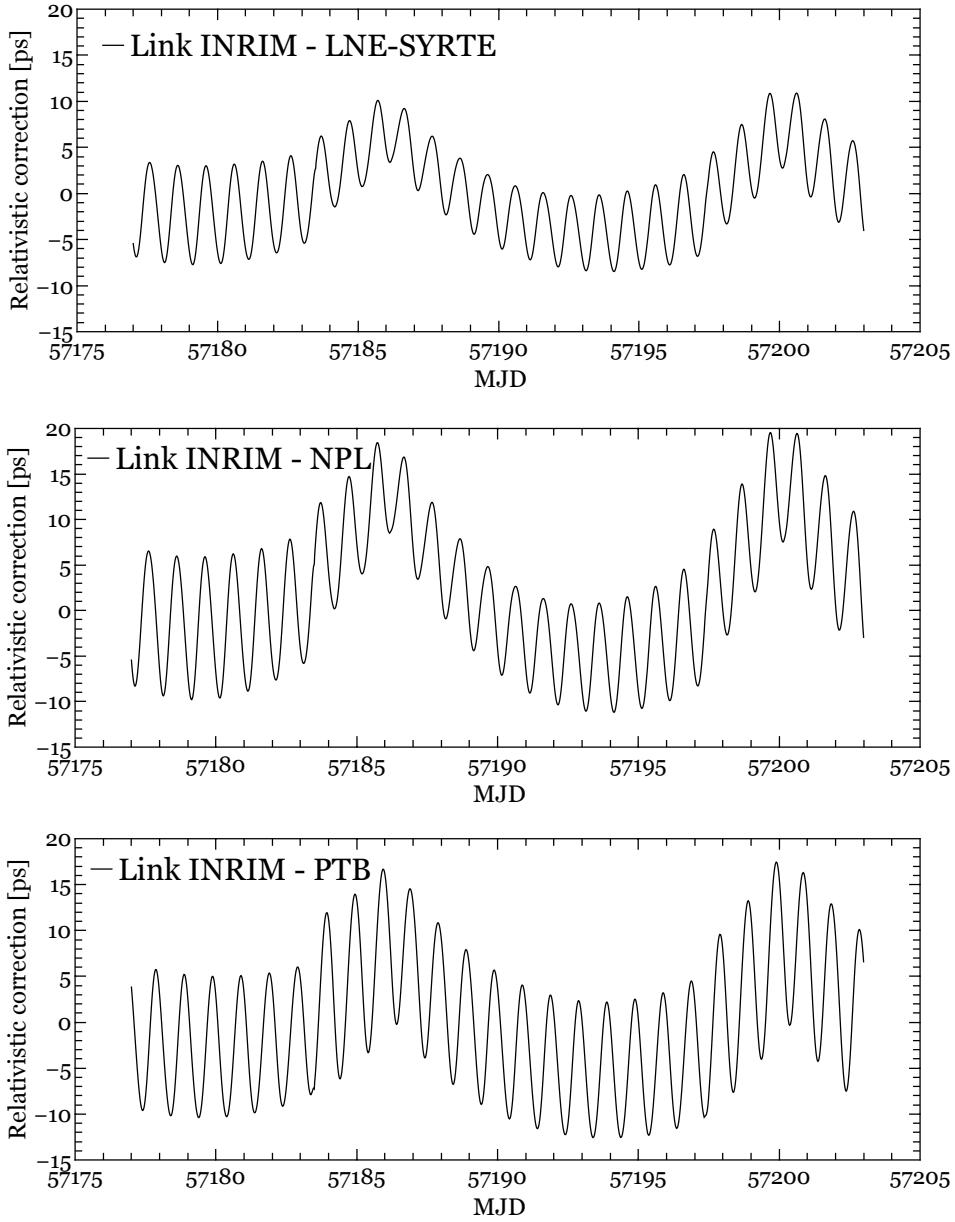

FIGURE 5.19: Sagnac corrections for three of the links during the clock comparison campaign (first figure out of two). An average value of several nanoseconds (different for each link) was subtracted from each time series.

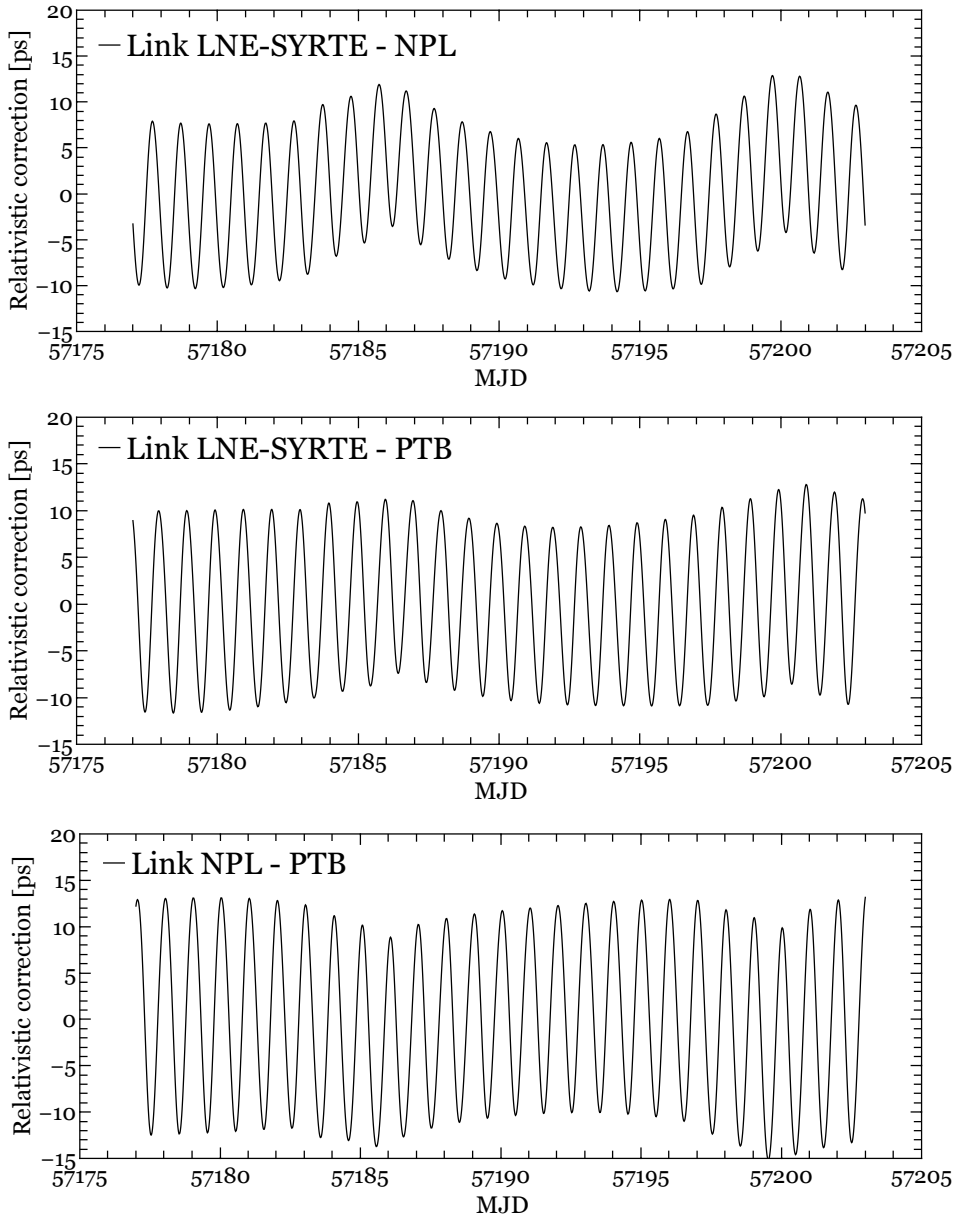

FIGURE 5.20: Sagnac corrections for three of the links during the clock comparison campaign (second figure out of two). An average value of several nanoseconds (different for each link) was subtracted from each time series.

The diurnal structure has the maximum amplitude on the link NPL – PTB, whereas the long-term oscillation is maximum on the link INRIM – NPL, and being in general more significant on the INRIM-related links.

The magnitude of both observations on the links depends most likely on the orientation of the baseline with respect to the signal paths, i.e. the lines-of-sight between the stations and the satellite.

Similar to the diurnal structure having its origin in the residual daily movement of the satellite, the long-term oscillation can also be referred to the satellite movement. Alongside with the gravitation of the Sun, other forces like the gravitation of the Moon, non-spherical parts of the Earth's gravitation and solar radiation pressure cause a displacement of the satellite with respect to its orbit. The effective gravitation of both Sun and Moon at a given time of the day changes with the position of the Moon during one month, the perturbation arising from this is maximum twice per month, when Sun, Moon and Earth are aligned in one line [188].

Chapter 6

Analysis of the clock comparisons

To calculate the relative frequency difference (and from there the frequency ratio in case of clocks based on different transitions) between two atomic clocks (AC) via TWSTFT (or GPS PPP), three sets of data are needed:

$$\begin{array}{lrcl} (1) & y_1 & = & y(\mathrm{AC}_1 - \mathrm{HM}_1)(t) \\ (2) & y_2 & = & y(\mathrm{AC}_2 - \mathrm{HM}_2)(t) \\ (3) & x_{\mathrm{link}} & = & x(\mathrm{HM}_1 - \mathrm{HM}_2)(t), \end{array} \tag{6.1}$$

where x denotes phase-time data and y fractional frequency data. The last one represents the phase difference between the HMs measured with the satellite links, and its properties relevant for the analysis are discussed in detail in the previous chapter. It is hereafter referred to as "link data". It is a phase measurement that can easily be converted into a time series of relative frequencies, if the measurements have a constant spacing:

$$\begin{aligned} y_{\mathrm{link}}(t) &= \frac{x_{\mathrm{link}}(t + \frac{\Delta t}{2}) - x_{\mathrm{link}}(t - \frac{\Delta t}{2})}{\Delta t} \\ &= y(\mathrm{HM}_1 - \mathrm{HM}_2)(t) \end{aligned} \tag{6.2}$$

The data sets (1) and (2) in Eq. 6.1, called hereafter "clock data", are the local measurements of the atomic clock (optical ion/lattice or microwave fountain) against the reference HM. Information about the clocks and a description of the corresponding data provided are given in the first section of this chapter. The sections following after describe the calculations, starting with an overview over the challenges faced, and then going into detail for the calculations of the frequency comparisons for the optical lattice and ion clocks (short optical clocks, OC) and the microwave fountain clocks (short fountain clocks, FC). The last section presents and discusses the results.

6.1 Clocks operated during the campaign

Table 6.1 provides an overview over all clocks operated during the campaign, including typical systematic uncertainties and the percentage of operation during the campaign (uptime), relative to the whole 26 d interval in case of the optical clocks, and relative to a fixed 12 d and 16 d interval, respectively, for the fountain clocks. Details on the intervals for the fountain clocks are given in Chapter 6.3.1, since the choice of these intervals originate from the way the data $y(\mathrm{FC} - \mathrm{HM})$ is provided, the calculation method and common uptimes. The last column of the table contains some references for the respective clocks.

TABLE 6.1: Overview of the clocks that were compared and their estimated systematic uncertainties u_B. In addition, the uptimes during the campaign are listed. For the optical clocks, the uptime refers to the whole duration of the campaign (26 d), whereas for the fountain clocks, two different measurement intervals were analysed (12 d and 16 d, see Chapter 6.3.1). This is the reason why in three cases an uptime span is indicated. The two optical clocks of NPL reach a combined uptime of 88%, i.e. when at least one of two clocks was in operation, and the two optical clocks of PTB a combined uptime of 61%.

Institute	Clock	u_B	Uptime	References
Optical clocks				
LNE-SYRTE	Sr2 (^{87}Sr lattice)	4.1×10^{-17}	68%	[40, 95]
NPL	^{87}Sr lattice	6.8×10^{-17}	77%	
	^{171}Yb$^+$ single-ion (E3)	1.1×10^{-16}	74%	[189]
PTB	^{87}Sr lattice	1.9×10^{-17}	49%	[40]
	^{171}Yb$^+$ single-ion (E3)	3.2×10^{-18}	33%	[76]
Fountain clocks				
INRIM	ITCsF2	2.3×10^{-16}	97%	[24]
LNE-SYRTE	FO1	3.6×10^{-16}	71% – 75%	[25]
	FO2	2.5×10^{-16}	77% – 79%	[25, 190]
	FO2-Rb	2.7×10^{-16}	80%	[25, 191]
PTB	CSF1	3.0×10^{-16}	98%	[22] [1]
	CSF2	3.0×10^{-16}	84% – 87%	[22] [1]

In order to calculate properly a relative frequency difference between the atomic clocks, the relativistic redshifts of the clock frequencies must be taken into account. For the calculation of the redshifts the difference of the gravity potential at the clock locations has to be determined. For this work, only static potential differences are

[1] The relevant systematic uncertainty budgets of CSF1 and CSF2 of PTB are in general close to those reported to the BIPM for the calculation of UTC/TAI for June 2015 (Circular T330 [192]). For CSF1, however, the distributed cavity phase shift was re-evaluated after the clock comparison campaign, which retrospectively results in a significantly reduced overall systematic uncertainty of CSF1.

TABLE 6.2: Data used to derive the relativistic redshifts of the clock frequencies. C_{RefMk} is the geopotential number for a specific nearby reference marker based on the geodetic GNSS/geoid approach [194, 195], ΔH is the local height difference between the clock and a specific reference marker with $\Delta H = H_{\mathrm{clock}} - H_{\mathrm{RefMk}}$, g is the local acceleration due to gravity derived from an FG5-X absolute gravimeter measurement (with an uncertainty far below the significant digits quoted here), and C_{clock} is the final geopotential number for the clock point. The underlying coordinate reference frame is ITRF2008 with the epoch 2005.0, and the zero reference potential for the geopotential numbers is $W_0 = 62\,636\,856.00\,\mathrm{m^2 s^{-2}}$. The uncertainties for ΔH and for the geopotential numbers C_{clock} are given in parentheses, the uncertainty of C_{RefMk} is $0.22\ \mathrm{m^2 s^{-2}}$.

Institute	Clock	Reference marker ID	Geopotential number for reference marker C_{RefMk} [$\mathrm{m^2 s^{-2}}$]	Height difference ΔH [m]	Local gravity acceleration g [$\mathrm{ms^{-2}}$]	Geopotential number for clock C_{clock} [$\mathrm{m^2 s^{-2}}$]	Redshift correction $\frac{\Delta\nu}{\nu}$ [10^{-15}]
INRIM	ITCsF2	CS104	2323.32	1.020(10)	9.8053	2333.32(24)	-25.9617(27)
LNE-SYRTE	Sr2	SR2	545.06	0.201(5)	9.8093	547.03(23)	-6.0865(25)
	FO1	FO1	613.42	0.761(10)		620.89(24)	-6.9083(27)
	FO2-Cs	FO2	579.63	0.962(10)		589.06(24)	-6.5542(27)
	FO2-Rb	FO2	579.63	0.886(10)		588.32(24)	-6.5459(27)
NPL	^{87}Sr	G4L10	96.54	1.290(10)	9.8118	109.20(24)	-1.2150(27)
	^{171}Yb$^+$ E3	G4L16	96.58	1.081(5)		107.19(23)	-1.1926(25)
PTB	^{87}Sr	PB02	763.84	0.538(3)	9.8125	769.12(22)	-8.5576(25)
	^{171}Yb$^+$ E3	KB02	753.04	1.001(3)		762.86(22)	-8.4880(25)
	CSF1	KB02	753.04	1.632(5)		769.05(23)	-8.5569(25)
	CSF2	KB02	753.04	1.526(5)		768.01(23)	-8.5453(25)

considered, since variations with time (due to, e.g., ocean tides) do affect the clocks only within the low 10^{-17} range [193].

The potential was determined with the GNSS/geoid method in a first approach, using an improved European gravimetric quasi-geoid model (EGG2015), which is based on new gravity measurements at reference points close to all clock sites. In a second step, the geometric leveling method is applied locally to determine the potential of the clock positions relative to these points. Table 6.2 shows all relevant parameters for this determination, including the differential redshift. The uncertainties for the differential redshift are less than 4×10^{-18}, which corresponds to an uncertainty lower than 4 cm in height [2]. More details about the gravity potential, the relativistic redshift and the methods for determination, including models used for the determination here, can be found in [15, 194, 195].

The clock data of the optical clocks is provided on a time grid of 1 s. The Allan Deviation of these time series $y(\mathrm{OC} - \mathrm{HM})(t)$ is depicted in Fig. 6.1. An algorithm similar to the modified Allan Deviation was used to treat the gaps on the data properly [176],

[2] The calculations of of the relativistic redshift were carried out by Leibniz University of Hanover (LUH, Institut für Erdmessung). The local gravity measurements were carried out by staff of the respective institutes, and collected by LUH. Table 6.2 with the caption was provided by H. Denker and other coauthors of [52].

based on [61]. For NPL and PTB, the data of the two local clocks was combined by using the locally measured difference between both and filling the gaps in the time series of one clock with the data from the other clock in case it was operating during that time. The observed instability here is, of course, the instability of the HM. Also, it has to be noted that the values for the Allan Deviations can not be directly compared with the modified Allan Deviations of the links, since the Allan Deviation does not distinguish between the white phase noise of the maser and flicker phase noise. In case of LNE-SYRTE, a cryogenic sapphire oscillator (CSO) is used to gain a lower short-term instability [196]. The hydrogen maser is steered approximately every 1 h by the CSO.

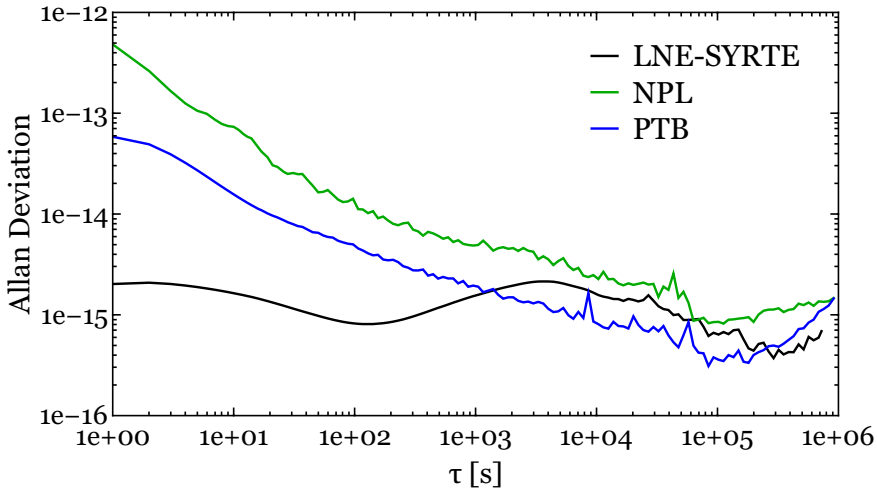

FIGURE 6.1: Allan Deviation of the frequency measurements between the optical clocks and the hydrogen masers. For NPL and PTB, the data sets used are from a combination of both clocks: the gaps of one data set are filled with data from the other one and shifted by the result of the local relative frequency difference measurement. At LNE-SYRTE, a cryogenic sapphire oscillator is used for averaging times below 1 h to gain a lower instability in this range.

6.2 Calculating the relative frequency difference between optical clocks

In the ideal case, all three time series from Eq. 6.1, y_1, y_2 and $y_{\text{link}}(t)$ (from $x_{link}(t)$, as calculated via Eq. 6.2) cover the same period, are continuous on the same time grid and show only white frequency noise. From that, the calculation of the frequency difference between the two clocks would be straight-forward:

$$y(\text{OC}_1 - \text{OC}_2)(t) = y_1(t) - y_2(t) + y_{\text{link}}(t) \tag{6.3}$$

A mean value $\bar{y}(\text{OC}_1 - \text{OC}_2)$ could be calculated, and for the estimation of the statistical uncertainty the standard deviation of the mean could be used.

However, as pointed out in the previous chapter for the link data, there are often disturbances in reality that can lead to excursions and gaps on the data, and there can

be other noise types and technical fluctuations as well. In addition to the incidents during the campaign that affected the TWSTFT data, data gaps are also observed on the optical clock data, so there is only limited common operation time of two clocks and the corresponding link. An overview over the uptimes of all optical clocks and the TWSTFT links can be seen in Fig. 6.2.

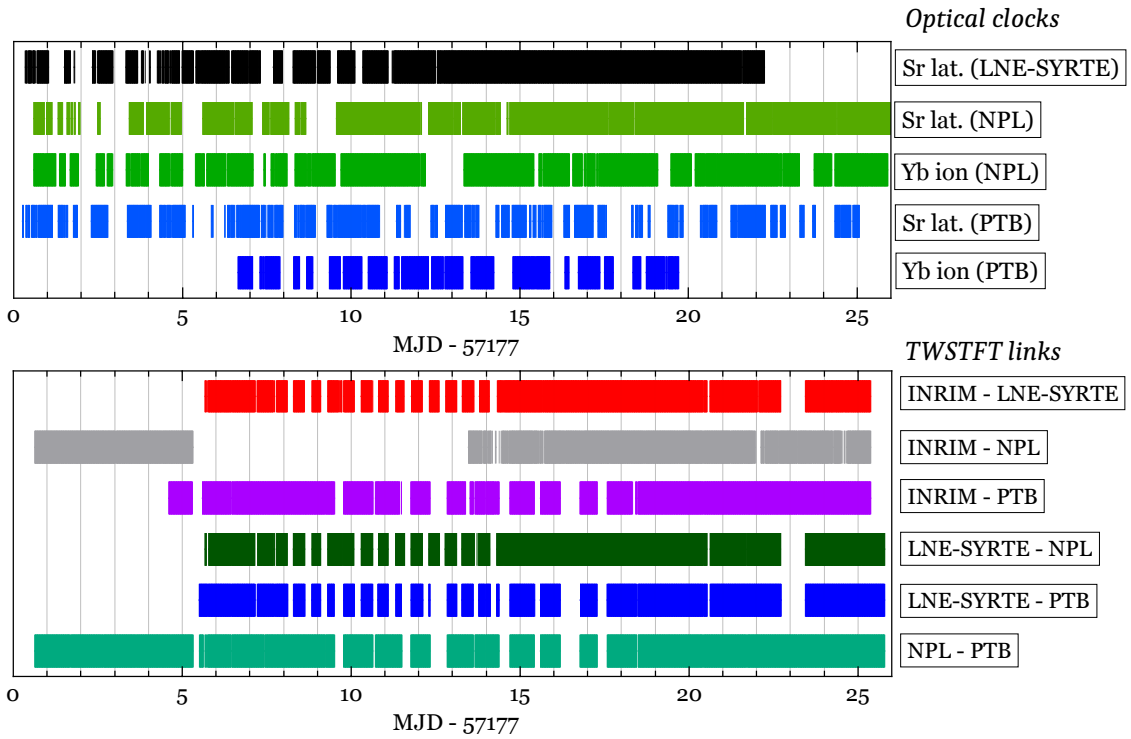

FIGURE 6.2: Periods of measurement times during the campaign of all optical clocks involved (above) and the broadband TWSTFT links (below, as in Fig. 5.2 in Chapter 5.2). Periods with technical disturbances resulting in outliers were already discarded.

One possibility is to combine the data according to Eq. 6.3 only for times t where all data sets overlap, but with this, the final time series would contain a lot of gaps and be dominated by the white and flicker phase noise of the link, and the respective uncertainty for a simple average (average with equal weights, so-called "Π"-averaging) in this case would be in the 10^{-14} range.

Another approach is to perform Π-shape pre-averaging of the three data sets separately before combining the values to one mean frequency difference, but in that case, the uncertainty is limited by the instability of the HM. So, a pre-average process for the link is required to suppress the white and flicker phase noise.

Thus, in order to find the best way to calculate the relative frequency difference between two clocks and the respective uncertainty, a compromise between the following tasks need to be found:

- minimize the phase noise of the link with appropriate averaging,
- use only overlapping data to have the HMs effectively cancel out,
- discard as few data as possible.

6.2.1 The tool for the uncertainty estimation

According to the *Guide to the Expression of Uncertainty in Measurement* (GUM) [53], the statistical uncertainty (type-A uncertainty) u_A corresponding to a mean value $\bar{y}$ of measurements y_i is the square root of the variance of the mean, $\sqrt{\sigma^2_{\bar{y}}}$. The commonly used estimator for that variance is the standard variance of the mean $s^2_{\bar{y}}$:

$$s^2_{\bar{y}} = \frac{\sum_{i=1}^{n} (y_i - \bar{y})^2}{n(n-1)} \tag{6.4}$$

However, this estimator is only unbiased in absence of correlations and therefore in the case of white noise (white frequency noise for y_i being relative frequency values). Based on approaches that take correlations and weights into account [197–199], a different estimator has been derived for this work. A detailed derivation can be found in Appendix B. Including the weights for this calculation does not only allow for a mean $\bar{y}(\mathrm{OC}_1 - \mathrm{OC}_2)$ based on non-equal weights, but also for the treatment of gaps: each time stamp on a given continuous time grid with a non-existing measurement value is assigned to a weighting factor of zero. The estimator for the variance of the mean $\bar{y}$ of N measurements with weights w used is the following:

$$s^2_{\bar{y}} = \sum_{i=1}^{N} w_i R_0 + 2 \sum_{l=1}^{l_\mathrm{cut}} R_l \sum_{j=1}^{N-l} w_j w_{j+l} \tag{6.5}$$

Here, R is a non-normalized estimator of the autocovariance, with R_0 as the estimator of the population variance, and R_l at lag l:

$$R_l = \frac{\sum_{i=1}^{N-l} \sqrt{w_i w_{i+l}} (y_i - \bar{y})(y_{i+l} - \bar{y})}{\sum_{i=1}^{N-l} \sqrt{w_i w_{i+l}}} \tag{6.6}$$

Several things should be noted for these formulas. First, it has to be noted that the weights are normalized, i.e. $\sum_{i=1}^{N} w_i = 1$. The sum in Eq. 6.5 over all R_l is the term taking into account all correlations for the lag $l > 0$. For white frequency noise, these R_l are zero, and the uncertainty is represented by the first term, which resembles the estimator for the variance of the mean for the presence of normalized weights. The R_l can be normalized by dividing R_l by R_0, which results in the ACF with the value 1 for $l = 0$. Positive correlations, i.e. $R_l > 0$, lead to an increased value for the statistical uncertainty, while negative correlations decrease the uncertainty, as, for example, in the case of white phase noise. Another important aspect in the introduction of a cutoff lag l_cut. Calculations in the literature show that the estimator for R_l becomes erroneous for larger lags l, thus, a cutoff lag needs to be chosen to take all significant correlations into account.

6.2.2 The calculation of the mean

With this tool at hand, the initial objective, the calculation process of the mean relative frequency difference, can be developed. The processing of the data to obtain an average relative frequency is depicted in Fig. 6.3 for the Yb^+ clock pair of NPL and PTB, shown for two days as example.

The method for the determination of the uncertainty puts a limitation to the preprocessing of the link phase data x_{link}: for the proper calculation of the R, the sample size should not be reduced significantly. Hence, instead of simple piece-wise averaging, a moving average was chosen, with the averaging window $\tau = 1\,\mathrm{d}$. With this, the link noise in general that is dominating up to averaging times of 0.5 ...1 d, but especially the white phase noise, can be suppressed. Also, diurnal oscillations or disturbing effects with periods close to 1 d are minimized. A weight is assigned to each $\bar{x}_{\mathrm{link},i}$, proportional to the number n of phase samples that are comprised in the averaging window, i.e. $n = 0...86400$. Additionally, the time stamps t were averaged in the same way, to assign each averaged phase value $\bar{x}_{\mathrm{link},i}$ to the effective point of time where the phase values are valid. However, in order to not generate additional samples via averaging, gaps are cut into the averaged data for the times where the original data had gaps, too. This step is illustrated in Fig. 6.3 (a): The black curve resembles the un-averaged phase values, the blue curve the averaged phase values $\bar{x}_{\mathrm{link},i}$. In a next step, the phase data were converted into relative frequency data y_{link} as in Eq. 6.2 on steps of $\Delta t = 1\,\mathrm{s}$. Investigations were made with larger Δt, however, it was found that this would introduce artificial correlations at lags l larger than the chosen l_{cut}. The sample number n of the averaged phase data were transformed accordingly into weights w_{link}:

$$w_{\mathrm{link}}(t_i) = \frac{n(t_i)n(t_{i+1})}{n(t_i) + n(t_{i+1})} \tag{6.7}$$

Both $y_{\mathrm{link}}(t)$ and the corresponding weights w_i can be seen in Fig. 6.3 (b). They are not yet normalized to unity.

For the same reason – to not artificially introduce correlations on the clock data – a pre-averaging was not done for the corresponding clock data y_1 and y_2. However, there is a benefit for the data of both PTB and NPL, where two clocks A and B (Sr and Yb^+) were operated: the gaps of clock A could be filled up in case clock B was running during that time by using the locally measured frequency ratio between both clocks. This is depicted in Fig. 6.3 (c) and (d). This procedure is justified, because the uncertainty for this measurement is negligible with respect to the uncertainty of the remote comparison, and was carried out in previous campaigns [200]. The values used here for $\nu(\mathrm{Yb})/\nu(\mathrm{Sr})$ were measured during the campaign, internally calculated by the respective working groups at NPL and PTB, and provided by these for this calculation.

The clock data $y_1(t)$ and $y_2(t)$ were subtracted for times t where both overlap (as a first step of Eq. 6.3), and simple weights w_{clock} were introduced:

$$w_{\mathrm{clock}}(t_i) = \begin{cases} 0 & \text{at gaps} \\ 1 & \text{elsewhere.} \end{cases} \tag{6.8}$$

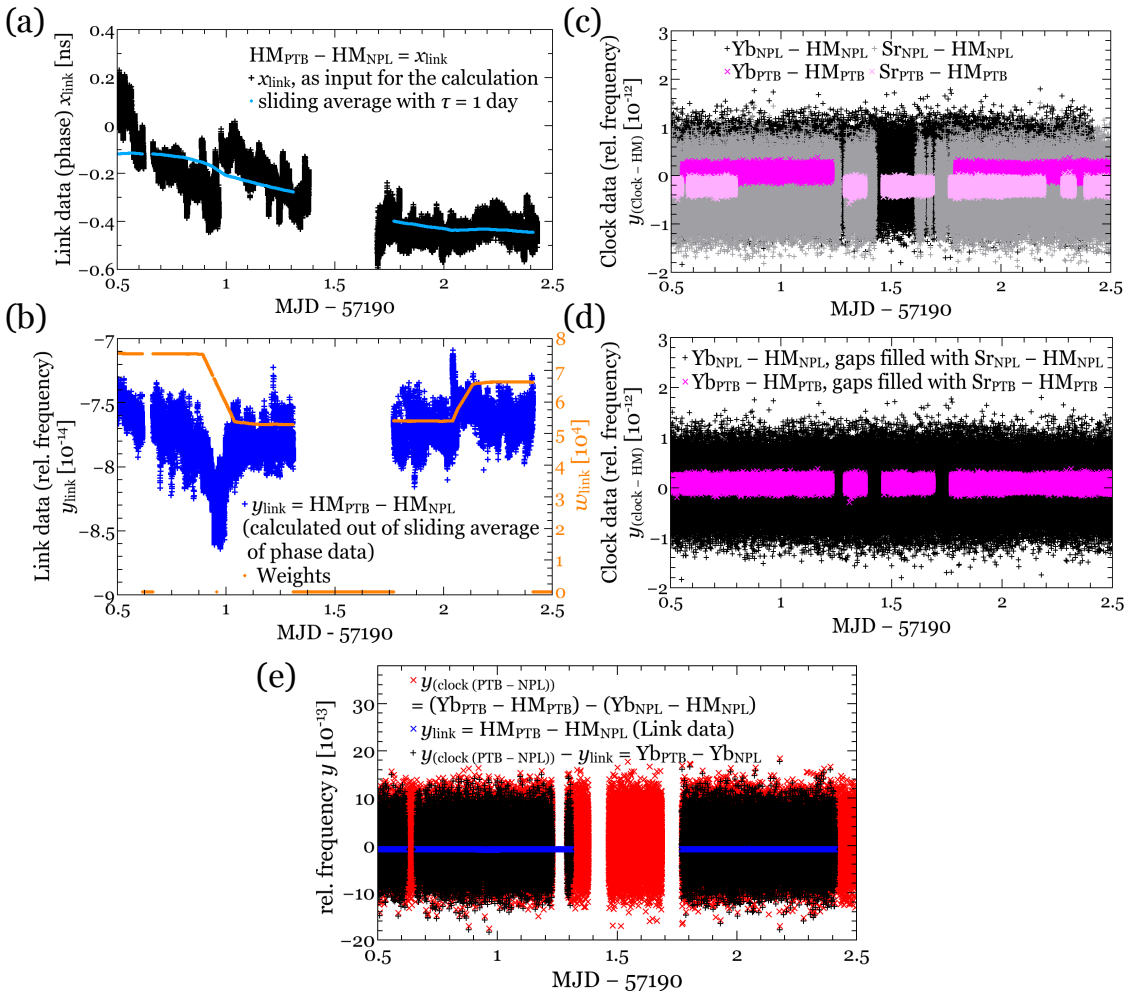

FIGURE 6.3: Scheme of data analysis procedure, shown for the comparison of Yb^+(PTB) and Yb^+(NPL) via TWSTFT for two days of the campaign. The upper left graph, (a), shows the phase data of the link between the masers of PTB and NPL, with the frequency offset of the whole measurement interval removed for a better visibility. The black symbols show the measured data, with outliers removed, the blue dots the moving average with an averaging window of 1 d. Data gaps from the original data are maintained for the sliding averages. The blue symbols in (b) show the relative frequency calculated from the averaged phase data in (a). The weights are depicted in orange. The graphs in (c) show the locally measured differences between the hydrogen maser and the optical clocks (in pink for PTB, in black/grey for NPL). The dark data are from the Yb clocks, the light data are from the Sr clocks. The Sr clock data is shifted by -3×10^{-13} for a better visibility. The Sr clock data are used to fill the gaps in the Yb data, which results in the graphs shown in (d). In (e), the final step is depicted. The two time series of (d) are merged into one $y_{\mathrm{clock(PTB-NPL)}}$ (in red), and in blue the frequency difference of the hydrogen masers (blue graph from (b)) is shown. Both time series are subtracted in order to get the frequency difference of the two Yb clocks (black symbols).

The result of this difference can be seen in red in Fig. 6.3 (e), where $y_{\mathrm{link}}(t)$ from (b) appears again in blue. After that, the second step of Eq. 6.3 is carried out by

merging both the frequency data from the link and from the clocks to one time series $y(\mathrm{OC}_1 - \mathrm{OC}_2)(t)$, shown in black in Fig. 6.3 (e). Normalized weights are calculated as follows:

$$w(t_i) = \frac{w_{\mathrm{clock}}(t_i) w_{\mathrm{link}}(t_i)}{\sum_{i=1}^{N} w_{\mathrm{clock}}(t_i) w_{\mathrm{link}}(t_i)}. \tag{6.9}$$

From $y(\mathrm{OC}_1 - \mathrm{OC}_2)(t)$ and $w(t)$, a weighted average is calculated, $\bar{y}(\mathrm{OC}_1 - \mathrm{OC}_2)$.

In case of GPS data, the link is on a time grid of 30 s. The procedure was adapted accordingly, using a moving average with τ = 30 s on the clock data y_1 and y_2 to establish a respective time grid. The PPP processing could be carried out for the whole duration of the campaign in case of NPL and PTB, so gaps on the data of $y(\mathrm{OC}_1 - \mathrm{OC}_2)$ were only originating from the optical clocks. In case of LNE-SYRTE, the PPP processing was limited to the period of MJD 57183.0 – MJD 57198.0 due to the data availability of the GPS receiver.

6.2.3 Estimation of the statistical uncertainty

For the statistical uncertainty, the estimator as according to Eq. 6.5 was used, with l_{cut} = 4000 in each case. The criterion for choosing an appropriate cutoff lag was a compromise between avoiding erroneous calculations for higher lags and taking into account existing correlations on the data, with a focus on positive correlations in order not to underestimate the uncertainty. The value 4000 was found by first analyzing the individual time series for correlations before processing, i.e. before averaging or merging. With this, intervals of several days interrupted by only a few short gaps could be taken for a calculation of an ACF. Secondly, the statistical uncertainty of $\bar{y}(\mathrm{OC}_1 - \mathrm{OC}_2)$ was calculated using different l_{cut}, and both a lower and a higher l_{cut} lead to a lower uncertainty. More details can be found in Appendix B.

For lower l_{cut} it is thus justified to assume that significant positive correlations are not taken into account properly. The fact that the uncertainty is decreased in case of higher l_{cut} might have different reasons, like the introduction of artificial correlations due to the processing or an erroneous calculation of the ACF due to the higher amount of gaps, but there is also the possibility that the higher amount of negative values of the ACF are "real correlations" and the decrease of the statistical uncertainty is justified. The decision to take l_{cut} = 4000 could therefore lead to a slight overestimation of the statistical uncertainty, but it was decided that taking this risk is a preferable solution in contrast to underestimate the uncertainty due to errors.

Regarding the two terms in Eq. 6.5, there is one thing interested to note with respect to the real data used. The first one, representing the biased standard deviation of the mean taking the weights into account, but disregarding the correlations, is approximately twice as large as the second one which handles the correlations, and both have an opposite sign, which means negative correlations still predominate on the ACF until the lag l_{cut}. Therefore, taking the correlations into account leads to a smaller statistical uncertainty than the estimator which is only unbiased for white frequency noise. This originates from the suppressed white and flicker phase noise.

Since the data used for the evaluation of the statistical uncertainty comprises both the link and the clock data, the contribution of the optical clocks to the statistical

uncertainty is already included in this value. It can be safely assumed that it is negligible compared to the contribution of the satellite links.

6.2.4 Estimation of the systematic uncertainty

For the systematic uncertainty, the considered contributions originate from both the clocks and the link. The systematic uncertainty from the clocks involved were evaluated independently from the campaign and can mostly be found in the references given in Table 6.1. In case of PTB and NPL, where gaps on the data of one clock were filled with data of the other clock by using the locally measured frequency ratio, a weighted uncertainty out of the two systematic uncertainties of the clocks was calculated, based on the amount of data used from the other clock to fill the gaps.

To estimate the systematic uncertainty from the satellite links, various influences were evaluated. In case of TWSTFT, a contribution from the ionospheric correction was investigated by calculating the corrections with different parameters (change of the coordinates, change of the height h as the center of the ionosphere), applying them and calculate the results. Deviations from the actual obtained results of 2×10^{-17} were found, which are taken as contributions to the systematic uncertainty.

From all pre-investigations of the hardware used for the campaign, the impact of temperature was found to be crucial, both in the laboratory and on the roof at the outdoor equipment. Since the calculation of a temperature correction for the data was not considered to be feasible, its impact has to be considered in the uncertainty. Fluctuations with a period of up to 1 d are significantly reduced due to the pre-averaging of the phase, and fluctuations in general are represented as statistical fluctuations on u_{A}. However, there is still the possibility of having a phase drift which is undetected by the statistical uncertainty evaluation, either due to a real temperature drift or oscillations that do not cancel out due to the presence of gaps.

As the relevant temperatures were carefully monitored during the campaign at all stations, an estimation of such a drift could be carried out by combining these measurements and approximate temperature coefficients to generate in a first step a time series of phase data that describes the impact of temperature on the link measurements over the whole campaign. In a second step, the same analysis process that was used for the original link phase data was performed, with inserting gaps for times where gaps were present in the original link data.

The absolute value of the resulting weighted mean of relative frequency was taken as temperature-induced contribution to the systematic uncertainty. Since both in- and outdoor temperature were measured and the respective equipment has different temperature coefficients, more than one time series of temperature-induced phase data was created per laboratory: two in the case of TWSTFT (in- and outdoor), and three in the case of GPS (indoor for the receiver, and two outdoor for the cables and the antenna, respectively). This results in having four contributions to the systematic uncertainty, i.e. four results of a relative frequency deviation, to one link in case of TWSTFT and six in case of GPS, which were added in the commonly used simplified way of error propagation: by calculating the square of each contribution, adding them and forming a square root of this sum.

For the TWSTFT links, the coefficients for both indoor and outdoor equipment as described in Chapter 3 were taken: 50 ps/K as a mean coefficient for the combination of TX and RX of one modem (indoor contribution) and 5 ps/K as the coefficient of the outdoor equipment (converters/amplifier/transceiver). The indoor equipment contributions were found to have values in the 10^{-18} range up to the low 10^{-17} range, depending mostly on the institute and thus the overall temperature stabilization. The outdoor equipment contributions were found to be varying not only by institute, but also for the links, which is a result of the different measurement intervals and gaps for the corresponding links. While most values are in the low 10^{-17} range, in case of the link between PTB and LNE-SYRTE, the LNE-SYRTE outdoor contribution is dominating the uncertainty with a value of 9×10^{-17}. This link has the largest amount of gaps while having a shorter measurement interval than other links. Thus, outdoor temperature fluctuations do not cancel out as well as for longer, uninterrupted measurement times. Since the outdoor equipment at PTB was kept in an environment of temperature stabilization, temperature differences between different days did not affect the equipment.

For the GPS measurements, temperature coefficients for the main components (receiver, antenna and antenna cable) were taken from the literature for the analysis [201–203]. From there, coefficients of 9 ps/K in case of PolaRx4 receivers (PTB and LNE-SYRTE) and 13 ps/K for the Dicom GTR50 receiver (NPL) were taken, based on measurements with receivers of the same company, but different models (PolaRx3 and Javad GTR, Javad receivers are used for Dicom GTR receivers). A coefficient of 10 ps/K, which is a general conservative estimation for antennas for measurement times longer than a few days, was taken for all institutes, and a value of 0.03 ps/(K·m) for the antenna cables, which were of the same type at LNE-SYRTE, NPL and PTB. Details about the cables can be found in table A.5 in Appendix A.

Different calculations were carried out for the cables, splitting the length of the cables in an indoor and outdoor contribution, depending on the length being in a stabilized environment and being exposed to the temperature changes at the outside. However, it was found that most cable contributions are smaller than 1×10^{-17}, even if the whole cable (up to 50 m) was considered to be part of the outdoor equipment. The contributions by the receivers are approximately in the same range, but similar to the observation for the case of TWSTFT, more stable than the outdoor cable contribution. For all links, the dominating contribution for the systematic uncertainty of GPS PPP is the contribution introduced by the antenna, varying from 0.1×10^{-16} to 1.1×10^{-16}. As in the case of TWSTFT, the contributions differ not only for the single laboratories, but also for the links. Even though GPS PPP data is almost continuous over the measurement period, the difference for the links introduced by the different gaps of the clock data can result in a significantly different contribution: In case of LNE-SYRTE, where the intervals are the same for both links, the respective contributions are 0.8×10^{-16} and 1.1×10^{-16}.

6.3 Calculating the relative frequency difference between microwave frequency standards (fountain clocks)

The limitations given by the clock data are different in the case of the fountain clocks. In contrast to the optical clocks, the fountain clocks were operated without any major interruptions, but the concept of operation usually provides frequency values

in intervals significantly longer than 1 s. Furthermore, the statistical uncertainty of the fountain clocks for averaging times of 1 d is in the lower 10^{-16} range, which is the same range of instability as the satellite link performance. For these reasons a different analysis procedure was applied for the fountain comparisons.

The high percentage of operation time of the fountain clocks allows the approach of determining average frequency values for each time series in eq. 6.3 separately before merging them to one average value $\bar{y}(\mathrm{FC}_1 - \mathrm{FC}_2)$.

So in a first step, a coherent measurement interval common for the fountain clocks and the TWSTFT links was identified. Since the mean frequency differences between the fountains and the hydrogen masers over a certain interval are provided by the fountain clock operators, one interval for all comparisons was chosen. The limitation for the beginning of this period was set by the change of satellite transponder, and the point in time for the ending of the period was defined by both the operation time of INRIM's fountain clock ITCsF2 and the TWSTFT link to LNE-SYRTE. The interval chosen was MJD 57183.0 – 57199.0 (Δt_{FC} = 16 d).

For each fountain clock an averaged value $\bar{y}(\mathrm{FC} - \mathrm{HM})$ was calculated for the specific interval. To evaluate the mean frequency difference between the distant hydrogen masers $\bar{y}_{\mathrm{link}}$, a linear fit of the measured phase data for the TWSTFT link during 24 h at the beginning and at the end of the interval was calculated. With this, a similar pre-averaging as for the optical clock comparison calculations was performed, with the same purpose: to suppress white and flicker phase noise and diurnal oscillations. In each case, the center of the 1 d-intervals for the linear fit was 0:00 UTC of the first/last day of the respective comparison interval. The resulting phase difference was then divided by the duration of the interval (Δt_{FC}).
From the averaged frequency values $\bar{y}_{\mathrm{link}}$, $\bar{y}_1$ and $\bar{y}_2$, the relative frequency difference was calculated similarly to eq. 6.3.

Again, the process was adapted for GPS accordingly. Due to the processing of GPS data on a daily base and several events limiting the data availability of receivers of INRIM and LNE-SYRTE, the interval used was shorter: MJD 57184.0 – 57196.0 (12 d).

6.3.1 Estimation of the uncertainty

For the estimation of the statistical uncertainty of the link, two considerations can be made: (1) The modified Allan Deviation σ_{mod} at an averaging time of τ = 1 d can be used for an uncertainty estimation for the linearly interpolated phase values, and (2) an estimation of the uncertainty for measurement periods of $\tau > \Delta t_{\mathrm{FC}}$ is given by the link uncertainty for the optical clock comparisons $\tau = \Delta t_{\mathrm{OC}}$. From these two points, an interpolation for the statistical uncertainty of Δt_{FC} = 16 d can be made. In order to do so, an assumption for the noise type at these averaging times and in between will be made, but having two points available, this assumption is more justified than just extrapolating from the last points of the modified Allan Deviation to the whole measurement interval. An overview of Δt_{OC} and Δt_{FC} for each comparison is given in Table 6.3.

Since the modified Allan Deviation is a biased estimator for the uncertainty, it needs to be converted into an uncertainty value by multiplying an additional factor, as shown in [62]. This conversion factor, however, depends not only on the type of weighted averaging, which is known, but also on the noise type. So an iterative

TABLE 6.3: Length of intervals for the comparison of fountain clocks (Δt_{FC}) and optical clocks (Δt_{OC}). Only for the link LNE-SYRTE – PTB a direct interpolation is possible, since INRIM was not involved in the optical clock comparisons. However, the data of the links with involvement of NPL were used as an estimation.

Link/Technique	Δt_{FC} in d	Δt_{OC} in d
INRIM – LNE-SYRTE (TWSTFT)	16	–
INRIM – LNE-SYRTE (GPS)	12	–
INRIM – PTB (TWSTFT)	16	–
INRIM – PTB (GPS)	12	–
LNE-SYRTE – PTB (TWSTFT)	16	16.4
LNE-SYRTE – PTB (GPS)	12	13.5
LNE-SYRTE – NPL (TWSTFT)	–	16.5
LNE-SYRTE – NPL (GPS)	–	13.5
NPL – PTB (TWSTFT)	–	24.4
NPL – PTB (GPS)	–	24.5

approach is taken: with an initial assumption about the noise type, the interpolation can be done and by determining the slope of the interpolation, an information about the noise type is gained and can be used for a new assumption.

In this way, the statistical uncertainty for the link LNE-SYRTE – PTB can be determined directly through interpolation. Without an uncertainty for optical clock comparisons with INRIM, however, the process for the INRIM-related links is adapted based on additional estimations: at first, the uncertainty at $\tau = 1$ d is estimated based on the same noise type as for the link LNE-SYRTE – PTB. For the extrapolation, then, an estimated slope, based on the average of all links analysed for the optical clock comparisons, is taken. Since the statistical uncertainty of the optical clock comparisons also takes into account the gaps from the clock data, it can be assumed that the statistical uncertainty for the fountain clock comparisons is slightly over-estimated when using the procedure.

The systematic uncertainty of the link was estimated in a similar way as for the optical clock comparisons: a time series of phase values was generated out of the recorded temperatures and temperature coefficients, and a mean frequency value was calculated in the same way as the average frequency difference of the link $\bar{y}_{\text{link}}$ was determined. These values are taken as systematic uncertainties. The temperature coefficients for the GPS equipment of INRIM are 13 ps/K for the Javad Legacy receiver, 0.5 ps/(K·m) for the antenna cable and 10 ps/K for the antenna. Similar observations as for the contributions for the optical clock comparisons could be made when comparing the in- and outdoor contributions of one technique. However, since the interval length is the same for each link and gaps depend only on gaps of the link, there are less variations for the respective contributions.

The estimation of the statistical uncertainties of the fountain clocks is based on the measured short-term instability and the known averaging behaviour for longer measurement times. In addition, a dead-time uncertainty was taken into account, as it generally can be found in the Circular T (publication by BIPM on UTC – UTC(k)) [192]. These two and the systematic uncertainties were provided by the fountain clock operators in INRIM, LNE-SYRTE and PTB.

6.4 Discussion of results

At first, the results of the comparisons of the optical clocks will be discussed. In Table 6.4 the results for the relative frequency differences between the optical clocks of the same type are listed, with the statistical and systematic uncertainty contributions. A graphical visualization of these results is depicted in Fig. 6.4. These kind of triangular plots are used for all clock comparisons in this work. The center of each axis is zero, and reaches 1×10^{-15} at each corner, which represents one institute, respectively. So a relative frequency difference of 0 between two clocks is shown at the center of each axis (which corresponds to a frequency ratio of 1 in case of clocks of the same type, and to the ratio of the absolute frequency values as confirmed by the International Commitee for Weights and Mesures (CIPM, Comité International des Poids et Mesures) and listed accordingly [71]). A deviation from a difference of 0 is shown with the respective sign with the following convention: The closer the difference is to one of the corners, the higher the frequency of the clock of that respective institute is compared to the one of the other corner.

TABLE 6.4: Results for the comparisons of optical clocks of the same type. The third column shows the average relative frequency difference ($\bar{y}(\mathrm{OC}_1 - \mathrm{OC}_2)$), $u_{\mathrm{B,c}}$ is the combined systematic clock uncertainty, $u_{\mathrm{A,l}}$ and $u_{\mathrm{B,l}}$ are the statistical and systematic uncertainties of the link, respectively, and u represents the combined overall uncertainty. All values are in 10^{-16}

Clock pair	link	difference	$u_{\mathrm{B,c}}$	$u_{\mathrm{A,l}}$	$u_{\mathrm{B,l}}$	u
Sr(LNE-SYRTE)	TWSTFT	0.9	0.8	3.0	0.7	3.2
– Sr(NPL)	GPS PPP	0.5		2.3	0.8	2.5
Sr(LNE-SYRTE)	TWSTFT	1.1	0.5	2.5	0.9	2.7
– Sr(PTB)	GPS PPP	-1.4		1.9	1.2	2.3
Sr(NPL)	TWSTFT	-2.9	0.7	3.3	0.5	3.4
– Sr(PTB)	GPS PPP	-2.5		1.5	0.6	1.8
Yb^+(NPL)	TWSTFT	0.2	1.1	3.3	0.5	3.5
– Yb^+(PTB)	GPS PPP	1.6		1.5	0.6	2.0

Firstly, the results are discussed from the link technique point of view. From Table 6.4, it can be seen that the combined uncertainties of the comparisons are 3.5×10^{-16} at maximum. Both satellite link techniques show similar uncertainties. Looking in detail, the GPS PPP has for the same links always a slightly lower (less than a factor of 2) uncertainty, a trend which originates from the fact that the combined uncertainties are dominated by the statistical uncertainties, which is larger for the TWSTFT links (up to more than a factor of 2 in case of the link between NPL and PTB). This is caused by the unforeseen technical difficulties on the TWSTFT measurements, leading to gaps and fluctuations on the data, while GPS PPP did not show any major disturbance during the measurement time and the data on the intervals are without interruption. On the other hand, the systematic uncertainty of GPS PPP is insignificantly higher by a a few 10^{-17} than the one of the TWSTFT links. As mentioned in Chapter 6.3.1, the main contribution is the impact of temperature

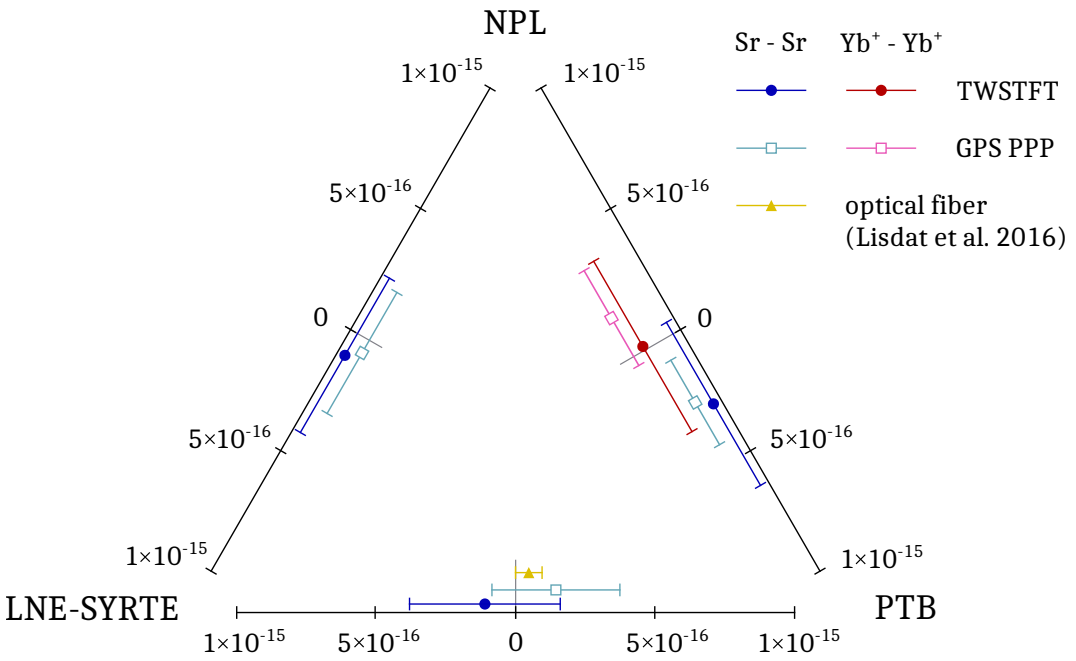

FIGURE 6.4: The results of the relative frequency differences for the optical clock comparisons between the three institutes LNE-SYRTE, NPL and PTB, for clocks of the same type. Each side of the triangle reaches from -1×10^{-15} to $+1 \times 10^{-15}$ for a comparison between clocks of the respective institute in the corners. The positive sign refers to the first clock in the difference OC1 – OC2, e.g. a point located between 0 and $+1 \times 10^{-15}$ on the PTB side on the line between LNE-SYRTE and PTB indicates a negative result for the comparison Sr(LNE-SYRTE) – Sr(PTB). The result for the fiber comparison are taken from [40].

on the antenna, which is a conservative estimate based on measurements of more than a decade ago. Choosing dedicated equipment and carrying out an evaluation of the temperature impact specifically for these kind of measurements would lead to a lower systematic uncertainty. The visualization in Fig. 6.4 shows that all results agree with each other within a 1-σ-uncertainty. This includes the result for Sr(LNE-SYRTE) – Sr(PTB) of a comparison carried out via optical fiber ($-0.47 \pm 0.5 \times 10^{-17}$ [40]) which was carried out simultaneously with this campaign. It is depicted here for comparison reasons.

Focusing on the aspect of the clock comparisons, it can be seen that most of the results are compatible with zero within a 1-σ-uncertainty, independent of the link technique. The PPP measurement for Sr(NPL) – Sr(PTB) deviates by 1×10^{-16}, which is still well within the 2-σ-uncertainty. The two comparisons that involve the Sr(NPL) clock show for both satellite link techniques an offset with the same sign corresponding to Sr(NPL). These observed deviations from zero may indicate that the frequency of this clock was indeed lower by a few 10^{-16} compared to the other Sr clocks during the campaign.

Deviations like these can best be detected by simultaneous comparisons. Here, the systematic uncertainty originating from all known effects for the clock was evaluated to be 6.8×10^{-17} for the time during the campaign, as indicated previously. However, later investigations of interleaved self-comparison of the clock data revealed an additional, uncharacterized frequency shift. It was found that the clock

TABLE 6.5: Results for the comparisons of optical clocks of different type. The third column gives the optical frequency ratio as an offset from the ratio $r_0 = 1.495\,991\,618\,544\,900$. The fourth column shows the average relative frequency difference ($\bar{y}(\mathrm{OC}_1 - \mathrm{OC}_2)$), $u_{\mathrm{B,c}}$ is the combined systematic clock uncertainty, $u_{\mathrm{A,l}}$ and $u_{\mathrm{B,l}}$ are the statistical and systematic uncertainties of the link, respectively, and u represents the combined overall uncertainty. All values are in 10^{-16}

Clock pair	link	$\frac{\nu_{\mathrm{Yb}^+}}{\nu_{\mathrm{Sr}}} - r_0$	$y_{\mathrm{Sr}} - y_{\mathrm{Yb}^+}$	$u_{\mathrm{B,c}}$	$u_{\mathrm{A,l}}$	$u_{\mathrm{B,l}}$	u
Sr(LNE-SYRTE)	TWSTFT	9.76	-4.9	1.2	3.0	0.7	3.3
– Yb^+(NPL)	GPS PPP	11.13	-5.8		2.3	0.8	2.7
Sr(LNE-SYRTE)	TWSTFT	4.59	-1.4	0.4	2.5	0.9	2.7
– Yb^+(PTB)	GPS PPP	8.40	-3.9		1.9	1.2	2.3
Sr(NPL)	TWSTFT	10.54	-5.4	0.7	3.3	0.5	3.4
– Yb^+(PTB)	GPS PPP	9.99	-5.0		1.5	0.6	1.8
Sr(PTB)	TWSTFT	6.44	-2.6	1.1	3.3	0.5	3.5
–Yb^+(NPL)	GPS PPP	8.58	-4.1		1.5	0.6	2.0

frequency could vary by up to 4×10^{-16}, depending on the delay between the spin preparation and the clock interrogation. It is assumed that this originates from the Doppler shift due to a radial motion in the lattice. However, this could not be verified in detail and the magnitude of the effect not evaluated, since the setup was modified after the campaign. The shift has now been eliminated by replacing the lattice laser delivery optics, which has greatly improved the spatial beam quality[3].

Table 6.5 shows the relative frequency differences for the clocks of different types (Sr lattice against Yb ion). They refer to the CIPM recommended values of 2017 for the absolute frequencies of the Yb^+ octupole transition, $\nu_{\mathrm{Yb}^+_{\mathrm{oct}}} = 642\,121\,496\,772\,645.0\,\mathrm{Hz}$ and for the Sr transition $\nu_{\mathrm{Sr}} = 429\,228\,004\,229\,873.0\,\mathrm{Hz}$ [204], which means that a zero would correspond to both clocks having this frequency as the transition. The results are visualized in Fig. 6.5, similarly to Fig. 6.4. All results deviate from zero with the same sign, i.e. $y(\mathrm{Sr} - \mathrm{Yb}^+) < 0$ for all comparisons. This is an indication that the true frequency ratio $\nu_{\mathrm{Yb}^+}/\nu_{\mathrm{Sr}}$ is different from the one recommended by CIPM by a few 10^{-16}, but since the combined uncertainty for the recommended values is 7.2×10^{-16} [204], the results are still compatible.

Table 6.6 shows the results for the remote frequency comparisons between the fountain clocks, which are depicted in the same way in Figs. 6.6 and 6.7 as the results of the optical clock comparisons. The relative frequency difference between Cs and Rb corresponds to zero for a Rb frequency of $6,834,682,610.904\,312\,6\,\mathrm{Hz}$, which is the CIPM 2017 recommended value [204]. The frequencies of all six fountains agree with each other within the 1-σ-uncertainty, which is between 4.8×10^{-16} and 7.7×10^{-16}. Furthermore, all techniques show good agreement within the uncertainty, including the optical fiber comparison carried out in parallel [205].

Looking at the uncertainties, the situation for the differences between the two satellite link techniques is a little different than for the optical clock comparisons. For the

[3]This section was provided by I. Hill for [52]

TABLE 6.6: Summary of the remote fountain clock comparisons. The third column gives the average fountain frequency difference, $u_{A,c}$ and $u_{B,c}$ are the combined statistical and systematic clock uncertainties (with the dead-time uncertainty as part of the statistical uncertainty), $u_{A,l}$ and $u_{B,l}$ correspond to the statistical and systematic link uncertainties, and u is the combined overall uncertainty. The statistical uncertainties of the clocks differ for the two link techniques due to the different measurement intervals. The value of the absolute frequency of the ^{87}Rb ground state hyperfine transition used in these comparisons is the CIPM recommended value 6,834,682,610.904 312 6 Hz of 2017 [204]. All values are in 10^{-16}.

Clock pair	link	difference	$u_{A,c}$	$u_{B,c}$	$u_{A,l}$	$u_{B,l}$	u
ITCsF2 (INRIM)	TWSTFT	-1.0	2.8	4.3	3.2	0.4	6.0
- FO1 (LNE-SYRTE)	GPS PPP	5.6	3.2		5.6	0.6	7.7
ITCsF2 (INRIM)	TWSTFT	-1.0	2.8	3.4	3.2	0.4	5.4
- FO2 (LNE-SYRTE)	GPS PPP	3.8	3.2		5.6	0.6	7.3
ITCsF2 (INRIM)	TWSTFT	0.8	2.7	3.5	3.2	0.4	5.4
- FO2Rb (LNE-SYRTE)	GPS PPP	6.9	3.1		5.6	0.6	7.3
ITCsF2 (INRIM)	TWSTFT	-1.0	2.9	3.8	5.5	0.3	7.2
- CSF1 (PTB)	GPS PPP	2.4	3.3		5.4	0.9	7.4
ITCsF2 (INRIM)	TWSTFT	1.2	3.3	3.8	5.5	0.3	7.3
- CSF2 (PTB)	GPS PPP	4.7	3.8		5.4	0.9	7.5
FO1 (LNE-SYRTE)	TWSTFT	0.7	1.4	4.7	2.6	0.3	5.5
- CSF1 (PTB)	GPS PPP	-3.2	1.7		2.0	1.0	5.5
FO1 (LNE-SYRTE)	TWSTFT	2.9	2.1	4.7	2.6	0.3	5.8
- CSF2 (PTB)	GPS PPP	-0.9	2.5		2.0	1.0	5.7
FO2 (LNE-SYRTE)	TWSTFT	0.7	1.3	3.9	2.6	0.3	4.9
- CSF1 (PTB)	GPS PPP	-1.4	1.5		2.0	1.0	4.8
FO2 (LNE-SYRTE)	TWSTFT	2.9	2.0	3.9	2.6	0.3	5.1
- CSF2 (PTB)	GPS PPP	0.9	2.4		2.0	1.0	5.0
FO2Rb (LNE-SYRTE)	TWSTFT	-1.1	1.2	4.0	2.6	0.3	4.9
- CSF1 (PTB)	GPS PPP	-4.5	1.4		2.0	1.0	4.8
FO2Rb (LNE-SYRTE)	TWSTFT	1.1	2.0	4.0	2.6	0.3	5.2
- CSF2 (PTB)	GPS PPP	-2.2	2.3		2.0	1.0	5.1

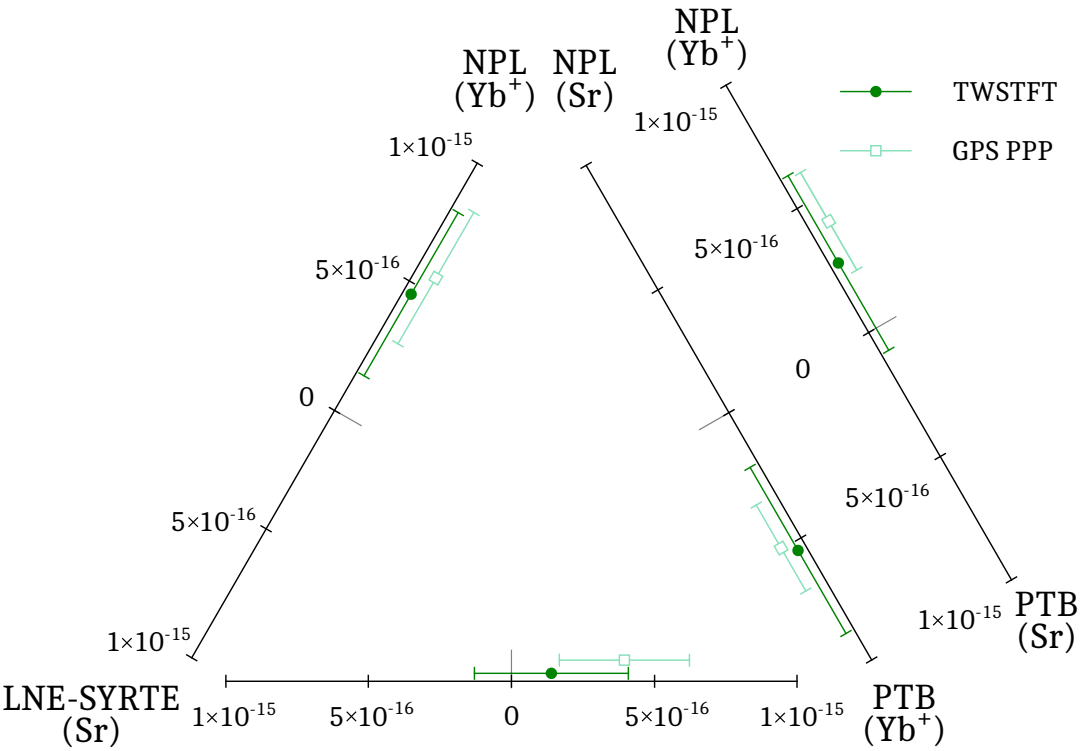

FIGURE 6.5: The results of the relative frequency differences for the optical clock comparisons between the three institutes LNE-SYRTE, NPL and PTB, similar to Fig. 6.4, but for clocks of different type. All results refer to the CIPM recommended values of 2017 for the absolute frequencies of the clock transitions for Yb^+ and Sr(lattice).

combined uncertainties, the statistical uncertainties of the fountain clocks are not negligible, and due to the shorter interval of the GPS PPP, this uncertainty is higher for all clocks in case of GPS PPP. Concerning the link uncertainties, the difference between the techniques depend strongly on the respective link.

For the statistical uncertainty, the modified Allan Deviation at 1 d averaging time is important. The link between LNE-SYRTE and PTB shows a significantly lower instability (by a factor of 3) than the INRIM-related links in case of GPS PPP, and the value itself for this link and this technique is lower than in case for TWSTFT for the same link. This leads to the fact that even with shorter intervals the statistical uncertainty of the GPS PPP link for all comparisons between LNE-SYRTE and PTB fountains is lower than for the same comparisons via TWSTFT. For the INRIM-related links it can be observed that in case of GPS PPP there are technical fluctuations leading to a larger instability at 1 d averaging time than for the LNE-SYRTE – PTB link and similar instabilities at this time as for the TWSTFT links of INRIM – LNE-SYRTE, and INRIM – PTB. Thus, the combination of this and the shorter measurement intervals causes a higher statistical uncertainty for the GPS PPP fountain clock comparisons between INRIM and LNE-SYRTE, and INRIM and PTB.

The systematic uncertainties of the link are again larger in case of GPS PPP than TWSTFT for all links, with differences up to 7×10^{-17} between both techniques. Here, too, the estimation of the antenna sensitivity results in a dominating contribution for the antenna for the systematic uncertainty of GPS PPP. In addition, there might be a stronger temperature trend over the GPS interval than over the TWSTFT interval. As a last point, temperature fluctuations over the day chosen as starting or ending

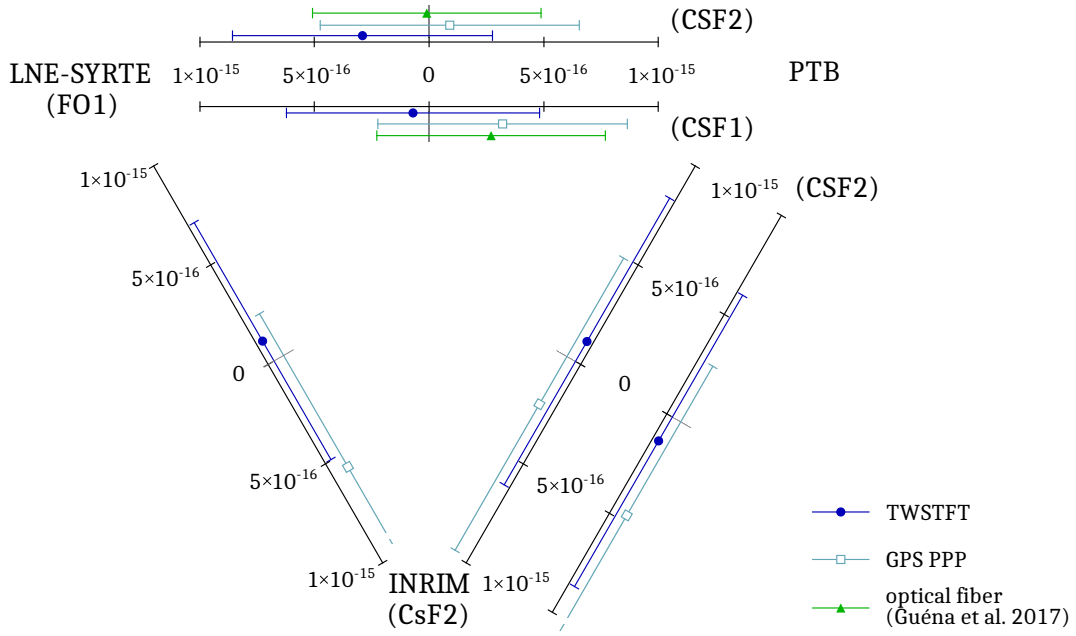

FIGURE 6.6: The results of the relative frequency differences for all fountain clock comparisons between INRIM and PTB, and all comparisons to FO1 of LNE-SYRTE. Each side of the triangle reaches from -1×10^{-15} to $+1 \times 10^{-15}$ for a comparison between the institutes in the corners. The positive sign refers to the first clock in the difference, e.g. a point located between 0 and $+1 \times 10^{-15}$ on the PTB side on the line between LNE-SYRTE and PTB indicates a negative result for the comparison FO1(LNE-SYRTE) – CsF1(PTB). The results for the fiber comparison are taken from [205].

point for the GPS intervals might not average out as good as for the days chosen for the TWSTFT interval.

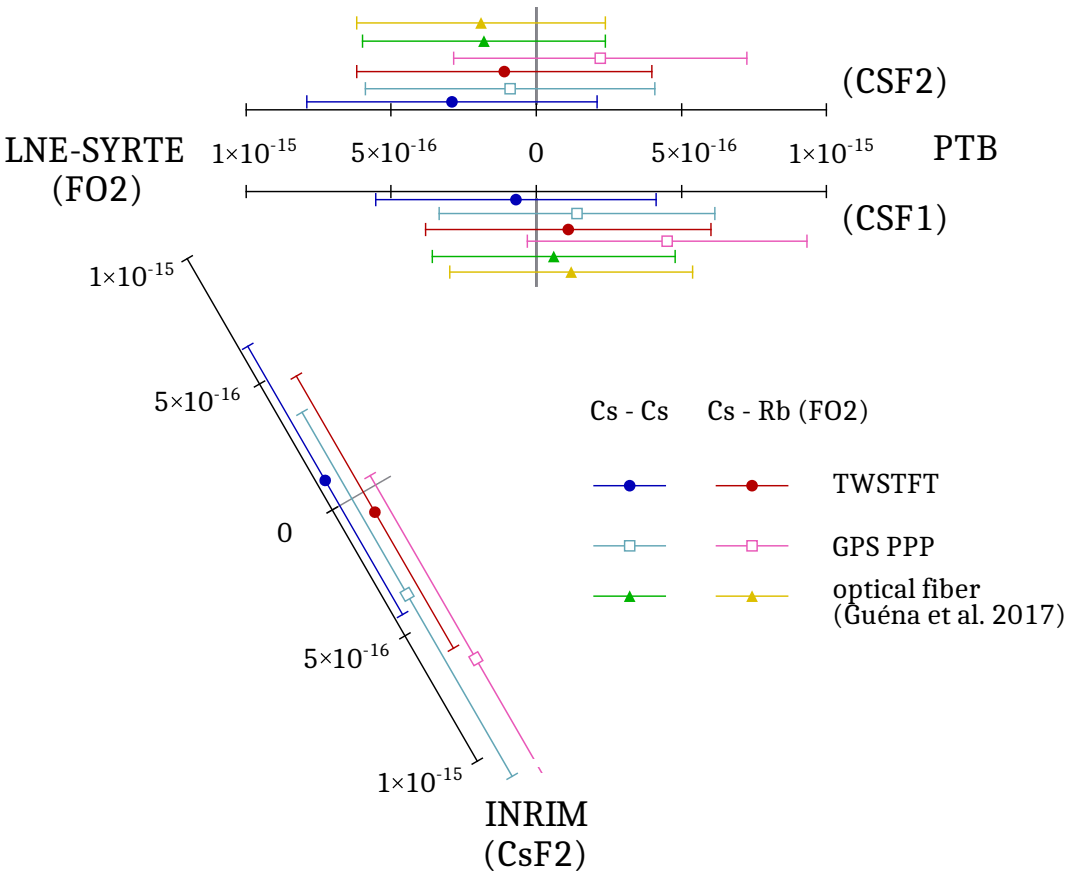

FIGURE 6.7: The results of the relative frequency differences for all fountain clock comparisons between FO2 (both Cs and Rb) of LNE-SYRTE and the Cs fountains of INRIM and PTB, depicted in a similar way as in Fig. 6.6. The results for the fiber comparison are taken from [205]. The third side of the triangle, which corresponds to the comparisons between INRIM and PTB, is left out, the results can be found in Fig. 6.6.

Chapter 7

Conclusion

Within this work, the first simultaneous optical clock comparison between four laboratories located in four different countries took place. Five optical single ion and lattice clocks as well as six microwave fountain clocks were compared over a total measurement period of 26 d, with duty cycles up to 77 % for the optical and 98 % for the fountain clocks. For carrying out this campaign, the satellite-based comparison technique TWSTFT was used and enhanced by implementing the full modulation bandwidth of 20 Mchip/s, which was used for measurements via satellites for the first time. In parallel, the GPS PPP technique was applied as a second, independent satellite-based technique, which allowed for a comparison between enhancements of the two techniques that are currently in operation on a daily base for almost all remote time scale and clock comparisons in the framework of TAI/UTC. To carry out this work, the collaboration between the respective different working groups of the institutes needed to be coordinated.

All results show good agreement: The results obtained with the two different techniques agree with each other within the 1-σ-uncertainty, and are also compatible with the results of a fiber comparison taking place at the same time between two of the four institutes [40, 205]. Clocks of the same transition agree with each other with their frequency within a 1-σ-uncertainty in all but one case, where the result lies still within a 2-σ-uncertainty interval. The differences here range from 0.2×10^{-16} to 2.9×10^{-16} for the optical clocks, and from 0.9×10^{-16} to 5.9×10^{-16} for the fountain clocks. Benefit could be made from the simultaneity of the comparisons: For the first time, three Sr lattice clocks could be compared at once, which allowed for the identification of a hitherto unknown offset in one of the clocks. The results of the comparisons of optical clocks of two different type revealed a systematic offset with respect to the frequency difference as given by the CIPM 2017 recommended values [204], hinting that the true frequency values of these clock transitions are still different by a few parts in 10^{16}, although the results are compatible within the combined 1-σ-uncertainty of the CIPM values. The relative frequency differences between Sr lattice and Yb single ion clocks range from -1.4×10^{-16} to -5.8×10^{-16}, while the the relative difference between the Cs and the Rb frequencies with respect to the CIPM recommended values was measured to be between -1.1×10^{-16} and 6.9×10^{-16}. Although the uncertainties of local comparisons of optical clocks and first international clock comparisons carried out with optical fibers show overall uncertainties lower by almost one order of magnitude or more, the results obtained within this work help to improve the overall picture of the optical clocks operated and their transition frequency, which is another step to identify suitable candidates for the redefinition of the SI second.

The overall comparison uncertainties are in the low 10^{-16} range for the optical clock comparison, between 1.8×10^{-16} and 3.5×10^{-16}. The link uncertainty dominates these estimations, although for the comparison to one of the clocks the systematic uncertainty contribution of the clocks adds up to a value larger than 1×10^{-16}. In case of fountain clocks, the uncertainty contributions from the clocks are in the same order of magnitude as the link uncertainty contributions, and the overall comparison uncertainty ranges from 4.8×10^{-16} to 7.7×10^{-16}. The overall uncertainty of the TWSTFT links is around 3×10^{-16} on average, which is the uncertainty that was aimed for. The uncertainties achieved in this work are significantly lower than the uncertainties of any previous clock comparison using satellite-based techniques [49, 200, 206].

For calculating the mean relative frequency difference for each clock pair, different data sets of phase and frequency data with different dominating noise types and non-common gaps needed to be combined. In order to reach nevertheless such sufficiently low uncertainties and not being limited by short-term noise processes or by the discard of too much data, a certain calculation method was found. The phase data set from the satellite link, which shows a higher noise amplitude, was averaged with a sliding mean before converting it into the frequency domain and combining it with the data sets from the measurement of the optical clocks against the hydrogen masers. At laboratories where two optical clocks were operated during the campaign, the locally measured frequency ratio could be used to fill gaps of one clock when the other one was running. For the uncertainty, an estimator for the standard deviation of the mean was derived that accounts for correlations and gaps on the data. A different approach was used for the fountain clock comparison due to the different properties of the measurement of the fountain against the hydrogen masers, but the results gained from the calculation of the optical clock comparisons were used for this approach.

The uncertainties reached are limited by a number of factors. One limitation is the residual impact of the hydrogen masers on the final combined data, which is present due to the fact that the link data (the difference between the HM) needed to be preaveraged while having different gaps as the data of the optical clocks vs hydrogen masers (clock data). Thus, even though the calculation manages to take gaps into account with a weighting procedure and for the correlation estimation, the amount of gaps should be reduced to a minimum on all measurements to benefit most from the high bandwidth TWSTFT. Another limitation is the estimation of the systematic uncertainty: for estimating the temperature influence, mean temperature coefficients were determined based on measurements carried out at one institute. A detailed analysis of all equipment involved would lead to the possibility of correcting the data for temperature influence, which would reduce both the systematic uncertainty and the statistical uncertainty, since temperature-induced fluctuations in the data have been treated statistically within this work, although the procedure was optimized to average out all fluctuations up to averaging times of 1 d. However, finding individual temperature coefficients for the equipment parts represents a huge effort and is practically not possible in all cases, e.g. for the outdoor-equipment. These considerations hold true for both TWSTFT and GPS. The temperature coefficients taken for the GPS receivers are based on literature on older models than the ones used for this work, and for the antenna, which is the dominating contribution, an estimation representing an upper limit was taken. Hence, future experiments aiming for lower uncertainties need to find a compromise by correcting the impact of equipment parts where the temperature coefficients can easily be determined. Furthermore, a more

conservative approach was taken for the estimation of the correlations: An estimation of a cutoff lag is necessary, since the calculation of the autocorrelation function is only based on a limited number of samples and becomes erroneous for larger lags. Here, the cutoff lag was chosen to not underestimate the uncertainty by taking into account these erroneous negative correlations, but to take rather positive correlations into account. By having larger uninterrupted samples of data to estimate truly existing correlations, this estimation can be done more precisely. However, the estimation of this cutoff lag is always a compromise and there is no guarantee that a more precise determination would decrease the uncertainty. The good agreement of most results while having a relatively large uncertainty (especially in case of the fountain clock comparison) supports the idea that the uncertainty estimation might be rather too conservative.

Considering these limitations, it can be said that the potential gain by using the full 20 Mchip/s modulation rate with the current TWSTFT equipment is not yet fully exploited with the results achieved. Despite all efforts to avoid disturbances and minimize gaps, the campaign was experiencing a lot of unforeseen incidents, like sudden equipment failure, external signal jamming or power cuts. However, the progress in the field of optical clocks leads to lower and lower uncertainties, thus additional improvements have to be implemented in TWSTFT in the future in order to competitive. In addition, leasing the necessary bandwidth on a satellite transponder to use the 20 Mchip/s modulation rate is costly. Future experiments can profit from the efforts made within this work before, during and after the measurement campaign, but the considerations above need to be taken into account.

Some of these efforts were the preparations carried out before the campaigns: Several studies and calculations were conducted in support of the broadband TWSTFT.

Sophisticated laboratory tests were performed with the TWSTFT equipment, especially the SATRE modem, to analyze the short- and long-term instability at full-bandwidth (20 Mchip/s) operation. The short-term instability scales inversely with the modulation band width as expected, and for averaging times longer than 1 d instabilities in the 10^{-17} range could be achieved. Technical disturbances limiting the instability in this range could be mostly identified and precautions were taken by choosing respective parameters at the modem or adapting the overall setup within the laboratory. Although it was found that the modems or even the single receiver channels within one modem are impacted to a different extend by sources of disturbance from inside or outside the modem, the tests revealed a deeper insight into the modem behavior that can be of use in the future for, e.g., using the modems for time comparisons via optical fibers, as it was already done in the past [158, 159, 164, 207].

In addition, corrections were calculated that turned out to be not strictly necessary for the level of uncertainty reached in this work, but should be taken into consideration for future measurements using either code-based TWSTFT or TWCP gaining at slightly lower uncertainties. The calculation of the ionospheric correction revealed that for inner-European links the corrections are necessary for uncertainties below 1×10^{-16} for frequency comparisons, or below 100 ps in case of time transfer. Although large differences in TEC values are not expected for baselines within Europe, they might occur and the values are worth to be estimated in this uncertainty range, especially in times of high solar activity. As shown in previous works, this is more crucial for intercontinental links [118, 131]. The Sagnac correction terms showed that relativistic corrections need to be taken into account for an uncertainty range below 100 ps. The calculated impact of the variation of the path delay difference was found

to be smaller than the impact of the Sagnac by at least a factor of 2. It can be easily compensated by adding an additional delay into the signal at the ground stations, so all signals arrive at the satellite at approximately the same time.

The second satellite-based technique used in this work is GPS PPP, and the achieved uncertainties here are in the same order of magnitude as broadband TWSTFT. The statistical uncertainty is lower than for TWSTFT, because GPS measurements were running with much less interruptions during the campaign. Hence, for the interval length used for the data analysis, the statistical uncertainty was mainly limited by the technique itself and the gaps on the clock data than by gaps and disturbances on the GPS data. However, in case of disturbances like interruptions or inexplicable jumps, PPP can be impacted, and thus limited, more strictly than TWSTFT. This is imposed by the way the data is processed: Due to the fact that the processing within one single batch is preferred over single daily batches due to the phase jumps at batch boundaries, only these technical disturbances can be cut out that can be clearly identified and do not affect the overall result before and after the disturbance. Otherwise the days when the disturbance occurs marks the limit of the overall measurement interval. As mentioned above, GPS PPP measurements would need a more sophisticated analysis of the temperature impact on the equipment. In addition, other systematic effects would need to be exploited in more detail. For example, multipath effects originating from signal reflections around the antenna are only roughly estimated in their contribution to the systematic uncertainty so far. Only recently some studies were launched to further investigate the subject [208]. In addition, due to the nature of data processing, which can only be carried out after the measurement because of the need of satellite clock, satellite orbit and atmospheric products, GPS PPP results can only be used with a certain delay, while TWSTFT allows for a real-time analysis of the data. Despite these considerations, with having no need for additional costs and the equipment being available in more laboratories, GPS PPP represents a good complement to broadband TWSTFT.

Furthermore, in the past few years GPS IPPP was developed as improvement of PPP. Studies show that for averaging times from a few hours onwards, this technique shows lower instabilities than PPP, reaching instabilities below 1×10^{-16} for about 10 d averaging times. However, the technique is not openly available yet, and although the data requirements are the same as for PPP processing, additional understanding for the modeling of certain parameters might be necessary. As an enhancement of PPP, it has, in direct comparison with broadband TWSTFT, similar advantages and drawbacks as PPP, and might therefore represent the future complement technique for TWSTFT.

Another satellite-based technique is TWCP, which was running for some time in parallel with broadband TWSTFT and GPS PPP within this work. TWCP has the advantage of only occupying a few kilohertz bandwidth on the satellite transponder, but the most suitable equipment was developed by NICT and is thus not available at most laboratories. The comparison of broadband TWSTFT with TWCP confirmed the superior instability of TWCP at averaging times up to a few hours as it was observed in previous measurements, but also the averaging behavior of $\tau^{-1/2}$ for most averaging times, so both techniques are at approximately the same level at 1 d. A more recent measurement shows the same instabilities in comparison with IPPP up to averaging times of 1 d [209]. However, for longer averaging times this experiment shows in the double differences of TWCP with GPS PPP and IPPP a slope of τ^{-1}, and demonstrates that TWCP is better than GPS PPP, and the double difference between

TWCP and IPPP reaches an instability below 1×10^{-16}. Currently, a new modem for both code and carrier phase two-way time transfer is under development, and although it only provides the conventional code modulation rate of 1 Mchip/s, the TWCP test measurements show instabilities in the 3×10^{-17} range for averaging times at 1 d [210].

New equipment showing improvements for code-based TWSTFT was also implemented at some laboratories in the past years. A Software Defined Radio receiver (SDR receiver) had been developed [211]. The signals transmitted by the SATRE modems are received in parallel to the conventional modems: in comparison, the diurnal oscillations are reduced, and the instability at a few hundreds of seconds is decreased by the factor of 3, and also for long-term instabilities up to one day averaging time a reduction by a factor of 2 can still be observed [212]. However, these measurements were carried out with a chip rate of 1 Mchip/s, and so far no comparisons of different modulation rates had been conducted, although a laboratory experiment comparing SATRE modem RX channels and SDR RX channels at high modulation rate woul be interesting, especially for long averaging times.

The technique most suitable for optical clock comparisons with respect to the uncertainty is the frequency transfer with optical fibers. Improvements had been made in recent years in this field. An instability in the 10^{-21} range could be evaluated for an averaging time of more than 15 d [213]. More and more optical fiber links are available, and first international link connections were established [40, 41]. Within European coordinated research projects first simultaneous clock comparisons between three laboratories took place [155]. New projects are launched with the goal to further enhance this technique [157, 214]. But even with more links available for the baselines of interest, several laboratories or links might be still difficult to access in the future, especially on an intercontinental scale. First tests on phase noise of optical submarine cables were conducted, but do not reach instabilities below 1×10^{-15} so far [215]. So for most links between laboratories today and for simultaneous comparisons, satellite-based techniques will continue to be first choice.

A few other link techniques are currently under development. VLBI, using astronomic radio sources, was used in an experiment for a proof-of-concept clock comparison between NICT in Japan and INRIM in Italy [216]. Due to the signal being weak in power, this technique requires radio telescope antennas of several meters in diameter and corresponding equipment that are only available in specific facilities. Another experiment was the use of an optical free space link for a clock comparison within the joint clock network at JILA and NIST in Boulder, USA [217]. So far, this technique is limited to very short baselines within the line-of-sight, and atmospheric turbulences and signal loss on the beam due to diffraction further limit the instability.

This work shows that 20 Mchip/s modulation rate TWSTFT can be used to achieve an improvement for remote clock comparisons by at least one order of magnitude compared to conventional TWSTFT with a chip rate of 1 Mchip/s or other satellite-based techniques that were used for comparison campaigns so far. The instability at all averaging times observed decreases with increasing bandwidth, so a clock comparison implementing TWSTFT can benefit from a higher bandwidth, as it is planned, e.g., for the ACES project. However, with decreasing instability more and more effects have to be taken into account, and the uncertainty of any comparison using this technique can be limited by these effects and gaps on the data.

Appendix A

Technical parameters and setup details for the measurement campaigns

A.1 Supplementary material for the SATRE modem characterization measurements

The table of code combination sessions (CCSs) of Chapter 3.1.4 (Table 3.2) will be given for completeness. The CCSs ID numbers refer to the code combinations as depicted in Fig. 3.15.

TABLE A.1: The code combination sessions (CCSs) carried out each day within one schedule for several days. For each period of 20 min, three codes out of 0 ...7 were chosen for the three modems S76, S410 and S427, so every possible combination of these codes could be tested. CCS IDs with a (*) contain code combinations that are implemented more than once. CCS IDS with (**) resemble a reverse transmitting/receiving direction for the modems with respect to the one of CCS #1.

CCS ID	Codes	S76 sends / receives	S410 sends / receives	S427 sends / receives
1 (*)	0,1,2	PRN # 0 / 1	PRN # 1 / 2	PRN # 2 / 0
2	0,2,3	PRN # 3 / 2	PRN # 2 / 0	PRN # 0 / 3
3	0,2,4	PRN # 0 / 4	PRN # 4 / 2	PRN # 2 / 0
4	0,2,5	PRN # 0 / 2	PRN # 2 / 5	PRN # 5 / 0
5	0,2,6	PRN # 6 / 0	PRN # 0 / 2	PRN # 2 / 6
6	0,2,7	PRN # 2 / 7	PRN # 7 / 0	PRN # 0 / 2
7	0,1,3	PRN # 1 / 0	PRN # 0 / 3	PRN # 3 / 1
8 (**)	0,1,4	PRN # 4 / 1	PRN # 0 / 4	PRN # 1 / 0
9	0,1,5	PRN # 1 / 0	PRN # 0 / 5	PRN # 5 / 1
10	0,1,6	PRN # 6 / 0	PRN # 0 / 1	PRN # 1 / 6
11	0,1,7	PRN # 0 / 1	PRN # 1 / 7	PRN # 7 / 0
12	0,3,4	PRN # 3 / 4	PRN # 4 / 0	PRN # 0 / 3
13	0,3,5	PRN # 0 / 3	PRN # 3 / 5	PRN # 5 / 0
14	0,3,6	PRN # 6 / 3	PRN # 3 / 0	PRN # 0 / 6
15	0,3,7	PRN # 7 / 0	PRN # 0 / 3	PRN # 3 / 7
16	0,4,5	PRN # 4 / 5	PRN # 5 / 0	PRN # 0 / 4
17	0,4,6	PRN # 6 / 4	PRN # 4 / 0	PRN # 0 / 6
18	0,4,7	PRN # 0 / 7	PRN # 7 / 4	PRN # 4 / 0
19	0,5,6	PRN # 5 / 0	PRN # 0 / 6	PRN # 6 / 5
20	0,5,7	PRN # 7 / 0	PRN # 0 / 5	PRN # 5 / 7
21	0,6,7	PRN # 6 / 7	PRN # 7 / 0	PRN # 0 / 6
22	1,2,3	PRN # 1 / 2	PRN # 2 / 3	PRN # 3 / 1
23	1,2,4	PRN # 1 / 4	PRN # 4 / 2	PRN # 2 / 1
24	1,2,5	PRN # 5 / 1	PRN # 1 / 2	PRN # 2 / 5
25	1,2,6	PRN # 2 / 6	PRN # 6 / 1	PRN # 1 / 2
26	1,2,7	PRN # 7 / 1	PRN # 1 / 2	PRN # 2 / 7
27	1,3,4	PRN # 1 / 3	PRN # 3 / 4	PRN # 4 / 1
28	1,3,5	PRN # 1 / 3	PRN # 3 / 5	PRN # 5 / 1
29	1,3,6	PRN # 6 / 1	PRN # 1 / 3	PRN # 3 / 6
30	1,3,7	PRN # 7 / 3	PRN # 3 / 1	PRN # 1 / 7
31 (*)	1,4,5	PRN # 1 / 4	PRN # 4 / 5	PRN # 5 / 1
32	1,4,6	PRN # 4 / 6	PRN # 6 / 1	PRN # 1 / 4
33	1,4,7	PRN # 1 / 4	PRN # 4 / 7	PRN # 7 / 1
34 (*)	1,5,6	PRN # 5 / 6	PRN # 6 / 1	PRN # 1 / 5
35	1,5,7	PRN # 1 / 5	PRN # 5 / 7	PRN # 7 / 1

CCS ID	Codes	S76 sends / receives	S410 sends / receives	S427 sends / receives
36	1,6,7	PRN # 6 / 7	PRN # 7 / 1	PRN # 1 / 6
37	2,3,4	PRN # 2 / 3	PRN # 3 / 4	PRN # 4 / 2
38	2,3,5	PRN # 5 / 2	PRN # 2 / 3	PRN # 3 / 5
39	2,3,6	PRN # 2 / 3	PRN # 3 / 6	PRN # 6 / 2
40	2,3,7	PRN # 7 / 3	PRN # 3 / 2	PRN # 2 / 7
41	2,4,5	PRN # 4 / 5	PRN # 5 / 2	PRN # 2 / 4
42	2,4,6	PRN # 2 / 4	PRN # 4 / 6	PRN # 6 / 2
43	2,4,7	PRN # 2 / 4	PRN # 4 / 7	PRN # 7 / 2
44	2,5,6	PRN # 6 / 5	PRN # 5 / 2	PRN # 2 / 6
45	2,5,7	PRN # 2 / 7	PRN # 7 / 5	PRN # 5 / 2
46	2,6,7	PRN # 6 / 7	PRN # 7 / 2	PRN # 2 / 6
47	3,4,5	PRN # 3 / 4	PRN # 4 / 5	PRN # 5 / 3
48	3,4,6	PRN # 6 / 3	PRN # 3 / 4	PRN # 4 / 6
49	3,4,7	PRN # 7 / 3	PRN # 3 / 4	PRN # 4 / 7
50	3,5,6	PRN # 3 / 5	PRN # 5 / 6	PRN # 6 / 3
51	3,5,7	PRN # 7 / 3	PRN # 3 / 5	PRN # 5 / 7
52	3,6,7	PRN # 3 / 7	PRN # 7 / 6	PRN # 6 / 3
53 (*)	4,5,6	PRN # 4 / 5	PRN # 5 / 6	PRN # 6 / 4
54	4,5,7	PRN # 7 / 4	PRN # 4 / 5	PRN # 5 / 7
55	4,6,7	PRN # 6 / 4	PRN # 4 / 7	PRN # 7 / 6
56 (*)	5,6,7	PRN # 5 / 6	PRN # 6 / 7	PRN # 7 / 5
57 (**)	5,6,7	PRN # 5 / 6	PRN # 7 / 5	PRN # 6 / 7
58 (*)	0,1,2	PRN # 0 / 1	PRN # 1 / 2	PRN # 2 / 0
59 (*)	0,1,2	PRN # 1 / 2	PRN # 2 / 0	PRN # 0 / 1
60 (**)	0,1,2	PRN # 1 / 0	PRN # 2 / 1	PRN # 0 / 2
61 (**)	0,1,2	PRN # 1 / 2	PRN # 0 / 1	PRN # 2 / 0
62 (**)	0,1,2	PRN # 2 / 0	PRN # 1 / 2	PRN # 0 / 1
63 (**)	0,1,2	PRN # 0 / 1	PRN # 2 / 0	PRN # 1 / 2
64 (*)	0,1,4	PRN # 4 / 1	PRN # 1 / 0	PRN # 0 / 4
65 (*)	0,1,4	PRN # 1 / 0	PRN # 0 / 4	PRN # 4 / 1
66 (*)	0,1,4	PRN # 0 / 4	PRN # 4 / 1	PRN # 1 / 0
67 (**)	1,4,5	PRN # 5 / 4	PRN # 1 / 5	PRN # 4 / 1
68 (**)	1,4,5	PRN # 1 / 5	PRN # 4 / 1	PRN # 5 / 4
69 (*)	1,5,6	PRN # 1 / 5	PRN # 5 / 6	PRN # 6 / 1
70 (**)	1,5,6	PRN # 1 / 6	PRN # 5 / 1	PRN # 6 / 5
71 (**)	4,5,6	PRN # 4 / 6	PRN # 5 / 4	PRN # 6 / 5
72 (**)	4,5,6	PRN # 5 / 4	PRN # 6 / 5	PRN # 4 / 6

A.2 Technical parameters and setups during the link test campaign

For the link test campaign, satellite operator SES provided transponder #3.001, which has an uplink frequency of 14.275 GHz and a downlink frequency of 11.475 GHz. The SATRE modems and SATRE modem parameters as in Table A.2 were used. While PTB and NPL set up a new TWSTFT roof station in the frame of the experiment, which were later assigned as PTB05 and NPL02, the other two institutes were using the antenna and outdoor equipment of a substitutional ground station: IT01 by INRIM, and OP02 by LNE-SYRTE.

TABLE A.2: SATRE modems used for the link test campaign, with the corresponding parameters.

Institute	Modem used	PRN code	TX frequency [Hz]
INRIM	S416	6	69,925,961
LNE-SYRTE	S321	1	70,037,317
NPL	S76	4	69,963,087
PTB	S410	5	70,074,116

A.3 Technical parameters and setups during the clock comparison campaign

Some changes in the setup and in the parameters were made for the clock comparison campaign. A TWCP experiment was implemented at PTB and LNE-SYRTE, using only a few kilohertz of the bandwidth. While the signal was split so one station could be used at LNE-SYRTE, a different station with a different antenna was used at PTB, named PTB04. Furthermore, SES could only provide a different transponder, #3.018, at the start of the campaign, resulting in different up- and downlink frequencies for the first few days. Table A.3 shows the different frequencies, with the center frequency of the transponder as the frequency used for TWSTFT, TWCP was assigned to a frequency at the edge of the transponder frequency band.

TABLE A.3: The up- and downlink frequencies during the two periods of the campaign for both techniques, TWSTFT and TWCP. TWSTFT uses the center frequency, since the full bandwidth is needed, whereas the TWCP uses a small frequency range at the lower edge of the transponder frequency band (17 MHz below the center frequency).

	frequencies 4th June – 9th June	frequencies 9th June – 29th June
Uplink TWSTFT	14.105 GHz	14.275 GHz
Downlink TWSTFT	12.605 GHz	11.475 GHz
Uplink TWCP	14.088 GHz	14.258 GHz
Downlink TWCP	12.588 GHz	11.458 GHz

Table A.4 provides the SATRE parameters at each institute, with a list of the received signals by RX channel. Since LNE-SYRTE could not participate during the first few days of the campaign, the configuration was slightly different during that time. The

parameters presented here are the ones for the second part of the campaign (21 d), where all institutes carried out the TWSTFT measurements.

TABLE A.4: SATRE modems used for the link test campaign, with the corresponding parameters.

Institute	Modem channel	Station received	PRN code (TX)	frequency (TX) [Hz]
INRIM	S416 TX		6	69,925,961
	S416 RX1	LNE-SYRTE		
	S416 RX2	NPL		
	S427 RX1	PTB		
LNE-SYRTE	S321 TX		0	70,037,317
	S321 RX1	LNE-SYRTE		
	S321 RX2	PTB		
	S503 RX1	NPL		
	S503 RX2	INRIM		
NPL	S76 TX		4	69,963,087
	S76 RX1	LNE-SYRTE		
	S76 RX2	PTB		
	S74 RX1	INRIM		
PTB	S410 TX		5	70,074,116
	S410 RX1	LNE-SYRTE		
	S410 RX2	NPL		
	S410 RX3	PTB		
	S280 RX1	LNE-SYRTE		
	S280 RX2	NPL		
	S280 RX3	INRIM		

TABLE A.5: GPS equipment used by the institutes. The receiver types are given together with the name of the receiver or station that is usually used by the institute for other GPS-related activities. The length of the antenna cable and the type of dieletric used plays a major role in the estimation of the temperature coefficient.

Institute	GPS receiver (station/rec. name)	ant. cable length [m]	ant. cable type (dielectric)
INRIM	Javad Legacy (INR3)	40	solid HDPE
LNE-SYRTE	Septentrio PolaRx4 (OPM8)	50	PE foam
NPL	GTR50 (NP11)	53	PE foam
PTB	Septentrio PolaRx4	30	PE foam

In addition to TWSTFT and TWCP, GPS stations were used to have an additional, independent comparison technique. Table A.5 shows the equipment of the stations. The antenna type is not listed, since the temperature coefficient taken for the uncertainty estimation was not antenna-specific.

Appendix B

Derivation of a tool for determining the statistical uncertainty

For a random variable Y an expectation value μ is defined

$$\mu = \mathbb{E}[Y], \tag{B.1}$$

with the corresponding variance σ^2:

$$\begin{aligned}\sigma^2 &= \mathbb{E}\left[(Y - \mathbb{E}[Y])^2\right] \\ &= \mathbb{E}\left[Y^2\right] - (\mathbb{E}[Y])^2 \\ &= \mathbb{E}\left[Y^2\right] - \mu^2.\end{aligned} \tag{B.2}$$

In case of a limited number n of measurements y_i of Y, the commonly used estimator for μ is the arithmetic mean $\bar{y}$:

$$\bar{y} = \frac{1}{n}\sum_{i=1}^{n} y_i. \tag{B.3}$$

Equally, an estimator s^2 for the variance σ^2 exists:

$$s_{y_i}^2 = \frac{1}{n-1}\sum_{i=1}^{n}(y_i - \bar{y})^2 \tag{B.4}$$

According to the *Guide to the Expression of Uncertainty in Measurement* (GUM) the statistical uncertainty of a measurement of y_i, also called type A uncertainty, is directly represented by the positive square root of a valid estimator for the variance of the mean, $\sigma_{\bar{y}}$ [53]. In the case where the n samples of the measurement are independent from each other, i.e. uncorrelated, the variance of the mean is defined as:

$$\sigma_{\bar{y}}^2 = \frac{\sigma^2}{n}, \tag{B.5}$$

with

$$s_{\bar{y}}^2 = \frac{s_{y_i}^2}{n} \tag{B.6}$$

representing such an estimator. Thus $s_{\bar{y}}$ directly resembles u_A. However, as already pointed out in the *GUM* and also by various other works, the estimator is biased in case of correlation between the n values of y_i [197, 198, 218], and thus not a suitable estimator to determine u_A. In [198] an estimate was made for the order of magnitude of this bias, and it is also pointed out that the arithmetic mean as in Eq. B.3 is an unbiased estimator in the presence of correlation, but only in case of equivalent observations y_i, meaning that the statistical properties do not depend on a shift in i. In the context considered here, this is the same property as being stationary. The following considerations only hold true for stationary processes, thus, it is assumed that the y_i underlie a stationary process.

The autocovariance ρ of y can be written as:

$$\begin{aligned}
\rho_l &= \frac{Cov[y_i, y_{i+l}]}{Var[y_i]} \\
&= \frac{\mathbb{E}[(y_i - \mu)(y_{i+l} - \mu)]}{\sigma^2} \\
&= \frac{\mathbb{E}[y_i y_{i+l}] - \mu^2}{\sigma^2} \\
&= \frac{C_l}{C_0}
\end{aligned} \tag{B.7}$$

with l being the lag. Dividing the covariance term C_l by the covariance at $l = 0$ (i.e. the variance) is a commonly used normalization, so ρ becomes 1 at lag 0. By using ρ, a correction factor γ for the variance of the mean $\sigma_{\bar{y}}^2$ can be derived [197, 219, 220]:

$$\sigma_{corr,\bar{y}}^2 = \gamma \frac{\sigma^2}{n} = \left(1 + 2 \sum_{l=1}^{n-1} \frac{(n-l)}{n} \rho_l\right) \frac{\sigma^2}{n}, \tag{B.8}$$

thus with

$$\gamma = 1 + 2 \sum_{l=1}^{n-1} \frac{(n-l)}{n} \rho_l. \tag{B.9}$$

In [198], γ is introduced via the ratio of n and a dimension called n_{eff}, which can be understood in most cases as an effective number of independent observations. However, in some cases this notation can become confusing, e.g. when $n_{\text{eff}} > n$. As can be seen from the equations above, in the case of all y_i being independent observations, ρ_l becomes zero for all $l > 0$, and the well-known equation Eq. B.5 is obtained. Also it becomes obvious that an overall positive sum in Eq. B.9, i.e. positive correlations, increases the variance and thus the estimator and the statistical uncertainty, whereas negative correlations lead to a decreasing. In the latter case, the relation $n_{\text{eff}} > n$ would be true.

Before a short overview over different autocovariances at different noise types will be given, the general expression of y_i will now be specified as a time series of relative frequency values on a constant time interval τ_0, with the relation of

$$y_i = \frac{x_{i+\Delta t/2} - x_{i-\Delta t/2}}{\Delta t} \tag{B.10}$$

to underlying phase data x_i on the same time interval τ_0, even if these phase data might not necessarily be available. Per default and if not clarified otherwise, $\Delta t = \tau_0$.

Fig. B.1 shows the autocovariances for different noise types: The noise was simulated and then a standard estimator of the autocovariance (see Section B.1 below) was used to calculate the autocorrelation function (ACF). The noise was simulated on the phase data x and the respective relative frequency data y was calculated from this by using Eq. B.10 and $\Delta t = 1\,\mathrm{s}$. It can be seen that only in case of white noise (white phase noise for x and white frequency noise for y) no correlations occur, $\rho_l = 1$ for $l = 0$, and $\rho_l = 0$ for all other l. In case of white phase and flicker phase noise, the ACF of y shows a negative value for $l = 1$ and approaches quickly zero for larger l (in theory, the autocovariance is zero for all $l > 1$). This means that γ would become smaller than 1 and the standard estimator for the variance of the mean would in fact overestimate the actual variance and thus the uncertainty. However, most other noise types have both positive and negative ρ_l, with the positive correlations dominating the lower lags.

However, in order to derive an estimator and thus the uncertainty from Eq. B.8 in case of real data, there are still two problems to be discussed:

(i) The variance can only be turned into an unbiased estimator in case the underlying correlations (and therefore all the noise processes and disturbances) are known and ρ is derived from these processes. In reality, this is not the case, instead, an estimator r is needed.

(ii) The derivation so far does not handle gaps on data.

Both will be covered in the next sections.

B.1 Finding an estimator for ρ

As seen in the previous section, most processes show with increasing l either negative ρ_l or reach a certain l where all ρ_l become zero afterwards or move around zero in a way that the overall sum over all ρ_l in this section of l would be zero.

In addition, estimators for ρ provide only limited knowledge for the coefficients with increasing l and can show an increasing noise and become erroneous. Thus, independently from the choice of the estimator r, a cutoff index l_{cut} should be determined to disregard all coefficients of r above.

In [199], an overview over the sources of biases in several estimators is given and the biases are calculated for different process models simulated using the Monte-Carlo method. It turned out that the actual choice of the estimator is not as crucial as the choice of the cutoff index l_{cut}. For this, there are very simplified approaches for adapting a "rule of thumb" of the literature [221], where it is stated that a sufficient good estimate for the autocovariance can be made for $l_{\mathrm{cut}} = n/4$. But also more

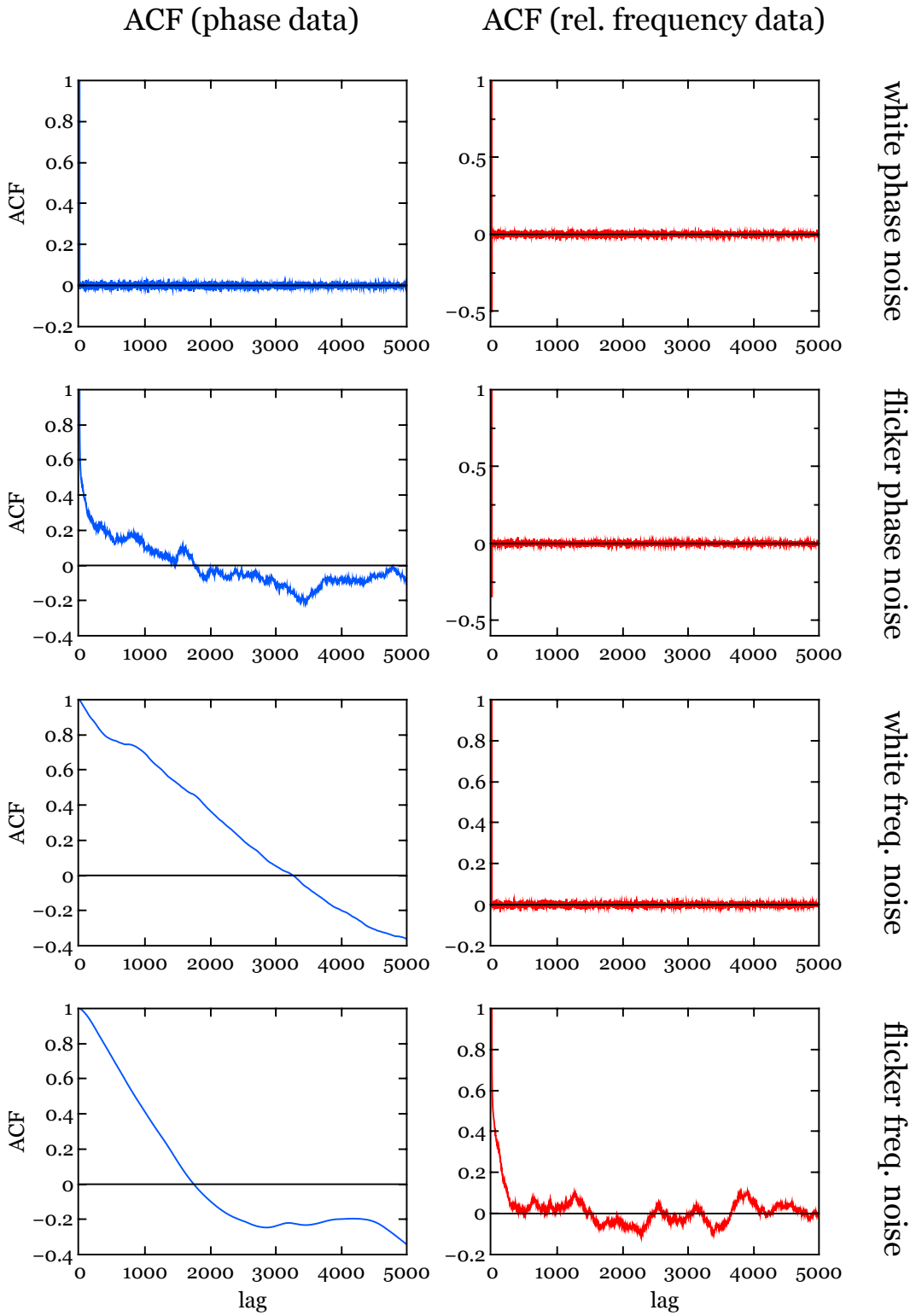

FIGURE B.1: Autocorrelation functions (ACF) as estimates of the autocovariance for different noise types. The noise was simulated and the ACF calculated with the standard estimator for ρ (see below in Section B.1). The left column (curves in blue) shows the ACF of the phase data x, and the right column (curves in red) for the relative frequency data y, converted from the phase data by using Eq. B.10 and $\Delta t = 1\,\mathrm{s}$.

sophisticated calculations based on the actual measurements y_i were applied [197]. The approach adapted for this work is the First Transit through Zero (FTZ) criterion, where l_{cut} can be calculated, but can also be subjectively chosen based on what is known about the underlying processes in order to discriminate between the significant non-zero coefficients of r_l and the noise at higher l. Since this approach might disregard "true" negative correlations as in Fig. B.1, the sum over the elements of r_l might be larger than the one over the actual unbiased ρ_l which leads in a consequence to a positively biased estimator for the variance of the mean.

Based on the considerations in previous, already mentioned works [197, 199], the standard estimator r which is widely used in most works and software to calculate the ACF is used as base in this work, too:

$$r_l = \frac{\sum_{i=1}^{n-l}(y_i - \bar{y})(y_{i+l} - \bar{y})}{\sum_{i=1}^{n}(y_i - \bar{y})^2} = \frac{R_l}{R_0} \tag{B.11}$$

for all coefficients from $l = 1 \dots n-1$, with R_l and R_0 as estimators for C_l and C_0, respectively.

Thus, the respective estimator for the variance of the mean is

$$s^2_{corr,\bar{y}} = \left(1 + 2\sum_{l=1}^{n-1}\frac{(n-l)}{n} r_l\right)\frac{s^2}{n} \tag{B.12}$$

This estimator is not unbiased, but only bias-reduced with respect to Eq. B.6. Apart from the residual bias due to r_l, other features introduce a bias that are discussed below in Section B.3.

B.2 Accounting for gaps on the data

In case of gaps on the data, the calculations and considerations above might become erroneous, as information might be lost and not taken into account correctly. This was already widely addressed within the field for the calculation of the Allan Deviation (see Chapter 2.1). A simple example is the processing of relative frequency data with an underlying white phase noise, as seen in Fig. B.1. Taking only every second value into consideration, the correlation vanishes and the process of the residual y_i becomes white frequency noise. Similarly, any short-range correlation can remain undetected or become less dominant when gaps on a regular time grid are introduced into the data. When data with irregular gaps are treated as if there were no gaps, i.e. "stitching together" blocks of measurement, correlation estimates become erroneous.

In order to take gaps into account, an approach similar to the calculation of the modified Allan Deviation as used in this work was taken. For that, the more general case of weights is considered.

Of course, this approach cannot restore missing information as in the example above where white phase noise on frequency data appears as white frequency noise if every second point is missing. In reality, however, it is much more likely to have irregular

gaps, and it is important to find a way to assign the data to the correct spacing without adding false information

Weights were already introduced for an estimator of the variance of the mean in presence of correlations in [197]. This does not only allow for a treatment of gaps - by attributing weights w_i of zero to indices i of missing data in y_i - but also for a consideration of cases where indeed non-uniform weighting of data is useful. The introduced weights w_i are normalized:

$$\sum_{i=1}^{n} w_i = 1, \tag{B.13}$$

so the quantities considered above become:

$$\bar{y} = \sum_{i=1}^{n} w_i \cdot y_i \tag{B.14}$$

for the mean, and

$$s_{y_i}^2 = \sum_{i=1}^{n} w_i (y_i - \bar{y})^2 \tag{B.15}$$

for the estimator of the population variance. A suitable estimator for C_l is

$$R_l = \frac{\sum_{i=1}^{n-l} \sqrt{w_i w_{i+l}} (y_i - \bar{y})(y_{i+l} - \bar{y})}{\sum_{i=1}^{n-l} \sqrt{w_i w_{i+l}}}, \tag{B.16}$$

which becomes $s_{y_i}^2$ for $l = 0$. This estimator is, similar to r in Eq. B.11, still biased. To the best of the knowledge of the author, an unbiased estimator for ρ does not exist.

The variance of the mean becomes:

$$\begin{aligned} \sigma_{\bar{y}}^2 &= \sigma^2 \left(\sum_{i=1}^{n} w_i^2 + 2 \sum_{l=1}^{n-1} \rho_l \sum_{j=1}^{n-i} w_j w_{j+i} \right) \\ &= C_0 \sum_{i=1}^{n} w_i^2 + 2 \sum_{l=1}^{n-1} C_l \sum_{j=1}^{n-l} w_j w_{j+l}, \end{aligned} \tag{B.17}$$

which results in the estimator for the variance of the mean:

$$s_{\bar{y}}^2 = R_0 \sum_{i=1}^{n} w_i^2 + 2 \sum_{l=1}^{l_{\text{cut}}} R_l \sum_{j=1}^{n-l} w_j w_{j+l} \tag{B.18}$$

In case the data is uncorrelated, R_l becomes zero for all lags l and only the term on the left with R_0 is left. This term corresponds to Eq. B.6 for the weighted mean. So, as above in the case of no weights, it can be seen that in case of overall positive correlations the uncertainty is larger than in case of no correlations.

Eq. B.17 can be derived as follows[1]:

At first, $\bar{y}^2$ can be written down as:

$$\begin{aligned}\bar{y}^2 &= \sum_{i=1}^{n}\sum_{j=1}^{n} w_i w_j y_i y_j \\ &= \sum_{i=1}^{n} w_i^2 y_i^2 + 2\sum_{i=1}^{n-1}\sum_{j=1}^{n-i} w_j w_{i+j} y_j y_{i+j}\end{aligned} \tag{B.19}$$

The expectation value of this term is:

$$\begin{aligned}\mathbb{E}\left[\bar{y}^2\right] &= \sum_{i=1}^{n} w_i^2 \mathbb{E}\left[y_i^2\right] + 2\sum_{i=1}^{n-1}\sum_{j=1}^{n-i} w_j w_{i+j}\mathbb{E}\left[y_j y_{i+j}\right] \\ &= \sum_{i=1}^{n} w_i^2 \left(C_0 + \mu^2\right) \\ &\quad + 2\sum_{i=1}^{n-1}\sum_{j=1}^{n-i} w_j w_{i+j}\left(C_i + \mu^2\right) \\ &= \sum_{i=1}^{n} w_i^2 C_0 + 2\sum_{i=1}^{n-1} C_i \sum_{j=1}^{n-i} w_j w_{i+j} \\ &\quad + \left(\sum_{i=1}^{n} w_i^2 + 2\sum_{i=1}^{n-1}\sum_{j=1}^{n-i} w_j w_{i+j}\right)\mu^2 \\ &= \sum_{i=1}^{n} w_i^2 C_0 + 2\sum_{i=1}^{n-1} C_i \sum_{j=1}^{n-i} w_j w_{i+j} \\ &\quad + \left(\sum_{i=1}^{n}\sum_{j=1}^{n} w_i w_j\right)\mu^2 \\ &= \sum_{i=1}^{n} w_i^2 C_0 + 2\sum_{i=1}^{n-1} C_i \sum_{j=1}^{n-i} w_j w_{i+j} + \mu^2.\end{aligned} \tag{B.20}$$

Thus, the variance of the weighted mean is:

$$\begin{aligned}\sigma_{\bar{y}}^2 &= \mathbb{E}\left[\bar{y}^2\right] - \mu^2 \\ &= \sum_{i=1}^{n} w_i^2 C_0 + 2\sum_{i=1}^{n-1} C_i \sum_{j=1}^{n-i} w_j w_{i+j}\end{aligned} \tag{B.21}$$

[1]This derivation was developed by E. Benkler. In contrast to Eq. B.8, the variance of the weighted mean for autocorrelated samples was, to the best knowledge of the author, never derived in the literature before.

B.3 Comments on biases

The estimator derived for this work is still biased for various reasons. One source of bias was already mentioned as the fact that a bias can be introduced based on the fact that a cutoff is made in r, although the use of a cutoff lag can reduce erroneous calculations within r. Also, to the best knowledge of the author, no unbiased estimator for ρ exists so far.

It should be also noted that, when applying the square root to an unbiased estimator, i.e. in order to transform the estimator of the variance into the deviation, the result is not unbiased anymore, since a square root is a non-linear function. This bias concerns also the use of the standard estimators that are unbiased in case of white noise (Eqs. B.4 and B.6). It is considered to be small enough that it is usually not taken into account, so the square root of any unbiased estimator of a variance can be taken as estimate for the deviation, and thus for the statistical uncertainty.

Another consideration is the non-multiplicativity of the expectation value: when using Eqs. B.8 and B.17 and inserting the estimators for both σ and ρ, the expectation value of the resulting estimator is not the product of the expectation values of the single estimators. Since both estimators are based on the same set of measurements y_i, they are not independent from each other. This was found to be not taken into consideration in most literature when a bias-reduced estimator for the variance of the mean in presence of correlations is derived. Because of the lack of discussion of this problem in the literature and the difficulty to estimate the order of magnitude of the resulting bias, it was considered to be negligible for this work, but studies on this subject might be interesting for the future.

A third point was mentioned by [198], where in addition to the variance of the mean as in Eq. B.8 and its estimator, an unbiased estimator for the population variance was derived:

$$s^2_{corr,y_i} = \frac{\sum\limits_{i=1}^{n} (y_i - \bar{y})^2}{n - \gamma} = s^2_{bias,y_i} \frac{n-1}{n-\gamma} \tag{B.22}$$

with s^2_{bias,y_i} as the biased estimator for the population variance as presented in Eq. B.4. Taking this unbiased estimator and inserting it into Eq. B.12 gives:

$$s^2_{corr,\bar{y}} = \gamma \frac{s^2_{corr,y_i}}{n} = \gamma \frac{n-1}{n-\gamma} s^2_{bias,\bar{y}} \tag{B.23}$$

Converting this to the case with weights, Eq. B.18 becomes:

$$s^2_{\bar{y}} = \frac{\sum_{i=1}^{n} w_i (y_i - \bar{y})^2}{\frac{1}{\sum_i^n w_i^2 + 2\sum_{l=1}^{l_{\mathrm{cut}}} r_l (\sum_{j=l}^{n-l} w_j w_{j+l})} - 1} \tag{B.24}$$

with

$$r_l = \frac{R_l}{R_0} \tag{B.25}$$

The difference between both is thus that in the consideration of the previous section R_0 was taken directly as estimator for σ^2, while in this case here a bias-reduced estimator was taken for σ^2. However, since this biased-reduced estimator depends on r and thus on R_0, it can never be completely substituted.

Calculations for $s_{\bar{y}}^2$ based on the data used in this work found a difference between Eq. B.18 and Eq. B.24 in the range of $1 \times 10^{-18} \ldots 2 \times 10^{-18}$ in all cases. It is thus negligible.

B.4 Discussion of the correlations on the data used in this work

In order to find a suitable value for l_{cut}, both the initial data sets y_{link} (converted from x_{link}), y_1 and y_2 as in Eq. 6.1 of Chapter 6.2.4 as well as the final processed series of relative frequency $y(\text{OC}_1 - \text{OC}_2)(t)$ (OC = Optical Clock) were analyzed for significant correlations. Fig. B.2 shows the calculated ACF for some selected data: (a) depicts the ACF of $y_{\text{Sr(PTB)}}$. For the calculation, an interval of several days with only few interruptions of only short duration (less than 1 h) was chosen. It can be seen that the first coefficients are negative, similar to flicker phase noise (see Fig. B.1), which corresponds to the dominant noise of the hydrogen maser (HM). (b) shows an enlargement of the first lags, and some weak positive correlations are visible that approach to zero for lags larger than 1000. This behavior was only observed for the y_1 and y_2 in case of PTB. In case of NPL, only the flicker phase noise contributions can be observed, while for LNE-SYRTE, due to the cryogenic sapphire oscillator, the ACF reflects mostly white frequency noise. The link data is dominated by the negative coefficients as in case of white phase noise, as expected. Both (c) and (d) show the ACF of the final processed $y(\text{Sr(PTB)} - \text{Yb(NPL)})(t)$, with (d) being again an enlargement for small lags. A combination of white and flicker phase noise is still dominant on the data according to the negative coefficients of r at the first lags. In addition, some negative correlations appear up to $l = 50$. The positive correlations observed in (b) are not visible. However, since this correlation is observed on the initial data and in order to not cut away correlations that can not be observed manually in the graphs but might still be on the data, $l_{\text{cut}} = 4000$ was chosen, even for the link LNE-SYRTE – NPL. The calculated ACFs show furthermore that up to this lag, no erroneous negative correlations would falsely decrease the uncertainty. This noise behavior is in agreement with the fact that the bias-reduced estimator results in a smaller uncertainty than the standard biased estimator.

It also becomes apparent that a simple calculation of l_{cut} with the FTZ criterion would not work: Even when taking into account the negative coefficients at small lags, the noise on the ACF would result in an immediate cutoff. Hence, when using this estimator to determine the uncertainty and thus using the ACF, a manual examination of the ACF is crucial.

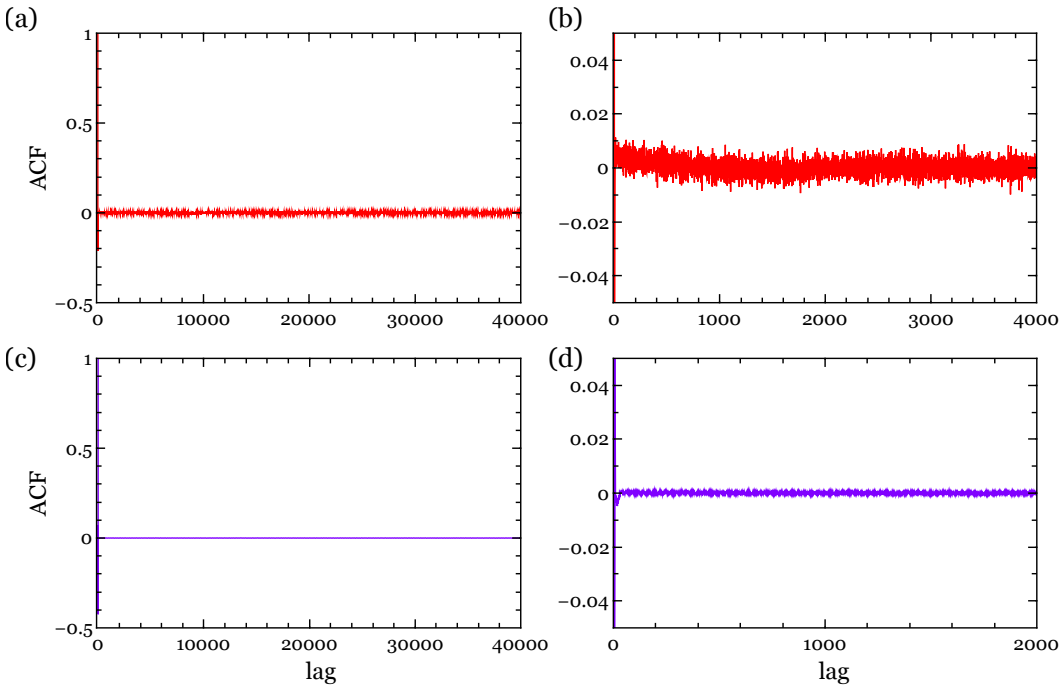

FIGURE B.2: ACFs of different time series used to calculate the mean relative frequency difference between the Sr clock at PTB and the Yb clock at NPL. (a) and (b) show the ACF of the difference of Sr and the hydrogen maser (HM) at PTB, with (b) being the enlargement for small lags. The data is dominated by the flicker phase noise of the HM. In addition, some positive correlations can be observed for $l < 1000$. (c) and (d) show the ACF of $y(\mathrm{Sr(PTB)} - \mathrm{Yb(NPL)})(t)$ after the data processing described in Chapter 6.2.4. Again, (d) is an enlargement for small lags. Negative coefficients dominate for the first few lags, while the positive correlation observed in (b) do not appear.

Bibliography

[1] *Comptes Rendus de la 13e CGPM (1967)*. 1969.

[2] J. Terrien. "News from the International Bureau of Weights and Measures". In: *Metrologia* 4.1 (1968), pp. 41–45.

[3] R.B. Langley, P.J.G. Teunissen, and O. Montenbruck. "Springer Handbook of Global Navigation Satellite Systems". In: ed. by P.J.G. Teunissen and O. Montenbruck. Springer, 2017. Chap. Introduction to GNSS, p. 9.

[4] *Galileo Initial Open Service Quarterly Performance Report Q1*. URL: https://www.gsc-europa.eu/sites/default/files/sites/all/files/Galileo-IS-OS-Quarterly-Performance_Report-Q1-2017.pdf.

[5] URL: http://www.sdcm.ru/smglo/st_glo?version=eng&repdate&site=extern.

[6] Y. Xu et al. "The comparison on the positioning performance between BeiDou and GPS". In: *ION GNSS 2013, Nashville, Tennessee, September 16 - 20, 2013*. 2013, pp. 369–382.

[7] J. C. Hafele and R E. Keating. "Around-the-World Atomic Clocks: Predicted Relativistic Time Gains". In: *Science* 177.4044 (1972), pp. 166–168. ISSN: 0036-8075.

[8] B. Altschul et al. "Quantum tests of the Einstein Equivalence Principle with the STE–QUEST space mission". In: *Advances in Space Research* 55.1 (2015), pp. 501–524. ISSN: 0273-1177.

[9] M. Fischer et al. "New Limits on the Drift of Fundamental Constants from Laboratory Measurements". In: *Phys. Rev. Lett.* 92 (23 2004), p. 230802.

[10] T. Rosenband et al. "Frequency Ratio of Al^+ and Hg^+ Single-Ion Optical Clocks; Metrology at the 17th Decimal Place". In: *Science* 319.5871 (2008), pp. 1808–1812. ISSN: 0036-8075.

[11] N. Huntemann et al. "Improved Limit on a Temporal Variation of m_p/m_e from Comparisons of Yb^+ and Cs Atomic Clocks". In: *Phys. Rev. Lett.* 113 (21 2014), p. 210802.

[12] L. Cacciapuoti and C. Salomon. "Space clocks and fundamental tests: The ACES experiment". In: *The European Physical Journal-Special Topics* 172.1 (2009), pp. 57–68.

[13] M. Vermeer. "Chronometric Levelling". In: *Geodeettinen Laitos, Reports of the Finnish Geodetic Institute* 83 (1983), pp. 1–7.

[14] Delva P. and Lodewyck J. "Atomic clocks: new prospects in metrology and geodesy". In: *Acta Futura* 7 (2013), pp. 67–78.

[15] T. Mehlstäubler et al. "Atomic Clocks for Geodesy". In: *Rep. Prog. Phys.* 81 (2018), p. 064401.

[16] A. D. Ludlow et al. "Optical atomic clocks". In: *Rev. Mod. Phys.* 87 (2 2015), pp. 637–701.

[17] St. Falke et al. "A strontium lattice clock with $3\times\ 10^{-17}$ inaccuracy and its frequency". In: *New Journal of Physics* 16.7 (2014), p. 073023.

[18] N. Huntemann et al. "High-Accuracy Optical Clock Based on the Octupole Transition in $^{171}Yb^{+}$". In: *Phys. Rev. Lett.* 108 (9 2012), p. 090801.
[19] C. W. Chou et al. "Frequency Comparison of Two High-Accuracy Al^{+} Optical Clocks". In: *Phys. Rev. Lett.* 104 (7 2010), p. 070802.
[20] K. Matsubara et al. "Direct comparison of a Ca^{+} single-ion clock against a Sr lattice clock to verify the absolute frequency measurement". In: *Optics express* 20.20 (2012), pp. 22034–22041.
[21] S. Weyers et al. "Distributed cavity phase frequency shifts of the caesium fountain PTB-CSF2". In: *Metrologia* 49.1 (2011), p. 82.
[22] S. Weyers et al. "Advances in the accuracy, stability, and reliability of the PTB primary fountain clocks". In: *Metrologia* 55.6 (2018), pp. 789–805.
[23] R. Li, K. Gibble, and K. Szymaniec. "Improved accuracy of the NPL-CsF2 primary frequency standard: evaluation of distributed cavity phase and microwave lensing frequency shifts". In: *Metrologia* 48.5 (2011), p. 283.
[24] F. Levi et al. "Accuracy evaluation of ITCsF2: a nitrogen cooled caesium fountain". In: *Metrologia* 51.3 (2014), p. 270.
[25] J. Guéna et al. "Progress in atomic fountains at LNE-SYRTE". In: *IEEE transactions on ultrasonics, ferroelectrics, and frequency control* 59.3 (2012), pp. 391–409.
[26] T.P. Heavner et al. "NIST-F1: recent improvements and accuracy evaluations". In: *Metrologia* 42.5 (2005), p. 411.
[27] M. Kumagai et al. "Evaluation of caesium atomic fountain NICT-CsF1". In: *Metrologia* 45.2 (2008), pp. 139–148.
[28] P. Gill. "When should we change the definition of the second?" In: *Philosophical Transactions of the Royal Society of London A: Mathematical, Physical and Engineering Sciences* 369.1953 (2011), pp. 4109–4130.
[29] F. Riehle. "Towards a redefinition of the second based on optical atomic clocks". In: *Comptes Rendus Physique* 16.5 (2015), pp. 506–515.
[30] P. Gill. "Is the time right for a redefinition of the second by optical atomic clocks?" In: *Journal of Physics: Conference Series*. Vol. 723. 1. IOP Publishing. 2016, p. 012053.
[31] J. Lodewyck. "On a definition of the SI second with a set of optical clock transitions". In: *Metrologia* 56.5 (2019), p. 055009.
[32] H.S. Margolis et al. "International timescales with optical clocks (ITOC)". In: *European Frequency and Time Forum & International Frequency Control Symposium (EFTF/IFC), 2013 Joint*. IEEE. 2013, pp. 908–911.
[33] G. Mura et al. "A transportable optical lattice clock using ^{171}Yb". In: *2013 Joint European Frequency and Time Forum International Frequency Control Symposium (EFTF/IFC)*. 2013, pp. 376–378.
[34] N. Poli et al. "A transportable strontium optical lattice clock". In: *Applied Physics B* 117.4 (2014), pp. 1107–1116.
[35] S. Vogt et al. "A transportable optical lattice clock". In: *Journal of Physics: Conference Series*. Vol. 723. 1. IOP Publishing. 2016, p. 012020.
[36] N. R. Newbury, P. A. Williams, and W. C. Swann. "Coherent transfer of an optical carrier over 251 km". In: *Opt. Lett.* 32.21 (2007), pp. 3056–3058.
[37] O. Terra, G. Grosche, and H. Schnatz. "Brillouin amplification in phase coherent transfer of optical frequencies over 480 km fiber". In: *Optics express* 18.15 (2010), pp. 16102–16111.
[38] K. Predehl et al. "A 920-kilometer optical fiber link for frequency metrology at the 19th decimal place". In: *Science* 336.6080 (2012), pp. 441–444.

[39] S.M.F. Raupach, Andreas Koczwara, and Gesine Grosche. "Brillouin amplification supports 1×10^{-20} uncertainty in optical frequency transfer over 1400 km of underground fiber". In: *Physical Review A* 92.2 (2015), p. 021801.

[40] C. Lisdat et al. "A clock network for geodesy and fundamental science". In: *Nature communications* 7 (2016).

[41] P. Delva et al. "Test of Special Relativity Using a Fiber Network of Optical Clocks". In: *Phys. Rev. Lett.* 118 (22 2017), p. 221102.

[42] B.M. Roberts et al. "Search for transient variations of the fine structure constant and dark matter using fiber-linked optical atomic clocks". In: *arXiv preprint arXiv:1907.02661* (2019).

[43] P. Defraigne, N. Guyennon, and C. Bruyninx. "GPS time and frequency transfer: PPP and phase-only analysis". In: *International Journal of Navigation and Observation* 2008 (2008).

[44] G. Petit and Z. Jiang. "Precise Point Positioning for TAI Computation". In: *International Journal of Navigation and Observation* 2008 (2008).

[45] S. Droste et al. "Characterization of a 450 km baseline GPS carrier-phase link using an optical fiber link". In: *New Journal of Physics* 17.8 (2015), p. 083044.

[46] G. Petit et al. "1×10^{-16} frequency transfer by GPS PPP with integer ambiguity resolution". In: *Metrologia* 52.2 (2015), p. 301.

[47] D. Piester et al. "On measurement noise in the European TWSTFT network". In: *IEEE transactions on ultrasonics, ferroelectrics, and frequency control* 55.9 (2008), pp. 1906–1912.

[48] T. Parker et al. "First comparison of remote cesium fountains". In: *Frequency Control Symposium and PDA Exhibition, 2001. Proceedings of the 2001 IEEE International*. IEEE. 2001, pp. 63–68.

[49] A. Bauch et al. "Comparison between frequency standards in Europe and the USA at the 10^{-15} uncertainty level". In: *Metrologia* 43.1 (2005), p. 109.

[50] M. Fujieda et al. "First comparison of primary frequency standards between Europe and Asia". In: *2007 IEEE International Frequency Control Symposium Joint with the 21st European Frequency and Time Forum*. IEEE. 2007, pp. 937–941.

[51] A. Zhang et al. "Comparison of Caesium fountain clocks in Europe and Asia". In: *European Frequency and Time Forum (EFTF), 2014*. IEEE. 2014, pp. 447–450.

[52] F. Riedel et al. "Direct comparisons of European primary and secondary frequency standards via satellite techniques". In: *Metrologia* 57.4 (2020), p. 045005.

[53] *Guide to the Expression of Uncertainty in Measurement*. ISO/TAG 4. Published by ISO, 1993 (corrected and reprinted, 1995) in the name of the BIPM, IEC, IFCC, ISO, UPAC, IUPAP and OIML. ISBN number: 92-67-10188-9, 1995. 1995.

[54] D. W. Allan. "Statistics of atomic frequency standards". In: *Proceedings of the IEEE* 54.2 (1966), pp. 221–230.

[55] W. J. Riley. *Handbook of frequency stability analysis*. US Department of Commerce, National Institute of Standards and Technology, 2008.

[56] D. W. Allan and J. A. Barnes. "A modified Allan variance with increased oscillator characterization ability". In: *Proceedings of the 35th Annual Frequency Control Symposium*. Vol. 5. 1981, pp. 470–475.

[57] R.A. Baugh. "Frequency modulation analysis with the Hadamard variance". In: *25th Annual Symposium on Frequency Control*. IEEE. 1971, pp. 222–225.

[58] D. W. Allan, M. A. Weiss, and J. L. Jespersen. "A frequency-domain view of time-domain characterization of clocks and time and frequency distribution systems". In: *Proceedings of the 45th Annual Symposium on Frequency Control 1991*. 1991, pp. 667–678.

[59] C. Hackman and T. E. Parker. "Noise analysis of unevenly spaced time series data". In: *Metrologia* 33.5 (1996), p. 457.

[60] P. Tavella and M. Leonardi. "Statistical Problems in the Analysis of Unequally Spaced Data". In: *Proceedings of the 30th Annual Precise Time and Time Interval (PTTI) Systems and Applications Meeting*. 1998.

[61] I. Sesia and P. Tavella. "Estimating the Allan variance in the presence of long periods of missing data and outliers". In: *Metrologia* 45.6 (2008), S134–S142.

[62] E. Benkler, C. Lisdat, and U. Sterr. "On the relation between uncertainties of weighted frequency averages and the various types of Allan deviations". In: *Metrologia* 52.4 (2015), p. 565.

[63] L. Essen, J. V. L. Parry, and Gordon Brims Black Mcivor Sutherland. "The caesium resonator as a standard of frequency and time". In: *Philosophical Transactions of the Royal Society of London. Series A, Mathematical and Physical Sciences* 250.973 (1957), pp. 45–69.

[64] A. Bauch et al. "CS2: The PTB's new primary clock". In: *IEEE Transactions on Instrumentation and Measurement* IM-36.2 (1987), pp. 613–616. ISSN: 1557-9662.

[65] J. L. Hall, M. Zhu, and P. Buch. "Prospects for using laser-prepared atomic fountains for optical frequency standards applications". In: *J. Opt. Soc. Am. B* 6.11 (1989), pp. 2194–2205.

[66] M. A. Kasevich et al. "Rf Spectroscopy in an Atomic Fountain". In: *Phys. Rev. Lett.* 63 (6 1989), pp. 612–615.

[67] A. Clairon et al. "Preliminary accuracy evaluation of a cesium fountain frequency standard". In: *Proceedings of the 5th Symposium on Frequency Standards and Metrology*. Ed. by J.C. Bergquist. 1996, pp. 49–59.

[68] S. R. Jefferts et al. "Preliminary accuracy evaluation of a cesium fountain primary frequency standard at NIST". In: *Proceedings of the 1999 Joint Meeting of the European Frequency and Time Forum and the IEEE International Frequency Control Symposium (Cat. No.99CH36313)*. Vol. 1. 1999, 12–15 vol.1.

[69] K. Szymaniec et al. "Evaluation of the primary frequency standard NPL-CsF1". In: *Metrologia* 42.1 (2005), pp. 49–57.

[70] C. Vian et al. "BNM-SYRTE fountains: recent results". In: *IEEE Transactions on Instrumentation and Measurement* 54.2 (2005), pp. 833–836. ISSN: 1557-9662.

[71] BIPM. *Practical realizations of the definitions of some important units - recommended values for standard frequency*. URL: `https://www.bipm.org/en/publications/mises-en-pratique/standard-frequencies.html`.

[72] S. Peil et al. "Evaluation of long term performance of continuously running atomic fountains". In: *Metrologia* 51.3 (2014), pp. 263–269.

[73] J. Guéna et al. "Demonstration of a dual alkali Rb/Cs fountain clock". In: *IEEE Transactions on Ultrasonics, Ferroelectrics, and Frequency Control* 57.3 (2010), pp. 647–653. ISSN: 1525-8955.

[74] R.M. Godun et al. "Frequency ratio of two optical clock transitions in $^{171}Yb^{+}$ and constraints on the time variation of fundamental constants". In: *Physical review letters* 113.21 (2014), p. 210801.

[75] Chr. Tamm et al. "Cs-based optical frequency measurement using cross-linked optical and microwave oscillators". In: *Physical Review A* 89.2 (2014), p. 023820.

[76] N. Huntemann et al. "Single-ion atomic clock with 3×10^{-18} systematic uncertainty". In: *Physical review letters* 116.6 (2016), p. 063001.

[77] A. A. Madej et al. "$^{88}Sr^{+}$ 445-THz Single-Ion Reference at the 10^{-17} Level via Control and Cancellation of Systematic Uncertainties and Its Measurement against the SI Second". In: *Physical review letters* 109.20 (2012), p. 203002.

[78] G. P. Barwood et al. "Agreement between two $^{88}Sr^{+}$ optical clocks to 4 parts in 10^{17}". In: *Phys. Rev. A* 89 (5 2014), p. 050501.
[79] K. Matsubara et al. "Frequency Measurement of the Optical Clock Transition of $^{40}Ca^{+}$ Ions with an Uncertainty of 10^{-14} Level". In: *Applied Physics Express* 1 (2008), p. 067011.
[80] M. Chwalla et al. "Absolute Frequency Measurement of the $^{40}Ca^{+}$ $4s^2S_{1/2}$ – $3d^2D_{5/2}$ Clock Transition". In: *Physical review letters* 102.2 (2009), p. 023002.
[81] Y. Huang et al. "Frequency Comparison of Two $^{40}Ca^{+}$ Optical Clocks with an Uncertainty at the 10^{-17} Level". In: *Physical review letters* 116.1 (2016), p. 013001.
[82] T. Rosenband et al. "Observation of the $^1S_0 \rightarrow ^3 P_0$ Clock Transition in $^{27}Al^{+}$". In: *Phys. Rev. Lett.* 98 (22 2007), p. 220801.
[83] S. M. Brewer et al. "$^{27}Al^{+}$ Quantum-Logic Clock with a Systematic Uncertainty below 10^{-18}". In: *Phys. Rev. Lett.* 123 (3 2019), p. 033201.
[84] S. A. Diddams et al. "An Optical Clock Based on a Single Trapped $^{199}Hg^{+}$ Ion". In: *Science* 293.5531 (2001), pp. 825–828. ISSN: 0036-8075.
[85] L. De Sarlo et al. "A mercury optical lattice clock at LNE-SYRTE". In: *Journal of Physics: Conference Series* 723 (2016), p. 012017.
[86] X. H. Fu et al. "Recent progress of neutral mercury lattice clock in SIOM". In: *2017 Joint Conference of the European Frequency and Time Forum and IEEE International Frequency Control Symposium (EFTF/IFCS)*. 2017, pp. 439–443.
[87] N. D. Lemke et al. "Spin-1/2 Optical Lattice Clock". In: *Phys. Rev. Lett.* 103 (6 2009), p. 063001.
[88] Takuya K. et al. "One-Dimensional Optical Lattice Clock with a Fermionic ^{171}Yb Isotope". In: *Applied Physics Express* 2 (2009), p. 072501.
[89] Ch. Y. Park et al. "Absolute frequency measurement of $^1S_0(F = 1/2) - ^3P_0(F = 1/2)$ transition of ^{171}Yb atoms in a one-dimensional optical lattice at KRISS". In: *Metrologia* 50.2 (2013), pp. 119–128.
[90] M. Pizzocaro et al. "Ytterbium optical lattice clock at INRIM". In: *Frequency Control Symposium & the European Frequency and Time Forum (FCS), 2015 Joint Conference of the IEEE International*. IEEE. 2015, pp. 300–303.
[91] Ryoichi Higashi & Hidetoshi Katori M. Takamoto Feng-Lei Hong. "An optical lattice clock". In: *Nature* 435 (2005), pp. 321–324.
[92] St. Falke et al. "The ^{87}Sr optical frequency standard at PTB". In: *Metrologia* 48.5 (2011), pp. 399–407.
[93] B.J. Bloom et al. "An optical lattice clock with accuracy and stability at the 10^{-18} level". In: *Nature* 506.7486 (2014), pp. 71–75.
[94] I. Ushijima et al. "Cryogenic optical lattice clocks". In: *Nature Photonics* (2015).
[95] J. Lodewyck et al. "Optical to microwave clock frequency ratios with a nearly continuous strontium optical lattice clock". In: *Metrologia* 53.4 (2016), p. 1123.
[96] X. Baillard et al. "Accuracy evaluation of an optical lattice clock with bosonic atoms". In: *Opt. Lett.* 32.13 (2007), pp. 1812–1814.
[97] T. Akatsuka, M. Takamoto, and H. Katori. "Optical lattice clocks with non-interacting bosons and fermions". In: *Nature Physics* (2008).
[98] J. J. McFerran et al. "Neutral Atom Frequency Reference in the Deep Ultraviolet with Fractional Uncertainty $= 5.7 \times 10^{-15}$". In: *Phys. Rev. Lett.* 108 (18 2012), p. 183004.
[99] H. M. Goldenberg, D. Kleppner, and N. F. Ramsey. "Atomic Hydrogen Maser". In: *Phys. Rev. Lett.* 5 (8 1960), pp. 361–362.
[100] A. Bauch et al. "Generation of UTC(PTB) as a fountain-clock based time scale". In: *Metrologia* 49.3 (2012), p. 180.

[101] G.D. Rovera et al. "UTC (OP) based on LNE-SYRTE atomic fountain primary frequency standards". In: *Metrologia* 53.3 (2016), S81.

[102] Th. Udem et al. "Accuracy of optical frequency comb generators and optical frequency interval divider chains". In: *Opt. Lett.* 23.17 (1998), pp. 1387–1389.

[103] R. Le Targat et al. "Experimental realization of an optical second with strontium lattice clocks". In: *Nature communications* 4 (2013).

[104] M. Pizzocaro et al. "Absolute frequency measurement of the $^1S_0-^3P_0$ transition of ^{171}Yb". In: *Metrologia* 54.1 (2017), pp. 102–112.

[105] N. Nemitz et al. "Frequency ratio of Yb and Sr clocks with 5×10^{-17} uncertainty at 150 seconds averaging time". In: *Nature Photonics* 10.4 (2016), p. 258.

[106] M. Takamoto et al. "Frequency ratios of Sr, Yb, and Hg based optical lattice clocks and their applications". In: *Comptes Rendus Physique* 16.5 (2015), pp. 489–498.

[107] N. Ohmae et al. "Direct measurement of the frequency ratio for Hg and Yb optical lattice clocks and closure of the Hg/Yb/Sr loop". In: *Opt. Express* 28.10 (2020), pp. 15112–15121.

[108] C. Costain et al. "Two-way time transfer via geostationary satellites NRC/NBS, NRC/USNO and NBS/USNO via Hermes and NRC/LPTF (France) via Symphonie". In: *Proc. 11th Annual PTTI Meeting*. 1979.

[109] L. et al Veenstra et al. "Frequency and time coordination via satellite". In: *Comsat Technical Review* 11 (1981), pp. 369–402.

[110] Ph. Hartl et al. "High accuracy global time transfer via geosynchronous telecommunication satellites with Mitrex". In: *Zeitschrift fur Flugwissenschaften und Weltraumforschung* 7 (1983), pp. 335–342.

[111] Ph. Hartl et al. *Spread spectrum time transfer experiment via INTELSAT*. Tech. rep. COMSAT LABS CLARKSBURG MD, 1984.

[112] M. Imae et al. "Two-way satellite time and frequency transfer networks in Pacific Rim region". In: *IEEE transactions on instrumentation and measurement* 50.2 (2001), pp. 559–562.

[113] V. Zhang et al. *Two-Way Satellite Time and Frequency Transfer Using 1 MChips/s Codes*. Tech. rep. NATIONAL INSTITUTE OF STANDARDS AND TECHNOLOGY, BOULDER, COLORADO, 2009.

[114] M. Fujieda et al. "Carrier-phase two-way satellite frequency transfer between LNE-SYRTE and PTB". In: *2016 European Frequency and Time Forum (EFTF)*. 2016, pp. 1–4.

[115] *Telstar N11 Footprints*. URL: `https://telesat.com/sites/default/files/satellite/telesat_satellitebrochure_telstar11n.pdf`.

[116] *The operational use of two-way satellite time and frequency transfer employing pseudorandom noise codes*. Recommendation ITU-R TF. 1153-4. ITU, Geneva, Switzerland, 2015.

[117] T.E. Parker and V. Zhang. "Sources of instabilities in two-way satellite time transfer". In: *Proceedings of the 2005 IEEE International Frequency Control Symposium and Exposition, 2005.* IEEE. 2005, pp. 745–751.

[118] D. Piester et al. "Studies on instabilities in long-baseline two-way satellite time and frequency transfer (TWSTFT) including a troposphere delay model". In: *Proc. 39th Annual Precise Time and Time Interval (PTTI) Systems and Applications Meeting, 27-29 Nov 2007, Long Beach, California, USA*. 2007, pp. 211–222.

[119] W.-H. Tseng et al. "Sagnac effect and diurnal correction on two-way satellite time transfer". In: *IEEE Transactions on Instrumentation and Measurement* 60.7 (2010), pp. 2298–2303.

[120] *SR620 Universal Time Interval Counter - Operating Manual and Programming Reference*.

[121] F.G. Ascarrunz, T.E. Parker, and S.R. Jefferts. *Pseudo-random code correlator timing errors due to multiple reflections in transmission lines*. Tech. rep. COLORADO UNIVERSITY AT BOULDER, 1998.

[122] F.G. Ascarrunz, T.E. Parker, and S.R. Jefferts. "Group-delay errors due to coherent interference". In: *Proceedings of the 1999 Joint Meeting of the European Frequency and Time Forum and the IEEE International Frequency Control Symposium (Cat. No. 99CH36313)*. Vol. 1. IEEE. 1999, pp. 198–202.

[123] T. Gotoh, M. Fujieda, and J. Amagai. "Comparison study of GPS carrier phase and two-way satellite time and frequency transfer". In: *2007 IEEE International Frequency Control Symposium Joint with the 21st European Frequency and Time Forum*. IEEE. 2007, pp. 1188–1193.

[124] V. Zhang and T. E. Parker. "A study of the diurnal in the transatlantic TWSTFT difference". In: *Proc. 2013 Asia-Pacific Time and Frequency (ATF) Workshop*. 2013.

[125] V. Zhang, T. Parker, and Sh. Zhang. "A study on reducing the diurnal in the Europe-to-Europe TWSTFT links". In: *2016 European Frequency and Time Forum (EFTF)*. IEEE. 2016, pp. 1–4.

[126] W Schäfer, A. Pawlitzki, and T. Kuhn. "Extension of two-way satellite time- and frequency transfer method to real-time operation and carrier phase measurements". In: *Proceedings of the 1999 Joint Meeting of the European Frequency and Time Forum and the IEEE International Frequency Control Symposium (Cat. No. 99CH36313)*. Vol. 1. IEEE. 1999, pp. 203–207.

[127] B. Fonville et al. *Development of carrier-phase-based two-way satellite time and frequency transfer (TWSTFT)*. Tech. rep. NAVAL OBSERVATORY WASHINGTON DC, 2005.

[128] M. Fujieda et al. "Carrier-phase-based two-way satellite time and frequency transfer". In: *IEEE transactions on ultrasonics, ferroelectrics, and frequency control* 59.12 (2012), pp. 2625–2630.

[129] W. Schäfer, A. Pawlitzki, and T. Kuhn. *New trends in two-way time and frequency transfer via satellite*. Tech. rep. TIMETECH GMBH STUTTGART (GERMANY), 1999.

[130] A. Kanj, J. Achkar, and D. Rovera. "Characterization of OP TWSTFT stations in colocation based on combined use of code and carrier phase data". In: *2012 European Frequency and Time Forum*. IEEE. 2012, pp. 477–482.

[131] M. Fujieda et al. "Carrier-phase two-way satellite frequency transfer over a very long baseline". In: *Metrologia* 51.3 (2014), p. 253.

[132] G. Petit and Z. Jiang. "GPS All in View time transfer for TAI computation". In: *Metrologia* 45.1 (2007), pp. 35–45.

[133] P. Defraigne and G. Petit. "Time transfer to TAI using geodetic receivers". In: *Metrologia* 40.4 (2003), p. 184.

[134] K. M. Larson et al. "Assessment of GPS carrier-phase stability for time-transfer applications". In: *IEEE Transactions on Ultrasonics, Ferroelectrics, and Frequency Control* 47.2 (2000), pp. 484–494. ISSN: 1525-8955.

[135] Z. Jiang, G. Petit, and P. Defraigne. "Combination of GPS carrier phase data with a calibrated time transfer link". In: *2007 IEEE International Frequency Control Symposium Joint with the 21st European Frequency and Time Forum*. IEEE. 2007, pp. 1182–1187.

[136] J. Kouba and P. Héroux. "Precise Point Positioning Using IGS Orbit and Clock Products". In: *GPS Solutions* 5 (2001), pp. 12–28.

[137] P. Defraigne, C. Bruyninx, and N. Guyennon. "PPP and phase-only GPS time and frequency transfer". In: *2007 IEEE International Frequency Control Symposium Joint with the 21st European Frequency and Time Forum*. IEEE. 2007, pp. 904–908.

[138] J. Ray and K. Senior. "Geodetic techniques for time and frequency comparisons using GPS phase and code measurements". In: *Metrologia* 42.4 (2005), p. 215.

[139] P. Defraigne and C. Bruyninx. "On the link between GPS pseudorange noise and day-boundary discontinuities in geodetic time transfer solutions". In: *GPS Solutions* 11.4 (2007), pp. 239–249. ISSN: 1521-1886.

[140] D. Orgiazzi, P. Tavella, and F. Lahaye. "Experimental assessment of the time transfer capability of precise point positioning (PPP)". In: *Proceedings of the 2005 IEEE International Frequency Control Symposium and Exposition, 2005.* IEEE. 2005, pp. 337–345.

[141] Delporte J. et al. "GPS Carrier-Phase Time Transfer Using Single-Difference Integer Ambiguity Resolution". In: *International Journal of Navigation and Observation* (2008).

[142] D. Laurichesse et al. "Integer Ambiguity Resolution on Undifferenced GPS Phase Measurements and Its Application to PPP and Satellite Precise Orbit Determination". In: *NAVIGATION* 56.2 (2009), pp. 135–149.

[143] G. Petit et al. "Sub 10^{-16} frequency transfer with IPPP: Recent results". In: *Frequency and Time Forum and IEEE International Frequency Control Symposium (EFTF/IFC), 2017 Joint Conference of the European*. IEEE. 2017, pp. 784–787.

[144] Piester D., Hetzel P., and Bauch A. "Recent time and frequency activities at PTB". In: *Proc. 34th Annual Precise Time and Time Interval (PTTI) Systems and Applications Meeting*. 2002, pp. 457–464.

[145] Sh.-Y. Lin and W.-H. Tseng. "The Portable Cesium Clock Time Transfer at the Nano Second Level". In: *Proceedings of the 51st Annual Precise Time and Time Interval Systems and Applications Meeting*. 2020.

[146] C. G. Parthey et al. "Improved Measurement of the Hydrogen $1S - -2S$ Transition Frequency". In: *Phys. Rev. Lett.* 107 (20 2011), p. 203001.

[147] S. Schiller et al. "The space optical clocks project: Development of high performance transportable and breadboard optical clocks and advanced subsystems". In: *2012 European Frequency and Time Forum*. 2012, pp. 412–418.

[148] J. Cao et al. "A compact, transportable single-ion optical clock with 7.8×10^{-17} systematic uncertainty". In: *Applied Physics B* 123.4 (2017), p. 112.

[149] S. Hannig et al. "Towards a transportable aluminium ion quantum logic optical clock". In: *Review of Scientific Instruments* 90.5 (2019), p. 053204.

[150] J. Grotti et al. "Geodesy and metrology with a transportable optical clock". In: *Nature Physics* (2018).

[151] D. Calonico et al. "High-accuracy coherent optical frequency transfer over a doubled 642-km fiber link". In: *Applied Physics B* 117.3 (2014), pp. 979–986.

[152] S. Droste et al. "Optical-frequency transfer over a single-span 1840 km fiber link". In: *Physical review letters* 111.11 (2013), p. 110801.

[153] P. A. Williams, W. C. Swann, and N. R. Newbury. "High-stability transfer of an optical frequency over long fiber-optic links". In: *JOSA B* 25.8 (2008), pp. 1284–1293.

[154] S. M. Foreman et al. "Remote transfer of ultrastable frequency references via fiber networks". In: *Review of Scientific Instruments* 78.2 (2007), p. 021101.

[155] *OFTEN: Optical Frequency Transfer - a European Network*. URL: `https://www.ptb.de/emrp/often_home.html`.

[156] D. Calonico et al. "The Italian optical link for time and frequency". In: *2017 Joint Conference of the European Frequency and Time Forum and IEEE International Frequency Control Symposium (EFTF/IFCS)*. 2017, pp. 156–159.
[157] Kronjaeger, J. "The TiFOON Project - Time and Frequency Over Optical Networks". In: *International Congress of Metrology*. Ed. by Array. 2019, p. 15001.
[158] D. Piester et al. "Time transfer through optical fibers (TTTOF): first results of calibrated clock comparisons". In: *Proc. 41st Annual Precise Time and Time Interval (PTTI) Systems and Applications Meeting, 16-19 Nov 2009, Santa Ana Pueblo, New Mexico, USA*. 2010, pp. 89–99.
[159] M. Rost et al. "Time transfer through optical fibres over a distance of 73 km with an uncertainty below 100 ps". In: *Metrologia* 49.6 (2012), p. 772.
[160] Z. Jiang et al. "Comparing a GPS time link calibration with an optical fibre self-calibration with 200 ps accuracy". In: *Metrologia* 52.2 (2015), pp. 384–391.
[161] S.-C. Ebenhag. "Time transfer over a 560 km fiber link". In: *European Frequency and Time Forum, EFTF'08, Toulouse, France, Apr.. 22-25, 2008*. 2008.
[162] V. Smotlacha, A. Kuna, and W. Mache. "Time transfer using fiber links". In: *EFTF-2010 24th European Frequency and Time Forum*. 2010, pp. 1–8.
[163] V. Smotlacha and A. Kuna. "Two-way optical time and frequency transfer between IPE and BEV". In: *2012 European Frequency and Time Forum*. 2012, pp. 375–378.
[164] O. Lopez et al. "Simultaneous remote transfer of accurate timing and optical frequency over a public fiber network". In: *Applied Physics B* 110.1 (2013), pp. 3–6.
[165] L. Hu et al. "A 300-kilometer optical fiber time transfer using bidirectional TDM dissemination". In: *Proc. 46th ION PTTI Meeting*. 2014, pp. 41–4.
[166] J. Kodet, P. Pánek, and I. Procházka. "Two-way time transfer via optical fiber providing subpicosecond precision and high temperature stability". In: *Metrologia* 53.1 (2015), p. 18.
[167] C. Grebing et al. "Realization of a timescale with an accurate optical lattice clock". In: *Optica* 3.6 (2016), pp. 563–569.
[168] Ph. Hartl and W. Schäfer. "Nutzung der Spread-Spectrum-Technik bei Kombination der Aspekte Navigation und Telekommunikation in Satellitensystemen (Teil I)". In: *Frequenz* 41.11-12 (1987), pp. 321–328.
[169] URL: `http://www.csgnetwork.com/julianmodifdateconv.html`.
[170] W Schäfer. private communication. 2014.
[171] *Report on the evaluation of relativistic effects for time and frequency transfer using TWSTFT*. Tech. rep. LNE-SYRTE, NPL, 2014.
[172] G. Petit and P. Wolf. "Relativistic theory for picosecond time transfer in the vicinity of the Earth". In: *Astronomy and Astrophysics* 286 (1994).
[173] L. Duchayne, F. Mercier, and P. Wolf. "Orbit determination for next generation space clocks". In: *Astronomy & Astrophysics* 504.2 (2009), pp. 653–661.
[174] *Method for applying the theory and available data to evaluate relativistic effects in TWSTFT*. Tech. rep. NPL, LNE-SYRTE, 2013.
[175] *Astra 3B wide beam foot print*. URL: `https://www.ses.com/our-coverage#/explore/satellite/337`.
[176] E. Benkler. private communication. 2015.
[177] J. Achkar et al. "Study of the OP-PTB link by carrier-phase two-way satellite time and frequency transfer". In: *2016 Conference on Precision Electromagnetic Measurements (CPEM 2016)*. 2016, pp. 1–2.

[178] B. Iglewicz and D. Hoaglin. *How to Detect and Handle Outliers*. Ed. by E. F. Mykytka. Vol. 16. The ASQC Basic References in Quality Control: Statistical Techniques. ASQC Quality Press, 1993.

[179] K. Lagler et al. "GPT2: Empirical slant delay model for radio space geodetic techniques". In: *Geophysical Research Letters* 40.6 (2013), pp. 1069–1073.

[180] J. A. Klobuchar. "Global Positioning System: Theory and Applications Volume 1". In: ed. by Bradford W. Parkinson and James J. Spilker Jr. American Institute of Aeronautics and Astronautics, Inc., 1996. Chap. Ionospheric effects on GPS, pp. 485–516.

[181] *GNSS Data Processing: Volume 1: Fundamentals and Algorithms*. ESA Communications, 2013.

[182] G. Xu. "GPS - Theory, Algorithms and Applications". In: Springer-Verlag Berlin Heidelberg New York, 2003. Chap. Physical Influences of GPS Surveying: Ionospheric effects, pp. 39–50.

[183] *NOAA website on TEC data for North America*. URL: `https://www.swpc.noaa.gov/products/north-american-total-electron-content`.

[184] *JPL website on ionospheric data*. URL: `https://iono.jpl.nasa.gov/index.html`.

[185] *Ionosphere GNSS products provided by ROB*. Retrieved in July 2017. URL: `ftp://gnss.oma.be/gnss/products/IONEX/`.

[186] *Satellite Lookout Angle Calculator*. Retrieved August 2017. URL: `http://www.satellite-calculations.com/Satellite/lookangles.htm`.

[187] R.J. Cosentino and D.W. Diggle. "Understanding GPS - Principles and Applications". In: ed. by Elliot D. Kaplan. Artech House Publishers Boston London, 1996. Chap. Differential GPS, pp. 321–383.

[188] E. M. Soop. "Handbook of Geostationary Orbits". In: Springer Netherlands, 1994. Chap. Perturbed Orbits, pp. 68–96.

[189] Ch. F. A. Baynham et al. "Absolute frequency measurement of the optical clock transition in with an uncertainty of using a frequency link to international atomic time". In: *Journal of Modern Optics* 65.5-6 (2018), pp. 585–591.

[190] J. Guéna et al. "Evaluation of Doppler Shifts to Improve the Accuracy of Primary Atomic Fountain Clocks". In: *Phys. Rev. Lett.* 106.13 (2011), p. 130801.

[191] J. Guéna et al. "Contributing to TAI with a secondary representation of the SI second". In: *Metrologia* 51.1 (2014), p. 108.

[192] BIPM Circular T. URL: `http://www.bipm.org/jsp/en/TimeFtp.jsp`.

[193] C. Voigt, H. Denker, and L. Timmen. "Time-variable gravity potential components for optical clock comparisons and the definition of international time scales". In: *Metrologia* 53.6 (2016), p. 1365.

[194] H. Denker et al. "Geodetic methods to determine the relativistic redshift at the level of 10^{-18} in the context of international timescales: a review and practical results". In: *Journal of Geodesy* 92.5 (2018), pp. 487–516. ISSN: 1432-1394.

[195] P. Delva, H. Denker, and G. Lion. "Chronometric Geodesy: Methods and Applications". In: *Relativistic Geodesy: Foundations and Applications*. Ed. by Dirk Puetzfeld and Claus Lämmerzahl. Fundamental Theories of Physics. Cham: Springer International Publishing, 2019, pp. 25–85.

[196] D. Chambon et al. "Design and metrological features of microwave synthesizers for atomic fountain frequency standard". In: *IEEE transactions on ultrasonics, ferroelectrics, and frequency control* 54.4 (2007), pp. 729–735.

[197] N. F. Zhang. "Calculation of the uncertainty of the mean of autocorrelated measurements". In: *Metrologia* 43.4 (2006), S276.

[198] A. Zięba. "Effective number of observations and unbiased estimators of variance for autocorrelated data-an overview". In: *Metrology and Measurement Systems* 17.1 (2010), pp. 3–16.

[199] A. Zięba and P. Ramza. "Standard deviation of the mean of autocorrelated observations estimated with the use of the autocorrelation function estimated from the data". In: *Metrology and Measurement Systems* 18.4 (2011), pp. 529–542.

[200] H. Hachisu et al. "Direct comparison of optical lattice clocks with an intercontinental baseline of 9000 km". In: *Optics letters* 39.14 (2014), pp. 4072–4075.

[201] J. Prillaman et al. *Continued Evaluation of Carrier-Phase GNSS Timing Receivers for UTC/TAI Applications*. Tech. rep. NAVAL OBSERVATORY WASHINGTON DC, 2010.

[202] J. Ray and K. Senior. "IGS/BIPM pilot project: GPS carrier phase for time/frequency transfer and timescale formation". In: *Metrologia* 40.3 (2003), S270.

[203] U. Weinbach. *Feasibility and impact of receiver clock modeling in precise GPS data analysis*. Univ., 2013.

[204] F. Riehle et al. "The CIPM list of recommended frequency standard values: guidelines and procedures". In: *Metrologia* 55.2 (2018), p. 188.

[205] J. Guéna et al. "First international comparison of fountain primary frequency standards via a long distance optical fiber link". In: *Metrologia* 54.3 (2017), p. 348.

[206] J. Leute et al. "Frequency Comparison of 171 Yb^+ Ion Optical Clocks at PTB and NPL via GPS PPP". In: *IEEE transactions on ultrasonics, ferroelectrics, and frequency control* 63.7 (2016), pp. 981–985.

[207] W.-H. Tseng and Sh.-Y. Lin. "A Survey of Time Transfer via a Bidirectional Fiber Link for Precise Calibration Services". In: *NCSLI Measure* 8.2 (2013), pp. 70–77.

[208] G. D. Rovera et al. "GNSS antenna multipath effects". In: *2018 European Frequency and Time Forum (EFTF)*. 2018, pp. 208–212.

[209] M. Fujieda et al. "Advanced satellite-based frequency transfer at the 10- 16 level". In: *IEEE transactions on ultrasonics, ferroelectrics, and frequency control* 65.6 (2018), pp. 973–978.

[210] M. Fujieda, R. Tabuchi, and T. Gotoh. "A New TWSTFT Modem with Code and Carrier Phases". In: *2019 Joint Conference of the IEEE International Frequency Control Symposium and European Frequency and Time Forum (EFTF/IFC)*. IEEE. 2019, pp. 1–2.

[211] Y.-J. Huang et al. "Stability improvement of an operational two-way satellite time and frequency transfer system". In: *Metrologia* 53.2 (2016), pp. 881–890.

[212] Z. Jiang et al. "Use of software-defined radio receivers in two-way satellite time and frequency transfers for UTC computation". In: *Metrologia* 55.5 (2018), pp. 685–698.

[213] D. Xu et al. "Reciprocity of propagation in optical fiber links demonstrated to 10^{-21}". In: *Opt. Express* 27.25 (2019), pp. 36965–36975.

[214] P. Krehlik et al. "CLONETS - clock network services: Strategy and innovation for clock services over optical-fibre networks". In: *2017 19th International Conference on Transparent Optical Networks (ICTON)*. 2017, pp. 1–2.

[215] C. Clivati et al. "Optical frequency transfer over submarine fiber links". In: *Optica* 5.8 (2018), pp. 893–901.

[216] T. Ido et al. “Intercontinental Comparison of Lattice Clocks Using a Broadband VLBI Technique”. In: *2019 Joint Conference of the IEEE International Frequency Control Symposium and European Frequency and Time Forum (EFTF/IFC)*. 2019, pp. 1–2.

[217] H. Leopardi et al. “Measuring Optical Frequency Ratios with Uncertainties Below 1017 via the Boulder Atomic Clock Network”. In: *2019 Conference on Lasers and Electro-Optics (CLEO)*. 2019, pp. 1–2.

[218] T.J. Witt. “Practical methods for treating serial correlations in experimental observations”. In: *The European Physical Journal Special Topics* 172.1 (2009), pp. 137–152.

[219] M.B. Priestley. *Spectral Analysis and Time Series*. Elsevier Amsterdam, 1981.

[220] N. F. Zhang. “Estimating process capability indexes for autocorrelated data”. In: *Journal of Applied Statistics* 25.4 (1998), pp. 559–574.

[221] G. E.P. Box et al. *Time Series Analysis: Forecasting and Control*. 5th Edition. Wiley Series in Probability and Statistics, 2016.

Acknowledgements

This work was carried out within a huge collaboration and the involvement of many people. First of all, I would like to thank my supervisor Ekkehard Peik, as well as Tanja Mehlstäubler and Philip Tuckey for examining this work.

Furthermore I am thankful to the whole ITOC consortium for the fruitful collaboration. Although the clock comparison campaign presented here is only a fraction of the whole ITOC project, the list of people involved is still very long. I would like to thank all of them for the effort, and for the data provided by them to our group at PTB. Special thanks goes to Ilaria Sesia, Joseph Achkar and Peter Whibberley for coordinating the TWSTFT measurements at INRIM, LNE-SYRTE and NPL, and for the discussions about TWSTFT and data analysis. I would also like to mention Helen Margolis and thank her for coordinating the ITOC project.

Some people who were not part of the official (original) ITOC consortium supported this work: I would like to thank Wolfgang Schäfer from TimeTech GmbH for sharing his insights on the SATRE modem, the colleagues from NICT, Miho Fujieda and Hiroshi Takiguchi, for providing the TWCP equipment and data, and Pascale Defraigne and Daniele Rovera for processing the GPS data, and for discussions and support within this subject.

I am thankful to the whole Time and Frequency group of PTB, including the colleagues from the fiber links and the Sr clocks, for all the discussions and the working environment. Especially I would like to thank the Time Dissemination group of PTB, Andreas Bauch, Dirk Piester, Julia Leute, Jürgen Becker, Thomas Polewka and Egle Staliuniene, for all their support. I am grateful to Andreas Bauch for giving me the opportunity to do the PhD in this field. Apart from the scientific work, I enjoyed the discussions about political and social topics with Julia – the arguments for veganism come in handy now. A special thanks goes also to Johannes Rahm for his motivational support and for never being tired to counter my pessimism.

In addition, I am grateful to my new colleagues at SYRTE for their endless patience with me finishing this work and for providing me the time needed. Without this, it would not have been possible for me to arrive at this point. Merci beaucoup !

Finally, I would like to mention the most important people: First, Erik Benkler, who, as the work package leader, has been the person I have worked closest with for all ITOC-related matters, and who had always been full of ideas. I would like to thank him for his extraordinary efforts not only for ITOC but also for investing a lot of his time and energy in PhD-student guidance. Second, Dirk Piester, who offered me both scientific and motivational backup in every situation. I am grateful for all his help for this work, also for proof-reading this manuscript carefully in the past months, but also for all the time he took to discuss and explain things in general. Special thanks goes also to Pierre Uhrich for his patience, his support for this work during my time at SYRTE and for making it possible that I had the time to finish this work.

Of course, I would also like to thank my family and friends who supported me during all these years and had been always there for me. Thank you!